



Università degli Studi di Genova

Facoltà di Scienze Matematiche, Fisiche e Naturali

PhD Thesis XXIII Cycle

**Searching for the muon decay  $\mu^+ \rightarrow e^+\gamma$ :  
the problem of the high resolution measurement  
of positron timing**

Dr. Matteo De Gerone

Supervisor:

Prof. Flavio Gatti

March 2011



*“The road of excess leads to the palace of wisdom.”*

*– William Blake*



# Contents

<b>Introduction</b>	<b>ix</b>
<b>1 The muon decay in the Standard Model</b>	<b>1</b>
1.1 The Standard Model . . . . .	1
1.1.1 The Lagrangian of the Standard Model . . . . .	2
1.1.2 Spontaneous symmetry breaking . . . . .	4
1.1.3 The muon decay in the Standard Model . . . . .	6
1.1.4 Neutrino mass and mixing . . . . .	7
1.1.5 $\mu^+ \rightarrow e^+\gamma$ decay in Standard Model with massive neutrinos	10
1.2 Physics beyond the Standard Model . . . . .	11
1.2.1 Standard Model open questions . . . . .	11
1.2.2 Grand Unified Theory . . . . .	13
1.2.3 Supersymmetric theory . . . . .	14
1.3 Muon decay in the new Models . . . . .	16
1.4 Muon decay phenomenology and history . . . . .	21
1.4.1 Event signature . . . . .	21
1.4.2 Physics background . . . . .	21
1.4.3 Accidental background . . . . .	22
1.4.4 History of the $\mu^+ \rightarrow e^+\gamma$ searches . . . . .	24
<b>2 The MEG Experiment</b>	<b>27</b>
2.1 Beam and target . . . . .	29
2.2 Positron spectrometer . . . . .	31
2.2.1 COBRA magnet . . . . .	33
2.2.2 Drift chambers . . . . .	38
2.2.3 Timing Counter . . . . .	40
2.3 Liquid Xenon calorimeter . . . . .	40
2.4 Trigger system . . . . .	44
2.5 DAQ system . . . . .	46
2.6 Experimental apparatus performances . . . . .	48
<b>3 The Longitudinal Timing Counter</b>	<b>49</b>
3.1 Detector concept and design . . . . .	49
3.2 Timing generalities . . . . .	51
3.3 Contributions to timing resolution . . . . .	53

3.3.1	PMTs transit time spread . . . . .	53
3.3.2	Scintillator time response and time of flight spread . . . . .	54
3.3.3	Energy release in the bar . . . . .	55
3.3.4	Expected performances . . . . .	56
3.4	Timing Counter design criteria . . . . .	56
3.4.1	PMT choice and characterization . . . . .	56
3.4.2	Scintillator . . . . .	61
3.4.3	Read out electronic and time extraction from data . . . . .	64
3.5	Final test . . . . .	66
<b>4</b>	<b>The Transverse Timing Counter</b>	<b>67</b>
4.1	Detector concept . . . . .	67
4.2	APD characterization . . . . .	69
4.2.1	Breakdown measurement . . . . .	70
4.2.2	Dark current characterization . . . . .	73
4.2.3	Gain characterization . . . . .	75
4.3	Scintillating fibers characterization . . . . .	76
4.3.1	Trapping efficiency . . . . .	77
4.3.2	Attenuation length . . . . .	78
4.3.3	Emission spectrum . . . . .	79
4.3.4	Geometrical effects on light loss . . . . .	79
4.4	Electronic readout . . . . .	86
4.4.1	Signal processing and signal to noise ratio . . . . .	86
4.4.2	Positron impact point resolution . . . . .	92
4.4.3	Efficiency . . . . .	93
<b>5</b>	<b>A study on TC calibration tools</b>	<b>95</b>
5.1	Gain equalization . . . . .	95
5.1.1	PMTs gain equalization . . . . .	96
5.1.2	Bar energy response equalization . . . . .	97
5.2	Time Walk correction . . . . .	98
5.2.1	Low level threshold optimization . . . . .	100
5.2.2	Further improvements in time walk correction . . . . .	101
5.3	Offsets equalization . . . . .	103
5.3.1	Interbar offset with cosmic . . . . .	103
5.3.2	Interbar offset with drift chambers . . . . .	108
5.4	High level threshold optimization . . . . .	109
5.5	TC-LXE calibration . . . . .	109
5.5.1	Boron sample . . . . .	110
5.5.2	Dalitz sample . . . . .	115
<b>6</b>	<b>The Timing Counter performances</b>	<b>117</b>
6.1	Study of intrinsic Timing Counter resolution . . . . .	117
6.1.1	Fit of the time difference distributions . . . . .	119
6.1.2	Run 2010 timing resolutions . . . . .	120

---

6.1.3	Resolutions stability . . . . .	123
6.1.4	Comparison between 2010-2009 results . . . . .	123
6.2	The $t_{e\gamma}$ resolution: the radiative decay sample . . . . .	127
6.3	Impact point resolution . . . . .	128
<b>7</b>	<b>Physics analysis and results</b>	<b>133</b>
7.1	Blinding box . . . . .	133
7.2	Probability density function . . . . .	134
7.2.1	Signal PDF . . . . .	135
7.2.2	Radiative decay PDF . . . . .	138
7.2.3	Accidental background PDF . . . . .	139
7.3	Likelihood analysis . . . . .	139
7.4	Normalization scheme . . . . .	142
7.5	Confidence level scan . . . . .	144
7.6	Upper limit on $\mu^+ \rightarrow e^+\gamma$ branching ratio . . . . .	144
	<b>Conclusions</b>	<b>147</b>
	<b>A Background</b>	<b>149</b>
A.1	Physics background . . . . .	149
A.2	Accidental background . . . . .	150
	<b>Bibliography</b>	<b>153</b>
	<b>List of Figures</b>	<b>159</b>
	<b>List of Tables</b>	<b>167</b>



# Introduction

The MEG (Muon to Electron Gamma) experiment aims to investigate the Lepton Flavour Violating (LFV) decay  $\mu \rightarrow e\gamma$  with a goal sensitivity on the Branching Ratio (BR) of  $10^{-13}$ , 2 order of magnitudes better than the current limit set by the MEGA collaboration.

The  $\mu \rightarrow e\gamma$  decay is a sensitive probe for searching new physics beyond the Standard Model (SM). In the SM itself, due to accidental symmetries, the lepton flavour violating decays in the charged sector are strongly suppressed (BR  $< 10^{-55}$ ), also taking into account the phenomenon of neutrino oscillations.

Conversely, in almost all the proposed extensions of the SM there are mechanism enhancing the BR for the  $\mu \rightarrow e\gamma$  close to  $10^{-13}$ , making it observable with a dedicated precision experiment.

In spite of the simple kinematics of the  $\mu \rightarrow e\gamma$  decay, whose signature is the observation of positron and gamma emitted collinearly in time coincidence with equal energy, the need for a high muon decay rate source poses severe background issues. In order to push the sensitivity of the  $\mu \rightarrow e\gamma$  decay BR down to 2 order of magnitude better than the existing limit, the whole experimental apparatus should obtain unprecedented resolutions on the observables characterizing the event: positron and photon energy, direction and timing.

This Ph.D. thesis deals with the development, the calibrations and the analysis of the Timing Counter (TC), the detector mainly devoted to the high resolution measurement of the positron timing. Moreover, the TC must provide a fast and efficient trigger signal to the data acquisition, and also give a precise measurement of the positron impact position on the detector itself. In order to obtain the best performances, the detector is split in two sub-detectors (namely longitudinal TC and transverse TC), each optimized for different complementary tasks.

The work is structured as follow: in chapter 1 a short theoretical introduction to the SM is given. The phenomenon of neutrino oscillations and the consequent modifications to the SM are explained. Then some new theories beyond the SM are introduced, together with their influences on muon decay phenomenology. Moreover, a description of the  $\mu \rightarrow e\gamma$  decay features is given, with particular attention to background sources, from which the experimental requirements needed to obtain the planned resolutions.

Chapter 2 fully describes each part of the MEG detector: the beam line, the positron magnetic spectrometer, the photon detector and the trigger and DAQ system.

Chapters 3 to 6 describe the TC role inside the MEG apparatus, from the basic development process to the final performances through the basic operating principles and detailed calibration developed in the commissioning stage. In particular, in chapter 3 the development and the basic operations of the longitudinal TC are exposed. The choice of the devices and their characteristics are described, together with the measurement performed in the detector R&D period in order to achieve the target resolution.

In chapter 4 the transverse Timing Counter will be described. Also in this case all the measurements made in the preliminary tests are reported. Moreover, some results about the  $z$  resolution and the detector efficiency are quoted.

Chapter 5 describes the calibration methods developed for the longitudinal TC in order to obtain the best from the detectors alone and to optimize the interfacing with the whole MEG apparatus. The results strictly connected with the Timing Counter performances such as timing and positioning resolutions and the detector stability are described in chapter 6.

Finally, in chapter 7 a summary of the data analysis strategy, together with the results achieved during the 2008 physics run will be given.

# Chapter 1

## The muon decay in the Standard Model

In this chapter the status of the knowledge about the muon decay in the context of Standard Model (SM), the theory that actually describes elementary particles and their interactions, will be reviewed. As we will see, events violating the lepton flavour conservation law are forbidden or strongly suppressed in this context, depending on the assumption on neutrino mass.

Anyway, currently the SM is not considered a definitive theory: although it describes with high precision a huge category of phenomena, some questions remain unanswered and new theories are proposed to explain this issues. Some of these theories predict measurable branching ratio for Lepton Flavour Violating (LFV) events like  $\mu \rightarrow e + \gamma$ . In this framework, the observation of such kind of events will be a proof of the existence of new physics beyond the Standard Model.

### 1.1 The Standard Model

The Standard Model is the theory that currently explains the interactions between elementary particles, in terms of a Lagrangian density with elementary fields as canonical variables associated to the particles, invariant under a set of local transformations (*gauge transformations*), which can be represented by a symmetry group. The vector bosons mediating the fundamental interactions are strongly related to the generators of the gauge group itself. The model is exhaustively represented by the  $SU(3)_C \times SU(2)_L \times U(1)_Y$  symmetry group, which describes the strong, weak and electromagnetic interactions. This symmetry is spontaneously broken at the energy scale of  $\sim 100 GeV$ , reducing to  $SU(3)_C \times U(1)_{em}$ <sup>1</sup>.

The model takes into account 3 generations of spin 1/2 fermions, (in each generation 2 quarks, 1 charged lepton and 1 neutral lepton),  $8 \oplus 3 \oplus 1$  vector bosons mediating the fundamental interactions and 1 scalar boson not yet observed, but which introduction is necessary to obtain the spontaneous symmetry breaking re-

---

<sup>1</sup>As a general reference for chapter 1 see [1], [2], [3], [4]

sulting in the introduction of particle masses in a gauge invariant way.

The  $SU(3)_C$  symmetry is connected with the invariance respect to rotation in the quark color space, and the 8 gluons mediating the strong interaction are related to the  $n^2 - 1$  generators of this group. The quarks are assigned to the fundamental representation of the group, the vector bosons to the adjoint one, and all the particles not influenced by strong interaction are assigned to the trivial one.

The  $SU(2)_L$  symmetry descends from the invariance, exact as long as the symmetry broken appears, for swapping in the left and right components of particle spinors. Three vector bosons are introduced, which couple only with the left handed component of the fields. For this reason, a new quantum number, the weak isospin  $T$ , is introduced. It is also more convenient to express the particles in terms of Weyl spinors, that means spinors with defined helicity<sup>2</sup>. The right handed components are assigned to the trivial representation ( $T = 0$ ), while to the fundamental representation of the group are then associated the left handed components, organized in doublets ( $T = 1/2$ ):

$$Q_L^i = \begin{pmatrix} u_L^i \\ d_L^i \end{pmatrix}, \quad L_L^i = \begin{pmatrix} \nu_L^i \\ e_L^i \end{pmatrix}, \quad (i = 1, 2, 3) \quad (1.1)$$

where  $Q$  and  $L$  represent respectively the quark and the lepton sector, the index  $L$  remind that only the left handed component interacts and the index  $i$  takes into account the three generations.

Finally, the  $U(1)_Y$  symmetry is associated to the invariance respect a phase transformation of the spinor fields. Another boson vector is correlated to this symmetry. Moreover a new quantum number, the hypercharge, defined by the Gell-Mann-Nishijima relation, is introduced:

$$Q = T_3 + \frac{Y}{2}, \quad (1.2)$$

where  $Q$  is the electric charge,  $T_3$  the third component of the weak isospin and  $Y$  the hypercharge.

The introduction of a mass term for the fermions via the definition of a scalar field breaks the chiral symmetry and induces mass terms also for the vector bosons of the  $SU(2)$  group, modifying also the characteristic of the boson correlated to the hypercharge symmetry, and thus leading to the well known electroweak interactions.

In the next section we will see this mechanism more in details.

### 1.1.1 The Lagrangian of the Standard Model

The Lagrangian of the Standard Model is built starting from the kinetic term for a free fermionic field:

---

<sup>2</sup>The helicity is defined as the projection of the spin  $\vec{s}$  onto the direction of momentum,  $\vec{p}$ :  
 $h = \vec{s} \cdot \vec{p}$

$$\mathcal{L}_{kin} = i\bar{\psi}\gamma^\mu\partial_\mu\psi, \quad (1.3)$$

where  $\psi$  represents a spinor,  $\bar{\psi}$  the conjugate one, and  $\gamma^\mu$  are the Dirac matrices. In order to have eq.1.3 invariant under a gauge transformation, it is necessary to introduce a covariant derivative,  $D^\mu$ :

$$D^\mu = \partial^\mu - igT_a A_a^\mu, \quad (1.4)$$

where  $A_a^\mu$  is the  $a$ -th vector boson of the adjoint representation of the group,  $T_a$  is the  $a$ -th generator of the group itself and  $g$  is the coupling constant between the boson and the spinor field.

Considering the gauge group of the SM, the whole covariant derivative is defined as:

$$D^\mu = \partial^\mu - ig_s \frac{\lambda_a}{2} G_a^\mu - ig \frac{\tau_b}{2} W_b^\mu - ig' Y B^\mu, \quad (1.5)$$

where  $\lambda_a$  ( $a = 1 \div 8$ ) are the  $SU(3)_C$  generators (Gell-Mann matrices),  $G_a^\mu$  are the vector bosons associated with the adjoint representation of the group,  $\tau_b$  ( $b = 1 \div 3$ ) represents the  $SU(2)_L$  generators (Pauli matrices) with  $W_b^\mu$  associated vector bosons,  $B^\mu$  is the boson related to the  $U(1)$  symmetry with hypercharge  $Y$  while  $g_s$ ,  $g$  and  $g'$  are respectively the coupling constant for the interactions.

Having introduced such tool, the interaction terms are automatically absorbed in the kinetic term of the Lagrangian. Moreover, a propagation term for the free boson has to be considered. This is a term like:

$$\mathcal{L}_{kin,bos} = -\frac{1}{4} F_a^{\mu\nu} F_{\mu\nu}^a, \quad (1.6)$$

with  $F^{\mu\nu}$  is defined as:

$$F_a^{\mu\nu} = \partial^\mu A_a^\nu - \partial^\nu A_a^\mu - gf_{abc} A_b^\mu A_c^\nu. \quad (1.7)$$

where  $f_{abc}$  is a set of constants (the *structure constant* of the group).

Before the symmetry breaking and the introduction of the bosonic and fermionic masses, the SM Lagrangian reduces only to the kinetic terms,  $\mathcal{L}_{SM} = \mathcal{L}_{kin}$ .

It is now possible to classify fermions on the basis of the gauge group representation, as shown in tab. 1.1 where quantum numbers of elementary particles are listed.

The Standard Model in its original formulation does not take into account a right handed neutrino field; nevertheless, if it exist, it will be assigned to the trivial representation of each group.

The model as described so far it is still not satisfactory: in fact, it does not include particle masses. In order to fix a mass term in a gauge invariant way, it is necessary to introduce a new scalar field in the theory.

	$G_\mu$	$A_\mu$	$W_\mu$	$Q_{iL}$	$u_{iL}$	$d_{iR}$	$l_{iL}$	$e_{iR}$	$\nu_{iR}$	$H$
$SU(3)_C$	8	1	1	3	3	3	1	1	0	1
$SU(2)_L$	1	3	1	2	1	1	2	1	0	2
$U(1)_Y$	0	0	0	$\frac{1}{6}$	$\frac{2}{3}$	$-\frac{1}{3}$	$-\frac{1}{2}$	-1	0	$\frac{1}{2}$

**Table 1.1:** Quantum numbers of elementary fields in the minimal Standard Model, also including right handed neutrino and Higgs boson. The  $SU(3)_C$ ,  $SU(2)_L$  and  $U(1)_Y$  representations are given.

### 1.1.2 Spontaneous symmetry breaking

A mass term can not be introduced in a straightforward way apart from a scalar field, i.e. a Dirac mass term with the form  $m\bar{\psi}\psi$  should not be allowed in the theory, because of the violation of the gauge invariance.

The introduction of a scalar field with vacuum expectation value (VEV) different from zero non zero masses terms both for fermions and bosons, as a term of interaction with the scalar field itself, without compromising the invariance of the theory.

Thus a new scalar field  $\phi$  (namely the Higgs boson) is assigned to the representation  $(1, 2)_{1/2}$ , as a doublet of weak isospin:

$$\phi = \begin{pmatrix} \phi^+ \\ \phi^0 \end{pmatrix}, \quad (1.8)$$

to which it is assigned a VEV

$$\langle 0|\phi|0\rangle = \begin{pmatrix} 0 \\ \frac{v}{\sqrt{2}} \end{pmatrix}. \quad (1.9)$$

where  $v$  is a free parameter of the theory.

With the introduction of the Higgs field, we obtain two more terms in the Lagrangian; the first one is a propagation and self-interaction term for the Higgs boson:

$$\mathcal{L}_H = (D_\mu\phi)^\dagger (D^\mu\phi) - V(\phi), \quad (1.10)$$

where the most general expression for a renormalizable potential is given by:

$$V(\phi) = -\mu^2\phi^\dagger\phi + \lambda(\phi^\dagger\phi)^2. \quad (1.11)$$

Such potential, conveniently chosen the values for  $\mu$  and  $\lambda$  parameters, gives the correct vacuum expectation value:

$m_W = gv/2$
$m_Z = v/2\sqrt{g^2 + g'^2}$
$m_Z/m_W = g/\sqrt{g^2 + g'^2} = \sqrt{1 - \sin^2\theta_W}$
$m_H = \sqrt{2\lambda}v$
$\sin\theta_W = g'/\sqrt{g^2 + g'^2}$
$e = g\sin\theta_W$

**Table 1.2:** Electroweak bosons masses, Higgs boson masses and electric charge expressed as a function of the SM parameters.

$$\langle\phi\rangle = \sqrt{\frac{\mu^2}{2\lambda}} = \frac{1}{\sqrt{2}}v, \quad v = \frac{\mu}{\sqrt{\lambda}}. \quad (1.12)$$

The physical Higgs mass is given by  $m_H = \sqrt{2\lambda}v$ . This does not affect the gauge invariance of the theory, but permits the existence of a set of 1-dimensional equivalent states, no one invariant for gauge transformation. In this sense we talk about *spontaneous symmetry breaking*. As a result, the gauge group of Standard Model is broken:

$$SU(3)_C \otimes SU(2)_L \otimes U(1)_Y \Rightarrow SU(3)_C \otimes U(1)_{em}. \quad (1.13)$$

The  $SU(3)$  gauge bosons, remain massless. On the other hand, the physical boson vectors result to be linear combinations of the gauge ones:

$$\begin{aligned} W_\mu^\pm &= \frac{W_\mu^1 \mp iW_\mu^2}{\sqrt{2}}, \\ Z_\mu &= -\sin\theta_W B_\mu + \cos\theta_W W_\mu^3, \\ A_\mu &= \cos\theta_W B_\mu + \sin\theta_W W_\mu^3. \end{aligned} \quad (1.14)$$

where  $\theta_W$  is a parameter (*Weimberg angle*) taking into account the *rotation* of the gauge fields, and it is strictly correlated with the coupling constants. While the photon remains massless, the weak interaction bosons acquire mass. The values of the bosons masses as a function of the theory parameters are listed in table1.2 together with the definition of  $\theta_W$  and Higg mass.

The second term created by the introduction of a scalar field is a Yukawa coupling (interaction between two fermions and a scalar field):

$$\mathcal{L}_Y = \bar{Q}_L^i \lambda_u^{ij} \phi^\dagger u_R^j + \bar{Q}_L^i \lambda_d^{ij} \phi d_R^j + \bar{L}_L^i \lambda_e^{ij} \phi e_R^j, \quad (1.15)$$

where  $\lambda_{u,d,e}^{ij}$  are  $3 \times 3$  dimensional matrices.

The introduction of  $\mathcal{L}_Y$  generates mass terms for all the fermions, excluded the neutrinos, because of the absence of a right handed component of the neutrino field. Substituting in eq.1.15 the scalar field  $\phi$  with its vacuum expectation value  $\langle\phi\rangle$  one obtains:

$$\mathcal{L}_Y = v\lambda_u^{ij}\bar{u}_L^i u_R^j + v\lambda_d^{ij}\bar{d}_L^i d_R^j + v\lambda_e^{ij}\bar{e}_L^i e_R^j + h.c. \quad (1.16)$$

The  $\lambda$  matrices that appear in the Yukawa term can be diagonalized by means of a unitary transformation:

$$V_L^\dagger \lambda_{u,d,e} V_R = \lambda_{u,d,e}^{DIAG}, \quad (1.17)$$

in order to obtain the explicit mass term for quarks and leptons generations.

The applied transformation involves in an obvious way the kinetic term of the Lagrangian. The neutral charge interaction term remains invariated; viceversa, the charged current interaction term behaves differently between adronic and leptonic sectors. Concerning the quarks, infact, the charged current can be written as:

$$J^\mu = \bar{d}_L \gamma^\mu V_L^{d\dagger} V_L^u u_L, \quad (1.18)$$

where the  $3 \times 3$  unitary not diagonal matrix  $V = V_L^{d\dagger} V_L^u$  (namely the *Cabibbo-Kobayashi-Maskawa matrix*) takes into account for the flavour transitions in quarks sector.

In the leptonic sector there isn't any an analog mixing matrix: the absence of a neutrino mass term (correlated to the absence of a right handed neutrino term) permits the "rotation" of the  $\nu_L$  field in such a way that charge current interaction is again diagonal in the flavour space. This implies that in the original formulation of the Standard Model transitions in leptonic sector are absolutely forbidden.

This characteristic is also more evident if we observe that the SM Lagrangian is invariant under a set of global trasformations of the spinors like:

$$\psi \rightarrow \psi e^{iL\theta}. \quad (1.19)$$

For each transformation of this kind an associated quantity is conserved (*Noether's theorem*): the SM Lagrangian is invariant under four of such transformations, which correspond to the conservation of the quantum number B (barionic quantum number) and  $L_i$  ( $i=1,2,3$ , leptonic quantum number for each family). Such kind of symmetries, not correlated to the gauge group transformation are called *accidental symmetry*.

### 1.1.3 The muon decay in the Standard Model

The muon interactions in the Standard Model are mediated by the  $A_\mu$ ,  $W_\mu^\pm$ ,  $Z_0$  bosons and the  $H$  field. Referring to the Lagrangian described in the previous section these interactions can be written as:

$$\begin{aligned}
\mathcal{L} &= e\bar{\mu}\gamma^\mu\mu A_\mu \\
&- \frac{g}{\sqrt{2}} (\bar{\nu}_{\mu L}\gamma^\mu\mu_L W_\mu^+ + \bar{\mu}_L\gamma^\mu\nu_{\mu L} W_\mu^-) \\
&- \sqrt{(g^2 + g'^2)} \left[ \bar{\mu}_L\gamma^\mu \left( -\frac{1}{2} + \sin^2\theta_W \right) \mu_L + \bar{\mu}_R\gamma^\mu \sin^2\theta_W \mu_R \right] Z_\mu^0 \\
&- \frac{m_\mu}{v} \bar{\mu}\mu H.
\end{aligned} \tag{1.20}$$

The standard muon decay,  $\mu^+ \rightarrow e^+\nu_e\bar{\nu}_\mu$ <sup>3</sup> is described by the charged weak interaction mediated by the  $W_\mu^\pm$  gauge bosons, namely the second line of eq.1.20. Due to its large mass, the  $W_\mu^\pm$  boson will propagate for a very short distance ( $\simeq 0.0025fm$ ). Thus the decay can be described by the point-like four fermions Fermi interaction given by:

$$\mathcal{L}_{Fermi} = -\frac{G_F}{\sqrt{2}} [\bar{\mu}\gamma^\mu(1 - \gamma^5)\nu_\mu\bar{e}\gamma_\mu(1 - \gamma^5)\nu_e + \bar{\nu}_e\gamma^\mu(1 - \gamma^5)e\bar{\mu}\gamma_\mu(1 - \gamma^5)\nu_\mu], \tag{1.21}$$

where  $G_F$  is the Fermi coupling, connected with the weak constant by the relation:

$$G_F = \frac{g^2}{4\sqrt{2}m_W^2}. \tag{1.22}$$

Eq.1.21 represents the main muon decay mode. Other muon decay modes are listed in tab. 1.3, which shows also upper limits (at 90% of confidence level) for lepton flavour violating decay modes.

### 1.1.4 Neutrino mass and mixing

As already seen in section 1.1.2, lepton flavour conservation is preserved in Standard Model because of vanishing of neutrino masses. Nevertheless, the observation of neutrinos oscillations indirectly shows that neutrinos have non vanishing mass [11], [12].

A mass term for neutrinos can be easily inserted in the Standard Model, adding to the Lagrangian a term like:

$$\mathcal{L}_\nu = \bar{\nu}_{\alpha R}\lambda_{\alpha\beta}^\nu e_{\beta L} H^\dagger + h.c. \tag{1.23}$$

where  $\lambda_{\alpha\beta}^\nu$  is the Yukawa coupling for the neutrino. Having a neutrino mass term, now we have to carefully distinguish between mass eigenstates and interaction eigenstates, because a mixing phenomena analog to what happens in the quark sector can now occur.

<sup>3</sup>Obviously the CPT conjugate decay  $\mu^- \rightarrow e^-\bar{\nu}_e\nu_\mu$  is described by the same term. Here we will refer to the  $m\mu^+$  decay being the kind of particle used in MEG experiment

Decay mode	Branching ratio	Reference
Non LFV modes		
$\mu^+ \rightarrow e^+ \nu_e \bar{\nu}_\mu$	$\simeq 100\%$	
$\mu^+ \rightarrow e^+ \nu_e \bar{\nu}_\mu \gamma$	$1.4 \pm 0.4\% (E_\gamma > 10 MeV)$	[5]
$\mu^+ \rightarrow e^+ \nu_e \bar{\nu}_\mu e^+ e^-$	$(3.4 \pm 0.4) \times 10^{-5}$	[6]
LFV modes		
$\mu^+ \rightarrow e^+ \bar{\nu}_e \nu_\mu$	$< 1.2\%$	[7]
$\mu^+ \rightarrow e^+ \gamma$	$< 1.2 \times 10^{-11}$	[8]
$\mu^+ \rightarrow e^+ e^- e^+$	$< 1.0 \times 10^{-12}$	[9]
$\mu^+ \rightarrow e^+ \gamma \gamma$	$< 7.2 \times 10^{-11}$	[10]

**Table 1.3:** Non-LFV and LFV muon decay modes.

To understand this phenomenon, consider a neutrino beam of definite flavour, produced at some initial time  $t = 0$ ; denoting flavour eigenstates by Greek indices and mass eigenstates by Latin indices, we have [13]:

$$\nu_\alpha = \sum_{i=1}^n U_{\alpha i}^* \nu_i. \quad (1.24)$$

with  $U$  a unitary matrix (known as the Pontecorvo-Maki-Nakagawa-Sakata matrix).

We can now write the Schroedinger equation for the mass eigenstates:

$$i \frac{d}{dt} \nu_i = H \nu_i, \quad (1.25)$$

where  $H$  represents the diagonal Hamiltonian. The time evolution of the mass eigenstates is given by:

$$\nu_i(t) = e^{-i(E_i t - p_i L)} \nu_i(0), \quad (1.26)$$

where  $E_i$ , eigenvalues of  $H$  and  $p_i$  are respectively the neutrinos energy and momentum and  $L$  is the distance travelled in the time interval  $t$ . Considering the fact that neutrinos are almost massless, one has:

$$L \simeq t; \quad E_i = \sqrt{p_i^2 + m_i^2} \simeq p_i + \frac{m_i^2}{2E}, \quad (1.27)$$

where  $m_i$  is the neutrino rest mass. Hence

$$\nu_i(t) \simeq e^{-i(m_i^2/2E_i)L} \nu_i(0) \quad (1.28)$$

Let now consider the time evolution of a neutrino created at  $t_0 = 0$  as an interaction eigenstate; at the generic time  $t$  this state will be described by:

$$\nu_\alpha(t) \simeq \sum_{i=1}^n U_{\alpha i}^* \exp\left(-i \frac{m_i^2}{2E} L\right) \nu_i(0). \quad (1.29)$$

The probability amplitude of observing the flavour  $\beta$  at the distance  $L$  is given by:

$$\begin{aligned} \langle \nu_\beta | \nu_\alpha(L) \rangle &= \sum_{i=1}^n U_{\alpha i}^* \exp\left(-i \frac{m_i^2}{2E} L\right) \sum_{j=1}^n U_{\beta j} \langle \nu_j | \nu_i \rangle \\ &= \sum_{i=1}^n \xi_i^{\alpha\beta} \exp(-i \epsilon_i L), \end{aligned} \quad (1.30)$$

where we have used the unitarity of  $U$  and we have defined:

$$\xi_i^{\alpha\beta} = U_{\alpha i}^* U_{\beta i}; \quad \epsilon_i = \frac{m_i^2}{2E}. \quad (1.31)$$

The corresponding probability is given by

$$\begin{aligned} P_{\nu_\alpha \rightarrow \nu_\beta} = |\langle \nu_\beta | \nu_\alpha \rangle|^2 &= \delta_{\alpha\beta} - 4 \sum_{i=1}^n \sum_{j=i+1}^n \operatorname{Re} \left( \xi_i^{\alpha\beta} \xi_j^{*\alpha\beta} \right) \sin^2 \frac{1}{2} (\epsilon_j - \epsilon_i) L \\ &\quad - 2 \sum_{i=1}^n \sum_{j=i+1}^n \operatorname{Im} \left( \xi_i^{\alpha\beta} \xi_j^{*\alpha\beta} \right) \sin(\epsilon_j - \epsilon_i) L \end{aligned} \quad (1.32)$$

In this scenario the total lepton flavour is still conserved, while the conservation of the individual lepton flavours is violated<sup>4</sup>.

Equation 1.32 takes a simpler form if one assumes CP invariance in the leptonic sector, and that only two flavours are involved in oscillations mechanism. In this case, the matrix  $U$  becomes a real orthogonal matrix depending on a single mixing angle:

$$\begin{pmatrix} \cos\theta & -\sin\theta \\ \sin\theta & \cos\theta \end{pmatrix} \quad (1.33)$$

---

<sup>4</sup>Formally this computation of  $P_{\nu_\alpha \rightarrow \nu_\beta}$  is unsatisfactory on many respects. Quantum states with defined momentum have infinite uncertainty in position, and therefore it makes no sense to talk about observation at distance  $L$ . A rigorous treatment requires definition of neutrino states as wave packets, which is equivalent to studying neutrino beams with a finite energy spread. The initial neutrino wave packet decomposes into mass eigenstate wave packets, each travelling with a different velocity, given by the average over the packet of the ratio of  $\vec{p}_i/E$ , and the oscillation due to interference among the different components is lost at a distance at which the wave packets cease to overlap. As long as this is not the case, the oscillation probability is correctly given by 1.32.

and the last term of 1.32 vanishes; therefore the oscillation probability reduces to:

$$P_{\nu_e \rightarrow \nu_\mu}(L) = \sin^2 2\theta \sin^2(\Delta m^2 L/4E). \quad (1.34)$$

Eq.1.34 is usually written as:

$$P_{\nu_e \rightarrow \nu_\mu}(L) = \sin^2 2\theta \sin^2(1.27 \Delta m^2 L/4E). \quad (1.35)$$

where the previously omitted factors  $\hbar$  and  $c$  are included,  $\Delta m^2$  is expressed in  $eV^2$ ,  $L$  is in  $Km$  and  $E$  is in  $GeV$ .

In conclusion, the necessary and sufficient conditions to have neutrino oscillations are:

- a non vanishing value at least for a neutrino mass term;
- a non vanishing value for at least one off-diagonal element of the mixing matrix  $V$ .

### 1.1.5 $\mu^+ \rightarrow e^+ \gamma$ decay in Standard Model with massive neutrinos

The Lagrangian of the Standard Model, including neutrino mass term, leads to new Feynman diagrams as shown in fig.1.1, and opens to the possibility for the existence of the  $\mu^+ \rightarrow e^+ \gamma$  decay.

Referring to eq.1.34 the expected  $\mu^+ \rightarrow e^+ \gamma$  decay rate is given by:

$$\begin{aligned} \Gamma(\mu^+ \rightarrow e^+ \gamma) &\simeq \frac{G_F^2 m_\mu^5}{192\pi^3} \frac{\alpha}{2\pi} \sin^2 2\theta \sin^2 \left( \frac{\Delta m^2 L}{4E} \right) \\ &\simeq \frac{G_F^2 m_\mu^5}{192\pi^3} \frac{\alpha}{2\pi} \sin^2 2\theta \left( \frac{\Delta m^2 L}{m_W^2} \right)^2, \end{aligned} \quad (1.36)$$

where it is possible to recognize the contribution coming from the standard muon decay  $\frac{G_F^2 m_\mu^5}{192\pi^3}$ , a  $\gamma$ -vertex and a term proportional to the neutrino oscillations probability (we have considered that  $\nu_e \rightarrow \nu_\mu$  oscillation should occur over a distance  $L \simeq 1/m_W$  and the energy flowing in the loop is of the order of  $m_W$ ).

The resulting Branching Ratio, normalized to the standard muon decay and including the currently measured values for neutrino oscillations parameters is given by [14]:

$$\begin{aligned} BR(\mu^+ \rightarrow e^+ \gamma) &= \frac{\Gamma(\mu^+ \rightarrow e^+ \gamma)}{\Gamma(\mu^+ \rightarrow e^+ \nu_e \bar{\nu}_\mu)} \simeq \frac{\alpha}{2\pi} \sin^2 2\theta \left( \frac{\Delta m^2}{m_W^2} \right)^2 \\ &\simeq \frac{1}{2 \cdot 137 \cdot \pi} \left( \frac{7 \cdot 10^{-5} eV^2}{80 GeV^2} \right)^2 \simeq 10^{-55}, \end{aligned} \quad (1.37)$$

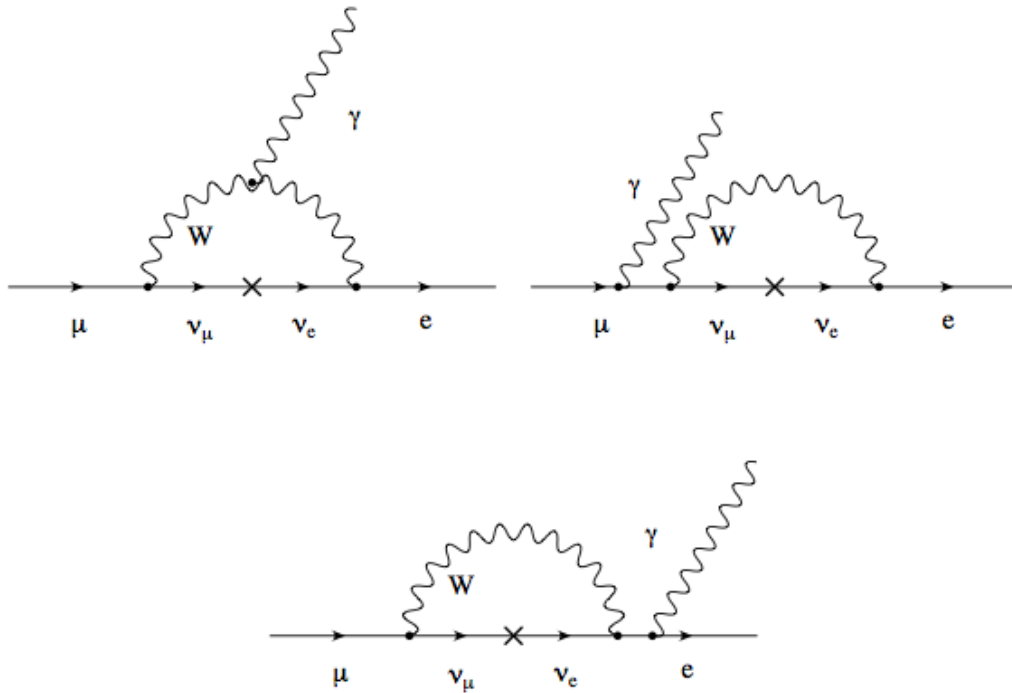


**Figure 1.1:** Feynman diagrams for the  $\mu^+ \rightarrow e^+\gamma$  decay in the Standard Model including massive neutrinos.

an extremely small value, obviously unmeasurable with the current technology.

In conclusion, also including a neutrino mass term in the SM definition, even if no more formally forbidden by the theory, lepton flavour violating events are strongly suppressed.

## 1.2 Physics beyond the Standard Model

The SM expectations always resulted in very good agreement with the huge number of experimental observations made in the last 40 years. Nevertheless, some aspects of the theory remain unexplained, thus inducing to make the assumption that SM is not a definitive theory but an approximation at low energy (that is, the energy currently accessible for particle physics experiments) of a more fundamental theory.

In this section the main fails of the Standard Model description will be summarized, then the main aspects of the new theories proposed to enlarge the SM framework will be briefly described.

### 1.2.1 Standard Model open questions

In spite of the vast experimental success of the Standard Model, it is commonly believed that this model is not the full picture of Nature and that New Physics

(NP) beyond the SM may exist, at some energy scale higher than the electroweak breaking (EW) scale ( $\Lambda_{EW} \sim 10^2 GeV$ ).

It is indeed clear that the SM cannot describe physics above the so called Planck scale ( $\Lambda_{PL} \sim 10^{19} GeV$ ). At this scale, gravitational effects become as important as the known gauge interactions and cannot be neglected. Indeed there are good reasons to believe that there is an additional NP between  $\Lambda_{EW}$  and  $\Lambda_{PL}$ . Let first recall the relevant problems related to experiments and observations [4], [15].

- As already said in sec. 1.1.4, there are two, related, experimental evidences for neutrino oscillations, coming from observation of atmospheric [16] and solar neutrinos [11], [17]. In both cases the measured fluxes are different from the expectations, and the discrepancy can be explained in an elegant and simply way introducing neutrino masses, that are not included in the original SM formulation.
- The standard Big Bang nucleosynthesis scenario is consistent with the observed abundance of light elements only for a certain range of baryon asymmetry. To generate baryon asymmetry, CP violation is required. The SM CP violation generates baryon asymmetry that is smaller by at least 12 orders of magnitude than the observed asymmetry. This implies that there must be new sources of CP violation, beyond the SM.
- Others cosmological observations lead to the introduction of some kind of “dark matter”, i.e. weakly interactive massive particles, not included in the SM framework.
- The three gauge couplings of strong, weak and electromagnetic interactions seem to converge to a unified value at a high energy scale.

There are also other “theoretical” deficiencies in SM. One of the most clear is the great number of free parameters that appear in the SM Lagrangian. Infact, the SM as exposed in the previous section contains 19 free parameters (9 fermions masses, not including neutrino masses, 4 parameters to describe  $V_{CKM}$  matrix, 3 coupling constants and the Higgs parameters  $v$  and  $m_H$ ) that are inserted *ad hoc* in the theory to get the consistency of the theory itself.

Moreover, other aspects remain unexplained:

- the Higgs mass requires an extremely fine tuning of the theory parameters, in order to get the stability of the mass itself (*naturalness problem*). Without anomalous cancellation, the natural Higgs mass scale should be the same as the Planck scale, as explained in 1.2.3;
- between the electroweak scale and the unification scale should be a huge range of energies without new physics (*hierarchy problem*).

Various models have been proposed in the last years in order to explain the problems listed above. Between them, the most important are those involving the so called Grand Unified Theory (GUT) and the Supersymmetric Theory (SUSY). Both models are based on the idea that the SM gauge group is a sub-group of a larger symmetry, broken at some energy scale; the results of this symmetry breaking should be the Standard Model as we currently know it. In particular, supersymmetry solves in a very elegant way the naturalness problem, and opens the possibility to have lepton flavour violating events with measurable Branching Ratios. In the following sections we will describe the main characteristics of the GUT and SUSY theories, then we will have a look at the predictions about LFV muon decay in the new frameworks.

### 1.2.2 Grand Unified Theory

The fundamental idea behind the Grand Unified Theory is that the gauge symmetry increases with the energy [15]. In this sense, the fundamental interactions should be different expressions of an unique interaction associated with some gauge group that embed the  $SU(3)_C \times SU(2)_L \times U(1)_Y$  SM group. The unification of the interactions occurs at some energy  $E_{GUT}$ , that should be of the order of  $10^{16} GeV$ .

The idea of a grand unification at such huge energies raises many difficult questions, but at the same time suggests a wonderful opportunity. Infact there is another enormous energy scale in quantum field theory, that is given by the scale at which the gravitational attraction of elementary particles should become comparable with the other fundamental interactions. Conventionally, one can define the *Planck scale* as the energy for which the gravitational interaction of particles become of the order of 1:

$$m_{PL} = (G_N/\hbar c)^{-1/2} \sim 10^{18} GeV. \quad (1.38)$$

Though this scale is still slightly higher than the scale at which the standard model coupling constants should meet, it is not unreasonable to suppose that grand unification is somehow related to the unification of gravity with the others fundamental interactions.

The minimal symmetry group that can embed the  $SU(3)_C \times SU(2)_L \times U(1)_Y$  SM group is  $SU(5)$  [18]. In the  $SU(5)$  framework the particle content of SM can be arranged into a 5-plet and a 10-plet (where the bar represents the adjoint representation of the fundamental representation). In the standard assignment, the  $\bar{5}$ -plet contains the charge conjugates of the right-handed down-type quark color triplet and a left-handed lepton isospin doublet, while the 10-plet contains the six up-type quark components, the left-handed down-type quarks color triplet, and the right-handed electron. This scheme has to be replicated for each of the three known generations of matter.

In this context, neutrinos are still massless; nevertheless, as in the SM, it is possible to add a right handed component into a singlet representation, without compromising the consistency of the theory. Although this model nice fits the

particle content of SM, it cannot be considered a reliable description of particle interactions: one of the main fail of the  $SU(5)$  description is the prediction of a proton decay rate completely in disagreement with the observations.

Another possible way to unify the fundamental interactions in a unique group is provided by the  $SO(10)$  group [19], [20]. It contains  $SU(5)$  as subalgebra. The advantage of  $SO(10)$  over  $SU(5)$ , as the group for grand unification, is that  $SO(10)$  admits a representation of dimension 16, in which it is easy to accommodate also a right handed neutrino. So in this framework one can easily give masses to neutrinos, explaining in a natural way the observation cited in sec. 1.2.1.

Though GUT theories provide some answers to some critical questions of the Standard Model, some other aspects, for example the hierarchy and the naturalness problems, remain unsolved. The latter two issues are elegantly explained introducing a new kind of symmetry in the model.

### 1.2.3 Supersymmetric theory

The fundamental idea of the Supersymmetric theory is the existence of a symmetry between fermions and bosons. The symmetry can be realized in nature if one assumes that for each particle of the SM exists a supersymmetric partner, which has the same internal quantum number and an intrinsic angular momentum which differs by half a unit from the SM one [21], [22], [23], [24].

Phenomenological applications of SUSY theories have been considered since the late 70s in connection with the naturalness problem (or the hierarchy problem) in the SM. The SM model can be regarded as being a low-energy approximation of a more complete theory, and is replaced by this at a high energy scale. Supposing that this high energy scale is close to the Planck scale ( $\simeq 10^{19} GeV$ ), the quadratic divergence appearing in the radiative corrections to the Higgs scalar mass becomes problematic, because of a precise fine tuning between the bare mass and the radiative corrections must be introduced to keep the electroweak scale well below this high energy scale. This problem can be avoided if SUSY is introduced, since the quadratic divergences are cancelled between fermionic and bosonic loop contributions.

Here we introduce the Minimal Supersymmetric Standard Model extension (MSSM). In MSSM, SUSY partners (which have different spin by 1/2 from the corresponding ordinary particles) are introduced for each particle in the SM. For quarks and leptons, complex scalar fields, namely squark ( $\tilde{q}$ ) and sleptons ( $\tilde{l}$ ), are introduced. The superpartner of the gauge boson is a gauge fermion (gaugino), and that of the Higgs field is called a higgsino ( $\tilde{H}$ ). The superpartners of gluons,  $SU(2)$  and  $U(1)$  bosons are respectively a gluino ( $\tilde{G}$ ), a wino ( $\tilde{W}$ ) and a bino ( $\tilde{B}$ ). After electroweak symmetry breaking, the SUSY partners of gauge bosons mix with each other and form two charged Dirac fermions, called charginos ( $\tilde{\chi}_i^\pm$ ,  $i=1-2$ ), and four Majorana fermions, called neutralinos ( $\tilde{\chi}_i^0$ ,  $i=1-4$ ). The SUSY model contains at least two Higgs doublet fields, required to give mass term to the particles. The particles content of the MSSM is listed in table 1.4.

Ordinary Particles		Susy Particles	
Particle	Spin	Particle	Spin
quark (q)	$\frac{1}{2}$	squark ( $\tilde{q}$ )	0
lepton (l)	$\frac{1}{2}$	slepton ( $\tilde{l}$ )	0
gluon (G)	1	gluino ( $\tilde{G}$ )	$\frac{1}{2}$
$W^\pm, Z^0, \gamma$	1	chargino ( $\tilde{\chi}_i^\pm$ ), (i=1-2)	$\frac{1}{2}$
Higgs boson (h,H,A, $H^\pm$ )	0	neutralino ( $\tilde{\chi}_i^0$ ), (i=1-4)	$\frac{1}{2}$

**Table 1.4:** Particle content of Minimal Supersymmetric Standard Model.

As already said, supersymmetry solves the problem of the naturalness of the Higgs mass. Let's now have a look more in details at this question.

In the calculation of the Higgs mass, the fermionic loop contributions lead to a divergence, given by

$$\Delta m_H^2(f) = -2N_f \frac{|\lambda_f|^2}{16\pi^2} \left[ \Lambda^2 + 2m_f^2 \ln \left( \frac{\Lambda}{m_f} \right) \right] \quad \Lambda \simeq M_{NewPhys} \quad (1.39)$$

as shown in fig.1.2. So, the Higgs predicted mass is dramatically higher than the expected value, apart from an extreme fine tuning of the parameters that seem to be really unnatural.

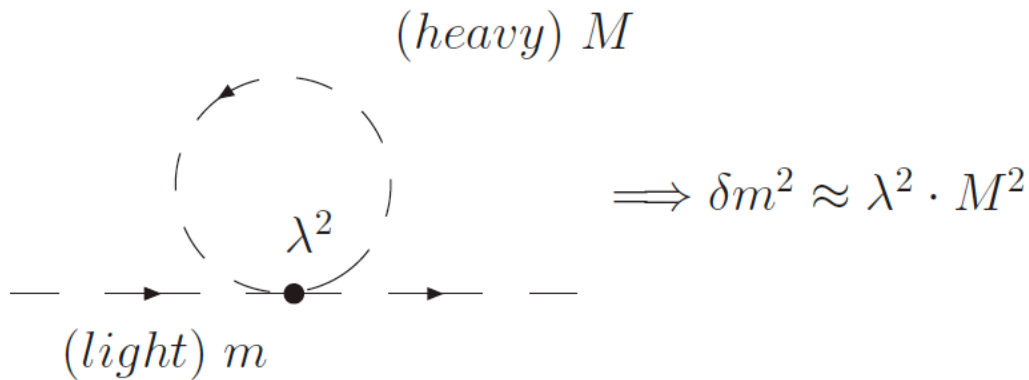


**Figure 1.2:** Radiative corrections to the Higgs boson mass.

The hypothesis of the existence of a bosonic (fermionic) supersymmetric partner for each fermion (boson) of the Standard Model results in a double of the Feynman diagrams that describes the loops, and elegantly solves the naturalness problem. The contributions coming from the bosonic loops cancel those from the

fermionic loops because of an additional  $-1$  factor due to the Fermi statistics, as shown in fig.1.3. We can recognize two types of contributions: one coming from the interaction of the heavy Higgs boson and its superpartner; in this case, the strength of the interaction is given by the Yukawa coupling  $\lambda$ . The other contribution comes from the gauge interaction from the heavy gauge boson and heavy gaugino, and it is proportional to the gauge coupling constant  $g$ .

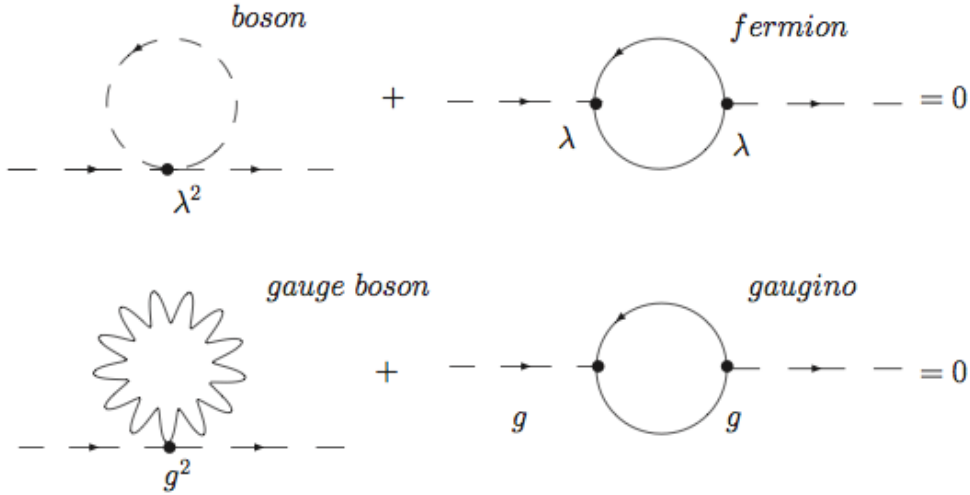


**Figure 1.3:** Cancellation of quadratic terms (divergencies) in Supersymmetric framework.

In both cases, the quadratic terms cancellation takes place. The cancellation is exact if the symmetry is unbroken, due to the following sum rule relating the masses of the superpartners:

$$\sum_{bosons} m^2 = \sum_{fermions} m^2. \quad (1.40)$$

If the symmetry is broken, the cancellation is no more exact; the difference between the bosons and fermions masses is given by

$$\sum_{bosons} m^2 - \sum_{fermions} m^2 = m_{SUSY}^2. \quad (1.41)$$

It is easy to understand that  $m_{SUSY}$  should not be very large ( $\sim TeV$ ) in order to make the tuning natural. This could be a hint about the existence of new physics at an energy scale of the order of  $\sim TeV$ .

### 1.3 Muon decay in the new Models

The introduction of new theory such as GUT and SUSY opens new scenarios for LFV events. In particular, we will now examine the muon decay in the framework

of the new theories [24].

In the  $SU(5)$  SUSY GUT model, LFV appears only in the right-handed sleptons sector for small or moderate values of  $\tan\beta$ , which is defined by the ratio of two Higgs vacuum expectation values,  $\tan\beta = \langle H_0^2 \rangle / \langle H_0^1 \rangle$ . The diagonal terms of the sleptons mass matrix can be examined on the basis where the Yukawa coupling constant for leptons is diagonalized. The off-diagonal elements of the right-handed slepton mass matrix on this basis become a source of LVF through the diagrams shown in fig. 1.4.

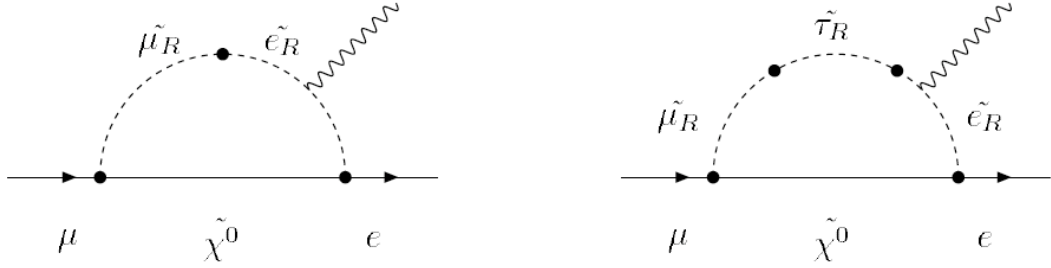


**Figure 1.4:** Feynman diagrams for the  $\mu^+ \rightarrow e^+ + \gamma$  decay in  $SU(5)$  SUSY GUT. The closed lines represent the flavor transitions due to the off-diagonal terms of the slepton mass matrices.

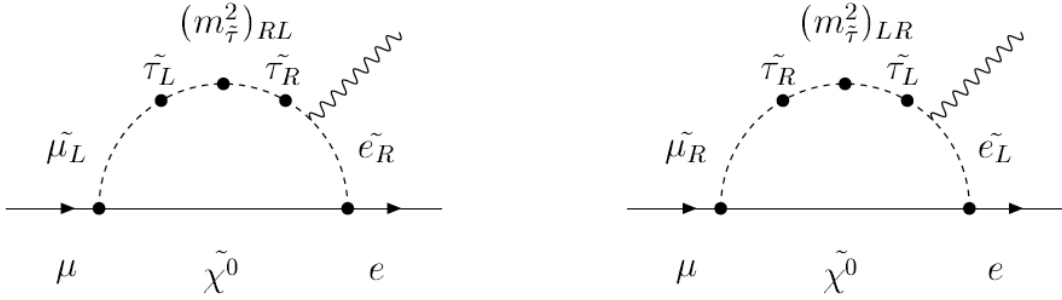


**Figure 1.5:** Feynman diagrams in  $SO(10)$  SUSY GUT which gave dominant contributions to the  $\mu^+ \rightarrow e^+ + \gamma$  process.  $(m_{\tilde{\tau}}^2)_{RL}$  and  $(m_{\tilde{\tau}}^2)_{LR}$  are proportional to  $m_{\tilde{\tau}}$ .

The predictions for the branching ratio of  $\mu^+ \rightarrow e^+ + \gamma$  decay are presented in fig. 1.6. The branching ratio is about  $10^{-14}$  for sleptons masses of few hundred  $GeV/c^2$ . The plot shows the BR of the  $\mu^+ \rightarrow e^+ + \gamma$  decay as a function of the right-handed slepton mass matrix element. Some parameters of the theory are fixed. In particular the figure refers to a set of SUSY input parameters: the  $SU(2)$  gaugino mass, indicated as  $M^2$  and the ratio of the two Higgs vacuum expectation values,  $\tan\beta$ .

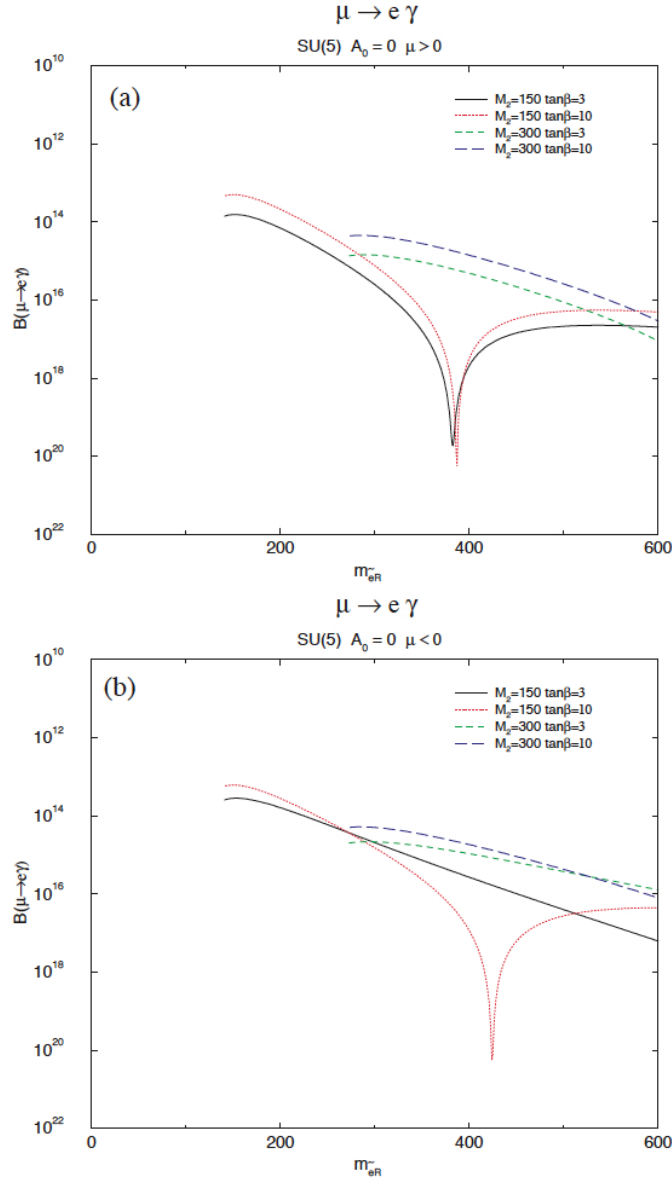


**Figure 1.6:** Predicted branching ratios for the  $\mu^+ \rightarrow e^+ \gamma$  decay in the  $SU(5)$  SUSY GUT based on the minimal supergravity model as a function of the right-handed slepton mass for four different sets of the SUSY input parameters of  $M_2$  (the  $SU(2)$  gaugino mass) and  $\tan\beta$  (the ratio of the two Higgs vacuum expectation values) [24].

Large LVF are expected in the  $SO(10)$  SUSY-GUT model. In the minimal  $SO(10)$  SUSY-GUT both the left-handed and the right-handed sleptons are subject to LVF effects. A large contribution comes from the diagrams shown in fig. 1.5, where the  $m_\tau$  is involved. In this case, the prediction for the branching ratio of  $\mu^+ \rightarrow e^+ \gamma$  is enhanced by factor  $(m_\tau/m_\mu)^2$  compared to the predictions of the minimal  $SU(5)$  SUSY-GUT. The BR of the muon LFV processes as a function of

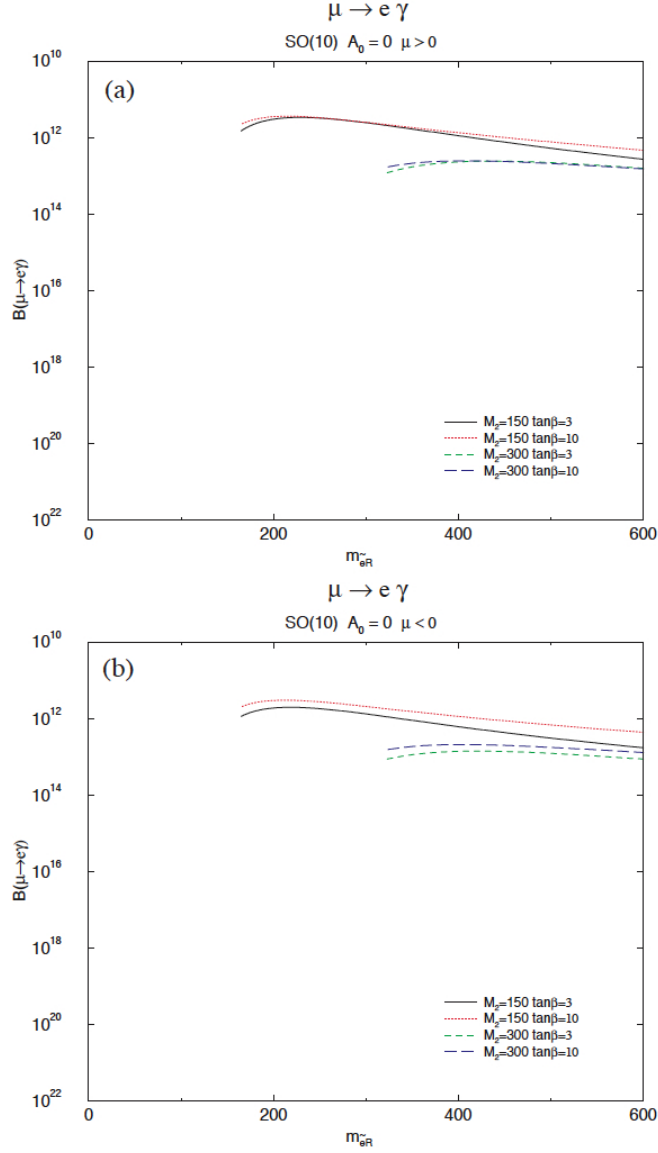


**Figure 1.7:** Predicted branching ratios for  $\mu^+ \rightarrow e^+\gamma$  decay in the SO(10) SUSY GUT model [24]. The input parameters are the same as in fig. 1.6.

the right-handed slepton mass is shown in fig. 1.7. The SUSY input parameters are the same as in fig. 1.6. The BR becomes comparable to the present experimental upper bounds.

In these framework the contribution to the LFV is led by the slepton mixing matrix coefficients. In analogy with SM physics, it is possible to model the slepton mixing matrix to be similar to the quark mixing matrix (CKM model) or to the neutrino mixing matrix (PMNS model). Fig. 1.8 shows the SO(10) SUSY-GUT predicted value for the  $\mu^+ \rightarrow e^+\gamma$  in the region of parameters that will be scanned by the LHC experiment in terms of  $\tan\beta$  and the  $\tilde{\chi}^0$  mass ( $M_{1/2}$ ). The MEG

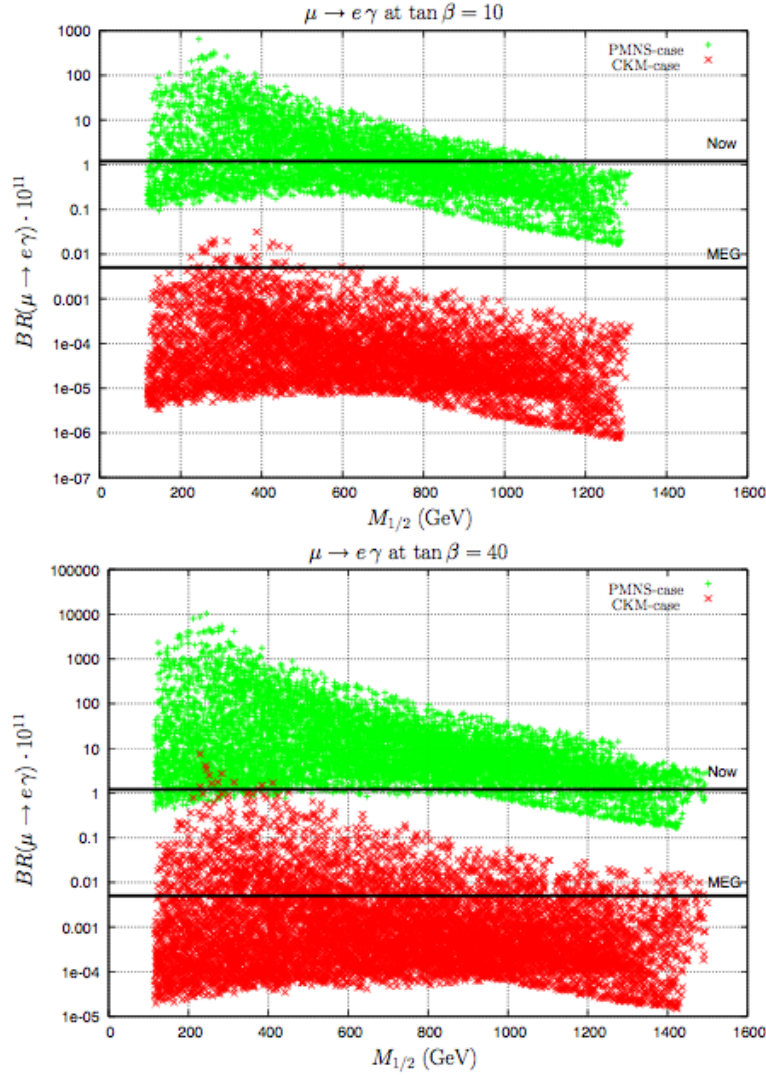


**Figure 1.8:** Scaled  $BR(\mu^+ \rightarrow e^+\gamma)$  vs.  $M_{1/2}$ . The plots are obtained by scanning the LHC accessible SUSY-GUT parameter space at fixed values of  $\tan\beta$  [24]. The horizontal lines are the present (MEGA) and the future (MEG) experimental sensitivities. Note that MEG will test the PMNS case and, for high  $\tan\beta$ , constrain the CKM one.

experiment, having a sensibility down to  $10^{-13}$  will explore a relevant part of the theory predictions. It is important to underline the fact that the MEG measurement is complementary to the LHC research: no measurement at the LHC collider is expected to measure the slepton mixing matrix coefficients.

## 1.4 Muon decay phenomenology and history

This chapter is concluded with a phenomenological treatment of the  $\mu^+ \rightarrow e^+\gamma$  decay and historical overview of the research in the field of the muon physic; in particular we will review the experimental apparatus of the MEGA experiment, that currently defines the  $\mu^+ \rightarrow e^+\gamma$  BR upper limit.

### 1.4.1 Event signature

The event signature of  $\mu^+ \rightarrow e^+\gamma$  decay at rest is an  $e^+$  and a photon emitted in coincidence, moving collinearly back-to-back with their energies equal to half the muon mass ( $m_\mu/2 = 52.8MeV$ ), as depicted in fig.1.9. The searches are done using a positive muon decaying at rest to fully utilize its kinematics. A negative muon is not suitable to be used, since it would be captured by a nucleus when it is stopped in a material.

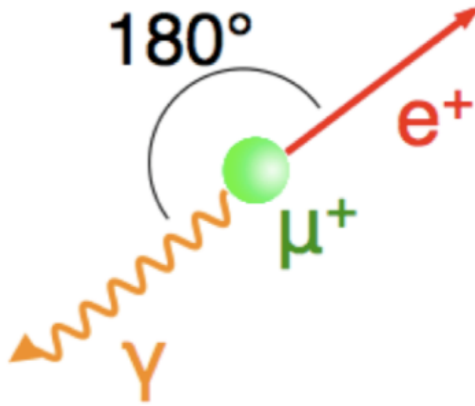


**Figure 1.9:**  $\mu^+ \rightarrow e^+\gamma$  event signature.

There are two major background sources [24]. One is the physical (correlated) background from radiative muon decay,  $\mu^+ \rightarrow e^+\nu_e\bar{\nu}_\mu\gamma$ , the other is an accidental coincidence of an  $e^+$  in a Michel muon decay,  $\mu^+ \rightarrow e^+\nu_e\bar{\nu}_\mu$ , accompanied by a high energy photon. In the following section I will explain deeper in details the characteristics and the contributes of each kind of background.

### 1.4.2 Physics background

The correlated background is given by the radiative muon decay,  $\mu^+ \rightarrow e^+\nu_e\bar{\nu}_\mu\gamma$ , when  $e^+$  and  $\gamma$  are emitted nearly back-to-back with two neutrinos carrying off a negligible amount of energy. The spectrum of photons from radiative decay is shown in fig.1.10.

The differential decay width of the radiative muon decay (RMD) is typically expressed as a function of  $x = 2E_e/m_\mu$ ,  $y = 2E_\gamma/m_\mu$  and  $z = \pi - \theta_{e\gamma}$ . In the

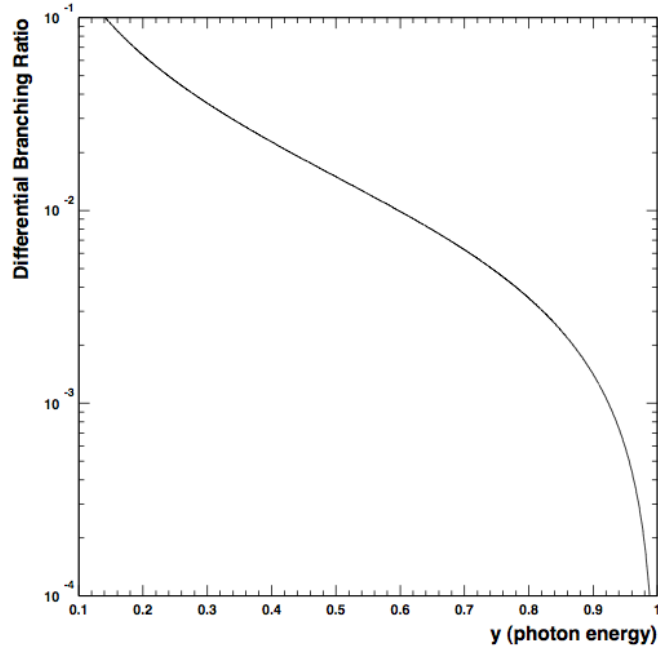


**Figure 1.10:** Differential branching ratio of the  $\mu^+ \rightarrow e^+ \nu_e \bar{\nu}_\mu \gamma$  decay as a function of the photon energy ( $y = 2E_\gamma/m_\mu$ ). This branching ratio is obtained by integrating over the  $e^+$  energy and the angle between an  $e^+$  and a photon.

signal region, defined by  $x = y = 1$  and  $z = 0$ , the width of radiative muon decay vanishes. Nevertheless the finite resolution of real detector spread outside the expected ranges both the event and the background distributions, thus introducing background events in the signal region, limiting the achievable sensitivity.

The probability to have a background event in the signal region can be computed integrating the differential radiative muon decay width in the signal bin, defined by  $(1 - \delta x, 1)$  and  $(1 - \delta x, 1)$  in the  $[E_e, E_\gamma]$  plane. Here  $x$  and  $y$  are the resolution on positron and photon energy respectively (see sec. A.1).

Fig.1.11 shows the fraction of the  $\mu^+ \rightarrow e^+ \nu \bar{\nu} \gamma$  decay for given value of  $\delta x$  and  $\delta y$  with unpolarized muons in the case  $\delta z < 2\sqrt{\delta x \delta y}$ . From this picture we can see that a value of 0.01 for both  $\delta x$  and  $\delta y$  is necessary in order to achieve a sensitivity limit at the level of  $10^{-15}$ .

### 1.4.3 Accidental background

The accidental background consists of a spatial and temporal coincidence between a positron and a  $\gamma$ -ray coming from uncorrelated physical events. While positrons can only originate from muon Michel decay, there are several sources for high energy photons generation. The main ones are radiative muon decays and positron interaction with the experimental environment, i.e. annihilation in flight or bremsstrahlung.

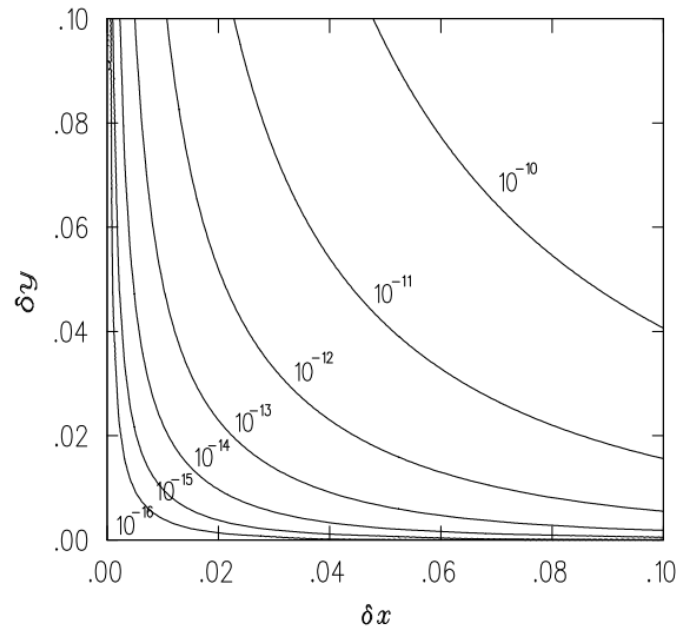


**Figure 1.11:** Effective branching ratio of the physics background from the  $\mu^+ \rightarrow e^+ \nu \bar{\nu} \gamma$  decay as a function of the  $e^+$  energy resolution ( $\delta x$ ) and photon energy resolution ( $\delta y$ ).

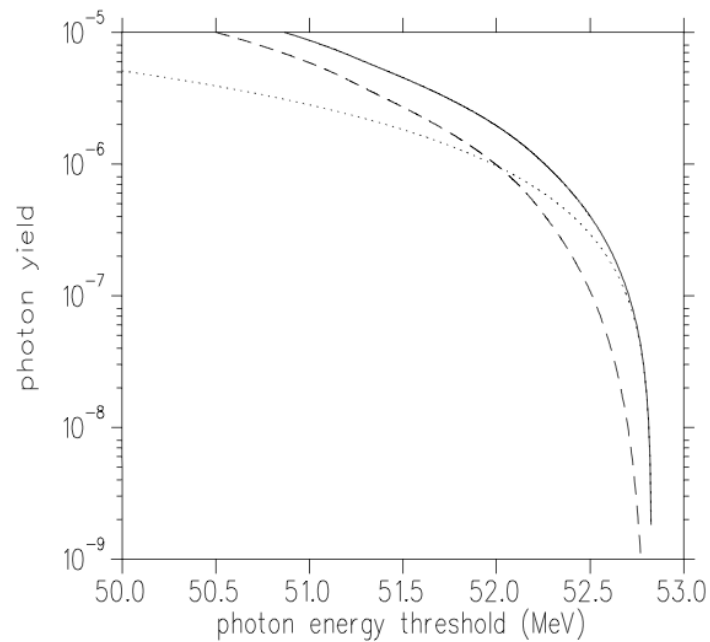


**Figure 1.12:** Integrated rates of backgrounds from annihilation-in-flight (dotted line) and radiative muon decay (dashed line) as a function of the photon energy. The sum of the two is shown by a solid line.

The contribution of positrons can be estimated by integrating the Michel spectrum over the range of the  $E_e$  signal window, and is found to be roughly proportional to the positron energy resolution (see sec. A.2).

In an analog way, the contribution of photons coming from radiative decay can be estimated by integrating the  $\mu^+ \rightarrow e^+ \nu_e \bar{\nu}_\mu \gamma$  spectrum over the  $E_\gamma$  signal window, while the contribution from annihilation in flight depends on the materials along the  $e^+$  tracks path. Fig.1.12 shows, for instance, the contribution of annihilation in flight for the case of  $e^+$  passing through a  $\mu$ -stopping target of  $50 \text{ mg/cm}^2$  and radiative muon decay for photons with energy between a given threshold and  $m_\mu/2$ . The  $\gamma$  contribution to the accidental background results to be proportional to  $(\delta y)^2$ .

Moreover, one has to take into account the contributions from space resolution and time resolution, respectively  $\frac{\delta\theta_{e\gamma}^2}{4}$  and  $\delta t_{e\gamma}$ .

Thus, the effective branching ratio of accidental background is given by:

$$B_{acc} = R_\mu \cdot (2\delta x) \cdot \left[ \frac{\alpha}{2\pi} (\delta y)^2 (\ln(\delta y) + 7.33) \right] \cdot \left( \frac{\delta\theta^2}{4} \right) \cdot (2\delta t) \quad (1.42)$$

For instance, taking some reference numbers like  $e^+$  energy resolution of 1% (FWHM), photon energy resolution of 6% (FWHM),  $\Delta\Omega_{e\gamma} = 3 \times 10^{-4} \text{srad}$ ,  $\Delta t_{e\gamma} = 1 \text{ns}$  and  $R_\mu = 3 \times 10^8 \mu/s$ ,  $B_{acc}$  is  $3 \times 10^{-13}$ . The accidental background becomes absolutely relevant, and dominates respect to the physical one. Therefore, it is critical to make significant improvements in the detector resolution in order to reduce the accidental background.

#### 1.4.4 History of the $\mu^+ \rightarrow e^+ \gamma$ searches

Experimental searches for  $\mu^+ \rightarrow e^+ \gamma$  have a history longer than 50 years. These searches require intense muon beams. Experimental efforts have been devoted to improving the detection resolutions of four variables, namely the positron energy, the photon energy, the relative timing between positron and photon, and the relative angle between positron and photon. Various kinds of apparatus have been developed in the past.

In table 1.5, several experimental results of 90% C.L. upper limit of  $\mu^+ \rightarrow e^+ \gamma$  decay in the past experiments are listed together with their achieved detection resolutions, while fig. 1.13 shows the improvement of the Branching Ratio measurement as a function of the time.

The upper limit quoted in the Particle Data Group [25] is  $B(\mu^+ \rightarrow e^+ \gamma) < 1.2 \times 10^{-11}$ , which was obtained by the MEGA collaboration at Los Alamos National Laboratory (LANL).

A schematical view of the MEGA spectrometer is shown in fig.1.14. The MEGA detector consisted of a magnetic spectrometer for the positron and three concentric pair-spectrometers for the photon. They were placed inside a superconducting solenoid magnet with a  $1.5T$  field. The positron spectrometer comprised eight cylindrical wire chambers and scintillators for timing. The positron energy res-

Place	Year	$\Delta E_e$	$\Delta E_\gamma$	$\Delta t_{e\gamma}$	$\Delta\theta_{e\gamma}$	Upper limit	Ref
TRIUMF	1977	10%	8.7%	$6.7ns$	-	$< 3.6 \times 10^{-9}$	[26]
SIN	1980	8.7%	9.3%	$1.4ns$	-	$< 1.0 \times 10^{-9}$	[27]
LANL	1982	8.8%	8%	$1.9ns$	$37mrad$	$< 1.7 \times 10^{-10}$	[28]
LANL	1988	8%	8%	$1.8ns$	$87mrad$	$< 4.9 \times 10^{-11}$	[10]
LANL	1999	1.2%	4.5%	$1.6ns$	$15mrad$	$< 1.2 \times 10^{-11}$	[8]

**Table 1.5:** Historical progress of search for  $\mu^+ \rightarrow e^+\gamma$  since the era of meson factories with 90% C.L. upper limits. The resolutions quoted are given as a full width at half maximum (FWHM).

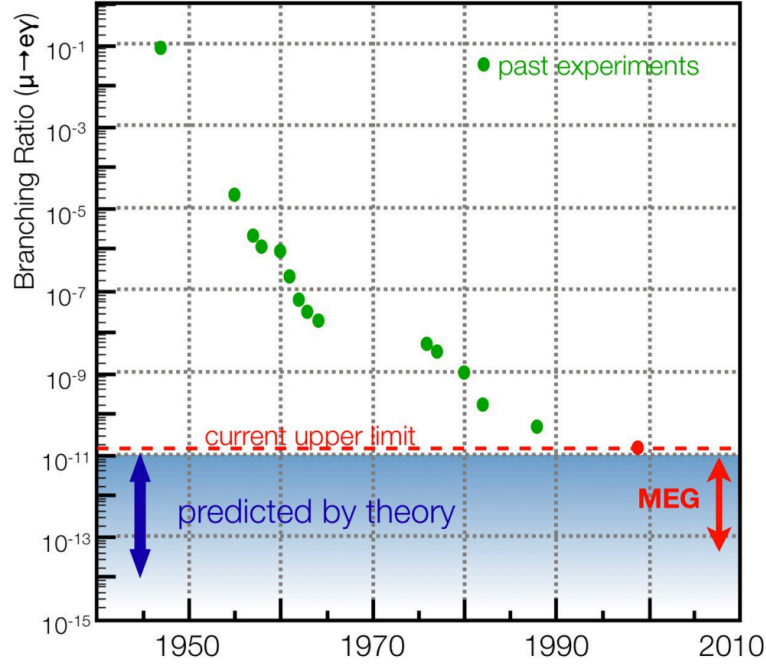


**Figure 1.13:** The improvement of the 90% C.L. upper limit on the  $\mu^+ \rightarrow e^+\gamma$  decay branching ratio as a function of the time.

olution (FWHM) was quoted from  $0.5MeV$  (0.95%) to  $0.85MeV$  (1.6%) for a  $52.8MeV e^+$ , depending on the number of helical loops of  $e^+$  tracks. For the pair-spectrometer, each layer had lead converters, Multiple Wires Proportional Counters, Drift Chambers and scintillators. The photon energy resolutions (FWHM) were  $1.7MeV$  (3.3%) and  $3.0MeV$  (5.7%) for the outer and inner Pb conversion layers, respectively. A surface  $\mu^+$  beam of  $29.8MeV/c$  was introduced along the detector axis, and was stopped in the muon-stopping target made of a thin tilted Mylar foil. All the charged particles from muon decays are confined within the

positron spectrometer. The intensity of the muon beam was  $2.5 \times 10^8 \mu/sec$  with a macroscopic duty factor of 6%. The total number of muons stopped was  $1.2 \times 10^{14}$ . By using the likelihood method, a new limit of  $1.2 \times 10^{-11}$  with 90% C.L. has been reported.

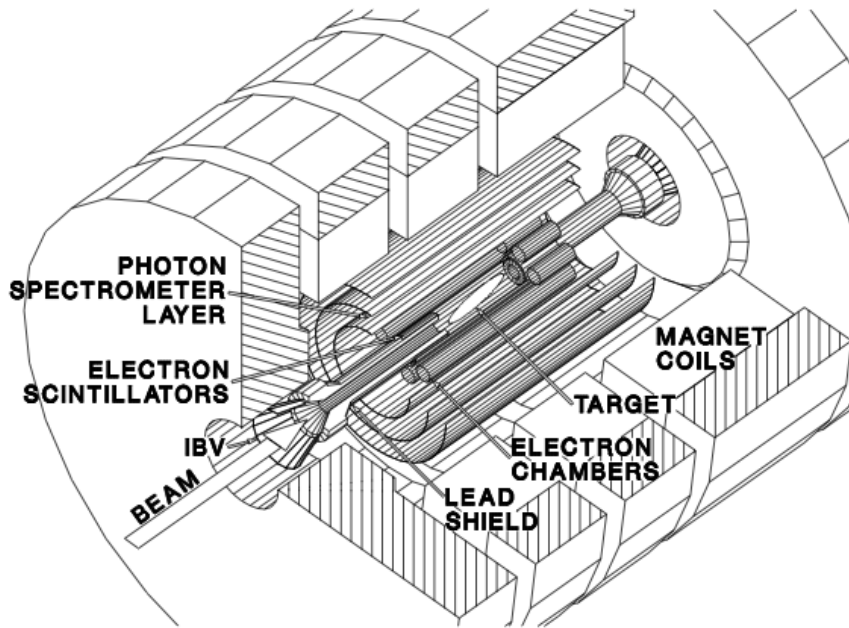


Figure 1.14: Layout of the MEGA experiment [8].

The MEG Collaboration proposal is to lowered this Branching Ratio of about 2 orders of magnitude, reaching the level of  $\sim 10^{-13}$ .

## Chapter 2

# The MEG Experiment

The MEG Experiment aims to improve the current limit on the Branching Ratio of the  $\mu^+ \rightarrow e^+\gamma$  of about 2 orders of magnitude, achieving a sensitivity of about  $10^{-13}$  [29], [30].

In this chapter I will describe shortly the experiment that the MEG collaboration has designed for the detection of  $\mu^+ \rightarrow e^+\gamma$  decay. This is a weak decay of muon at rest in the apparatus frame giving output two bodies: a positron and a gamma. Both particles go out in opposite directions with the same energy.

The event is thus completely reconstructed by measuring 5 kinematics variables with high accuracy:

- $E_e = E_\gamma = \frac{m_\mu}{2} = 52.8 \text{ MeV}$
- $t_{e\gamma} = 0$
- $\phi_{e\gamma} = \theta_{e\gamma} = 180^\circ$

The MEG apparatus is a result of a trade-off among several requirements of the various detectors in order to obtain:

- the highest possible resolutions on those kinematic observables;
- an excellent background rejection (see sec.1.4.3);
- a precise calibration and monitoring of systematic errors.

The MEG experiment is running at the Paul Scherrer Institute (Villigen, CH) where the world's most intense continuous  $\mu$ -beam (up to  $3 \times 10^8 \mu/s$ ) is available. The use of a continuous source instead of a pulsed one is necessary in order to minimize the background, which rises proportionally with the instantaneous  $\mu$  stopping rate, as described in 1.4.3.

The  $\mu$  beam is focused to the target by a system of magnetic lenses (see sec. 2.1). The target is a thin plastic foil fixed at the center of a quasi-solenoidal superconductive magnet, called COBRA (COnstant Bending RAdius) magnet. The magnetic field provided by COBRA allows the momentum selection of the

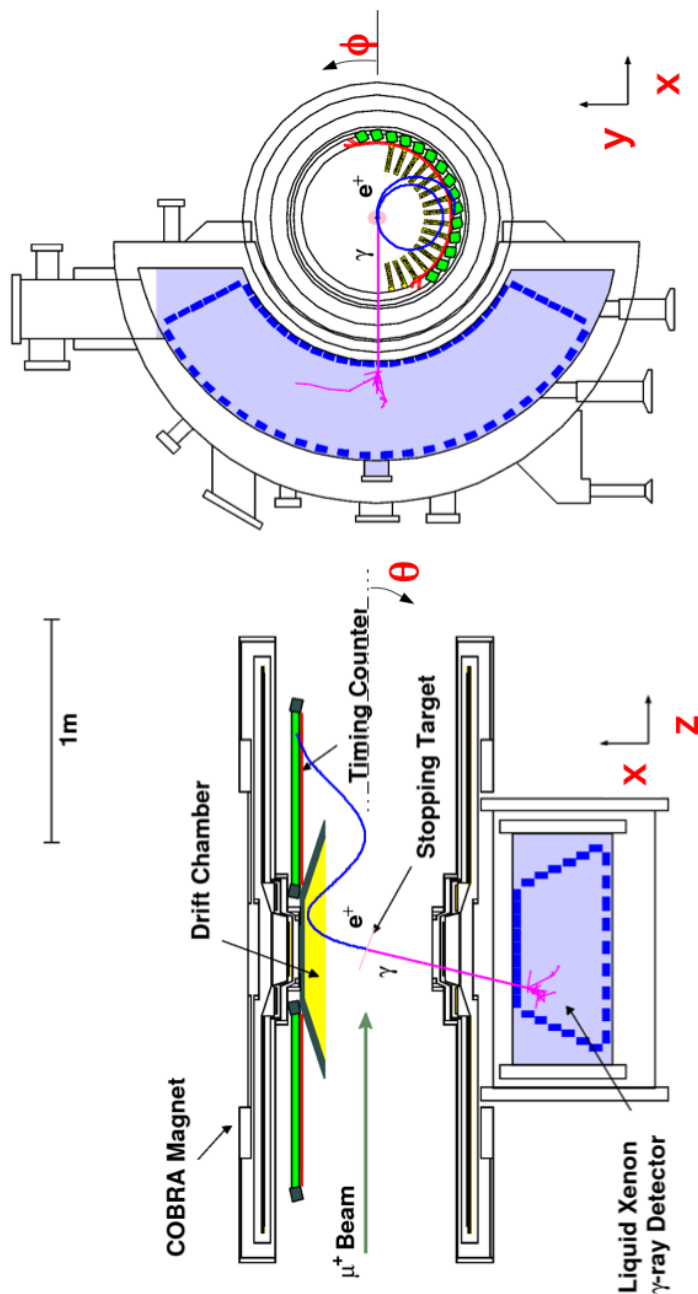


**Figure 2.1:** Side and front view of the MEG experiment detector layout. The coordinates systems used in the experiment are also shown.

positrons in the  $40 \div 55 \text{ MeV}$  energy range with cyclotron orbits smaller than  $40 \text{ cm}$  of diameter. In this particular case the magnetic field is such that the positron bending radius is independent from the emission angle. Further the transversus momentum is adiabatically transferred in the longitudinal direction allowing a faster removal of positrons from the spectrometer central section. This minimize the multiple hits of those positrons that are emitted at large angles on the tracking (Drift Chambers) and timing (Timing Counter) detectors (see sec. 2.2).

While all the positrons are bounded inside the magnet volume, the emitted photons pass through the thin magnet wall and reach the LXe calorimeter, that consists of a volume of  $\sim 0.8 \text{ m}^3$  of liquid Xenon readout by photomultiplier tube. All the photon kinematic variables are measured by the LXe calorimeter (see sec. 2.3).

A schematic view of the apparatus is showed in fig.2.1. The coordinates system is such that the beam line corresponds to the  $z$  axis, and the plane orthogonal to this direction is called the  $r - \phi$  plane. In the following we will use rectangular  $(x, y, z)$ , cylindrical  $(r, z, \phi)$  or spherical  $(r, \phi, \theta)$  coordinates. The origin of the coordinates system is always chosen in the center of the target.

## 2.1 Beam and target

The PSI cyclotron (fig. 2.2) accelerates protons up to  $590 \text{ MeV}$  energy, with a beam current of  $\sim 1.9 \text{ mA}$ . The main characteristics are reported in tab.2.1.

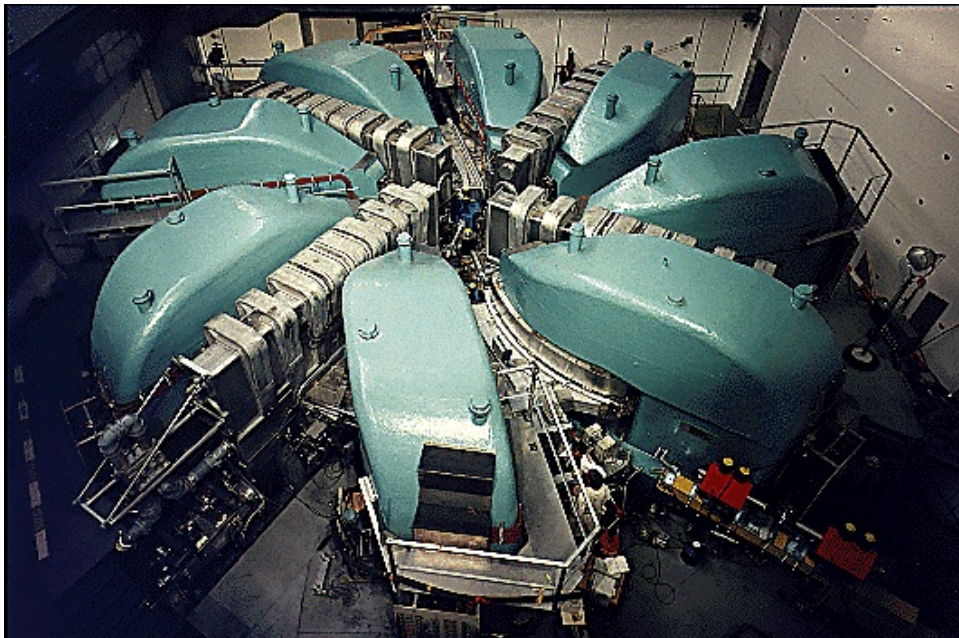


**Figure 2.2:** Picture of the Paul Scherrer Institute  $590 \text{ MeV}$  proton cyclotron.

Secondary beams of pions are generated at 2 different target stations, that are distinguished by their respective thicknesses:  $7 \text{ mm}$  for the M target (*Mince*, thin)

Injection energy	72 MeV
Extraction energy	590 MeV
Extraction momentum	1.3 GeV/c
Relative energy spread (FWHM)	1.2%
Beam emittance	2 mm × π mrad
Beam current	> 1.8 mA DC
Accelerator frequency	50.63 MHz
Time between pulses	19.75 ns
Bunch width	0.3 ns

**Table 2.1:** Main characteristics of PSI cyclotron proton beam.

and  $40 \div 60$  mm for the E target (*Epais*, thick). The 2 targets feed 7 different pion and muon beam line. The channel used by the MEG experiment, namely the  $\pi E5$  channel, selects low energy muons product in the E target, with an angle of about  $175^\circ$  respect to the primary beam direction. The main characteristics of the  $\pi E5$  channel are reported in tab. 2.2.

With a proper choice of the extraction parameters it is possible to select only the *surface muons* [31], [32], that means, only those muons which are produced close to the target surface. For pions decaying at rest in the target, the resulting surface muons have 28 MeV/c momentum and can be easily stopped in a thin target (like the MEG one), in such a way to reduce the multiple scattering phenomena that could affect particles coming from thick target.

The selected beam passes through a series of magnetic elements (see fig.2.3) that perform the beam optimization: selection of low momentum  $\mu$ , rejection of spurious beam content ( $e^+$ ), degrading and focusing the  $\mu$  beam, and realizing the coupling between  $\mu$  beam and the magnet volume.

Many studies were done with different magnetic elements layout, also using dedicated simulations based on beam optics simulator software (TRANSPORT [33]) and beam tracking simulator (TURTLE [34]). The final configuration is mainly made by the following elements:

- a quadrupoles triplet, that preliminary focuses the beam coming from the primary beam line;
- an electrostatic separator (*Wien filter*), that cuts down the positron content of the muon beam. After passing through the separator, the positron contamination in the beam is less than 1%. The separation between positron and muon is equal to  $7.2 \sigma$ , as shown in fig.2.4.

Solid angle acceptance	150 <i>msr</i>
Momentum range	20 ÷ 120 <i>MeV/c</i>
Length	10.4 <i>m</i>
Relative momentum band (FWHM)	10%
Relative momentum resolution (FWHM)	2%
Horizontal emittance	15.3 <i>cm · rad</i>
Vertical emittance	3.6 <i>cm · rad</i>
Spot size	4 × 4 <i>cm<sup>2</sup></i>

**Table 2.2:** Main characteristics of  $\pi E5$  beam line.

- a second quadrupoles triplet that re-focuses the beam after the separator stage;
- a beam transport solenoid (BTS) that carries the  $\mu$  beam in the COBRA volume. Inside the transport solenoid a  $\mu$ -momentum degrader (Mylar sheet of 300  $\mu m$  thickness) is placed. The degrader further reduces the muon momentum, thus optimizing the fraction of muons stopped in the thin target.

At the BTS exit the beam shows an elliptical spot with typical dimensions  $\sigma_x = 5.5 \text{ mm}$  and  $\sigma_y = 6.5 \text{ mm}$ .

The target consists in a elliptical polyethylene sheet with 175 $\mu m$  thickness that is mounted with a slanting angle of 22° respect to the beam direction (fig. 2.5). This configuration maximizes the thickness crossed by muon and at the same time minimizes the outcoming positron energy loss.

The positron spectrometer volume is filled with He in order to reduce to a minimum level the multiple scattering of particles. The whole system made of the degrader, the target and the He atmosphere is the best compromise for assuring high beam quality together with low positron momentum degradation. On the target surface few holes are shaped. with the purpose of testing the goodness of the positron track reconstruction processes from Drift Chamber hits, and extract the resolution on the muon vertex decay reconstruction (see sec. 7.2.1).

## 2.2 Positron spectrometer

The positron spectrometer consists of 3 key elements: the superconductive solenoid COBRA, which provides a quasi-solenoidal magnetic field with gradient in both axial and radial directions, a system of drift chambers, radially aligned in the center of the magnet providing the measurement of positron direction and momentum

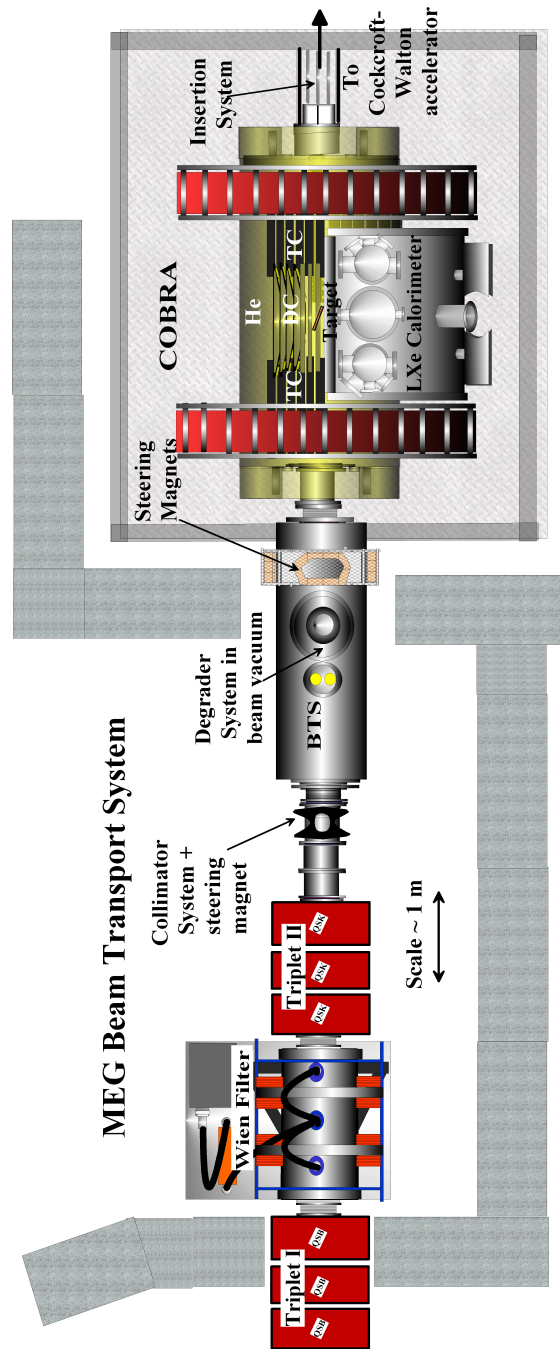


**Figure 2.3:** Schematic view of the MEG beam line configuration.

and the Timing Counter, which purpose is the precise timing of the positron at the end of its trajectory and topological trigger of first level. In chapters 3 and 4 I will describe extensively the Timing Counter to which I have devoted my Ph.D. thesis work.

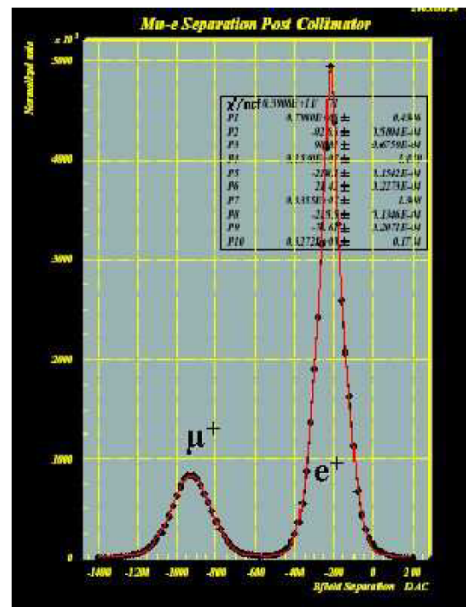


**Figure 2.4:** Muon - electron separation in MEG muon beam, after crossing electrostatic separator.

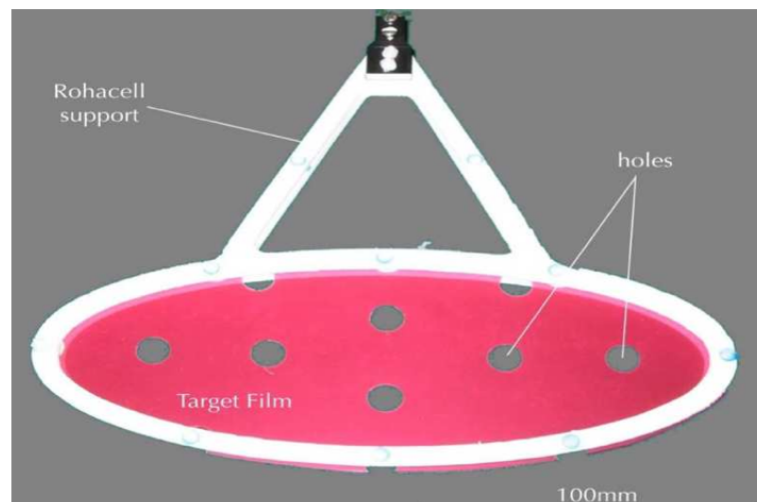


**Figure 2.5:** Picture of the MEG target. The holes on the surface are used for testing the reconstruction algorithm of drift chamber system, and to extract the muon decay vertex resolution.

### 2.2.1 COBRA magnet

The COBRA magnet [35] consists of a main superconducting magnet and a pair of compensation (non superconducting) coils; a picture of the magnet is shown in fig. 2.6, while in fig. 2.7 a schematic draw is sketched.

The compensations coils are necessary to minimize the stray magnetic field



**Figure 2.6:** The COBRA magnet.

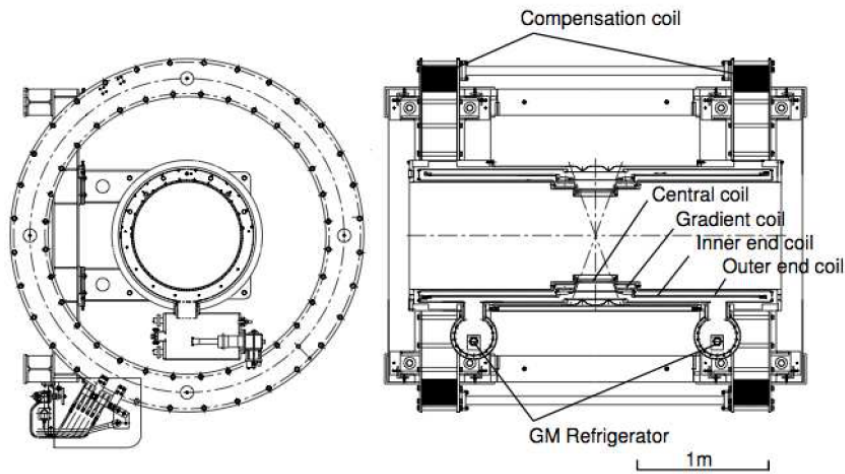


**Figure 2.7:** Schematic draw of the COBRA magnet.

in the position of the Liquid Xenon calorimeter as shown in fig. 2.8: indeed a magnetic field greater than 50 *Gauss* affects the performances of the calorimeter because strongly reduces the photomultiplier gains.

The main magnet is designed to obtain a magnetic field with a wanted gradient, with maximum intensity  $B_0 = 1.27 T$  at the center. It is manufactured with 5 coils with different radii: a central coil, 2 gradient coils and 2 end coils. The coils are obtained by a multifilament Nb-Ti cable embedded in an aluminum matrix. This structure provides to the system the necessary mechanical strength reducing the

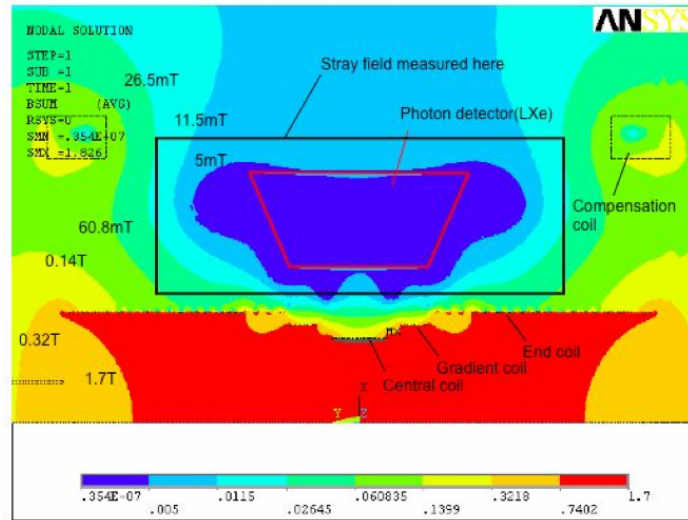


**Figure 2.8:** COBRA magnetic field map. Note how the compensation coils act to reduce field intensity in the calorimeter region.

need of external support. In this way it is possible to minimize the quantity of material the photons having pass trough, thus reducing the interaction probability of gamma rays before entering the calorimeter.

The behavior of the magnetic field versus the distance from the center is shown in fig. 2.9. The main characteristics of the COBRA magnet are listed in tab. 2.3.

Magnetic solenoidal spectrometer of this kind have the advantage of radial energy selection, therefore it is possible to set a detection energy threshold for the tracking detector (Drift Chambers) simply placing them at opportunely chosen radii: this lets to cut out the low energy part of the positron from Michel decay mode  $\mu^+ \rightarrow e^+ \nu_e \bar{\nu}_\mu$ . The expected positron rate as a function of the distance form the COBRA axis is shown in fig.2.10.

Coil	Central	Gradient	Inner End	Outer end	Compensation
Type	Super	Super	Super	Super	Resistive
Inner diam (mm)	700	810	920	920	2210
Outer diam (mm)	712.4	820.6	929.5	929.5	2590
Length (mm)	240.3	110.4	189.9	749.2	265
Layers	4	4	3	3	14
Inductance (H)	1.64	0.62	0.35	2.29	0.54
Current (A)	360	360	360	360	360
Energy (KJ)	106	40	23	148	35
Weight (Kg)	9	4	7	28	1620

**Table 2.3:** Main characteristic of COBRA magnet.

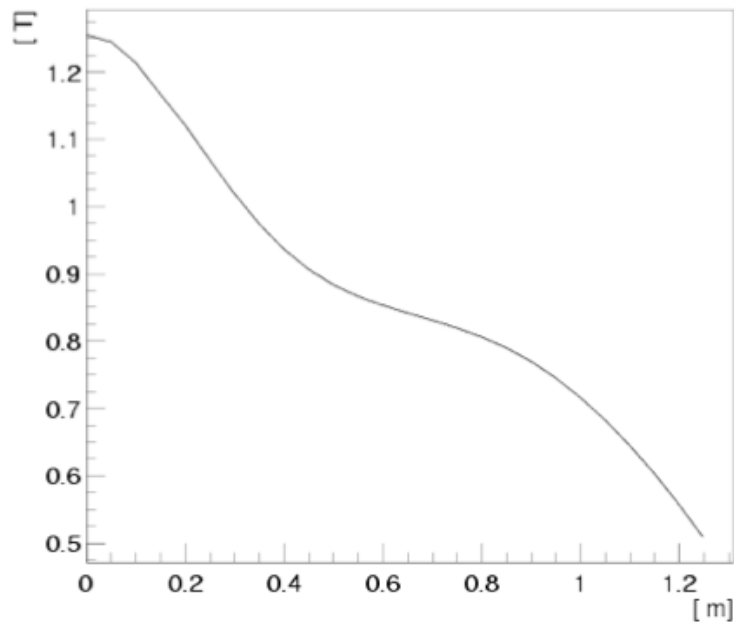


**Figure 2.9:** Magnetic field intensity as a function of the distance from the COBRA center.

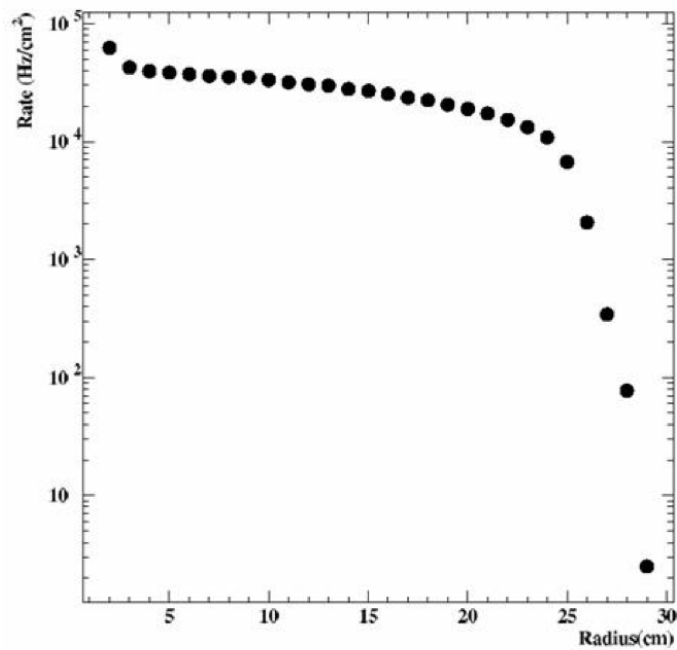


**Figure 2.10:** Rate of Michel positron as a function of the distance from COBRA axis.

Pure solenoidal field doesn't match the MEG requirements in terms of tracking efficiency and momentum reconstruction, because:

- positrons emitted with an angle of about  $90^\circ$  respect to beam axis presents a very small pitch of the helicoidal trajectory; jamming the detector with multiple turns with a consequent loss of efficiency (fig.2.11a);
- for a fixed value of outgoing momentum, the bending radius of the curved trajectory depends from emission angle, resulting in a complication in track selection and momentum measurement (fig. 2.11b).

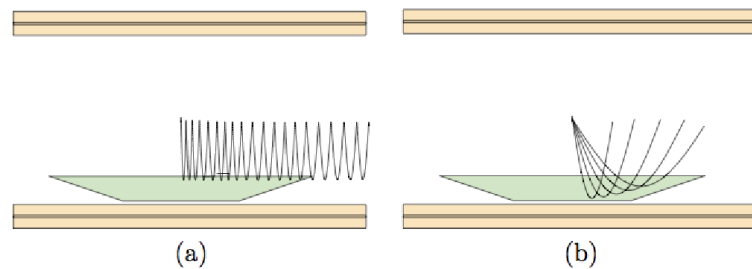


**Figure 2.11:** Behavior of particle in an uniform solenoidal magnetic field: (a) trajectory made by a positron emitted at  $88^\circ$  respect to the beam axis; (b) trajectories of monochromatic positrons emitted at different angles.

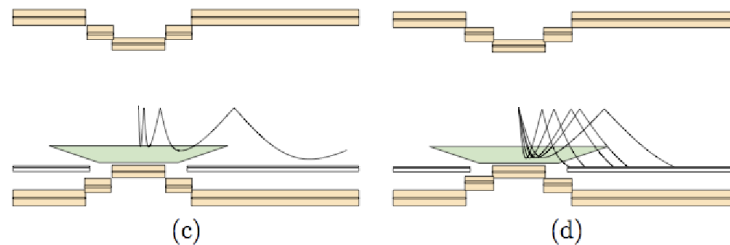


**Figure 2.12:** Advantages for a quasi-solenoidal magnetic field with gradient along beam axis direction: (c) trajectory made by a positron emitted at  $88^\circ$  respect to the beam axis; the positron is faster extracted from the DC region; (d) trajectories of monochromatic positrons emitted at different angles. The bending radius results to be independent from emission angle.

Such complications can be avoided using a quasi-solenoidal field, with a proper gradient; in the case of COBRA magnet the gradient is in the direction of the beam axis and also in the radial direction. This particular field map allows positrons emitted with angle near to  $90^\circ$  to make only 1–2 turns inside the chambers. Moreover, the radius of the trajectory depends only on the module of the momentum and not on transverse component; thus it is possible to tune the field intensity in such way that only positrons with energy near  $52.8 \text{ MeV}$  (signal positrons) can cross the chambers (fig.2.12 c,d).

## 2.2.2 Drift chambers

Positron trajectories are detected by 16 thin ( $2.0 \times 10^{-3} X_0$  along positron trajectory) Drift Chambers (DC) radially aligned in the center of the COBRA magnet (fig.2.13) [36], [37]. The chambers have a trapezoidal shape: the sensitive area extends from a radius  $r = 19.3 \text{ cm}$  to  $r = 27 \text{ cm}$ , while in the  $z$  direction they cover  $|z| < 50 \text{ cm}$  for the inner radius and  $|z| < 21.9 \text{ cm}$  for the outer radius, corresponding to an angular acceptance of  $|\cos\theta| < 0.35$  and  $|\phi| < 60^\circ$  for signal positrons. The layout of the drift chambers tracking system is shown in fig.2.13.

Each chamber is made up of two staggered arrays of drift cells. Each cell is filled with a 50% He and 50%  $C_2H_6$  gas mixture. This mixture was chosen in order to achieve the best compromise between charge yield and gain ( $\sim 65e^-/cm$ ) and multiple scattering.

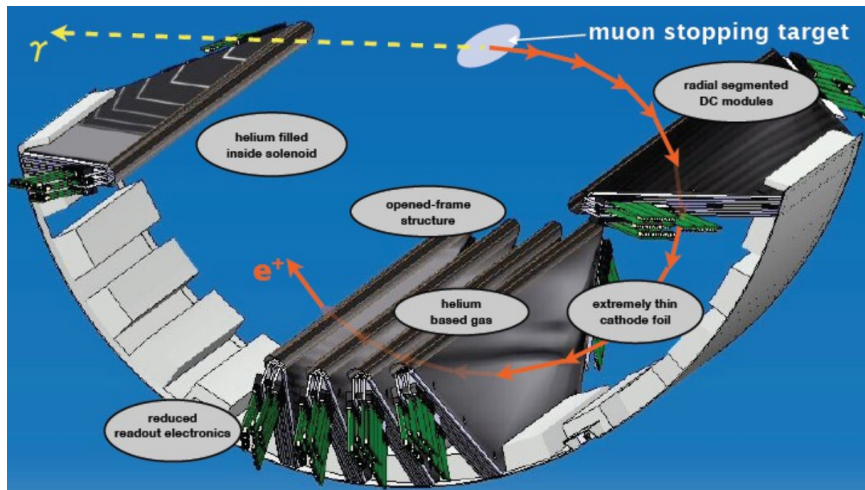


**Figure 2.13:** Schematic representation of the drift chambers layout.

The structural view of a drift chamber is shown in fig.2.14. The chamber walls, acting as cathodes, are made by an extremely thin ( $\sim 12\mu m$ ) polyamide foil coated with  $250nm$  aluminum deposition. An array of sense and potential wires is fixed to a carbon frame, that also realize the chamber structure.

The staggered-cell configuration allows to simultaneously measure the radial coordinate and the hit timing with intermediate resolution of  $5 \text{ ns}$ . The difference between the drift times  $t_1 - t_2$  in two adjacent cells gives the r-coordinate of the track with  $200\mu m$  accuracy, while the mean of the measured times gives the absolute timing with a precision of  $\sim 5 \text{ ns}$  (fig.2.16). From the analysis of the charge ratios between the two wire ends it is possible to obtain a measurement of the  $z$  position with  $1 \text{ cm}$  accuracy. Moreover, the thin layer of aluminum deposit is patterned in such way to obtain a so called “Vernier Pad” [38], as shown in fig.2.15. Within one period of the Vernier Pad ( $5 \text{ cm}$ ) the  $z$  coordinate can be estimated with the ratio of the charge induced in each pad, obtaining a refinement of the  $z$  resolution to an accuracy of  $\sim 500\mu m$ .

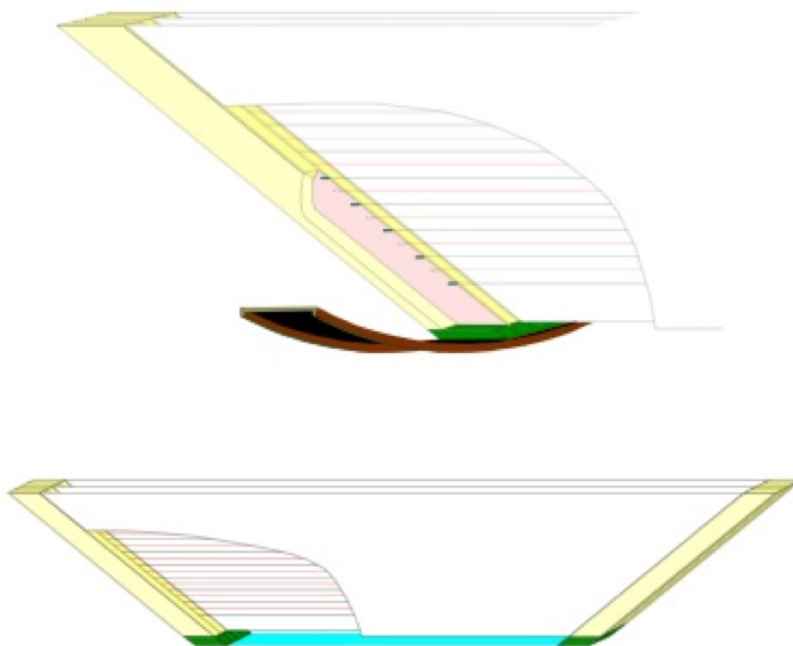


**Figure 2.14:** Schematic view of a single drift chamber.

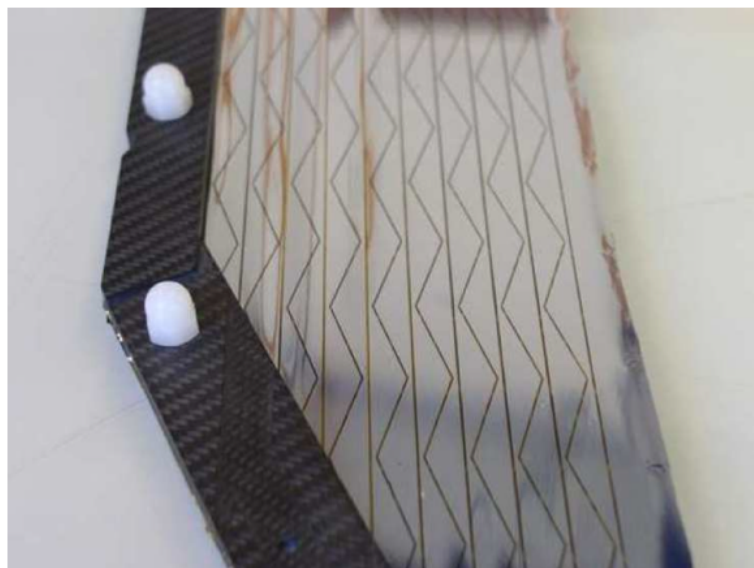


**Figure 2.15:** Picture of a chamber wall. The aluminum deposition is shaped in such way to obtain a particular triangular pattern known as Vernier Pad.

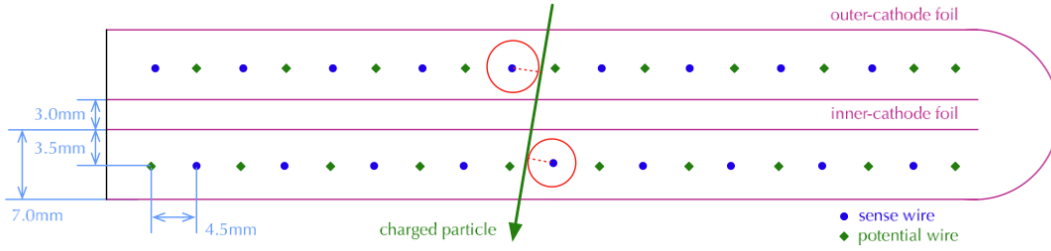


Figure 2.16: Drift chamber section and hit reconstruction.

### 2.2.3 Timing Counter

Finally the positron trajectory is brought at the end to the Timing Counter. Details about the Timing Counter design and operations will be extensively treated in chapters 3 and 4. Here we only summarize the main characteristics.

The detector is designed to obtain an extremely high resolution (100 ps FWHM) for the positron impact time measurement, and, at the same time, it must be able to give an efficient and fast signal for the data acquisition (event selection via direction match with LXe reconstructed events) for gamma time coincidence and topological trigger of first level. Another crucial requirement is the determination of the positron impact point, both for triggering and track reconstruction purposes.

The detector is structured in two independent sub-detectors, namely the longitudinal and the transverse detector. Both detectors are based on fast optical devices: scintillating bars coupled to photomultiplier tubes and scintillating fibers coupled to avalanche photodiodes, respectively for the longitudinal and transverse sub-detector. There are two identical Timing Counter modules, which are placed *upstream* and *downstream* the target, at  $r = 31.9$  cm. Each detector covers the angular range  $-140^\circ < \phi < 15^\circ$ ,  $0.08 < |\cos\theta| < 0.35$ , and extends along the beam axis in the range  $27.6$  cm  $< |z| < 108.0$  cm.

A picture of one Timing Counter module is shown in fig. 2.17.

## 2.3 Liquid Xenon calorimeter

The detection of gamma energy, timing and direction is performed by the Liquid Xenon (LXe) Calorimeter [39], [40], [41], a C-shaped homogenous liquid Xenon volume which is surrounded by photomultiplier tubes and is placed outside the COBRA magnet as shown in fig. 2.1 and 2.18. This particular shape of the detector was chosen in order to minimize the volume with respect to the angular acceptance of the detector. The front wall of the calorimeter is placed 65 cm far from the target position, and the Liquid Xenon thickness is 45 cm. The fiducial volume of the detector corresponds to a solid angle  $\Delta\Omega/4\pi \simeq 12\%$  (corresponding to  $|\cos\theta| < 0.35$  and  $120^\circ$  in  $\phi$ ).

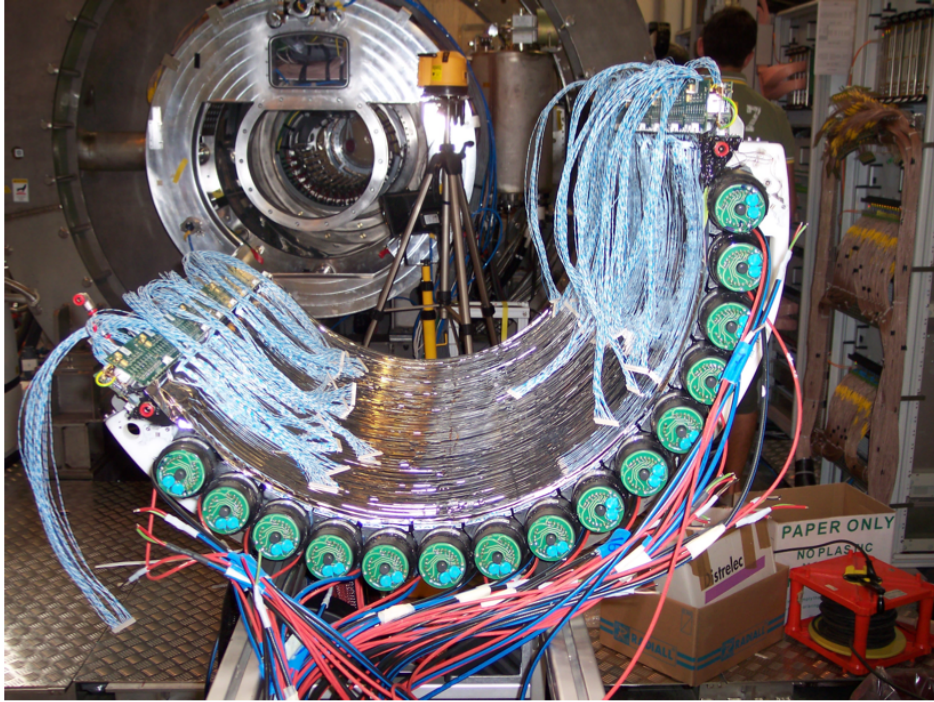


**Figure 2.17:** Picture of the downstream Timing Counter module in front of the COBRA magnet.

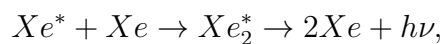
The calorimeter is filled with  $\sim 800 L$  of liquid Xenon at  $165 K$  and pressure of  $3 atm$ . 846 photomultiplier tubes are immersed in the Xenon for best light collection. The external view of the cryostat system and the inner view of the calorimeter are shown in fig. 2.19.

The fast scintillation light emitted at  $\lambda = 178nm$  is directly connected by the PMTs. The Xenon presents remarkable characteristics that are useful for calorimetric purposes:

- short radiation length, resulting in limited thickness of the detector;
- high light yield ( $\sim 4 \cdot 10^4 \gamma/MeV$ , comparable to the NaI response), which guarantees a good energy resolution;
- the scintillation process has a short rise time, together with a short decay time ( $4 ns$ ). This property minimizes the problem of events pile-up and allow to achieve good time resolution.

The main characteristics of liquid Xenon as an active medium are summarized in tab. 2.4.

The scintillation mechanism involves excited Xe atoms ( $Xe^*$ ) and  $Xe^+$  ions produced by charged particles and can be described as follows:



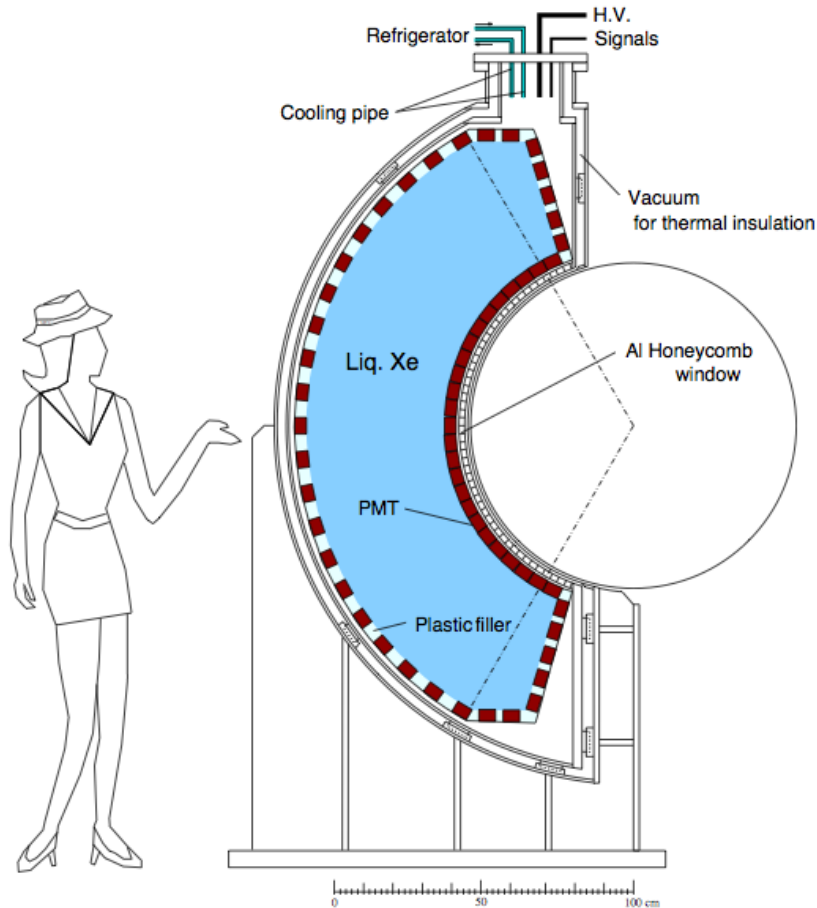
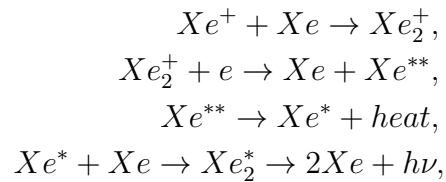


**Figure 2.18:** Schematic side view of the Liquid Xenon calorimeter.

or, more detailed:



where  $h\nu$  is an ultraviolet photon emitted via decay of  $Xe_2^*$  excimer. Being the binding energy of the excited excimer significantly less than the first excited state of a Xe atom, and being the fact that excimer does not exist in the ground level but only in the excited one, the liquid Xenon results transparent to its scintillation

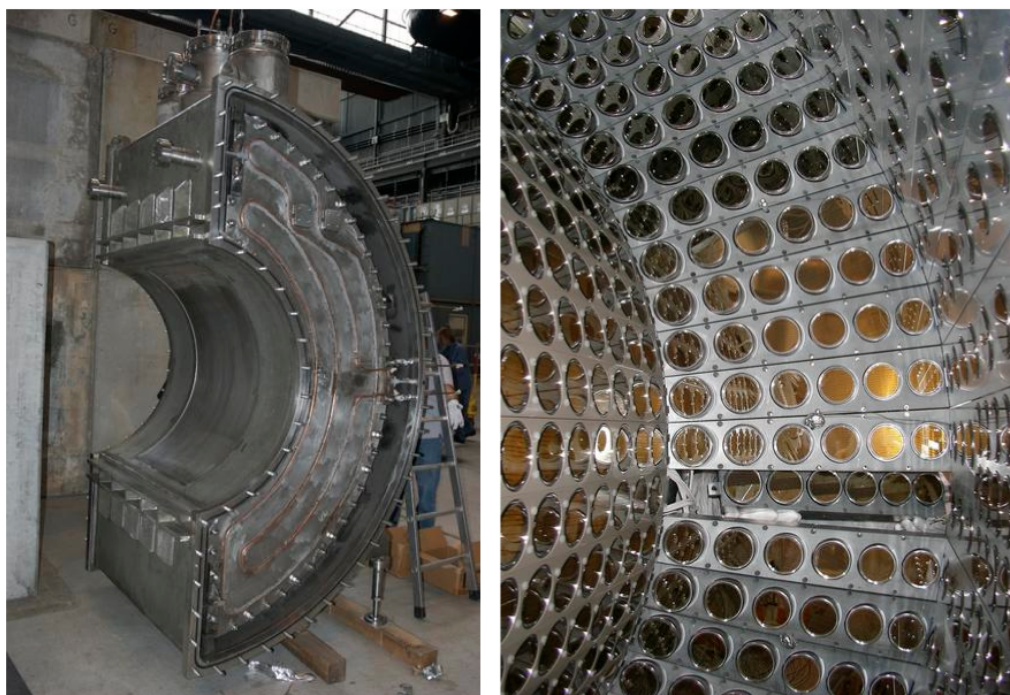


**Figure 2.19:** (*left*) Picture of the cryostat vessel; (*right*) Picture of the cryostat inside.

Atomic number	54
Density	$2.95 \text{ g/cm}^3$
Boiling point	165 K
Fusion point	161 K
Energy deposit per scintillation photon	24 eV( $\gamma$ ), 19 eV( $\alpha$ )
Emission peak	177 nm
Radiation length	2.77 cm
Decay time	4 ns, 22 ns, 45 ns
Absorbtion length	> 100 cm
Attenuation length	$\sim 40 \text{ cm}$
Refractive index	$1.6 \div 1.72$

**Table 2.4:** Main characteristics of Xenon as scintillating medium.

light and the absorption length can be quite large ( $\gg 1m$ ). The latter is a very important characteristic for building calorimeter purposes. Nevertheless the presence of impurities like  $O_2$  or  $H_2O$  in the Xe can result in an inhomogeneous absorption of light with consequently worsening of energy resolution. For this reason a purification system [42] was developed and implemented; moreover, Xenon response and performances are continuously monitored during the whole run time.

A simulation of an event reconstructed in Liquid Xenon is shown in fig. 2.20.

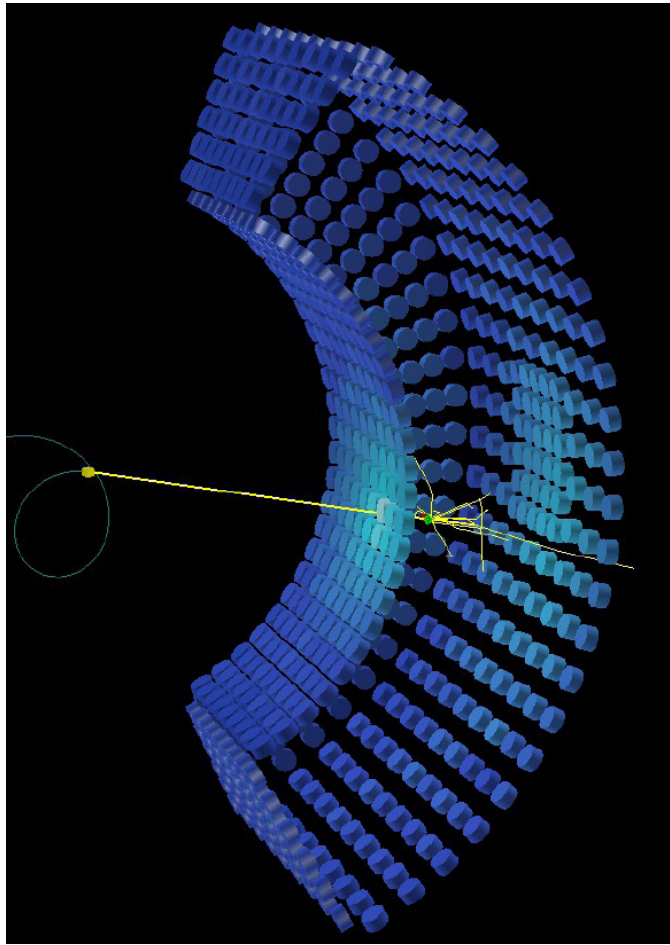


**Figure 2.20:** Example of reconstructed event in the Liquid Xenon calorimeter.

## 2.4 Trigger system

The trigger system processes with a proper acquisition and logic hardware the signals coming from the fast detectors, namely the Timing Counter and the Liquid Xenon, to select  $\mu^+ \rightarrow e^+ + \gamma$  like events and sensibly reject the background, keeping an acceptable acquisition rate [43], [44], [45].

The main informations used at trigger level are:

- the  $\gamma$  energy and time, reconstructed by the Xenon calorimeter;
- the positron time, given by Timing Counter;
- the direction match between the reconstructed directions of the two particles.

The information on the positron momentum by the drift chambers is not used, being too slow because of the delay of the electrons drift time in the gas.

The  $\gamma$  energy is reconstructed by summing all PMTs charges, each one weighted by its gain and quantum efficiency. The selected energy threshold for the MEG

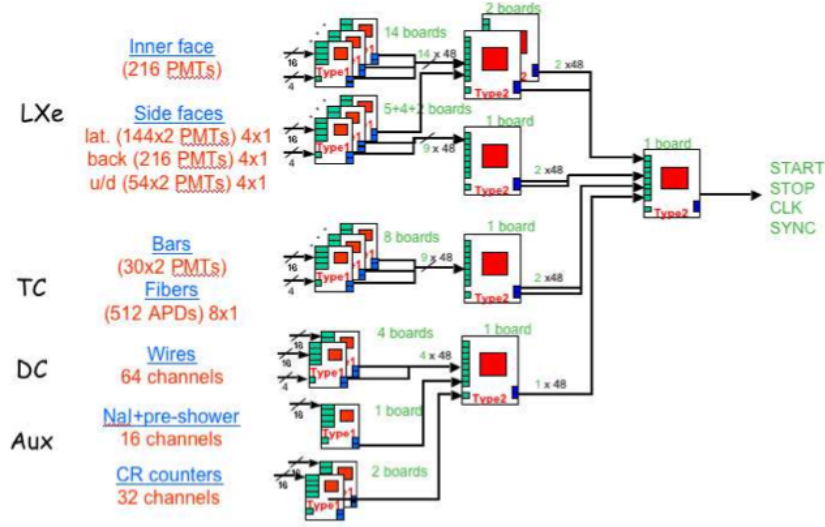


**Figure 2.21:** The structure of the trigger system: the two board types are used for the  $\gamma$  calorimeter and for the positron tracker. The boards are arranged in a tree-like structure.

trigger is  $E_\gamma > 45 \text{ MeV}$ . The efficiency for detecting the  $\gamma$  signal is  $\epsilon_\gamma = 98\%$ . The  $\gamma$  background in the LXe calorimeter comes both from annihilations in flight and muon radiative decays. The background rejection, normalized to the number of muon radiative decays with  $E_\gamma > 10 \text{ MeV}$ , is  $f_\gamma = 8 \times 10^{-3}$ .

The  $\gamma$  timing is extracted from the rise time of the waveform associated with the PMT which shows the maximum signal, while the positron timing is evaluated using the mean of the times measured by the two PMTs of each bar. Details about the positron time extraction will be given in chapter 3. The  $\gamma$ -positron coincidence time window is set to  $10 \text{ ns}$ .

The  $\gamma$  direction is extracted using the coordinates of the PMT with the largest pulse, and assuming the photon as coming from the center of the target. Positron direction is reconstructed by using information on positron impact point by Timing Counter. Both bars and fibers provide information in an independent way. The combined informations about  $\gamma$  positron direction is used to reject non collinear events. The overall efficiency of the direction match selection is estimated to be  $\epsilon_{\gamma e} = 99\%$ . The background rejection factor for the  $\phi$  and  $\theta$  coordinates are respectively  $f_\phi = 0.2$  and  $f_\theta = 0.5$ .

It is possible to evaluate the expected trigger rate in the experimental condition as:

$$R_\gamma = R_\mu \times P(\mu^+ \rightarrow e^+ \nu_e \bar{\nu}_\mu \gamma | E_\gamma > 10 \text{ MeV}) f_\gamma \frac{\Omega}{4\pi} = 2.2 \times 10^3 \text{ ev/s} \quad (2.1)$$

where  $R_\mu = 10^8 \mu/s$  is the muon stopping rate on the target,  $P(\mu^+ \rightarrow e^+ \nu_e \bar{\nu}_\mu \gamma | E_\gamma > 10 \text{ MeV}) = 1.4\%$  is the probability that a  $\gamma$  coming from a radia-

tive decay has energy greater than  $10MeV$  and  $\frac{\Omega}{4\pi}$  is the calorimeter geometrical acceptance.

The expected positron rate (single bar rate) is  $R_{TC} = 2 \times 10^6$  events. Combining  $R_\gamma$  and  $R_{TC}$ , taking into account the background rejection factors and considering a coincidence time window of  $10 ns$  we expect a MEG like trigger rate given by:

$$R_{TRG} = 2R_\gamma R_{TC} f_\theta f_\phi \Delta T \simeq 10 Hz. \quad (2.2)$$

The trigger hardware is mainly based on two types of boards: a first level trigger board, that receives the analog signals and perform a digitization at  $100MHz$  by means of Flash Analog-to-Digital Converter (FADC), and the second level trigger boards, based on Fast Programmable Gate Array (FPGA), which operates on the digitized signal applying different algorithm depending of the kind of implemented trigger. A third board (Ancillary board) is added to the trigger system to provided the clock and the synchronization signals to all other boards. A schematic view of the trigger system is shown in fig.2.21.

## 2.5 DAQ system

The signals from all detectors are digitized by a  $2GHz$  sampling chip developed at the PSI [46] and based on the so called Domino Ring Sampler (DRS). Each DRS board has 8 data acquisition channels plus 2 auxiliary channels (used for calibrations purposes), each having 1024 sampler and holders (S-H) capacitors on a single chip. A so-called ‘‘domino wave’’ circuit generates short pulses which opens the analog switches of the S-Hs of each channel. The Domino wave is generated by a series of inverters, whose speed is controlled by an analogue voltage [47]. An on-chip phase-locked loop (PLL) rephases the Domino wave to an external reference clock thus ensuring a high stability over temperatures and power supply voltage changes. Time jitter is also controlled by the same mechanism.

The Domino wave can be stopped by an external trigger, after which the S-Hs capacitors are read out and digitized by a commercial ADC. The readout speed is  $40MHz$ . A simplified scheme of the DRS layout is shown in fig.2.22.

Each chip is housed on dedicated VME boards equipped with a 12 bit flash ADCs and FPGAs, thus the configuration of the DAQ can be changed and optimized during the set up of the experiment. A simplified scheme of data acquisition system is shown in fig. 2.23. All the  $\sim 1000$  PMTs channels of the experiment are digitized at a sampling speed of  $2GHz$ , while the  $\sim 3000$  drift chambers channels are digitized with a lower sampling speed of  $500 Ms/s$ . A high quality low jitter timing calibration signal is distributed and sampled in all DRS boards in order to obtain the best timing resolution by keeping all boards synchronized.

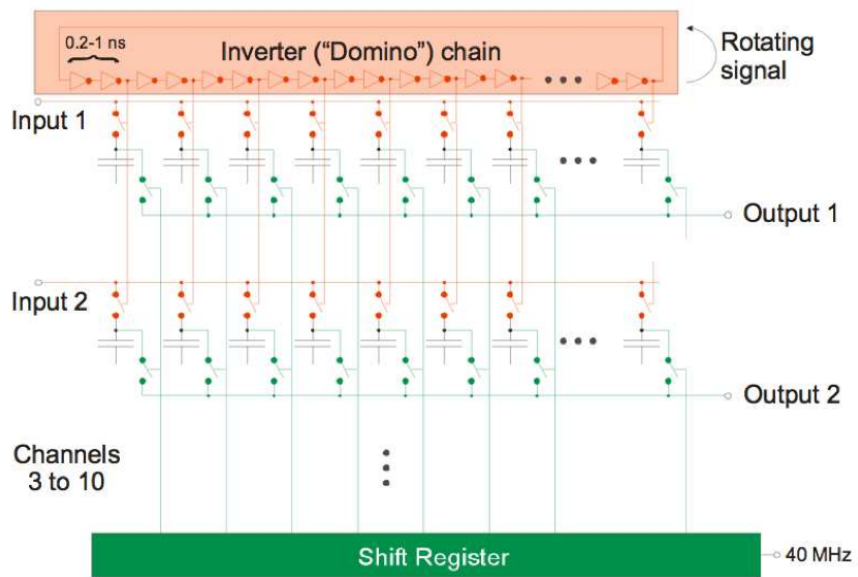


Figure 2.22: A simplified layout of the Domino Ring Sampler chip.

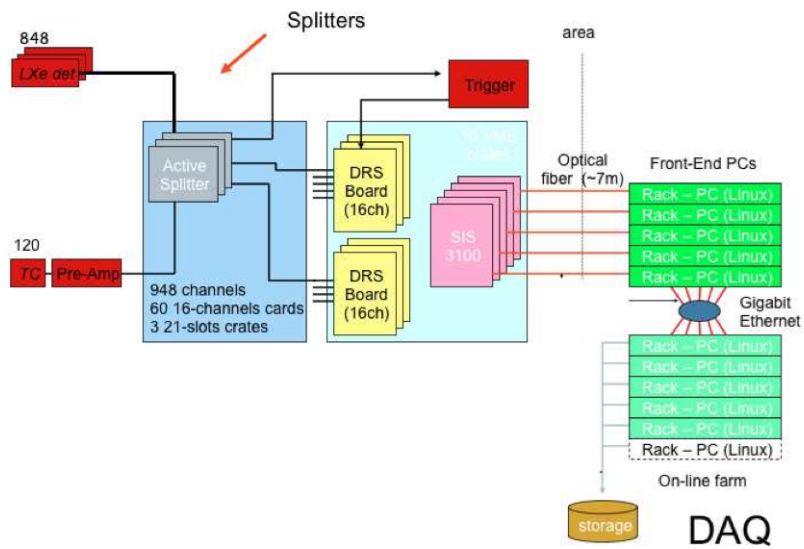


Figure 2.23: Schematic representation of the Data Acquisition System of the MEG experiment.

## 2.6 Experimental apparatus performances

I summarize here the performances obtained of MEG apparatus during the first two years of data acquisition: 2008 and 2009. In tab. 2.5 the main results for each kinematic variables involved in the signal recognition are listed, together with some details about the DAQ time and the achieved sensitivity. Moreover, the final results with the measured upper limit on the  $\mu \rightarrow e\gamma$  branching ratio are anticipated. All details about the analysis technique used to extrapolate those numbers from data will be given in chapter 7.

The 2010 data are still under analysis while I was writing, so that I omit here the latest results. Some anticipation about the Timing Counter performances during the last year run will be given in chapter 6.

	2008	2009
Gamma energy (%)	2.0 ( $w > 2.0$ cm)	2.0 ( $w > 2.0$ cm)
Gamma timing (ps)	80	67
Gamma position (mm)	5(u,v)/6(w)	5(u,v)/6(w)
Gamma efficiency (%)	63	58
$e^+$ timing (ps)	< 125	< 125
$e^+$ momentum (%)	1.6	0.61 (core)
$e^+$ angle (mrad)	10( $\phi$ )/18( $\theta$ )	6.2( $\phi$ )/9.4( $\theta$ )
$e^+$ efficiency (%)	14	40
$e^+ - \gamma$ timing (ps)	148	151 (core)
$\mu$ decay point (mm)	3.2(y)/4.5(z)	3.3(y)/3.3(z)
Trigger efficiency (%)	66	91
Stopping $\mu$ rate ( $s^{-1}$ )	$3 \times 10^7$	$2.9 \times 10^7$
DAQ time /Real time (days)	48/78	35/43
S.E.S. @90% box	$5 \times 10^{-12}$	$1.4 \times 10^{-12}$
Expected $N_{BG}$	0.5	1.2
Sensitivity	$1.3 \times 10^{-11}$	$3.5 \times 10^{-12}$
BR upper limit obtained	$2.8 \times 10^{-11}$	$9.5 \times 10^{-12}$

**Table 2.5:** Summary of the experimental apparatus performances during the run 2008-2009. The resolution values are given in  $\sigma$ . The achieved sensitivity and the final results are also listed.

## Chapter 3

# The Longitudinal Timing Counter

The MEG experiment was conceived with the aim to push the timing resolution between the individual detection of positron and gamma within 150 *ps*. This comes out mainly from the spread of the gamma timing in the LXe calorimeter, the reconstructed time of flight of the positron and the Timing Counter impact timing.

The Timing Counter plays a key role because its design should ensure an intrinsic timing resolution for positron of 100 *ps* FWHM. Further, it must get out signals both for fast triggering process based on gamma time coincidence and topological correlation between gamma and positron hit positions. This argument is discussed in ([48], [49]).

The choice and the characterization of the devices and the calibrations of the detector play a fundamental role in defining the detector performances. In this chapter the Longitudinal Timing Counter concept, design and commissioning is described. I will start describing the working principles of the detector, then the adopted solutions and the final accomplishments will be summarized. The calibration methods developed to obtain the best from the detector will be described in chapter 5.

### 3.1 Detector concept and design

The main tasks of the longitudinal Timing Counter are the measurement of the positron time and impact point with a high efficiency triggering capability [50], [51]. To obtain very high timing resolution, the active volume of the detector have been divided in 15 adjacent 4 *cm* thick and 80 *cm* long plastic scintillating bars coupled to PMTs.

The Timing Counter is composed by two specular modules, positioned in the *up-* and *down-stream* sector respect to the target; the structure of scintillating bars is placed inside the magnet, in a barrel-like assembly as shown in fig. 3.1. This geometry has been selected for matching the corresponding back to back acceptance angle of the Liquid Xenon Calorimeter.

The  $\mu \rightarrow e\gamma$  positrons emitted in the nominal acceptance angular ( $0.08 <$

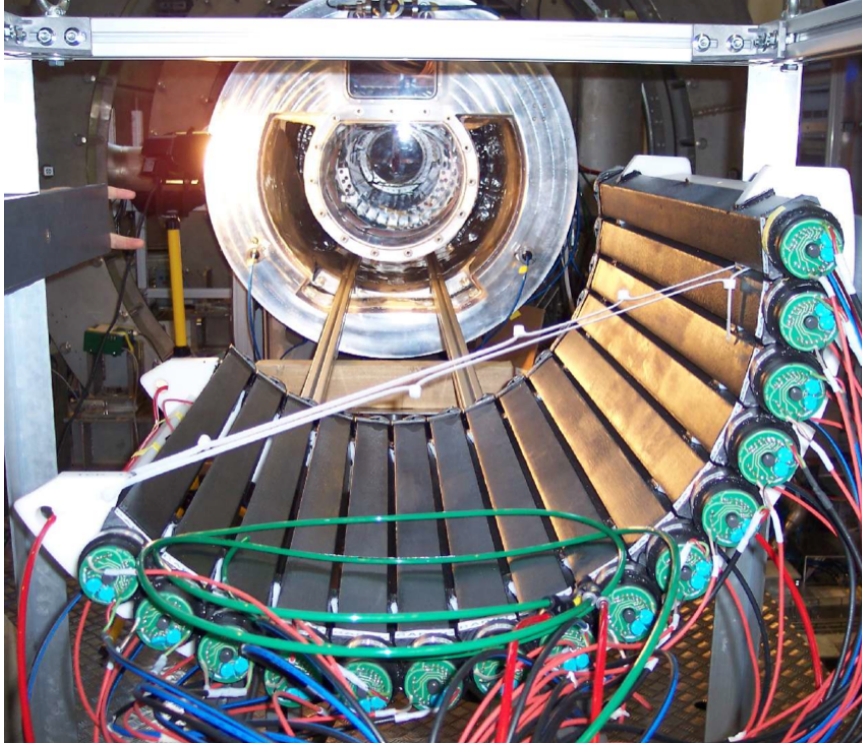


**Figure 3.1:** Picture of Timing Counter with bar exposed.

$|\cos\theta| < 0.35$ ,  $-140^\circ < \phi < 15^\circ$ ) hit on of the TC modules after a flight of about 1.5 turns in the drift chambers. In the following, we will refer to a single TC module.

In the conceptual design for achieving high timing resolution it has been exploited the idea of maximize the sensitivity to the first scintillation photons emitted by a plastic scintillator with fast rise time and good attenuation length. The practical realization is to collect only photons guided by total internal reflection; thus, each bar is contained in a light absorbing housing as shown in fig.3.2, to prevent highly scattered photons from reaching the PMTs.

The plastic scintillator was chosen to be the BICRON BC404, which has the best available compromise between rise time of the emission ( $0.6 \text{ ns}$ ) and attenuation length ( $\geq 140 \text{ cm}$ ).

The bars thickness was chosen in such a way to obtain an adequate photostatistic, needed to reduce effects correlated to PMTs transit time spread (see 3.3.1). The minimum value that fits the constraints due to the available space in the magnet was found to be  $4 \text{ cm}$ : the bars were shaped with approximately  $4 \times 4 \text{ cm}^2$  squared section as described in sec. 3.4.2.

Moreover, in order to improve as much as possible event fluctuations of the detector light response versus the impact angle spread if trajectories in the  $x$ - $y$  plane bars are tilted respect  $z$ -axis of an angle  $\alpha = 20.5^\circ$  (see 3.4.2).

Monte Carlo simulations shows that after bar rotation the average impact angle in the  $x$ - $y$  plane is approximately perpendicular and the tracks that travel the

whole thickness of the scintillator are maximized. A similar counter shape versus trajectory matching in the  $y$ - $z$  plane was not done because this would require curved bars.

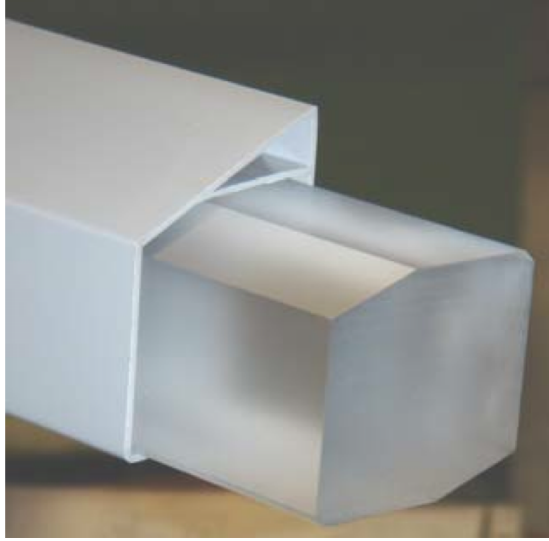


**Figure 3.2:** Picture of a Timing Counter bar inside the plastic socket before surface polishing and black painting of the socket. Note the particular shape of the bar section, made in order to optimize the particle trajectories inside the scintillator.

## 3.2 Timing generalities

In this section the basics of the timing counter operations will be described [52].

Considering a positron that impinges on a TC bar, as shown in fig 3.3, the information from the PMTs positioned on each end of the bar can be written as:

$$t_{in} = T_{phys} + b_{in} + TW_i + \frac{\frac{L}{2} + z}{v} \quad (3.1)$$

$$t_{out} = T_{phys} + b_{out} + TW_i + \frac{\frac{L}{2} - z}{v}, \quad (3.2)$$

where  $T_{phys}$  is the “real” time of impact of the positron on the bar,  $b_{in,out}$  are fixed offsets due to the different electronic chain,  $TW_{in,out}$  are contributions from Time Walk effect and  $v$  is the effective velocity of light in the bar. The subscript  $in$  and  $out$  are referred to the “more” internal and “more” external position inside the COBRA magnet. The centre of the  $z$  axis is taken in the middle of the bar.

In such conditions the impact time can be easily evaluated as the average of the two PMTs times:

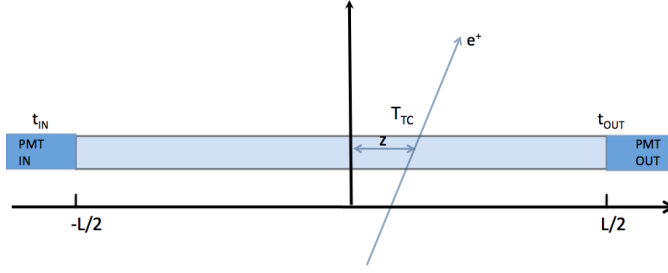


**Figure 3.3:** Definitions of the quantities involved in positron timing. See text for details.

$$T_{phys} = \frac{t_{in} + t_{out}}{2} - \frac{b_{in} + b_{out}}{2} - \frac{TW_{in} + TW_{out}}{2} - \frac{L}{2v}. \quad (3.3)$$

The determination of the factors  $b$  and  $TW$  will be discussed hereinafter in deeper detail.

On the other hand, taking into account the time difference between the two pulses we can obtain the reconstruction of the positron impact point:

$$z = \frac{v(t_{in} - t_{out})}{2} - \frac{v(b_{in} - b_{out})}{2} - \frac{v(TW_{in} - TW_{out})}{2}, \quad (3.4)$$

or, more simply,

$$z = \frac{v \cdot (t_{in}^* - t_{out}^*)}{2}, \quad (3.5)$$

where  $t^*$  takes already in account the time corrected with the contributions mentioned above.

The information about impact point can also be extrapolated in a different way evaluating the ratio between the charges delivered by the two PMT pulses:

$$Q_{in} = E \cdot G_{in} \cdot e^{-\frac{L+z}{2\lambda}} \quad (3.6)$$

$$Q_{out} = E \cdot G_{out} \cdot e^{-\frac{L-z}{2\lambda}}, \quad (3.7)$$

where  $E$  is the energy released inside the bar,  $G$  takes into account several contributions (i.e. the scintillator yield, PMT quantum efficiency and gain),  $\lambda$  is the attenuation length of the bar. Taking the ratio we obtain:

$$\frac{Q_{in}}{Q_{out}} = \frac{G_{in}}{G_{out}} - \frac{2z}{\lambda} \quad (3.8)$$

which, solving for  $z$  and taking the logarithm, leads to:

$$z = \frac{\lambda}{2} \left( \ln \frac{Q_{in}}{Q_{out}} - \ln \frac{G_{in}}{G_{out}} \right) \quad (3.9)$$

Moreover, the product  $Q_{in} * Q_{out}$  is proportional to the square of the energy released in the bar:

$$Q_{in} \cdot Q_{out} = E^2 \cdot G_{in} \cdot G_{out} \cdot e^{-\frac{L}{\lambda}}. \quad (3.10)$$

Note that combining equations (3.5), (3.9) and (3.10) one obtains a way to evaluate effective velocities and attenuation lengths of TC bars.

The two impact point reconstructions are used in different stages in the data acquisition. Positron timing from PMTs time difference is used in offline analysis after a series of corrections necessary to get the best estimate from the signals, providing also a good z resolution, while the online algorithm needs real time response. Therefore, the trigger system is based on the charge ratio positron reconstruction, that doesn't need offline calibrations.

### 3.3 Contributions to timing resolution

In order to obtain the goal timing resolution of 100ps FWHM or better, it is necessary to evaluate the sources of resolution worsening, and apply some tricks useful to reduce these contributions, coming from:

- the intrinsic PMT time response, due to the different transit time of electrons through the dynodes chain (transit time spread, TTS),
- the intrinsic spread in the scintillating process (rise time, fall time and FWHM of the light signal),
- the spread in the energy release process,
- the propagation mechanism of photons emitted isotropically, resulting in a wider distribution of the photons arrival time on each PMT cathode;
- the readout electronics.

In the following sections each contribution will be discussed in details and quantified.

#### 3.3.1 PMTs transit time spread

Concerning the photomultiplier tubes, one of the most disturbing issue to face in detector realization is the need to work inside a strong magnetic. This affects both the gain and the intrinsic time resolution of the devices, thus having important implication in PMTs choice. As I will discuss more in details in sec. 3.4.1, a special kind of PMTs, namely *fine-mesh* PMTs, was chosen because of their low sensitivity to magnetic field.

The intrinsic time resolution of the device is estimated using the *transit time spread* (TTS) [53], [54], [55]. In fact, due to the stochastic nature of the multiplication process in the dynodes chain, any electronic avalanche will have slightly

different transit time along the chain itself, depending both on PMTs intrinsic characteristics (shape and disposition of the dynode, dimensions of photocathode) and on external factors (bias voltage, voltage divider, magnetic field strength and orientation). The width of this distribution is called TTS and is usually quoted for a single photoelectron extracted at the cathode. In a realistic case, with the emission of  $N$  photoelectrons, the TTS will rescale as  $\sqrt{N}$ , whence the advantage of a scintillator with very high light yield.

The measured value of the TTS is  $\sim 600$  ps FWHM, to be rescaled by the number of photo electrons produced in a time interval equal to the TTS itself, quoted as  $N_{TTS} \simeq 900$ .

The measured value of the TTS is 2 or 3 times greater than the typical value measured on standard PMTs: this is a consequence of the configuration of the dynode chain of *fine-mesh*

### 3.3.2 Scintillator time response and time of flight spread

Let's consider the same system depicted in 3.3. The signal observed at the bar end is given by the superimposition of the signals coming from each photon generated in the scintillation processes. Every single photon will arrive at the cathode surface with a delay:

$$\Delta t = T_i - T_{phys}, \quad (3.11)$$

where  $T_{phys}$  is the impact time on the Timing Counter bar. The distribution of the delay time is strictly related in a obvious way with the probability density function (pdf) of the scintillator emission time. If we consider a single photon emission, the delay time that this photon can assume will be known with an uncertainty given by the  $\sigma$  of the scintillator pdf, which has a behaviour like:

$$I = I_0 \left( e^{-\frac{t}{\tau_1}} - e^{-\frac{t}{\tau_2}} \right), \quad (3.12)$$

where  $\tau_1$  and  $\tau_2$  are respectively the fall and the rise time of the scintillator.

If we consider the emission of  $N$  photons, we can define the lowest delay as

$$\Delta t_{min} = \min\{\Delta T_i\}. \quad (3.13)$$

whose r.m.s. is rescaled as the squared root of the number of photons generated in the scintillator processes that arrive at the PMT cathode. This number can be evaluated as the ratio between the bar geometrical acceptance (defined by the limit reflection angles, correlated with the refractive index of the bar) and the whole solid angle. This was estimated to be 6.6% of the total number of generated photons, meaning  $N_{pe} \sim 6 \cdot 10^3$ . This indicates the need to have a scintillator with the better light yield possible.

The characteristics that lead us in the choice of scintillator were:

- higher possible light yield, to increase overall photo-statistic;

- shorter possible rise and fall time, meaning that light emission is narrow and most of the photons are emitted in the leading edge.

The characteristics of the chosen scintillator will be described in sec. 3.4.2.

Moreover, in the calculation we have also to consider the spread of the optical path travelled by the photons inside the bar. This was calculated by means of Monte Carlo simulation, and result to be  $\sigma_{flight} \simeq 1.2 ns$ .

### 3.3.3 Energy release in the bar

Another fundamental source of uncertainty is the spread of the energy release inside the scintillator, continuously distributed along positron trajectories inside the bar, rather than fully localized in a point-like region. Also an additional contribution due to the positron incidence angle should be taken into account: both were evaluated using Monte Carlo simulations (as will be shown in sec. 3.4.2).

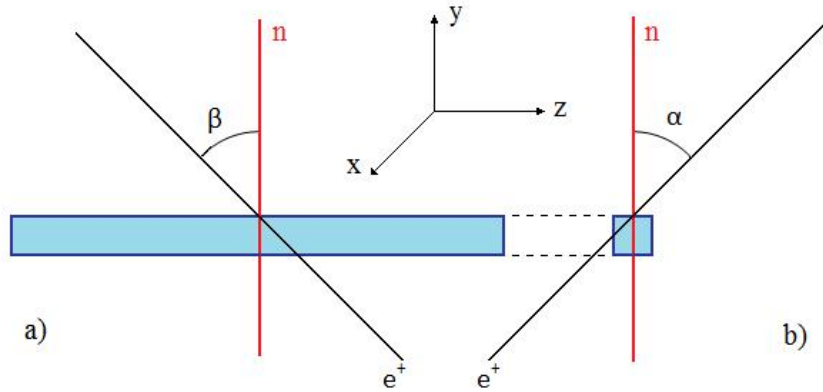


**Figure 3.4:** Sketch of the definitions of the angles  $\beta$  (a) and  $\alpha$  (b);  $n$  is the normal to the bar surface. See text for details.

In particular the important quantities in the optical spread evaluation, are respectively the angles  $\alpha$  ( $\beta$ ) formed by the normal to the bar surface with the projection of positron tracks on  $x - y(y - z)$  planes (as described in fig. 3.4), and were studied by Monte Carlo simulations; the effect due to  $\alpha$  was made negligible rotating the bar around their axis by an angle  $\hat{\alpha} = 20.5^\circ$ , corresponding to the mean value of  $\alpha$ , in such way the positrons impinge orthogonally to the bar surface. Thus one can calculate the mean length of the energy released in the bar that is in first approximation proportional to the projection of the positron tracks in  $z$  direction:

$$\langle \Delta T_E \rangle \simeq \frac{l \sin \beta}{v_{eff}} \simeq 200 ps, \quad (3.14)$$

where we consider a mean positron track length of  $5 cm$  and  $\beta = 40^\circ$ , both extrapolated from Monte Carlo simulation, and the length has been converted in time units introducing the effective velocity of light in bar,  $v_{eff} \simeq 14.7 cm/ns$ .

In order to estimate the contribution to the overall time resolution, one has to calculate the convolution between a rectangular function with width equal to  $\langle \Delta T_E \rangle$  with the scintillator response already described in sec. 3.3.2, and the extract the width of the resulting function. The result was found to be  $\sigma_E \simeq 1.0 \text{ ns}$

### 3.3.4 Expected performances

It is now possible to evaluate the expected time resolution for a Timing Counter bar, by taking into account all the contributions listed in the previous sections, as:

$$\sigma = \sqrt{\sigma_{el}^2 + \frac{\sigma_{TTS}^2}{N_{TTS}} + \frac{\sigma_{flight}^2 + \sigma_E^2}{N_{pe}}} \simeq 30 \text{ ps}, \quad (3.15)$$

where  $\sigma_{el}$  represents the contributions coming from the electronic devices used to process the PMTs signals. In the first test made at the Beam Test Facility in Frascati (Rome, Italy) the electronic contribution was estimated to be  $\sigma_e \simeq 15 \text{ ps}$ .

We have to keep in mind that this number must be taken as an intrinsic lower limit for the scintillator-PMTs system resolution, given by the system itself and its features (physical processes, geometry, devices characteristics). In this calculation we have considered an ideal case, in which real world effects (additional noise from EMI pick-up, digitizer jitter, time reconstruction algorithm systematic errors, rate dependent events from crowding bars) are not taken in account. As we will see in chapter 6 the time resolution in the real experimental conditions is slightly worse. Nevertheless, it is important to remark that eq.3.15 shows that the resolution target value of the Timing Counter is fully feasible.

## 3.4 Timing Counter design criteria

We will describe now more in details the characteristic of the devices chosen in the Timing Counter realization.

### 3.4.1 PMT choice and characterization

As already stated in sec. 3.3.1 a strong constraint in Timing Counter design is the fact that PMTs must operate in a high magnetic field ( $B_{inner} = 1.27 \text{ T}$ ,  $B_{outer} = 0.4 \text{ T}$ ), being the detector positioned inside the COBRA volume. It's well known that magnetic field severely affects PMTs performances [53], [54], [55], both gain and the transit time spread by acting on secondary electrons trajectories. Moreover, important characteristics to be considered in the PMT choice were:

- transit time spread as low as possible, to reduce intrinsic PMT contribution to timing resolution;
- good geometrical matching between the PMTs sensitive area and the scintillator surface to reduce at a negligible level the inefficiency correlated to light losses;

- optimum cathode quantum efficiency in correspondence of the peak of the scintillator light emission, to have the maximum number of photons converted in photoelectrons on the cathode;

In the Timing Counter project has been decided to use a particular kind of photomultiplier tube, namely *fine-mesh* photomultipliers (HAMAMATSU R5924 [56]), that guarantee good performances also in high magnetic field, and also fit the requests listed above. The main characteristics of the used PMTs are listed in tab. 3.1.

Diameter	2"
Diam. of sensitive area	39mm
Number of dynodes	19
Quantum efficiency (390nm)	22%
Gain (B=0)	$1.0 \times 10^7$
Gain (B=1T)	$2.5 \times 10^5$
Rise time	2.5ns
Mean anodic current	$100\mu A$

**Table 3.1:** Main characteristic of HAMAMATSU R5924 photomultiplier tubes.

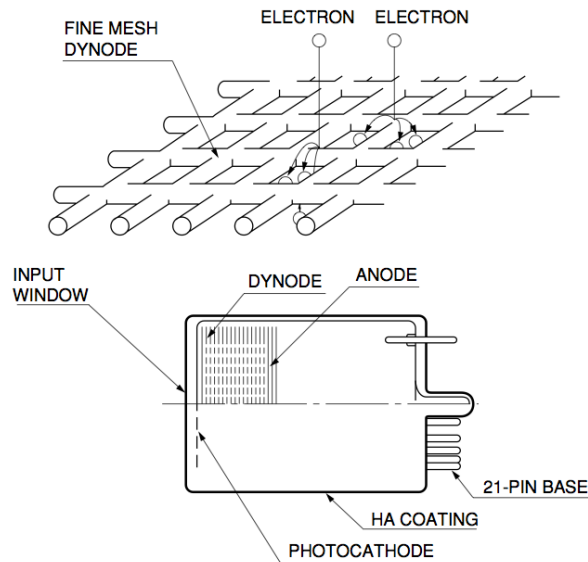


**Figure 3.5:** (*up*) Fine mesh dynode layout; (*down*) schematic of HAMAMATSU R5924 PMTs [56].

The working principle of a fine-mesh photomultiplier is the same as a conventional PMT; the remarkable difference is in the dynode configuration, depicted in

fig. 3.5. In this case, the multiplying structure is made by a set of very fine mesh with reticular step  $\sim 10\mu m$ , stacked with less than  $1mm$  distance between consecutive layers (dynodes): this geometry prevents electrons losses due to curved trajectories in a magnetic field. In such way, it is possible to obtain only a small decrease in gain also in the very harsh working conditions of the MEG experiment.

An extensive campaign of preliminary test was done to measure the behaviour of the main PMT parameters (gain, TTS, rate capability) as a function of magnetic field intensity and direction with respect to the PMT axis to take advantage from a careful design of the detector [57], also considering that the mechanical constraints left some room for PMTs displacement as shown in fig.3.6.

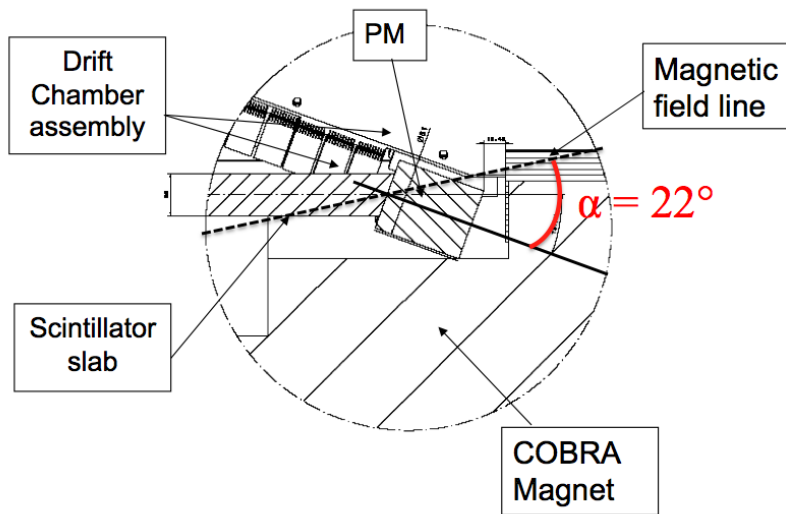


**Figure 3.6:** Particular of the PMT displacement with respect to the end of the scintillator bar. The mechanical constraints from COBRA magnet profile and Drift Chamber structure are also shown.

Here will be reported only the results about the gain, transit time spread and overall time resolution. The measurements were done in the COBRA magnet, keeping the PMTs in the same working condition of the experiment, with a magnetic field variable from 0 to  $1.2 T$  and exploring a set of angular position in the range  $0^\circ < \alpha < 60^\circ$ .

In fig. 3.7 the gain as a function of the magnetic field intensity for different angles is plotted, taking the PMTs at a constant voltage of  $2KV$  (close to the final working point). The graphs clearly show the dependence of gain versus magnetic field intensity. Moreover, the gain worsening in the range  $\alpha \sim 20^\circ \div 30^\circ$  is much lower with respect  $\alpha < 20^\circ$  or  $\alpha > 30^\circ$ .

Dependencies of transit time spread and time resolution were verified, as shown in 3.8 and 3.9, in the angular range  $0^\circ < \alpha < 30^\circ$ . While the transit time spread is almost independent from the angle, resulting in just a 10% of variation for the highest field values, the time resolution show a worsening of about a factor 2 in the

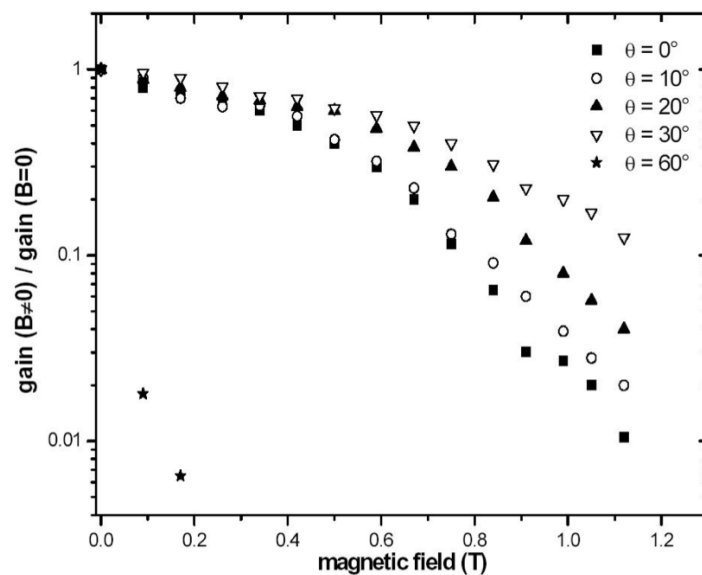


**Figure 3.7:** PMT gain in magnetic field normalized to “null” field gain, as a function of magnetic field intensity measured for different angle between PMT axis and magnetic field lines.

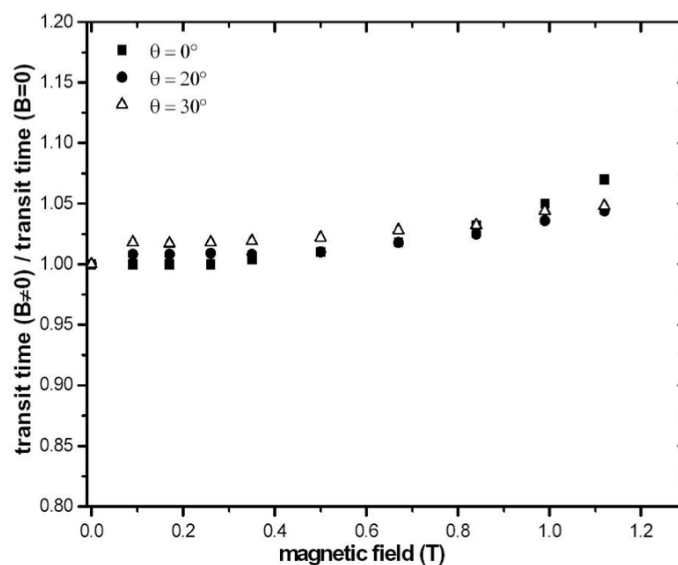


**Figure 3.8:** TTS normalized to “null” field TTS, for a PMT in magnetic field as a function of field intensity, measured for different angle between PMT axis and magnetic field lines.

comparison between  $\alpha = 0^\circ$  and  $\alpha = 30^\circ$ . This last effect is obviously correlated with the corresponding worsening of PMT gain shown in fig. 3.7.

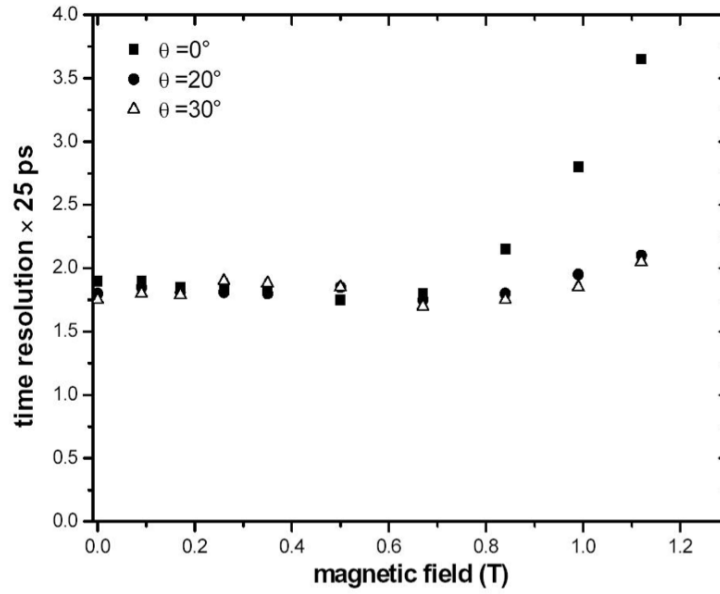


**Figure 3.9:** Behaviour of the PMT time resolution in magnetic field, as a function of magnetic field intensity for different angles between PMT axis and magnetic field lines.

Thus, the angular range  $20^\circ < \alpha < 30^\circ$  was found to be the best one for the PMT tilting angle with respect to the magnetic field line: considering also the mechanical constraints, the final PMTs position was chosen to be  $\alpha = 22^\circ$ , as shown in fig. 3.6.

### 3.4.2 Scintillator

As already remarked in sec. 3.3.2, to obtain the desired performances the use of a scintillating material with the fastest time response, together a high light yield is required. The final outcome of the R&D process was that the ideal candidate is the BC404 plastic scintillator, whose main characteristics are summarized in tab. 3.2 [58].

Material	Polyvinyltoluene
Density	$1.032g/cm^3$
Light yield (% Anthracene)	68
Rise time	0.7ns
Fall time	1.8ns
Pulse width (FWHM)	2.2ns
Attenuation length	140cm
Emission peak	$408nm$
Refractive index	1.58

**Table 3.2:** Main characteristic of BC404 plastic scintillator.

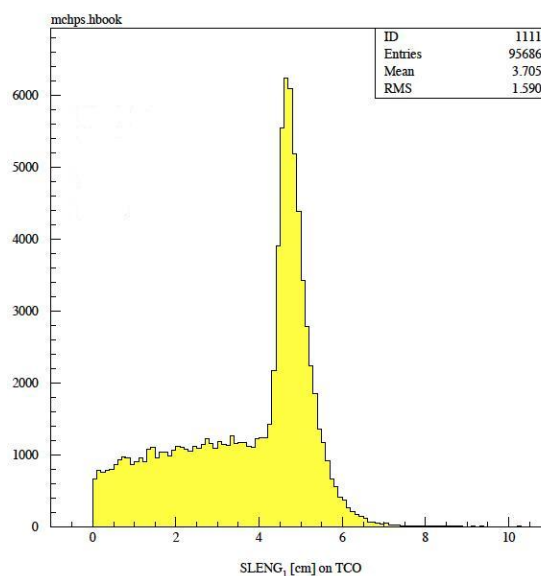


**Figure 3.10:** Track length distributions inside timing counter bar for michel positron

Bar sizes and placement were evaluated using Monte Carlo simulations, together with test beam campaign. In order to obtain a good photostatistic for  $\mu \rightarrow e\gamma$  positrons, the minimum path length in scintillator was found to be 4 cm, that was used as bar thickness. A plot of the track distribution inside the scintillating bar is shown in fig. 3.10. Moreover, the geometrical constraints on the

minimum radius allowable for the bar detector led to particular section of the bars, shown in fig. 3.11, with cut corner angles. The bars are directly coupled to the PMTs with a good match between bar shape and 2" PMTs sensitive area.

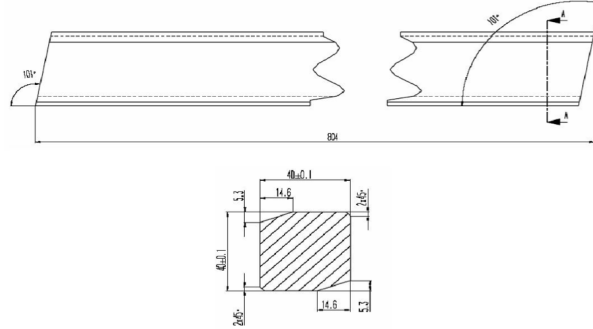


**Figure 3.11:** TC bar geometry: (*up*) side view. The cut shape of each end side is optimized to obtain the best tilt angle between PMT axis and magnetic field lines; (*down*) section view. The edges of the bar were shaped in such a way to satisfy the mechanical constraints, together a bar rotation along its major axis.

The spread of positron trajectories inside the bars was studied and minimized by means of Monte Carlo simulations. The definitions for significative angles  $\alpha$  and  $\beta$  was already given in fig. 3.4. The results are shown in fig.3.12 and fig.3.13.

In fig.3.12 is reported the simulation of the distribution of positron hit angle on bar surface: in the plot,  $\alpha^*$  is the impact angle *after* having tilted the bar around its axis, as explained in sec.3.4. One can see that the width of this distribution is  $\sim 9^\circ$ , thus resulting in a negligible effect in time resolution.

The plot in fig.3.13 shows the simulation of the  $\beta$  angle. The mean value of this distribution was used in section 3.3.3 to evaluate the contribution to the time resolution.

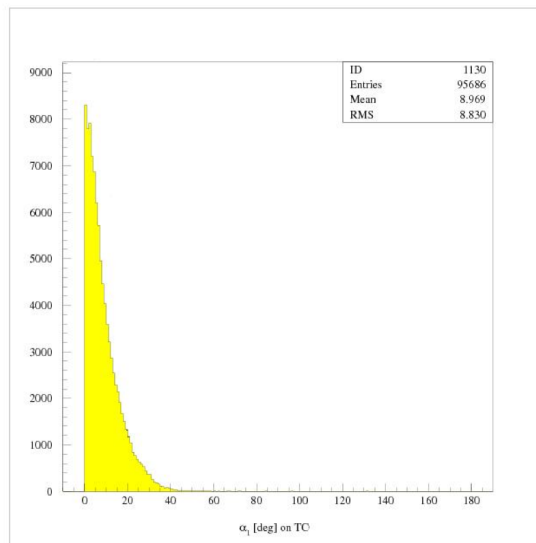


**Figure 3.12:** Monte Carlo simulation of the impact angle between the projection of the positron track on the  $x - y$  plane and the normal to the surface of the bar,  $\alpha^*$

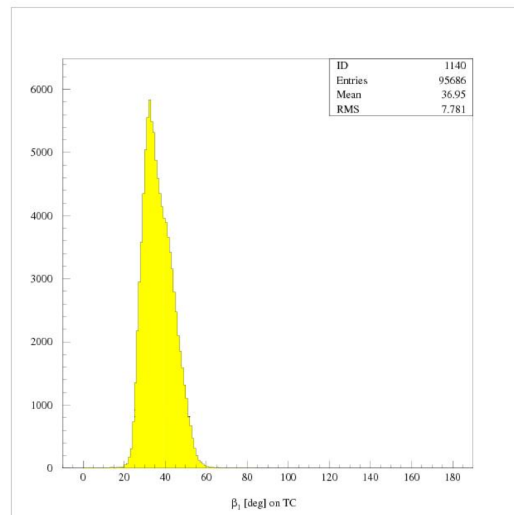


**Figure 3.13:** Monte Carlo simulation of the impact angle between the projection of the positron track on the  $z - y$  plane and the normal to the surface of the bar,  $\beta$ .

### 3.4.3 Read out electronic and time extraction from data

In order to preserve the performances obtained by our detector, a custom made electronic was designed and developed. A schematic representations of the electronic readout chain of the Timing Counter channels is shown in fig. 3.14.

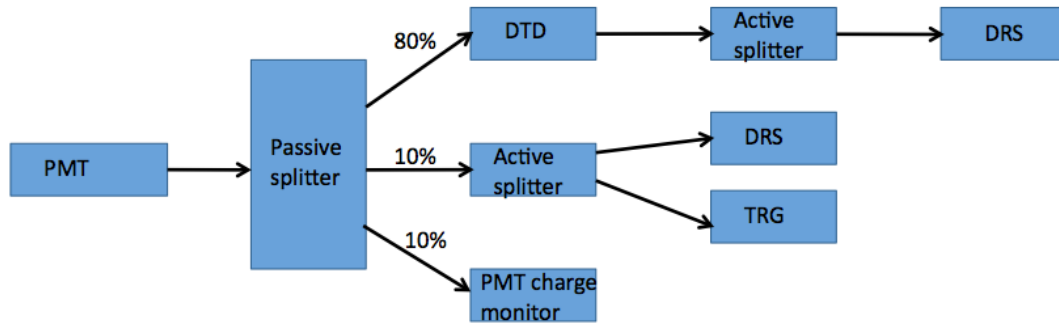


**Figure 3.14:** Schematic representation of the Timing Counter electronic readout chain.

Each PMTs signal passes through a passive splitter, with different attenuation factors:

- 80% is sent to the Double Threshold Discriminator boards, with square pulse output (NIM standard);
- 10% is sent to an active splitter, that made two identical copies of the signals, sent respectively to the trigger boards and to the digitizer boards;
- the last 10% is sent to a charge integrator for monitoring purposes.

This configuration permits us to take advantage of some benefits:

- the dynamic range of the digitizer and trigger boards is not saturated by the analog signal;
- we have the possibility of pushing the gains of PMTs, obtaining high signal to noise ratio, satisfactory time resolutions also without applying Time Walk corrections (see .5.2); moreover, we can set a threshold level to a few photons;
- robustness against digitizer ADC non linearities jitter averaging over the discriminator output pulse length.

The Double Threshold Discriminator (DTD) is a high bandwidth, low noise and ultra-low jitter comparator in which two different thresholds are set. The lower one is set as low as possible, compatibly with the noise level of the PMT signal, in order to reduce the effect of Time Walk on timing resolution (for a complete treatment of the Time Walk issue, see sec. 5.2). The higher threshold

is set to reject noise spikes and events with low energy deposit, coming from particles crossing a few millimeters of scintillator and from secondary particles, giving low energy background. The value of the high threshold determines the detector efficiency and is set accordingly to the trigger threshold. When a pulse height is larger than the higher threshold a logic NIM signal is fired and digitized by a DRS channel. The optimization of the value for the two thresholds will be described in sec. 5.2.1 and sec. 5.4.

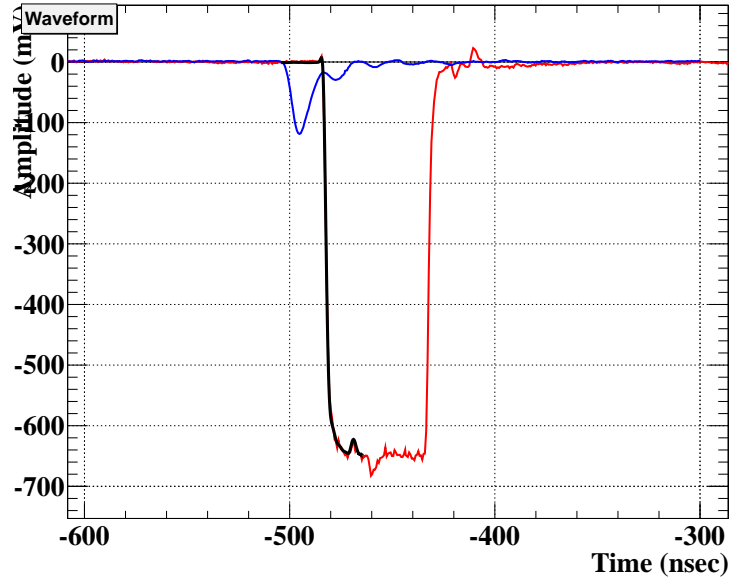


**Figure 3.15:** Timing counter signals: in red the Double Threshold Discriminator output with the template fit superimposed (black), in blue the analog signal digitized by the DRS.

The impact time of positron on Timing Counter is obtained starting from the DTD NIM waveforms output. For each channels some pulses are mediated, in order to obtain a mean waveform of the pulse, the *template waveform*. In this way one obtains a reference pulse to be used in the fitting procedure [59].

The fit has two free parameters:

- the baseline level, that is, the mean voltage level of the considered channel;
- the leading edge of the pulse, that means the starting point of the pulse, corresponding to the point with greater derivative.

The leading-edge is used as a measurement of the arrival time of positron. As explained in section 3.2 this time is affected by some systematic uncertainty that mainly arise from Time Walk effects, and will be discussed in the follow paragraph. In fig. 3.15 are shown the NIM output from a DTD channel (red) with the template waveform superimposed (black) and the corresponding analog signal (blue).

### 3.5 Final test

An extensive test was performed at the Beam Test Facility of Frascati (Roma), where it is available an electron/positron beam with energy up to  $500 \text{ MeV}$ . The beam is absolutely well collimated (typical beam spot dimensions are of the order of  $5 \text{ mm}$ ), and it is possible to have bunches of 1 or 2 electrons, thus preventing effects due to multiple hits on bar. The test was performed orienting the bar in such a way to reproduce the MEG positron impact average angles, thus reproducing the experimental conditions.

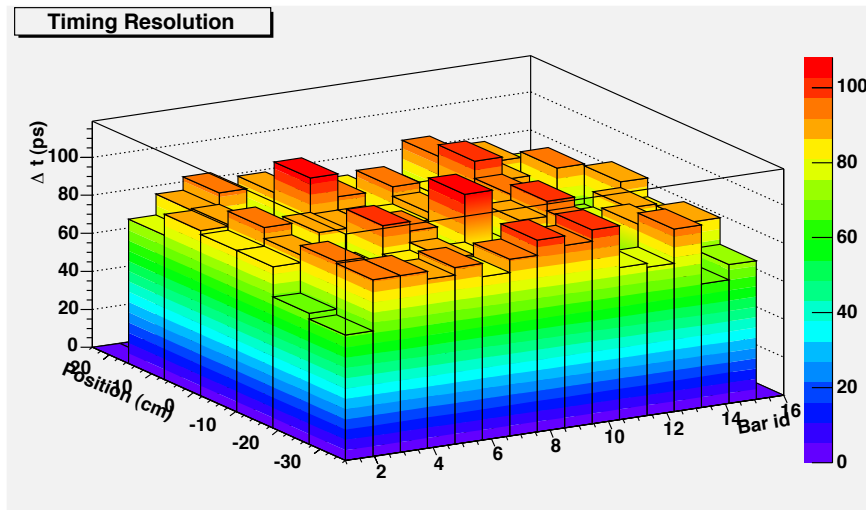


**Figure 3.16:** Time resolution as a function of impact point position and bar number achieved during the beam test at the Beam Test Facility of Frascati.

During this test the time resolution was estimated evaluating the resolution of the quantity  $\Delta T = T_1 - T_2$ , that is the time difference between the two opposite PMTs of each bar.

The resolution was measured for different impact points along the bars, and the results are shown in fig. 3.16. The timing resolution is generally higher than the required value, being worse than  $100 \text{ ps}$  only in a few points: this confirm us the possibility to reach the target Timing Counter resolution. Nevertheless, we have to consider the fact that in the final experimental conditions, some issues can worse the detector resolutions, as will be explained in sec. 6.1.2.

---

## Chapter 4

# The Transverse Timing Counter

The first proposed purpose of the Transverse Timing Counter is to provide a direct geometric pattern signal of the event to be fed into the Trigger processor. Later it has been recognized that the possibility to improve the  $z$  recognition to about 1 *cm* could have been useful for positron track reconstruction.

In this chapter the design criteria (sec. 4.1) and the devices (sec. 4.2 and sec. 4.3) used in the detector realization will be presented. Finally, the results achieved in the run 2010 will be shown. For general reference for this chapter, see [60], [61].

### 4.1 Detector concept

The Transverse Detector consists of two modules, each formed by an array of 256 scintillating fibers (Bicron BCF20) read out by Avalanche PhotoDiodes (APD) HAMAMATSU S8664-55 [62], segmented along  $z$  direction and covering the inner surface of the longitudinal detector barrel.

The small cross section of the fibers ( $5 \times 5 \text{ mm}^2$ ) allows for a good spatial resolution and perfect match with the APD sensitive area ( $5 \times 5 \text{ mm}^2$ ). In order to fit the mechanical constraints, fibers are curved with two different shapes, leading to some losses in the fiber light transmission that has been studied and recovered by using a reflective wrapping.

APDs have some attractive features: compactness, high quantum efficiency of about 80%, insensitivity to magnetic field [63], quite fast response but low gains (up to  $10^3$ ), even if biased near the breakdown voltage. This last point has some negative implications on detector stability and noise performances that has required a long work for achieving best signal to noise ratio, as we will see in the following.

The Front End electronics is mounted on the detector to perform signal processing very close to the diode, in order to reduce the stray capacitance; each APD signal is read-out by a high gain low noise voltage amplifier, discriminated and acquired by an FPGA-based VME board integrated in the data acquisition system.

Groups of 8 APDs are mounted on same board that provides common bias,

the analog sum, and the 3 bit digital word of hit pattern. Because of mechanical constraints, a double row of FE boards is prepared to host APDs, so adjacent fibers go alternatively to either board. Therefore a couple of boards manage 16 APD-fiber blocks covering a region of  $\Delta z \sim 9.6 \text{ cm}$ . Analog signals from each FE are sent to the trigger boards, where the signals corresponding to 2 adjacent bunches of 8 fibers are summed together, providing an independent measure of the impact point to be merged with the one coming from the longitudinal detector.

A picture of the transverse timing counter is shown in fig. 4.1.

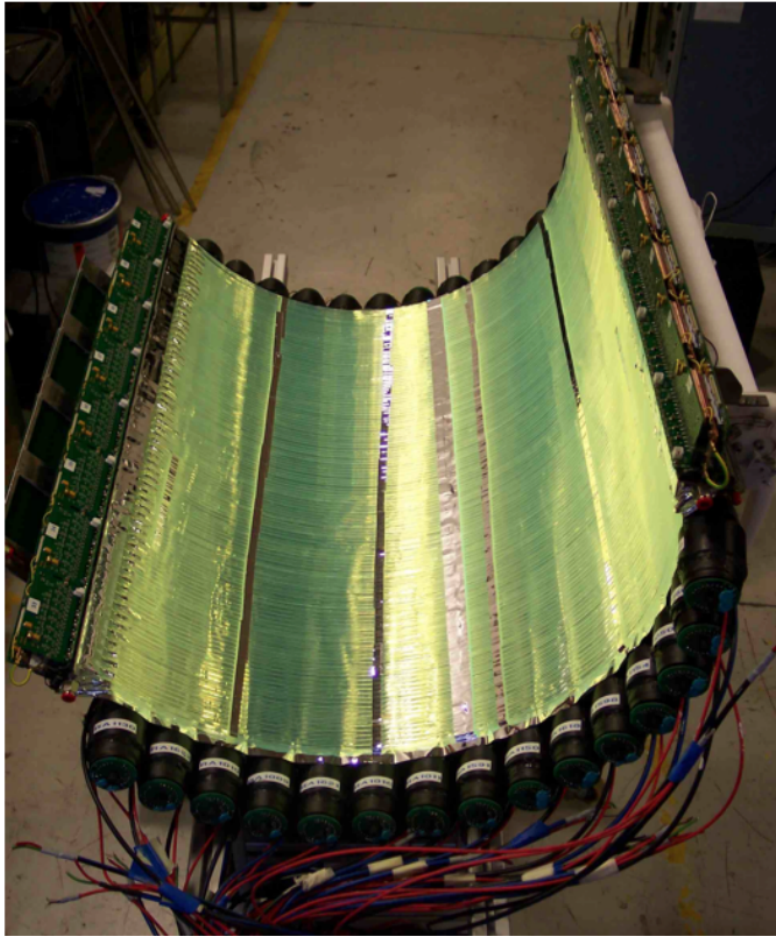


**Figure 4.1:** Picture of the Timing Counter with scintillating fiber exposed.

The original proposal of a transverse detector made like the longitudinal one (see chapter 3) was rejected because, several disadvantages coming from a PMT-based system:

- the bars displacement, that should be orthogonal respect to the magnetic field lines, demands an angle between PMTs axis and field lines greater than the limit angle measured for fine mesh PMTs (see sec. 3.4.1). Moreover, the alternative of using an optimized light guide would have been a very

complicated issue, in particular concerning the implementation of an efficient signal transport system outside the COBRA magnet;

- the use of PMTs instead of avalanche photodiodes would have required a larger segmentation resulting in a decrease of the achievable resolution on positron impact point.

The realization of a scintillating fibers system read-out by APD permits to bypass these problems: the use of APDs allows signal read-out directly inside the COBRA magnet, without the need to use light piping to transport signal outside the magnet itself; moreover, the reduced dimensions of the devices results in a compact detector, suitable for mechanical integration in the MEG apparatus layout. Scintillating fibers guarantee an optimal matching with APDs sensitive area, and make possible a thin detector with a 5 *mm* pitch along the  $z$  axis.

Nevertheless, the realization of such a kind of detector presents some technical challenges to be solved:

- the need to operate the APDs in the proximity of the junction breakdown voltage, far away from the usual working point, in order to obtain the highest signal multiplication before the electronic amplification and signal shaping; it should be noted that the APDs came from the CMS production and therefore are optimized for operation at low gain (50), in which the excess noise contributions are less significant;
- the necessity to work with curved square scintillating fibers, that have light losses at the corners and at low curvature radii;
- the realization of a support structure, which acts as cooled thermal bus with temperature stability better than 0.5 degrees.

These issues will be described deeper in details in the next sections.

## 4.2 APD characterization

An avalanche photodiode is a photodiode that owns an internal multiplication mechanism [64]: a simplified sketch of the APD operations is shown in fig. 4.2. The multiplication process is due to the profile of the doping concentration, resulting in a high field avalanche region, and it is activated by the voltage applied to the APD. The free charge carriers generated by the incident radiation are accelerated sufficiently between collisions to create additional electron-hole pairs along the collection path. Because of lattice dynamics (thermal agitation mainly) the gain factor is very sensitive to temperature and applied voltage, therefore avalanche photodiodes require well-regulated high-voltages power supply and a precise monitoring of the working temperature.

A schematic draw of the APD is shown in fig. 4.3, while the main characteristics of the devices are summarized in tab 4.1. The chosen photodiodes are realized

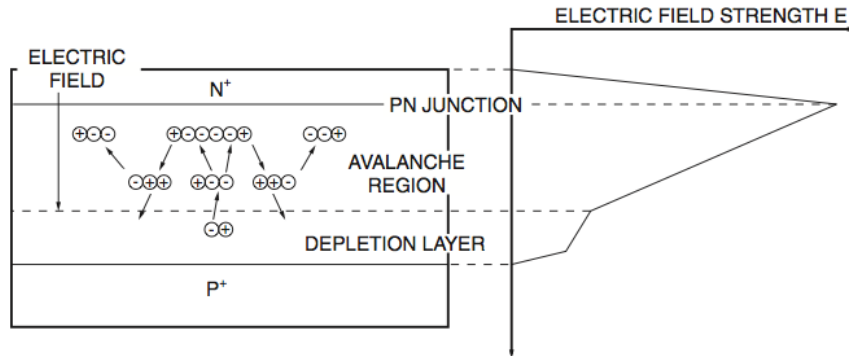


**Figure 4.2:** Schematic draw of the multiplication process inside the APD [62].

Sensitive area	$5 \times 5 \text{ mm}^2$
Spectral response range	$320 \div 1000 \text{ nm}$
Peak sensitivity wavelength	$600 \text{ nm}$
Quantum efficiency (420nm)	70%
BD voltage typ.	400 V
BD voltage max.	500 V
$V_{BD} - T$ coefficient	0.78 V/K
Dark current typ.	10 nA
Dark current max.	100 nA
Capacitance	80 pF

**Table 4.1:** Main characteristics of HAMAMATSU S8664-55 APD.

via epitaxial growing on a low resistivity Si substrate. The thickness of the p-doped material, realizing the p-n junction, is lower than  $7 \mu\text{m}$ , thus minimizing the amount of ionizing radiation absorbed in this region and keeping only the depletion region sensitive to the radiation itself, in order to have a more uniform response. An additional layer of n-doped material decreases the device capacitance and increases stability with respect to applied voltage variations [65].

The APD working parameters are strongly temperature dependent. In particular, the gain is inversely proportional to the temperature, while BD increases with temperature [66]. The gain behaviour is due to the fact that a temperature decrease implies an increase of the mean free path of the charge carriers inside the device, that means a lower energy loss for elastic scattering with the crystal lattice. For the same reason, also the breakdown voltage will change together with temperature. The behaviour of the dark current will be explained in sec. 4.6.

### 4.2.1 Breakdown measurement

The first issue to face with during the detector realization is the measurement of the breakdown (BD) voltage, related to the need for a high gain that forces the

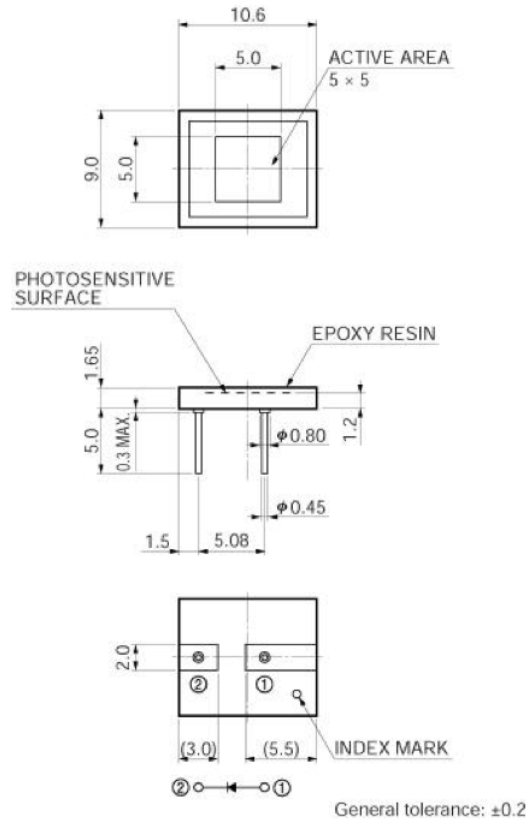


**Figure 4.3:** Schematic draw of HAMAMATSU S8664-55 APD [62].

APDs working point to be very close to the BD itself.

The BD occurs at the voltage sufficiently high to have the multiplication process self-sustained [67]; in this circumstance thermally generated electron-hole pairs (ehp) can trigger an avalanche resulting in an exponential increase of the generated current, and a corresponding huge amount of recorded pulses. In order to determine the BD voltage for each device, a bench test has been developed: an APD is mounted on a copper support and completely obscured to prevent the environment light from generating unwanted pulses. A  $10M\Omega$  load resistor is put in series to the device, as shown in fig. 4.4.

The current flowing from APD on the resistor generates on the latter a voltage drop, measured by a high precision multimeter. Until the bias voltage  $V_{bias}$  is far from the breakdown point, the voltage drop across the resistor  $V_R$  is negligible (few  $mV$ ), because the dark current is of the order of  $10^{-9} A$ ; vice versa, when the bias voltage approaches the BD value, both the current and the measured potential drop  $V_R$  increase exponentially. We define the breakdown condition when  $V_R > 1 V$ , corresponding to a dark current greater than  $100 nA$ ; then we estimate  $V_{BD}$  as:

$$V_{BD} = V_{bias} - V_R. \quad (4.1)$$

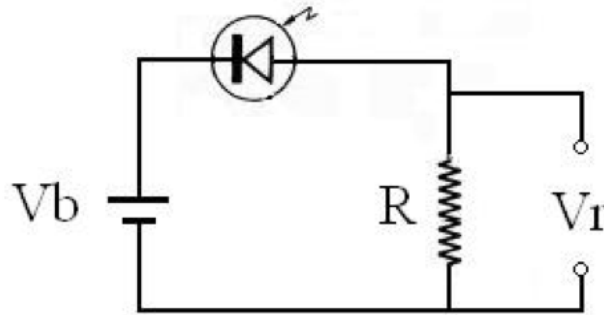


**Figure 4.4:** Wiring diagram of the APD breakdown voltage measurement.

This rough estimate of the BD voltage is used to group 8 by 8 the APDs with matched performance, because each group of 8 APDs belonging to a single electronic board with common bias voltage.

The apparatus is also suitable to measure the BD variations with temperature, which is regulated by means of a recirculating system, coupled to the APD copper support, with  $0.1^\circ$  accuracy and great stability. The obtained results are shown in fig. 4.5. The basic principle of a recirculating system with thermoelectric coller was applied to the final detector too.

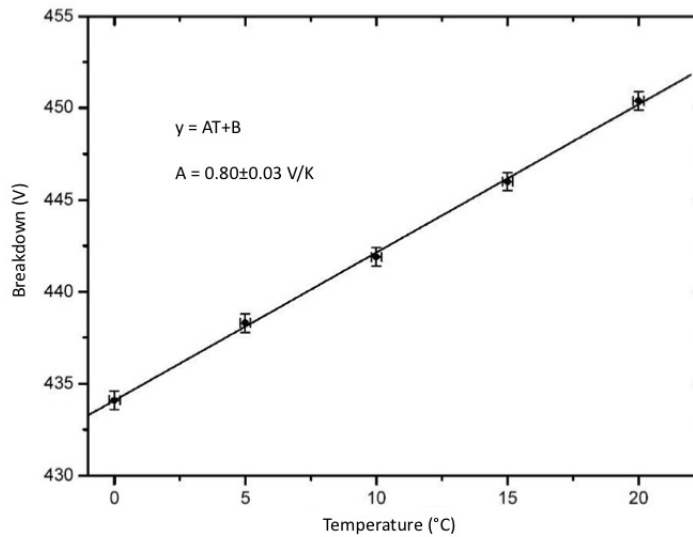


**Figure 4.5:** Breakdown voltage as a function of temperature, with linear fit superimposed.

The data have been fitted by means of a linear function as shown in fig. 4.5, obtaining the result:

$$\frac{dV}{dT} = 0.80 \pm 0.03 \text{ V/K}, \quad (4.2)$$

in very good agreement with the manufacturer data sheet (see tab. 4.1). The precise knowledge of the breakdown-temperature correlation will be used during the data acquisition to make fine adjustment of the voltage supply, optimizing the devices performances.

### 4.2.2 Dark current characterization

As expected for any semiconducting junction, the thermal excitation generates free electron and hole carrier in the depleted layer. The resulting current is called *dark current*.

Generally, inside any semiconductor device the probability to generate an electron-hole pair by thermal agitation decreases by lowering the temperature, following the law:

$$p(T) \propto e^{-\frac{E_{gap}}{kT}}, \quad (4.3)$$

where  $E_{gap}$  is the energy gap between valence conduction bands.

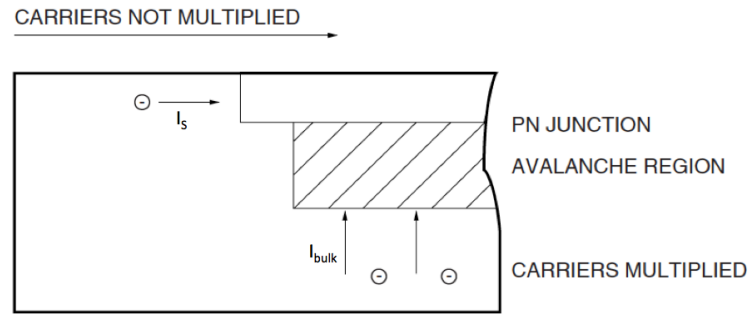


**Figure 4.6:** Schematic representation of the two components that characterized the dark current inside an avalanche photodiode (from HAMAMATSU).

The APD dark current, due to the presence of an internal mechanism of multiplication, can be expressed as the sum of two components as shown in fig. 4.6 [66], [68], [69]:

- surface leak current flowing through the interface between the PN junction and Si oxide layer,  $I_S$ ;
- internal bulk current, generated inside the Si substrate,  $I_{bulk}$ .

The surface leakage current is not multiplied because it does not flows in the avalanche region, while the internal does, thus the total dark current  $I_D$  is given by:

$$I_D = I_S + G \cdot I_{bulk}, \quad (4.4)$$

where  $G$  is the gain of the device.

It is important to emphasize again here that the multiplication process increases with decreasing temperature, so that the behaviour of the dark current as a function of the temperature will be different depending on the voltage bias. In particular two competing effects are presents:

- variation of number of thermally generated carriers with temperature;
- increase of a gain of a single ehp with decreasing  $T$ .

Depending on applied bias, one of these two mechanisms become dominant resulting in a subsequent behaviour of  $I_D$ .

In fig. 4.7 the dark current measurements obtained during the detector RD are shown. The measurements have been performed using the same procedure already described in sec. 4.2.1.

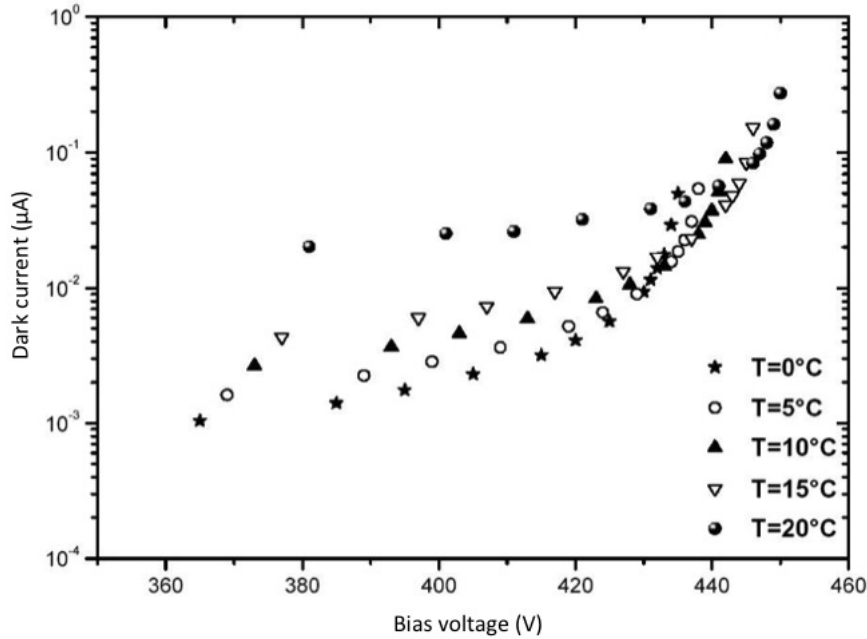


**Figure 4.7:** Dark current behaviour as a function of bias voltage, for different working temperatures.

For bias voltage far away from the BD voltage, where the surface current dominates, the dark current is nearly constant, and greater currents correspond to greater temperatures. Vice versa, in proximity of the breakdown voltage the surface current becomes negligible while the internal current is relevant, thus the dark current increases exponentially, and, fixing the bias voltage, it is greater for low temperatures.

This suggests us again the need to have a complete control of the devices temperature, avoiding abrupt variations that could affect the detector operations.

### 4.2.3 Gain characterization

The APD gain is defined as:

$$G = \frac{N_{el}}{N_{ph}}, \quad (4.5)$$

where  $N_{ph}$  is the number of incident photons on the APD sensitive area, while  $N_{el}$  is the number of generated photoelectrons. The measurement was performed using the apparatus depicted in fig. 4.8.

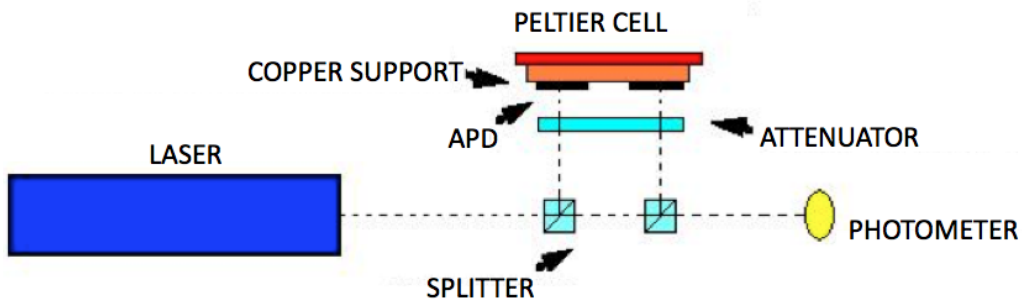


**Figure 4.8:** Sketch of the apparatus used to measure the APD gain.

The APD under test is illuminated by means of a pulsed laser with  $\lambda = 408 \text{ nm}$ , rise time  $200 \text{ ps}$  and width  $\tau \sim 4 \text{ ns}$ , in order to reproduce a light pulse similar to the scintillating fibers output. The fiber output is a broad spectrum peaked around  $500 \text{ nm}$ . The gain and the quantum of the device are independent from the radiation wavelength in the range  $400 \div 500 \text{ nm}$ , therefore the performed test results to be a good approximation of the real experimental conditions.

The laser output crosses a series of semi-reflecting optical filters, which have the purpose to divide the beam, directing it simultaneously on the APD under test, on a calibrated APD used as reference device and on a photodiode connected to a high precision photometer, which realize, given the transmission coefficient of the optical filters, the real time monitoring of the light intensity incident on APDs.

Before illuminating the APD surface, the laser beam was attenuated in order to prevent APD operations in a non linear region. Both APDs are read-out by charge amplifiers, which outputs are connected to the data acquisition system. The temperature is controlled by means of a Peltier cell, which keeps APDs at the constant temperature  $T = 20.0 \pm 0.2 \text{ }^\circ$ .

It is now possible to measure the gain of the devices, taking in mind eq. 4.5 and considering that the mean number of photons impinging on the APD surface at each pulse is given by:

$$N_{ph} = \frac{P\epsilon}{fE_{ph}A}, \quad (4.6)$$

$f$	2 KHz
$E_{ph}$	3 eV
$A$	5000
$G$ (420nm)	450 mV/pC
$\epsilon$	0.7

**Table 4.2:** Summary of the values the parameters of eq. 4.6 and 4.8

where  $P$  is the mean power of laser beam measured by the photometer,  $f$  is the repetition rate of the pulses,  $E_{ph}$  is the photon energy,  $A$  the attenuation factor of the optical system and finally  $\epsilon$  is the APD quantum efficiency.

The number of photoelectrons produced by the APD is given by:

$$N_{el} = \frac{V_{out}}{eG}, \quad (4.7)$$

where  $V_{out}$  is the amplifier output,  $G$  its gain and  $e$  represents the electron charge.

Thus substituting eq. 4.6 and 4.7 in eq. 4.5 one obtains:

$$G = \frac{N_{el}}{N_{ph}} = \frac{V_{out}}{eG} \cdot \frac{fE_{ph}A}{P\epsilon}. \quad (4.8)$$

In tab. 4.2 the values of the parameters used in eq. 4.6 and 4.8 are listed.

The obtained result is shown in fig. 4.9, which demonstrates a typical behaviour of gain as a function of the applied voltage in the region near the breakdown point. The breakdown voltage for the considered APD resulted to be  $V_{BD} = 403.8 V$ . The data points were fitted by means of an exponential function, obtaining as a result  $V_{BD} = 403.9 \pm 0.7$ , in very good agreement with the prediction made.

The measurement has confirmed that it is possible to obtain sufficiently high gain,  $G \sim 200 \div 500$  keeping the APD in a voltage range  $3 \div 5 V$  below the breakdown voltage.

### 4.3 Scintillating fibers characterization

In the transverse Timing Counter realization scintillating fibers BCF20 from Saint Gobain were used [70]. These fibers presents a squared  $5 \times 5 mm^2$  section and emission spectrum peaked at  $\lambda = 492 nm$ . The main characteristics of the fibers are summarized in tab. 4.3.

The fibers are characterized by a double step refractive index cladding type, that increases the devices trapping efficiency (see sec. 4.3.1). The number of photons a fiber can trap depends in fact on the maximum internal reflection angle allowed. This angle is directly correlated with the ratio between the fiber reflective index and the external material reflective index. Impurities of the fiber surface, such as dust, scratches, fingerprints, that can occur during fiber manipulation,

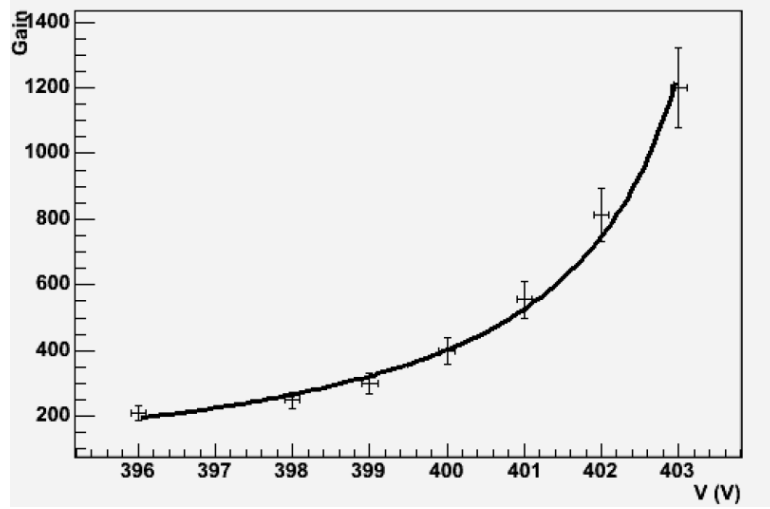


**Figure 4.9:** APD gain as a function of applied voltage, close to the breakdown point, with exponential fit superimposed.

can strongly influence the trapping efficiency. Adding a second layer of cladding material (in this case polymethylmethacrylate, PMMA) a protective interface is created, that prevents deterioration of the primary one, thus avoiding efficiency worsening.

### 4.3.1 Trapping efficiency

The trapping efficiency  $\eta$  is defined as the ratio between the number of photons that fiber is able to convoy outside itself and the total number of photons created by incident radiation. This number can be easily estimated for squared section fibers from the formula [71]:

$$\eta = \frac{\Omega}{4\pi} = \frac{4}{4\pi} \int_{\theta=\theta_l}^{\pi/2} \sin\theta d\theta \int_{\phi=\phi_l}^{\pi/2} d\phi, \quad (4.9)$$

where  $\Omega$  represents the good solid angle, given by the limit angles  $\theta_l$  and  $\phi_l$ , defined by:

$$\theta_l = \sin^{-1} \left( \frac{n_1}{n_2} \right), \quad (4.10)$$

where  $n_1$  and  $n_2$  are respectively the refraction indexes of the material outside the fiber and the fiber material itself. The integral of eq. 4.9 has been evaluated using the data reported in tab. 4.3 obtaining  $\eta = 0.073$ , in agreement with the manufacturer data sheet.

Nevertheless, we decided to measure the trapping efficiency. For this measurement, a test fiber was illuminated by means of a laser beam ( $\lambda = 408 \text{ nm}$ ). Before impinging on the fiber, the beam passes through a 50 : 50 splitter; one half of the

	Single cladding	Double cladding
Fiber dimensions	$5mm \times 5mm \times 1m$	$5mm \times 5mm \times 1m$
Core material	Polystyrene	Polystyrene
1st cladding material	Acrylic	Acrylic
2nd cladding material		Fluor-Acrylic
Core refractive index	1.60	1.60
1st cladding refractive index	1.49	1.49
2nd cladding refractive index		1.42
1st cladding thickness	4%	4%
2nd cladding thickness		2%
Emission peak	$492nm$	$492nm$
Attenuation lenght	$> 3.5m$	$> 3.5m$
Trapping efficiency	4%	7.3%
Scintillation decay time	2.7ns	2.7ns

**Table 4.3:** Main characteristics of multicladding BCF20 scintillating fibers, compared with single cladding scintillating fibers (data from Saint-Gobain).

light is read by a photometer, while the remaining part crosses a diffuser before entering in the fiber. In this way we are sure that the beam does not directly crosses the fiber, introducing a possible source of systematic errors due to preferential orientation of light inside the fiber. At one end of the fiber a second channel of the photometer is collocated. The fiber trapping efficiency is then evaluated as the ratio between the intensities measured by the photometer inputs. We found  $\eta_{meas} = 6.6 \pm 0.5\%$ , a value slightly lower than expected.

### 4.3.2 Attenuation lenght

The measurement of the attenuation length was performed using the experimental setup shown in fig. 4.10.

A  $^{90}Sr$  source positioned on one side of the fiber is used to excite the fiber itself. The end-point of the  $^{90}Sr$  @2.2 MeV allows for a good simulation of MEG positron energy loss in fiber, thus permitting to estimate available signals in real working conditions as well as attenuation length. On the other side of the fiber a PMT coupled to a little slice of scintillator is positioned, with the purpose to collect the electrons that fully cross the fiber and to generate a trigger signal. The APD used to read-out the fiber is opticalt connected at one end of the fiber and its signal amplitude is acquired by an ADC together with a multichannel analyzer.

Moving the source along the fiber it is possible to measure the APD response as a function of the source distance, and thus the fiber transport properties, by means of the analysis of the amplitude spectra acquired with the multichannel analyzer. The obtained results are shown in fig. 4.11. Data were fitted by means

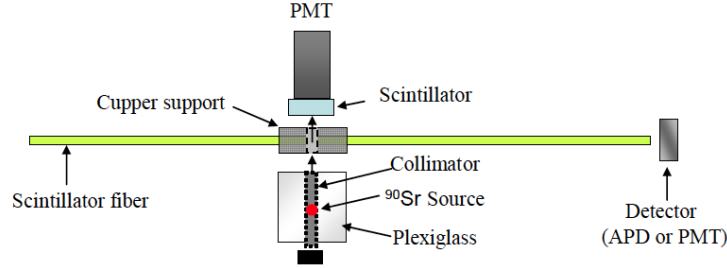


**Figure 4.10:** Sketch of the experimental setup used in the measurement of the scintillating fibers attenuation length.

of a double exponential function:

$$y = Ae^{x/x_{01}} + Be^{x/x_{02}}, \quad (4.11)$$

obtaining  $x_{01} = 22.3 \pm 0.5 \text{ cm}$  and  $x_{02} = 260 \pm 15 \text{ cm}$ .

The first exponential is typically caused by direct light, self absorption and re-emission due to both the wavelength shifter and the residual superimposition of emission and absorption band of dopant fluors. At high path length, where the wavelength is fully shifted to the emission band and these effects are negligible, the core attenuation length appears clearly [72].

### 4.3.3 Emission spectrum

In order to measure the fiber emission spectrum, a UV lamp ( $\lambda = 365 \text{ nm}$ ) was used to excite the scintillating fibers. The light output passes through a monochromator and then is read out by a photomultiplier tube. The acquired spectrum is shown in fig. 4.12.

We found a peak around  $498 \text{ nm}$ , in very good agreement with the manufacturer data sheet.

### 4.3.4 Geometrical effects on light loss

The particular structure of the transverse detector and the mechanical constraints forced us to give the fibers a curved shape in order to perfectly match the longitudinal detector radius; moreover, the different pitch of fibers and APD system forced us to have a double APD row, resulting in two different shapes for the fiber end on the APD side. A sketch of the two fiber profiles is shown in fig. 4.13. The common part has a curvature radius  $r_0 = 288.9 \text{ mm}$ ; the end part shape can be either a single curve with radius  $r_A = 173.7 \text{ mm}$  or a “S-like” double curve with radii  $r_{B1} = 17.5 \text{ mm}$  and  $r_{B2} = 22.5 \text{ mm}$ .

Especially in this latter case the end shape strongly influences the fiber trapping efficiency, because of inefficient reflection of the light in the final part of the fiber itself. For this reason, a coating in the curved part of fibers was necessary to obtain

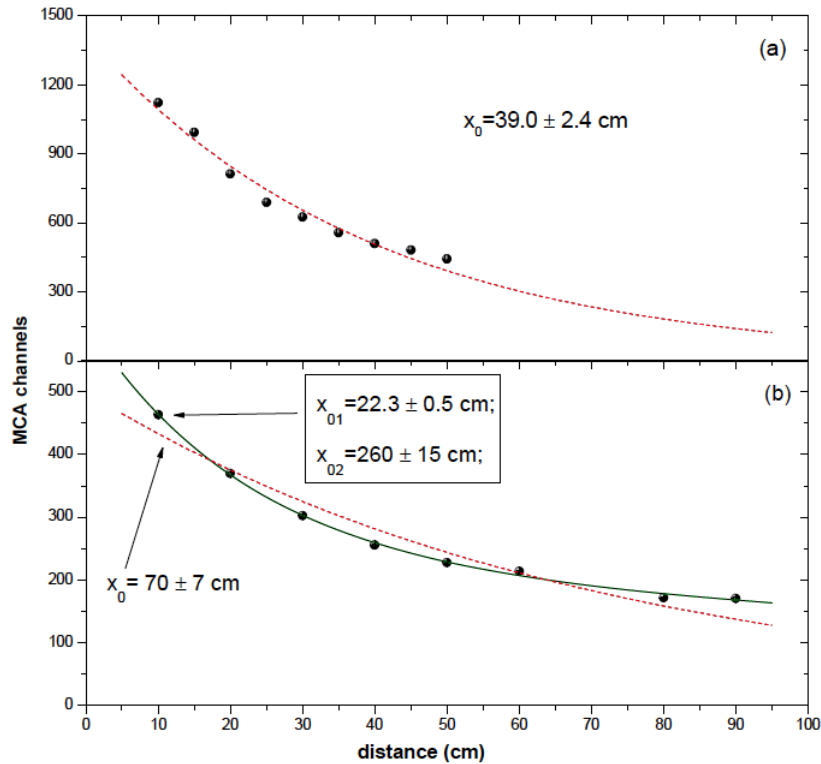


**Figure 4.11:** Fiber attenuation length measurement. a) Single exponential fit.  
b) Double exponential fit.

a satisfactory recovery of the scintillation light. We tested few possible solutions, namely:

- reflective paint produced by KODAK (Kodak White Reflective Coating);
- alluminated mylar;
- reflective foil produced by 3M (3M radiant mirror film).

All these materials guarantee a reflectivity  $> 99\%$ . The tests were performed using the experimental apparatus already described in sec. 4.3.2.

In fig. 4.14 the results obtained are shown, together with the comparison with the performances of a straight fiber kept as a reference fiber during all tests.

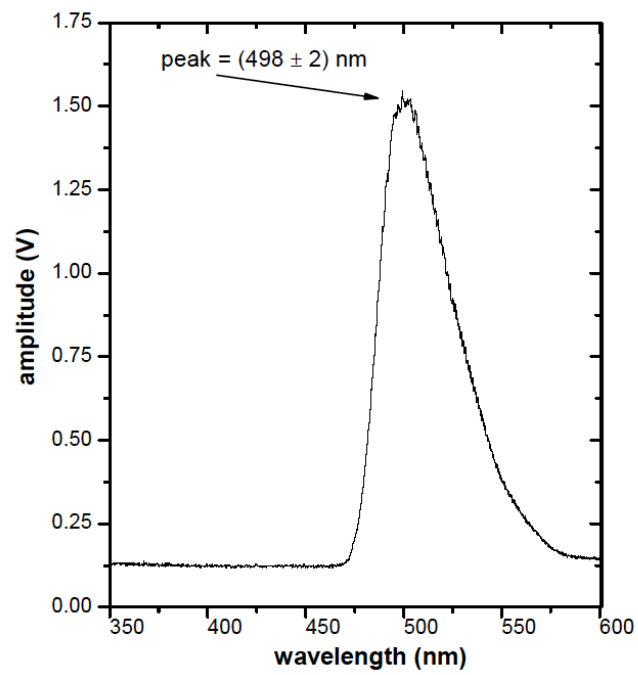


Figure 4.12: Measured fiber emission spectrum.

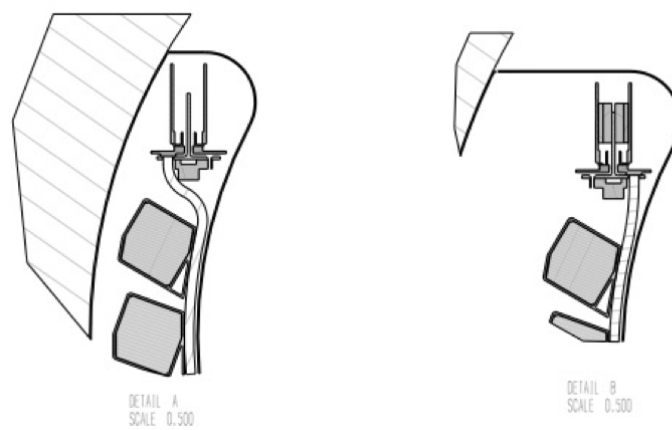
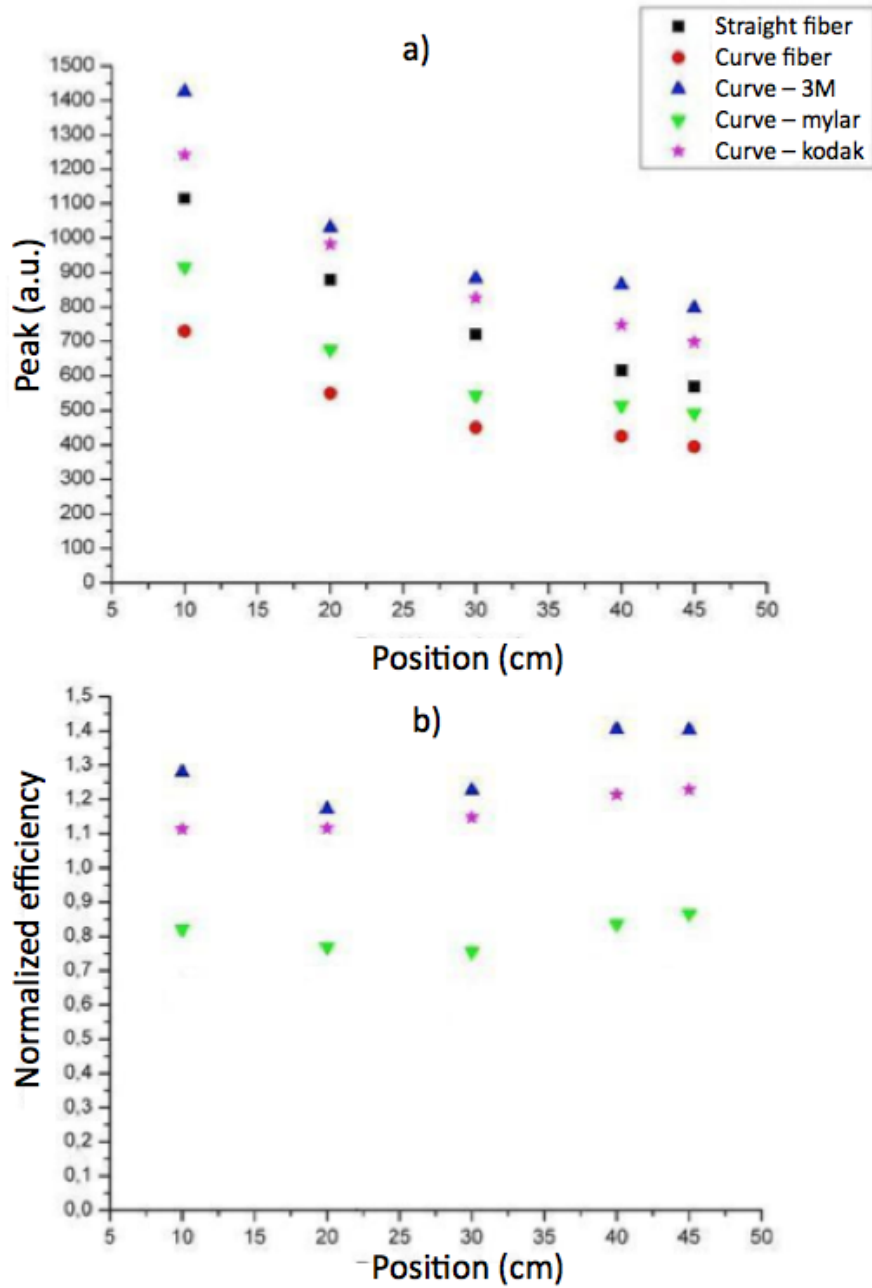


Figure 4.13: Section of transverse detector, highlighting the two different profiles of scintillating fibers end.



**Figure 4.14:** a) Comparison between the performances of the curved fiber with coats under test and te straight fiber. b) Comparison between the coated fiber transport efficiency, normalized to the efficiency of the straight fiber.

The best results were achieved using the 3M reflective foil. So we decide to cover each terminal part of the fibers with a slice of reflective foil, as shown in fig. 4.15.



**Figure 4.15:** Details of the scintillating fiber with covered surface.

Two final tests were performed in order to compare the performances of the scintillating fiber in the final experimental configuration. The first one was to evaluate the fiber response as a function of the distance between the source and the detector, being the bias voltage of the APD fixed. We tested 4 different bias voltages. The results are shown in fig. 4.17, where an increase in the APD output signal of the order of  $50 \div 100\%$  depending on the APD voltage supply can be observed.

The last test was done fixing the detector position and varying the APD bias voltage, as shown in fig. 4.16. Also in this case we found an increase of about a factor 2 in the detector performances. Both these test confirmed us that the fiber wrapping with high reflectance material is in practice the best way to recover light in our curved square fibers.

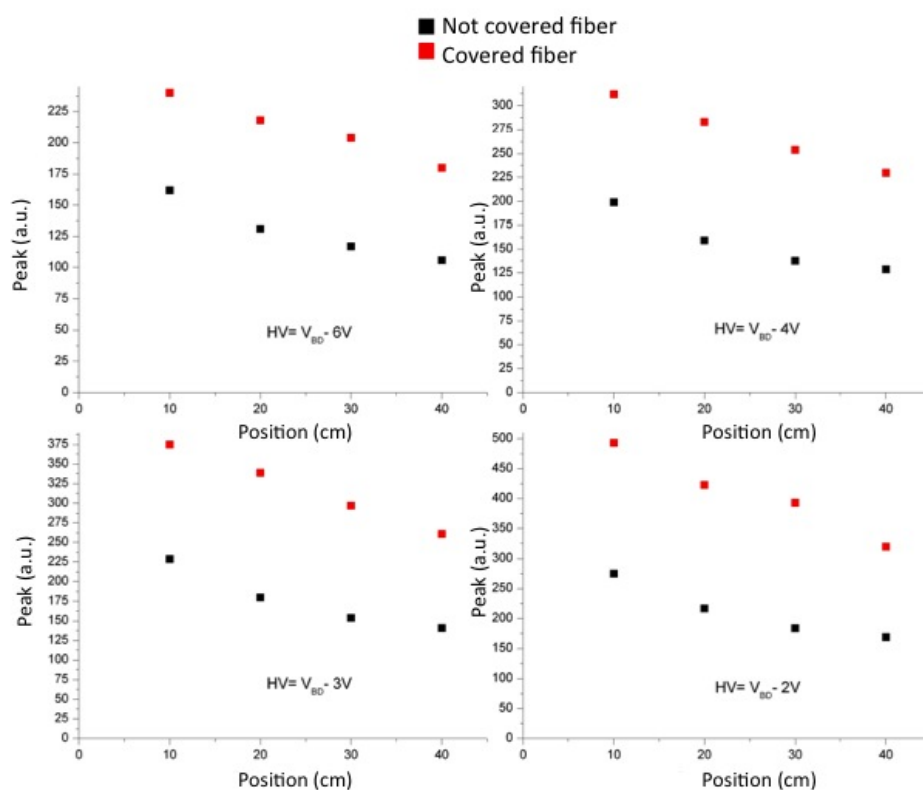


**Figure 4.16:** Comparison between the performances of the covered fibers respect to the naked ones, being the detector bias voltage fixed and varying the distance between source and detector.

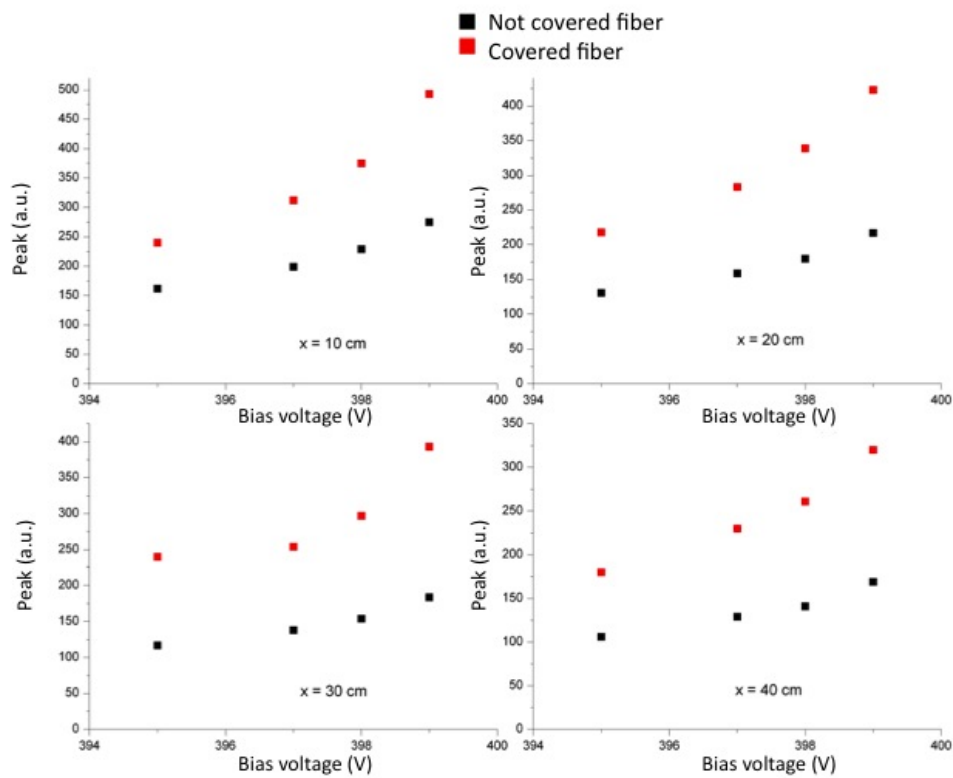


**Figure 4.17:** Comparison between the performances of the covered fibers respect to the naked ones, being the detector-source distance fixed and varying the APD bias voltage.

## 4.4 Electronic readout

The APD Front-End electronics is mounted directly on the same support on which are mounted the photodiodes, as shown in fig. 4.18. In this way it is possible to process and amplify the analog signals very close to the devices, in order to reduce as much as possible the stray capacitance that should get worse the devices performances.

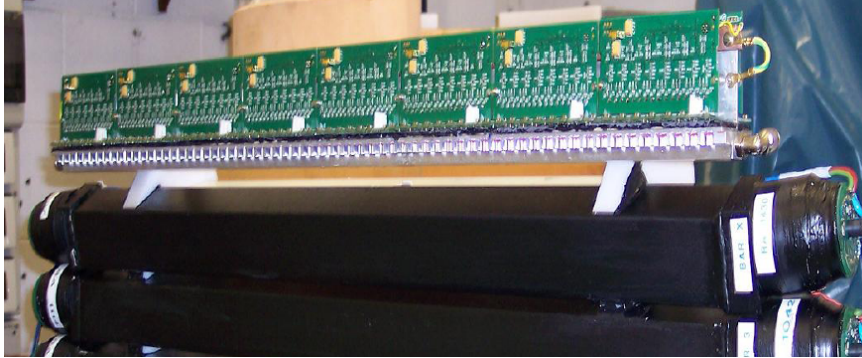


**Figure 4.18:** Wiring diagram of the single channel APD analog signal amplifier.

The electronics is designed in such a way to realize the two tasks of the transverse Timing Counter: provide a trigger signal to the data acquisition system, based on the sum of 16 adjacent fibers, and furnish an event reconstruction based on the discriminated single fiber signal in offline analysis.

For this reasons, groups of 8 APDs are accommodate on the same board (Front End boards, FE) that provides common bias; signals from APDs on same board are summed up and sent to the trigger system. At trigger level another sum stage is performed: in this way, from the trigger point of view, each Timing Counter sector is divided in 16 sections, each covering  $\Delta z \sim 9.6 \text{ cm}$ . The analog signals are sampled by a digitizer at  $66 \text{ MHz}$ .

Moreover, the single analog signal passes through a discriminator stage. For each digitizer sample, the fiber hitmap is saved and recorded. This data will be used in the offline analysis in order to identify the hit fiber, and reconstruct the positron impact point with a resolution of the order of  $1 \text{ cm}$ , in an independent way with respect to the bar reconstruction.

### 4.4.1 Signal processing and signal to noise ratio

In order to identify the request on the signal amplifier, first of all we have to quantify the order of magnitude of the APD signal. The number of photoelectrons generated at the APD output by a positron crossing the fiber can be estimated as:

$$n_{pe} = E \cdot d \cdot Y \cdot \eta_F \cdot \eta_{APD} \cdot e^{-x/x_0} \cdot G \cdot K, \quad (4.12)$$

where  $E$  is the positron energy deposit in the fiber for length unit ( $2 \text{ MeV/cm}$  for  $\sim 52.8 \text{ MeV}$  positrons),  $d$  is the length of the trajectory inside the fiber ( $\sim 5 \text{ mm}$ ),  $Y$  is the fiber light yield ( $8 \cdot 10^3 \gamma/\text{MeV}$ ),  $\eta_F$  and  $\eta_{APD}$  are respectively the fiber and the APD efficiencies (7% and 80%, see sec. 4.3.1 and sec. 4.2), the exponential term takes into account the fiber attenuation, being  $x$  the distance between the impact point and the APD and  $x_0$  the typical fiber attenuation length (see sec. 4.3.2), and  $G$  is the APD gain (see sec. 4.3.2). Finally,  $K$  represents the light recovered using the fiber wrapping; its value is  $\simeq 2$ , as shown in sec. 4.3.4.

Considering, for example, an impact point  $x = 30 \text{ cm}$  and an APD gain of 500, and substituting all numbers in eq. 4.12, we obtain  $n_{pe} \simeq 10^5$  electrons at the APD output, corresponding to  $\sim 16 \text{ fC}$  in charge. Considering a device capacitance of  $80 \text{ pF}$ , the order of magnitude of the maximum signal at the APD output will be  $2 \times 10^{-4} \text{ V}$ . This means that we need an amplifier stage with gain  $10^3$  or more to obtain signals suitable to be used for our purposes.

For this reason a dedicated amplifier system has been designed; in order to obtain the desired gains, we decide to split the amplification system in two stages, with gain 50 and 100 respectively. The wiring diagram of the APD amplifier is shown in fig. 4.19.

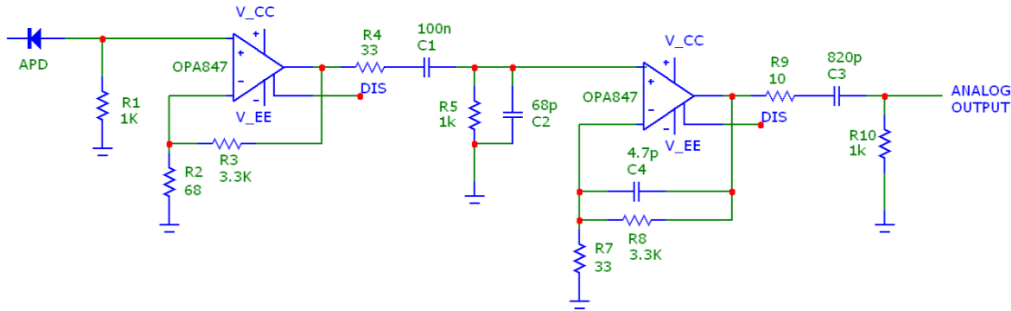


**Figure 4.19:** Schematics of a single APD amplifier.

Dedicated simulations based on a commercial simulation software (TINA [73]) was used to study the electronic chain response, in conjunction with bench test on prototypes to optimize the PCB design; in fig. 4.20 the Bode gain plot of the system is shown. As one can see, the full circuit behaves as a passband filter, with cut frequencies  $f_1 = 1.3 \text{ MHz}$  and  $f_2 = 11.3 \text{ MHz}$ , thus shrinking the bandwidth to  $10 \text{ MHz}$ . This results in a sensible noise reduction.

The expected noise can be calculated using a simplified model of the system, shown in fig. 4.21. In this model we have considered only the noise induced by the first stage, that is amplified by a factor  $5 \times 10^3$ ; the noise of the second stage will be negligible, being amplified only by a factor 100. There are 4 contributions to the total noise:

**Amplifier voltage noise:** can be evaluated as:

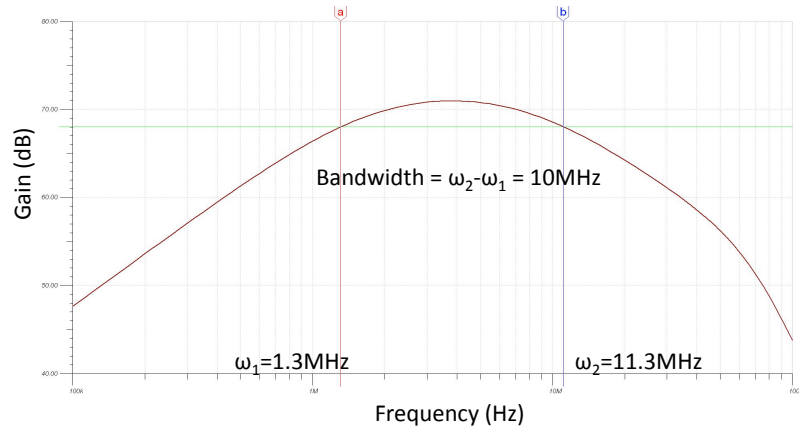


**Figure 4.20:** Bode gain plot of a single channel APD analog signal amplifier.

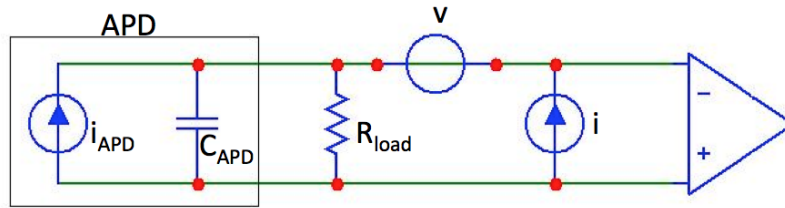


**Figure 4.21:** Equivalent circuit for amplifier noise study.

$$V_v^{out} = v \cdot \sqrt{B} \cdot G \simeq 15 \text{ mV r.m.s.} \quad (4.13)$$

where  $v$  is the equivalent input voltage noise of the amplifier ( $0.85 \text{ nV}/\sqrt{\text{Hz}}$ ).

**Amplifier current noise:** can be evaluated as:

$$V_i^{out} = i \cdot \sqrt{B} \cdot Z_1 \cdot G \simeq 20 \text{ mV r.m.s.} \quad (4.14)$$

where  $i$  is the equivalent input current noise and  $Z_1$  the input impedance. The last is given by the parallel of APD capacitance ( $80 \text{ pF}$ ) and the load resistor  $R_{load}$ ; this results in a limited bandwidth of  $2 \text{ MHz}$  for the input current noise.

**APD shot noise:** coming from the APD dark current. Its contribution can be evaluated as:

$$V_{APD}^{out} = \sqrt{2ei_{APD}} \cdot R_1 \cdot \sqrt{B} \cdot G \cdot M \simeq 30 \text{ mV r.m.s.} \quad (4.15)$$

where  $e$  is the electric charge,  $i_{APD}$  the APD dark current ( $i_{APD} = 100 \text{ nA}$ );  $M$  is the so called “excess noise factor”; it was measured during the first APDs bench tests, and its value was found to be  $\sim 10$ .

**Resistor thermal noise:** this is correlated to the thermal agitation inside the resistance, and can be evaluated as:

$$V_R^{out} = \sqrt{4 \cdot k_B \cdot T \cdot R \cdot B} \cdot G \simeq 40 \text{ mV r.m.s.} \quad (4.16)$$

where  $k_B$  is the Boltzmann constant,  $T$  the temperature of the resistor ( $300 \text{ K}$ ). Here we consider only the contribution of  $R_1$ , ( $R_{load}$  in fig. 4.21) the only one that will be amplified.

From the calculation shown above, one can evaluate the total noise as the quadratic sum of each contribution:

$$V_{noise} = \sqrt{(V_v^{out})^2 + (V_i^{out})^2 + (V_{APD}^{out})^2 + (V_R^{out})^2} \simeq 55 \text{ mV r.m.s.} \quad (4.17)$$

Considering an APD signal of about  $2 \times 10^{-4} \text{ V}$  at the amplifier input as previously calculated, resulting in  $\sim 1 \text{ V}$  at the amplifier output, we obtain for the signal to noise ratio:

$$\frac{S}{N} = \frac{1 \text{ V}}{65 \text{ mV}} \simeq 20, \quad (4.18)$$

a satisfactory result that guarantee good APD operations. This result was confirmed by the measurement performed on a prototype board, as shown in fig. 4.22.

After being amplified, the analog signals are summed up and sent to the trigger system. A set of amplitude spectra acquired by the trigger system is shown in fig. 4.23. In these plot one can see clearly the separation between the signal peak and the noise, resulting in an efficient trigger threshold definition. In the lower panel (corresponding to APD biased just  $1 \text{ V}$  below the BD condition) one can clearly see that the noise level is increased dramatically by the amplification of dark current.

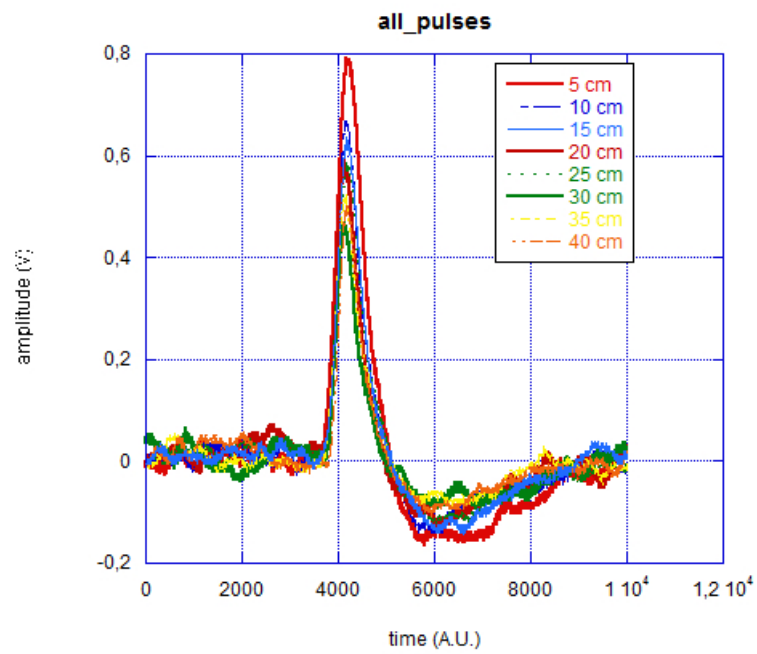


**Figure 4.22:** APD signal as a function of the positron impact point along the fiber.

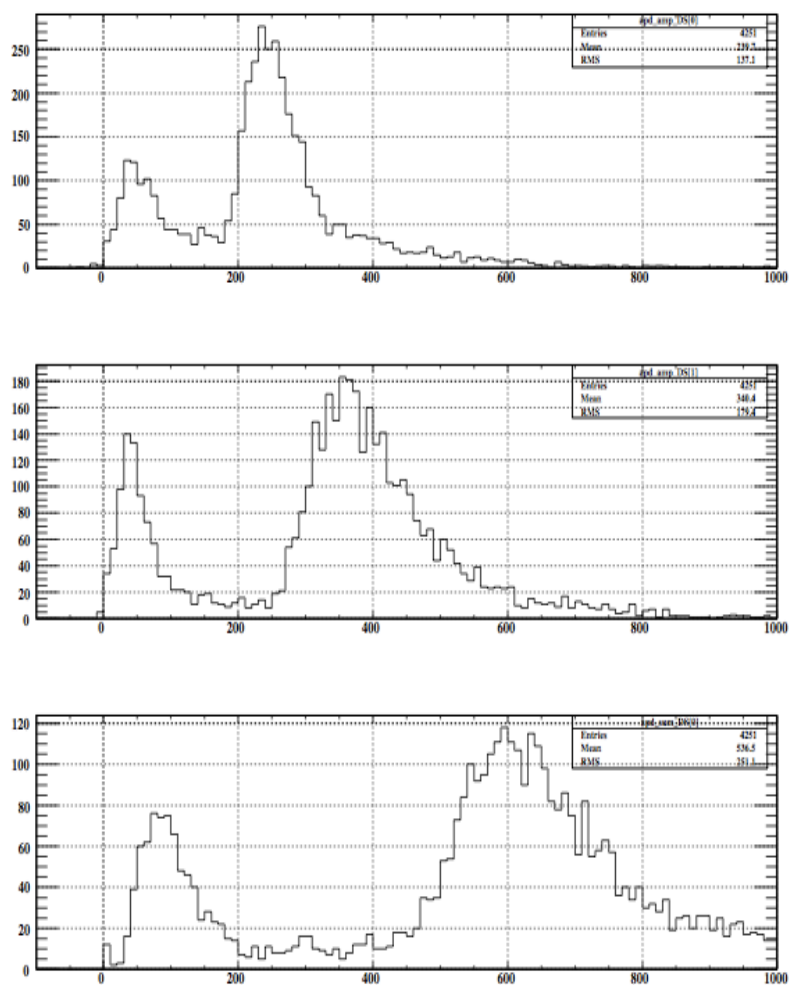


**Figure 4.23:** Analog signal from 2 FE summed up together (equivalent to 16 APDs), as acquired by the trigger system as a function of the FE applied HV: (*up*) nominal HV value (3 V under BD point); (*centre*) nominal HV value increased by 1 V; (*down*) nominal HV value increased by 2 V.

### 4.4.2 Positron impact point resolution

Each individual fiber signal passes also through a discrimination stage; the output of each discriminator is then sampled and stored in the data file, in order to be processed in the offline analysis. In such a way, for each event one can define which fibers have fired the discriminator, thus obtaining the hitmap of the fiber detector. This is a very useful tool to obtain a positron impact point determination in a completely independent way with respect to the longitudinal detector.

The detector resolution can be defined as the width of the distribution of the differences between the fiber and the bar reconstructed  $z$ ,  $\Delta Z = Z_{fiber} - Z_{bar}$ . An example of these distributions obtained during the 2010 physics run is shown in fig. 4.24.

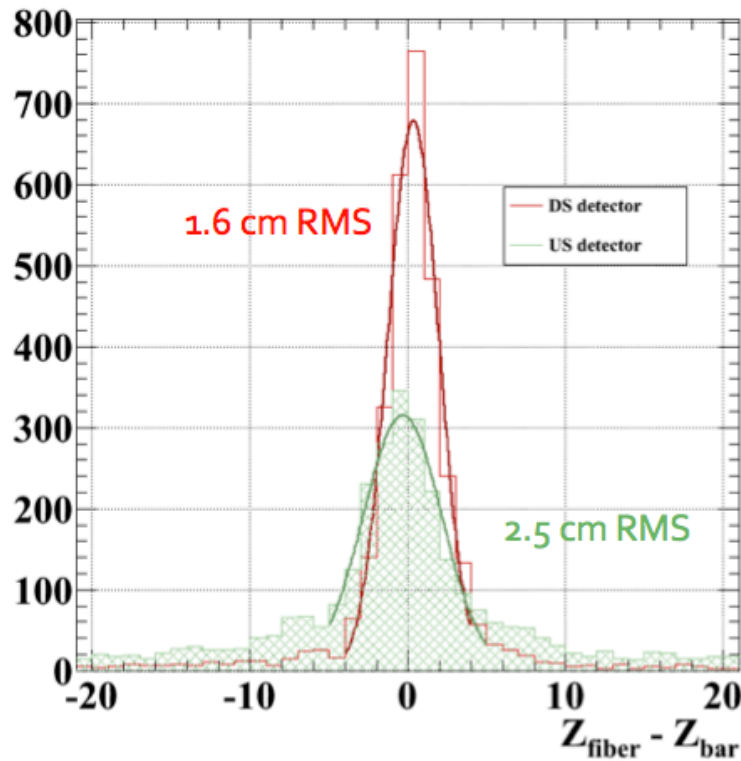


**Figure 4.24:** Plot of the  $\Delta Z = Z_{fiber} - Z_{bar}$  distributions for upstream (green) and downstream (red) Timing Counter sectors.

The obtained resolutions are  $1.6\text{ cm}$  and  $2.5\text{ cm}$  for the downstream and upstream sectors respectively. The differences between the two detectors are related to differences in the electronic noise level. Some “hot” channels (oscillating APDs that generate many hits not correlated to physical events on fibers) were found, mainly in the upstream side. This problem will be investigated during the 2011 beam shut down.

### 4.4.3 Efficiency

The final point in the evaluation of the transverse Timing Counter performances is the determination of the efficiency of the detector. For this purpose, an useful tool is provided by cosmic rays that pass through 2 bars positioned at the external side of the Timing Counter, as depicted in fig. 4.25. This selection on bars hit guarantees also that at least one fiber should fire a hit, being crossed by the cosmic ray. A dedicated trigger was developed in order to exclude the central bars of each TC sector (in the MEG trigger numbering convention this is called TRG24).

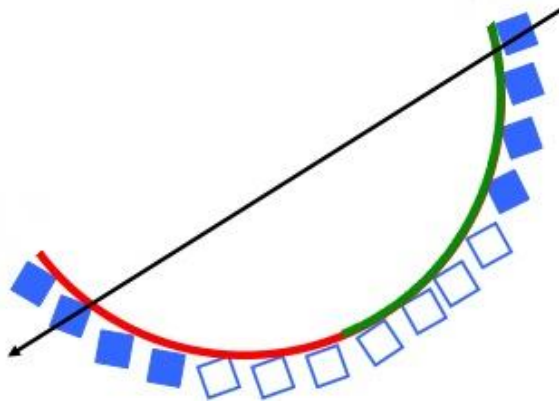


**Figure 4.25:** Sketch of the TRG type used for determination of APD system efficiency (TRG24, see text for details).

The efficiency is evaluated calculating the ratio between the number of event triggered by the the bar and the number of event with a fiber hit recorded. The results are presented in tab. 4.4.

Fiber cluster	DS TRG	US TRG	DS hit	US hit	DS eff.	US eff.
0	33	107				
1	204	340	130	309	0.64	0.91
2	444	559	173	473	0.39	0.85
3	538	521	504	520	0.94	1.00
4	491	373	475	373	0.97	1.00
> 4	720	401	711	401	0.99	1.00
total	2430	2301	1993	2076	0.82	0.90

**Table 4.4:** Transverse detector efficiency.

The resulting efficiencies are 82% and 90% respectively for the down-stream and up-stream module. The difference between the two sector can be explained by the fact that during 2010 data acquisition a section of the down-stream module, corresponding to 32 fibers ( $\simeq 12\%$  of the sensitive area) was blind because of a hardware failure.



---

## Chapter 5

# A study on TC calibration tools

As already described in chapter 3, the TC operation needs the accurate knowledge of a number of typical parameters for the physical calibration of the time scale, the time difference respect the other detectors, the space scale for positron reconstruction. Further all these parameters need to be monitored over the full data acquisition. Thus, a full set of calibrations was developed to obtain the best Timing Counter performances [52].

First of all, the PMT gain equalization is needed to optimize the working point, for equalization of charge/energy ratio among all scintillating bars. This allows a reliable  $z$  reconstruction for triggering purpose. Once the pulse shape is fixed, it is necessary to evaluate the contributions of time walk effect, which is the first order correction to the timing resolution caused by the relative amplitude spread of pulse height. Afterwards, it must be evaluated the offsets associated to the different electronic chains that gives rise to a spatial bars alignment. Having completed the calibrations strictly related to the Timing Counter, the time offset between each bar of the detector and the Liquid Xenon calorimeter is measured.

The calibration procedure will be described step by step more in details in this chapter.

### 5.1 Gain equalization

PMTs gain equalization is a first step required for an uniform response, necessary to obtain almost similar pulse shape for PMTs belonging to the same bars, both for timing measurement and for triggering algorithm optimization. This gives an easier and more reliable estimation of positron impact point via charge ratio, which is used by the trigger processor for the positron impact point reconstruction. For the same reason, equalized energy spectra are needed also between different bars.

A useful tool are the cosmic rays crossing the detector: they have the advantage of the flat spatial distribution over all the detector, together with rather well defined energy spectrum. One can thus evaluate both factors: gain unbalance between PMTs on the same bar and inter-bar gain adjustment.

A dedicated set of runs were taken at the beginning of each data acquisition, in

order to have a satisfactory statistic for each PMTs pair. At this stage, the trigger is based only on Timing Counter information and requires to have a coincident signal on both PMTs on single bar. More precisely, we collect data that generate signals with at least  $40mV$  amplitude on each PMTs and at least  $100mV$  as sum, whit single bar multiplicity. In the MEG framework this kind of trigger is labeled as TRG22, and the same convention is adopted hereinafter. The choice of the trigger thresholds levels is related to the necessity of reject low energy events that pass only through few millimeters of the bars [45].

An adequate set of such data can be used to evaluate gain unbalance between PMTs on same bars and different bars and, iterating the procedure  $2 \div 3$  times, one can achieve a gains uniformity of  $\sim 10\%$ .

### 5.1.1 PMTs gain equalization

The equalization is achieved using signals from cosmic rays events hitting the bars: because of the spatial flatness of cosmic rays spectrum, the charge and amplitude spectra of the inner and outer PMTs should not be affected too much by geometrical effects (i.e. spread of the trajectories).

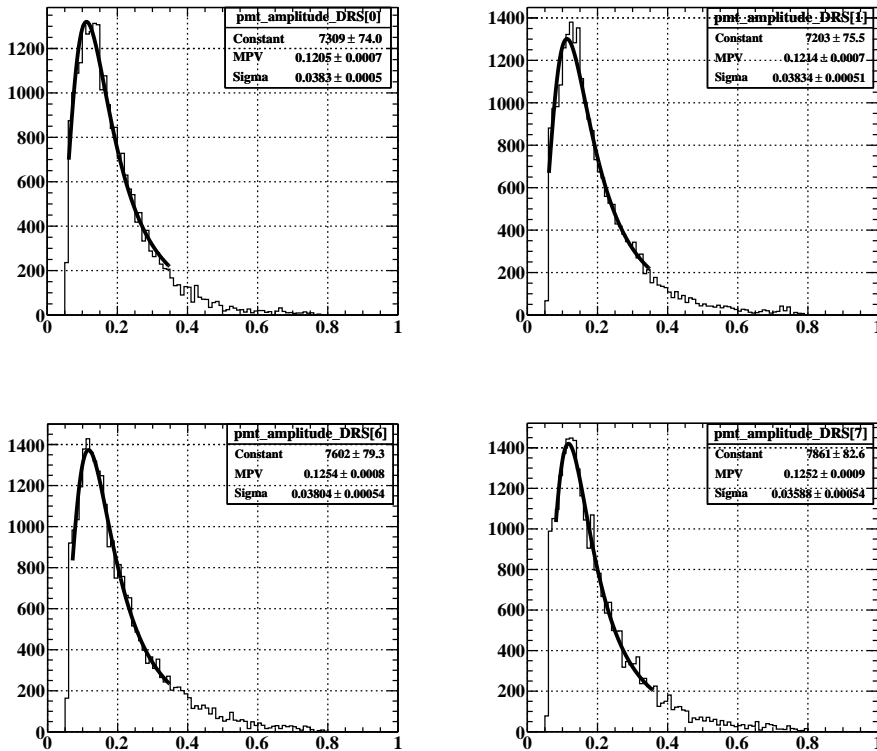


**Figure 5.1:** Pulse spectra for different PMTs with Landau fit superimposed. The amplitude equalization is achieved within 10%.

For each PMT the pulse amplitude and charge spectra are acquired, with the

condition that the pulse has fired the Double Threshold Discriminator. The threshold was set for these runs to 500  $mV$ . The cut over the high thresholds together with the trigger conditions allow to reject events that pass through only a little slice of scintillator. It is straightforward to fit the pulse spectra in order to obtain the value of the convolute Landau distribution.

Since the PMT gain-voltage relation is given by:

$$G = K \cdot V^\alpha, \quad (5.1)$$

where  $K$  and  $\alpha$  are parameters determined in the R&D period, it is easy to tune the photomultipliers voltage supply in order to equalize their response, “moving” the peak of the Landau distribution; in fact, the ratio between the peaks is directly proportional to the ratio between the PMTs gains.

In fig. 5.1 amplitude spectra for different pmts after equalization are shown. The uniformity of gain is achieved within  $\sim 10\%$  of precision.

### 5.1.2 Bar energy response equalization

As already shown in sec. 3.2, the product of the charges delivered by two PMTs of each bar is direct proportional to the energy released inside the bars. Being the cosmic rays spatial spectrum uniformly distributed on the Timing Counter, triggering on each bar we can obtain quite similar convolute Landau distributions peak in the case of well equalized PMTs. An example of a spectrum acquired with a TC bar is shown in fig. 5.2.

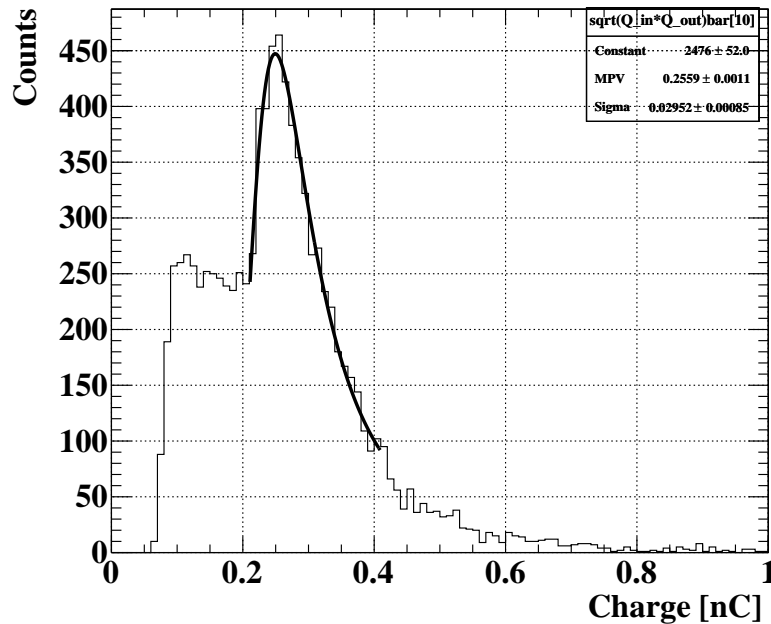


**Figure 5.2:** Example of charge Landau distribution with fit superimposed.

Each spectrum is then fitted and the peak position is extracted, in the same way as described in sec. 5.1.1. In this way, taking both information from single PMT and Landau spectra it is possible to obtain a quite good equalization of all TC PMTs.

The summary of the peaks positions for each bar as obtained after a couple of optimization steps is shown in fig. 5.3.

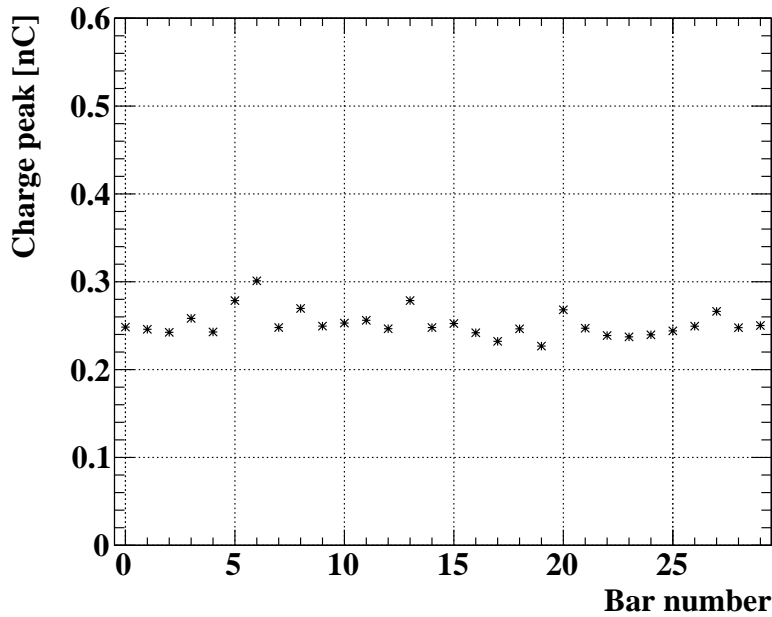


Figure 5.3: Summary of the fitted Landau peak.

The final equalization achieved for bar spectra is about 15%. Further fine tunings are performed in the trigger system, introducing an algorithm with a proper choice of constants. In this way the equalization in the data taking conditions is about  $1 \div 2\%$ .

## 5.2 Time Walk correction

The so called Time Walk (TW) effect is given by the time distribution of the crossing instant of a fixed threshold by pulses of different amplitudes. A graphical example is shown in Fig. 5.4. Because of its dependence from pulse amplitude, this effect directly influences the timing resolution, but can be estimated and corrected in an event by event basis.

For each PMTs a reference waveform template is prepared: several PMT waveforms are recorded, normalized to a same amplitude and averaged over the whole reference waveform set, in order to obtain a template with interpolated points. First of all, the waveform is “inverted”, obtaining a plot of the signal time delay as

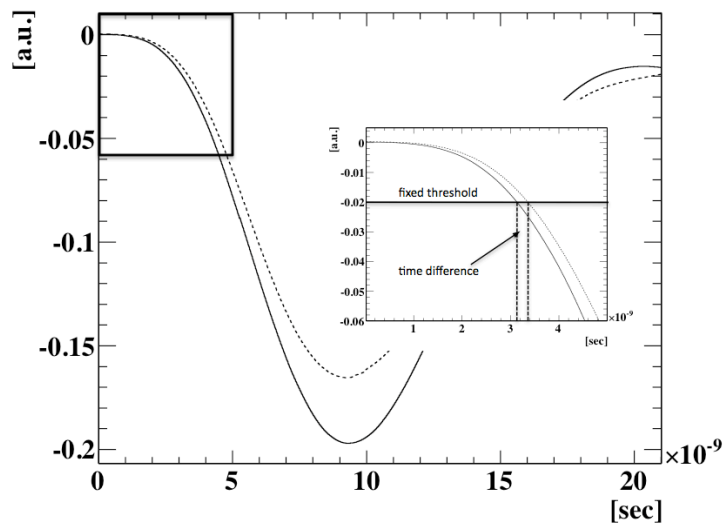


Figure 5.4: Time walk effect

a function of the normalized amplitude. An example of an inverted pulse is shown in fig. 5.5.

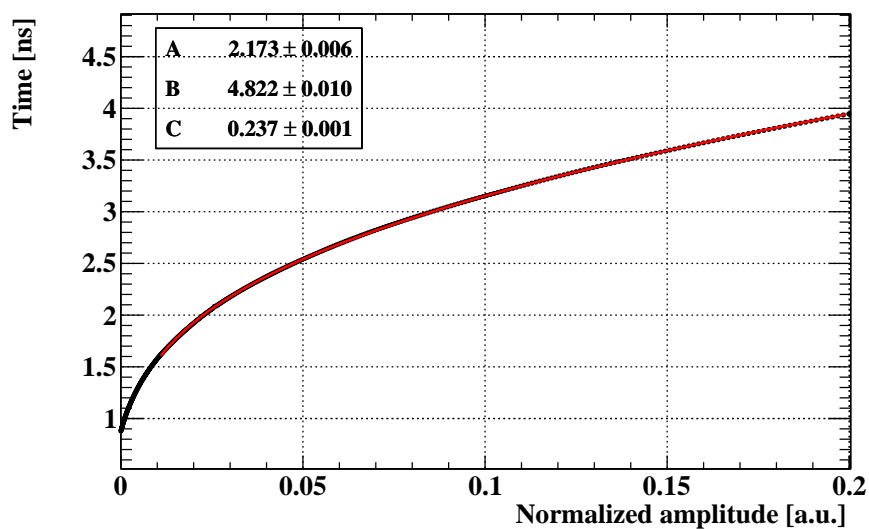


Figure 5.5: Time vs amplitude with time walk correction with fit superimposed.

The inverted pulse is then fitted with the function (fig. 5.5):

$$TW = A + B\sqrt{x} + C \log x, \quad (5.2)$$

where  $A$ ,  $B$  and  $C$  are free parameters and  $x$  represents the ratio between the low level threshold value (LLT, which is fixed) and the pulse amplitude.  $x$  is the parameter that can be used to estimate the TW delay of discriminator triggering, simply starting from the LLT value and pulse amplitude.

The time walk correction gives out a net improvement of time resolution by a factor 2. A qualitative example is shown in 5.6.

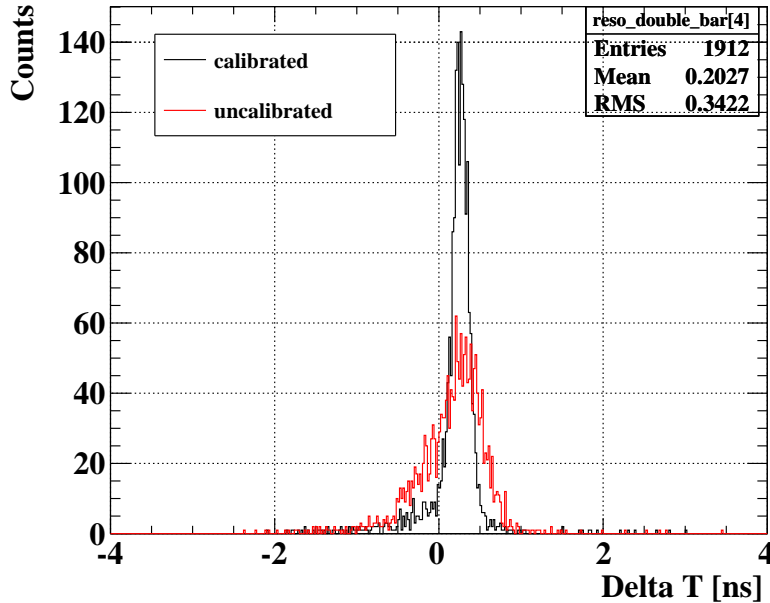


**Figure 5.6:** Comparison between the time difference distributions for two adjacent bars; the red line represents uncalibrated data, the black line represents the calibrated ones.

A summary of the bar performances is given in fig. 5.7, quoted on a double bar sample (see sec. 6.1), both for a calibrated and uncalibrated data. In many cases the improvement of the timing resolution is significant: the mean value of the resolution for uncalibrated data is  $\sim 200ps$ , while the mean value of the calibrated sample resolution is  $\sim 75ps$ .

### 5.2.1 Low level threshold optimization

Being directly involved in the timing performances, both directly and through the Time Walk correction algorithm, the low level threshold value must be accurately chosen in order to maximize the time resolution. For this reason, dedicated set of data taking runs were taken just at the beginning of the physics data acquisition phase, using the same beam configuration and triggering on the Timing Counter alone (TRG22).

We have scanned the range  $10 \div 30 mV$  with  $5 mV$  step; for each data sample, the resolution was quoted with the double and triple samples evaluation method

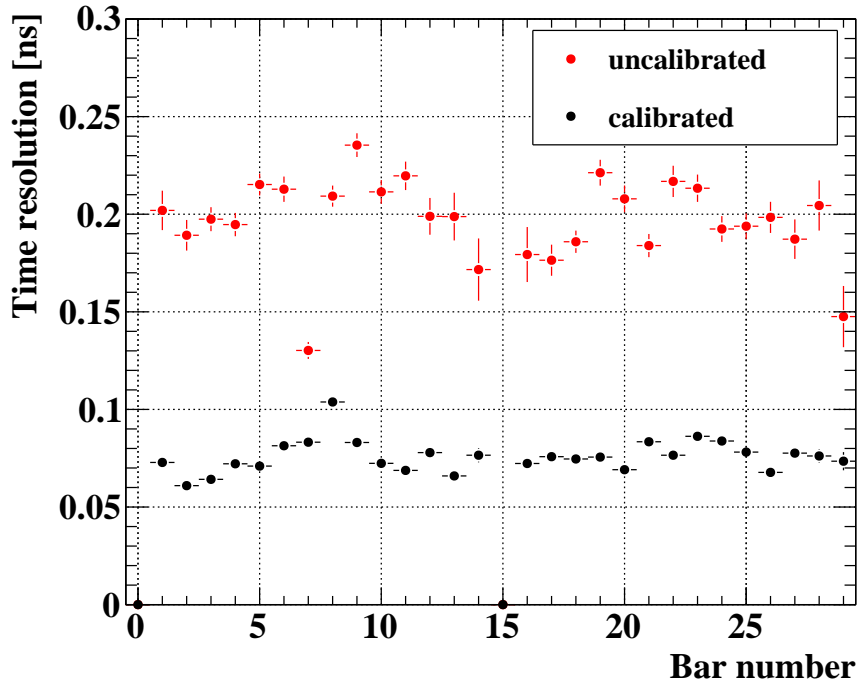


**Figure 5.7:** Comparison between the resolution obtained on double sample using calibrated (black markers) and uncalibrated (red markers)

described in sec. 6.1 and finally a comparison was made. In fig. 5.8 the comparison between the results obtained with LLT values of 10 and 25  $mV$  is reported. The latter value of threshold maximize tge resolution and it was set as default for the whole MEG data acquisition time. The result that the relatively high threshold of 25  $mV$  gives out better result respect to a lower one could be at a glance surprising, considering that lower the threshold is, lower the time walk correction. This effect is easily explained having a deeper look at the time walk correction. This will be done in the next section.

### 5.2.2 Further improvements in time walk correction

Although the resolutions obtained with the current time walk correction are quite satisfactory (the results will be given more in detail in chapter 6), being around  $\sim 75 ps$ , some improvements are under study in order to get better results. With regard to the hardware limit set by the devices intrinsic characteristics (see sec. 3.3), we can think about a further improvement of about 10  $ps$ .

We can estimate the margin of improvement in a simple way, by evaluating the difference between the time extracted from the template waveform and the time reconstructed using the time walk correction formula. This quantity is plotted as example for one PMT in fig. 5.9. It is quite evident that the current calibration works very well for  $x > 0.01$ . Considering a LLT value of 25  $mV$ , this means

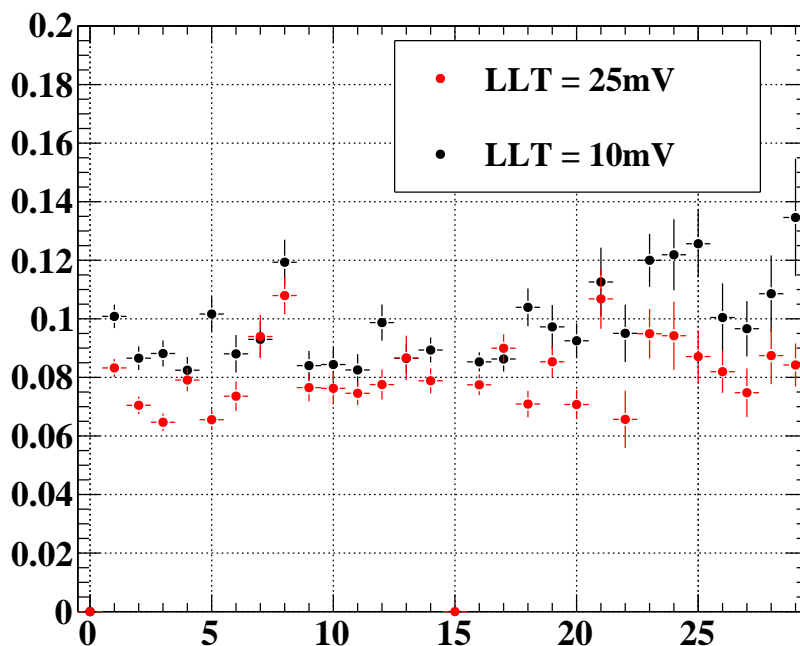


**Figure 5.8:** Comparison between the resolutions obtained on double sample using TW calibrated data, with two different values of the low level threshold: 10 *mV* (red markers) and 25 *mV* (black markers). The best results were achieved using 25 *mV* as LLT.

that the time walk correction is reliable for pulse amplitude lower than 2.5 *V* (this value can be slightly different for each PMT).

The possible ways to improve the TW could be:

- divide the events in two categories, with a cut represented by the limit ratio defined above. In such a way, for events with bad fit-template accord (low  $x$  ratio) an additional correction could be added, just fitting the time walk residuals distribution;
- change the function used in the fit, adding more parameters in order to allow more degrees of freedom in fit procedure;
- considering the possibility to create a position dependent template for different impact points, in order to take into account possible effects due to geometry, light propagation, different track spread as a function of the impact point.

All these three possibilities are currently under study. The results will be presented as soon they will be ready, and hopefully used by the beginning 2011 run time.

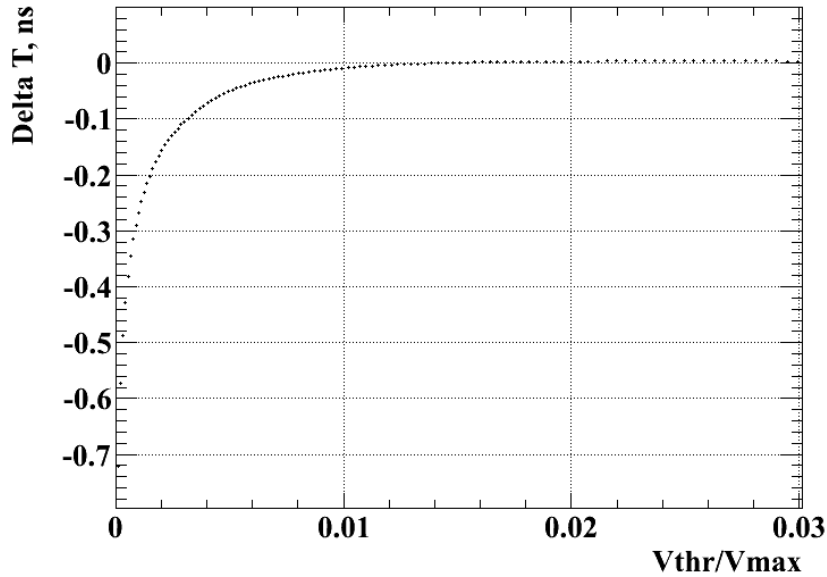


**Figure 5.9:** Plot of the difference between the inverted template waveform and the time calculated by means of eq. 5.2.

## 5.3 Offsets equalization

After having optimized the pulse shape characteristics one needs to study the offsets that different electronic chains can generate between different PMTs. This effect is a pure systematic constant error, being a constant offset for each PMT. On the other hand, this influences the mean of the time different distributions, and consequently the  $z$  alignment on the bar, resulting in a wrong  $z$  reconstruction of the impact point via the time difference method (sec. 3.2).

The offsets are evaluated using two different methods based on analysis of independent data samples. The first one is based on evaluation of cosmic rays hitmap distribution on each bar; the second one is based on the comparison between the  $z$  reconstruction provided by the Timing Counter and the reconstruction independently provided by the extrapolation of the positron tracks reconstructed by Drift Chambers to the Timing Counter. The two calibrations methods will be described in details in the next sections.

### 5.3.1 Interbar offset with cosmic

The first way used to evaluate the offset is based on cosmic rays. For each bar, the time difference between inner and outer PMT spectra is acquired. The flatness of the spectrum should be well reproduced by the hitmap distribution for well equalized PMTs. Note that the use of Michel events should be avoided for offsets estimation, due to the sharp asymmetry of Michel spectra on bars.

An example of an acquired spectrum is shown in fig. 5.10.

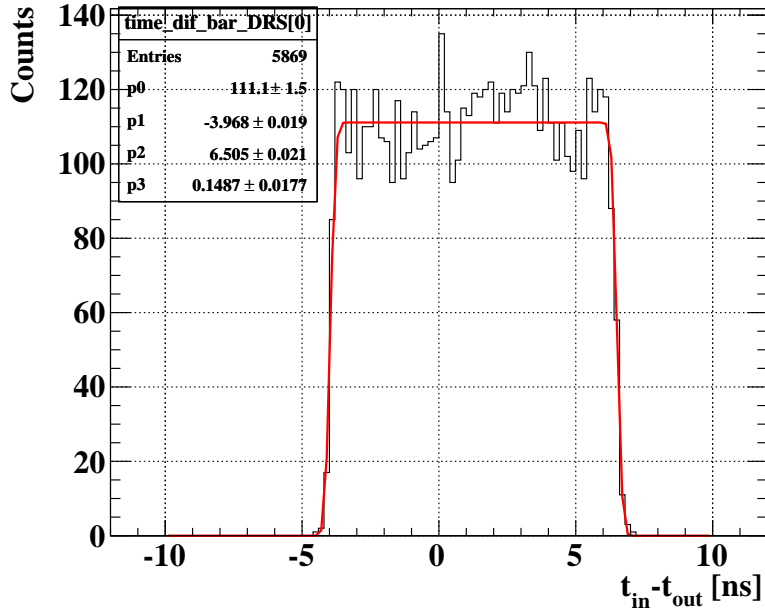


**Figure 5.10:**  $\Delta t$  distribution for cosmic rays events with fit superimposed.

Being the  $z$  reconstruction obtained starting from the time difference (as shown in eq. 3.5) it is easy to identify the  $z$  offset in each bar by fitting the  $z$  distribution with a step like function (fig. 5.10) whose outputs are the half maximum values of left and right edges: the  $z$  offset is estimated by averaging these values, while the comparison of their difference with the hardware fixed bar length gives a hint about the effective velocity.

The offsets calculated in this way are then applied on the  $z$  reconstruction. Fig. 5.11 shows the hitmap distributions in the  $z - \phi$  plane for cosmic rays before (upper panel) and after (lower panel) applying the calibration. It can be clearly seen how the rectangular shape of the bar array is well reproduced in the two dimensional hitmap after the calibration.

In order to have a clear understanding of the final experimental conditions, the same calibrations constant were applied to a Michel sample. The results are shown in fig. 5.12. Also in this case the bars result to be very well justified, confirming the reliability of the used calibration.

The summary of the calculated offset is shown in fig. 5.13. The achieved alignment is better than 1  $mm$ .

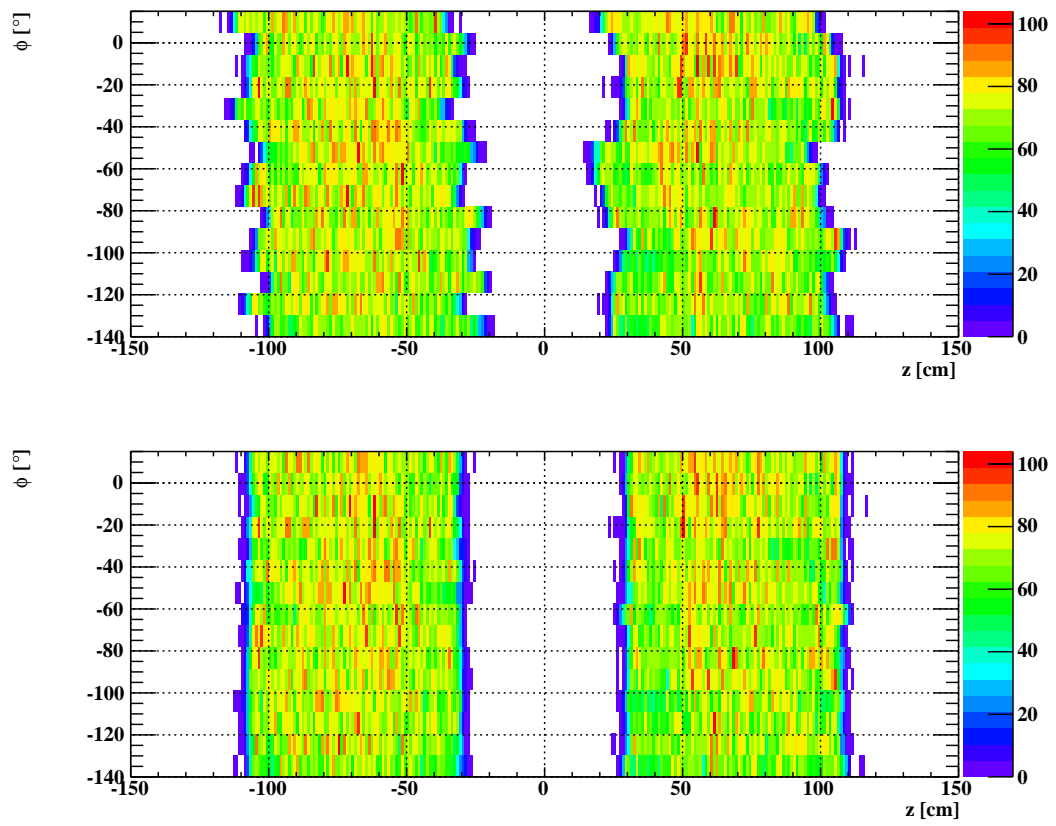


**Figure 5.11:** Comparison between uncalibrated (upper panel) and calibrated (lower panel) cosmic rays hitmaps.

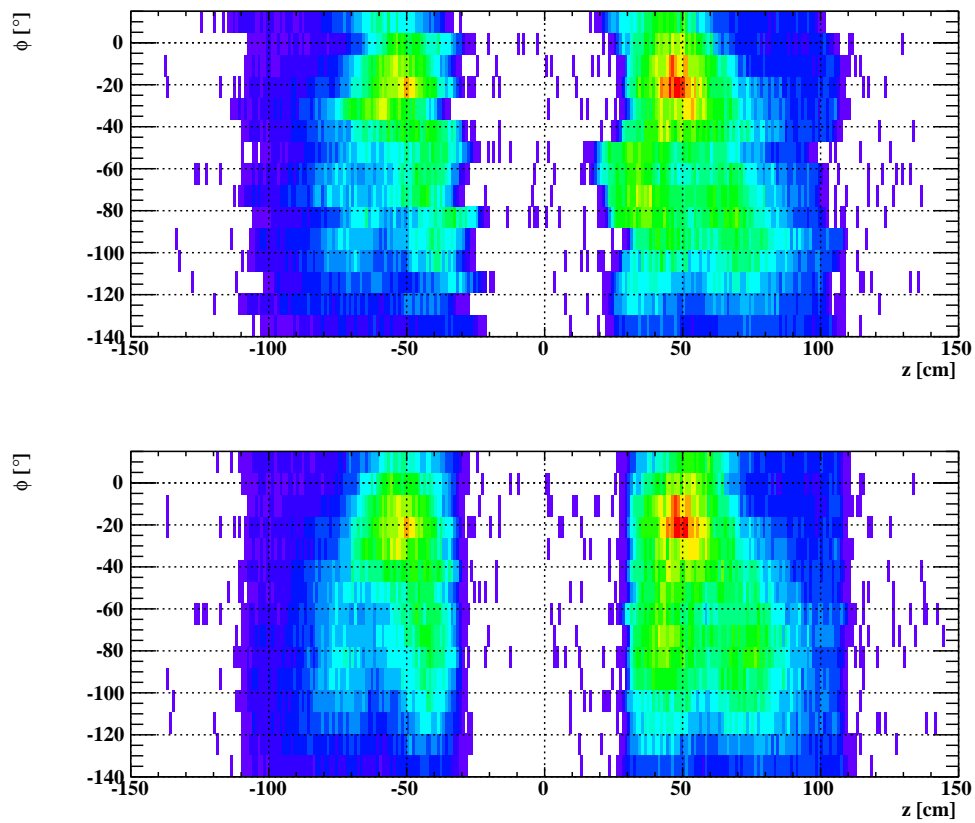


**Figure 5.12:** Comparison between uncalibrated (upper panel) and calibrated (lower panel) Michel events hitmaps. The offsets used here are the same calculated for fig. 5.11

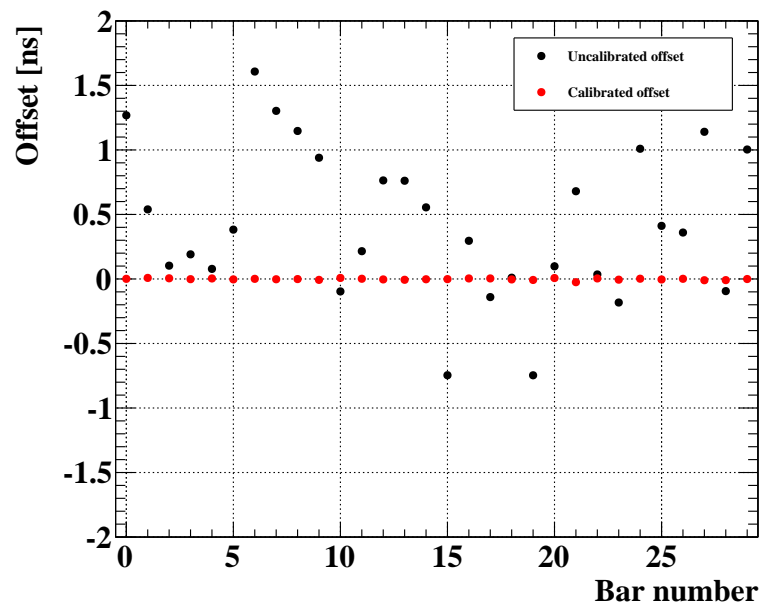


**Figure 5.13:** Comparison between calibrated (red markers) and uncalibrated (black markers) bar offsets, calculated on cosmic rays sample.

### 5.3.2 Interbar offset with drift chambers

The bar offsets can be evaluated also in a different way, using information about positron impact point provided by the Drift Chambers in Michel runs. For this kind of data, in fact, we can compare the impact point measured independently by both detectors, evaluating the offset between Drift Chambers system and each bar. An example of the distribution of  $\Delta z = z_{dc} - z_{tc}$  is shown in fig. 5.14. All distributions are then fitted with a gaussian function. The means of each distribution represent the offset between DC and the considered bar.

This is proved to be a very powerful tool to calibrate the detector. In fact, while cosmic rays offer the best way to evaluate Timing Counter offset between the bars without giving information about the absolute displacement of the detector with respect to the rest of the experimental apparatus, the using of Michel sample permits to get the detector position in the COBRA reference system.

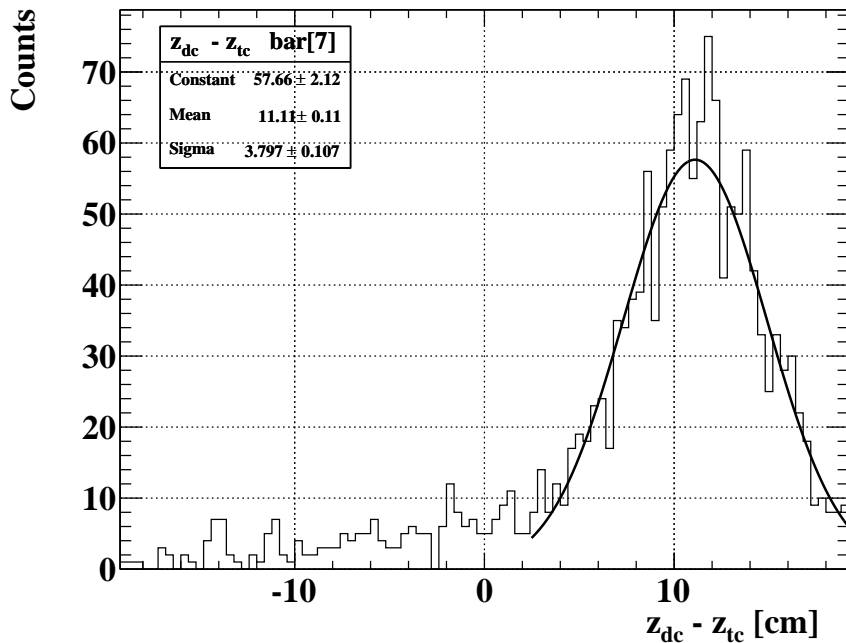


**Figure 5.14:** Example of  $z_{dc} - z_{tc}$  distribution evaluated on Michel data, with gaussian fit superimposed. The mean of the distribution correspond to the offset of the bar.

Of course, assuming a reliable  $z$  reconstruction by the DC system, the offset values calculated with Michel events and cosmic rays events must be compatible. The comparison between the offsets calculated using different methods is shown in fig. 5.15, where it is possible to see a good agreement between the two sets of calibration constants.

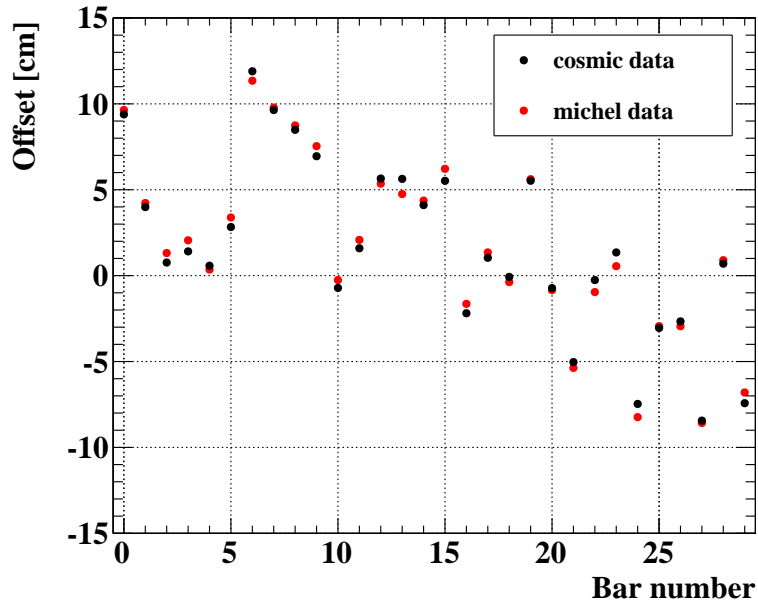


**Figure 5.15:** Comparison between offset calculated using cosmic rays data (black markers) and Michel data (red markers).

## 5.4 High level threshold optimization

The last parameter for proper TC operations is the determination of the best value for the high level threshold. As already explained in 3.4.3 the high level threshold directly influences the Timing Counter efficiency, and it must be chosen accordingly to cut already performed by the trigger system, based on a cut placed in the valley between the noise peak and the Landau peak.

We define here the Timing Counter reconstruction efficiency as the ratio between the number of hits fired by the DTD divided by the total number of events triggered.

In fig. 5.16 the behaviour of the TC efficiency as a function of the high level threshold in the range  $250 \div 600$   $mV$ , with  $50$   $mV$  step, is reported. The efficiency is about 100% for threshold value of  $400$   $mV$ ; no significant improvements are visible for lower values. Moreover, lowering too much the threshold implies other problems, such as rate effects on NIM signal, events pile-up and low energy spurious hits entering in the data set.

We decide to keep  $400$   $mV$  as the default value for physics data acquisition.

## 5.5 TC-LXE calibration

Once the timing counter bar system has been calibrated, it is necessary to “synchronize” the TC with the Liquid Xenon calorimeter. For this purpose, we need a data sample that correlates the two detectors. Two main physics processes provide

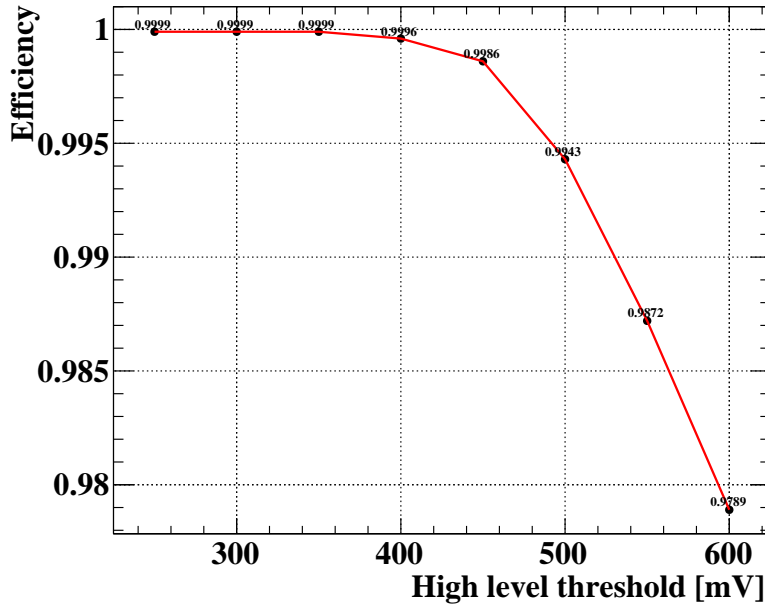


Figure 5.16: High level threshold efficiency.

a viable method: two photons emission by a Boron target and Dalitz decay of  $\pi^0$ . Both of them are not obtainable with the normal  $\mu$  beam and need dedicated setup developed for calibrations purposes. More details will be given in the follow.

### 5.5.1 Boron sample

A dedicated Cockcroft-Walton (CW) accelerator technique has been implemented [41] to obtain special reactions useful in calibrating the experimental apparatus: (in particular, energy resolution and scintillation of Liquid Xenon). The MEG CW provides up to 1 MeV protons that impinges on a  $Li_2B_4O_7$  target, inducing the  ${}^{11}_5B(p, \gamma){}^{12}_6C$  reaction, which is resonant at 163 KeV.

The Boron reaction provides two  $\gamma$  rays with energy 4.4MeV and 11.7MeV, that are emitted and can be simultaneously detected by Timing Counter and Xenon calorimeter. A sketch of the experimental layout is shown in fig. 5.17

A dedicated trigger has been developed to select such events. The  $\gamma$  energy distribution as measured by the calorimeter is plotted in fig. 5.18, where the two peaks are clearly recognizable.

For each bar, the distribution of the time difference between the TC and the Xenon is acquired. An example is shown in fig. 5.19. Each distribution is then fitted by means of a gaussian function. In a way similar to that already discussed in sec 5.3.2 the mean of the gaussian function gives a direct measurement of the time offset between the two detectors, and can be used to evaluate the calibration constants one has to apply to obtain well timing alignment between detectors.

The summary of the extracted offsets is plotted in fig. 5.20. In order to have

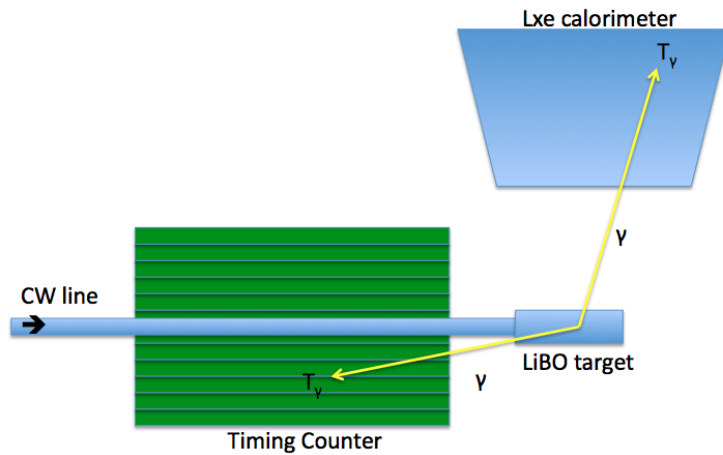


Figure 5.17: Sketch of the experimental layout in the Boron events.

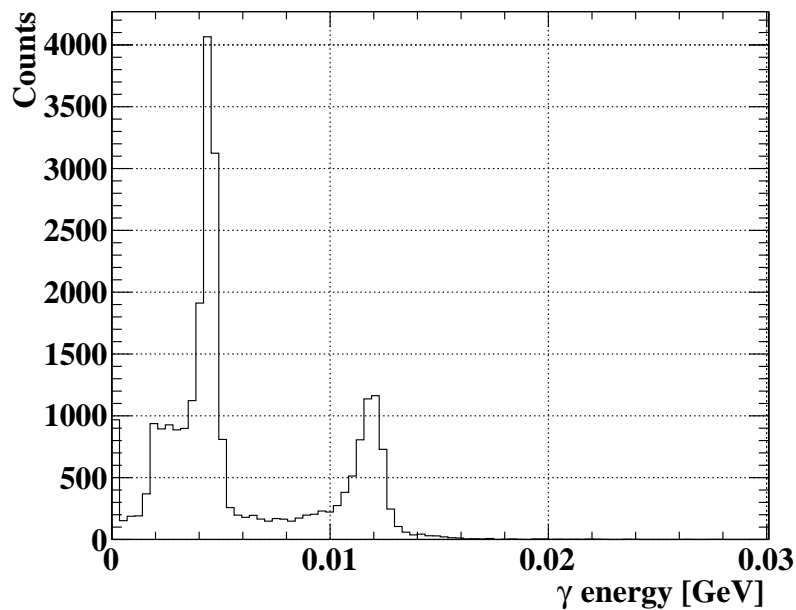


Figure 5.18:  $\gamma$  energy spectrum for Boron events. The peaks at 4.4 MeV and 11.7 MeV are clearly recognizable.

a reliable estimation of the timing, one has to choose a reference bar to join the Xenon detector, and then all the other TC bars are aligned to the reference one. For the 2010 data taking bar number 20 was arbitrarily chosen as the reference for all other bar offsets. The rescaled offsets are shown in fig. 5.21.

The calculated offsets are then inserted in the MEG Database and used during the offline analysis to correct the TC-LXe relative timing. In fig. 5.22 the offsets before and after the calibration are shown. It is possible to see the effect of

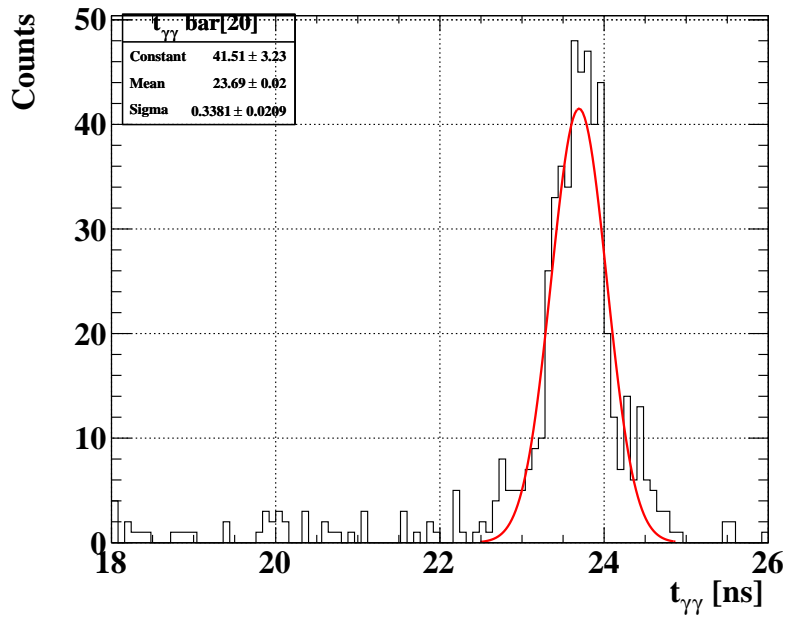


Figure 5.19: Example of  $t_{\gamma\gamma}$  distribution.

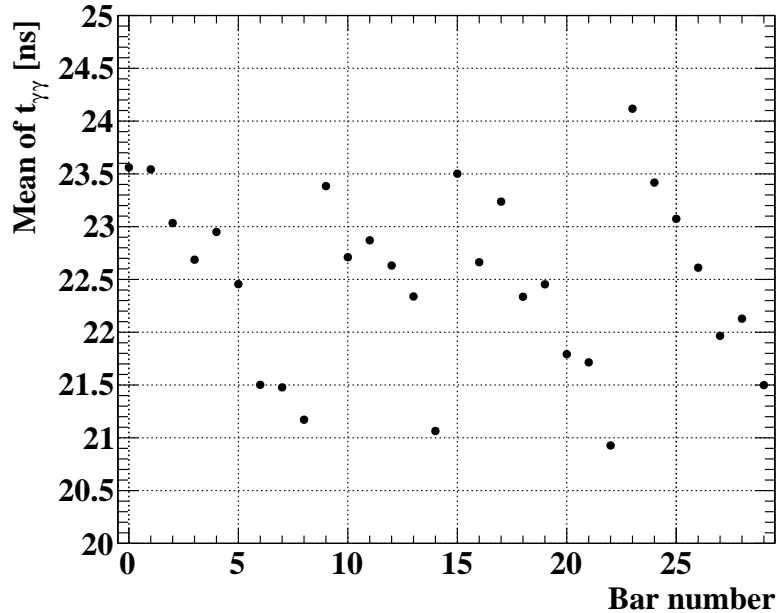


Figure 5.20: Mean of  $t_{\gamma\gamma}$  distributions as a function of bar number.

the offset evaluation, corresponding to a clear time alignment of the bar around  $23.5 \text{ ns}$ . The achieved precision in the alignment is about  $100 \text{ ps}$ , limited by some systematic effects in the fit procedure.

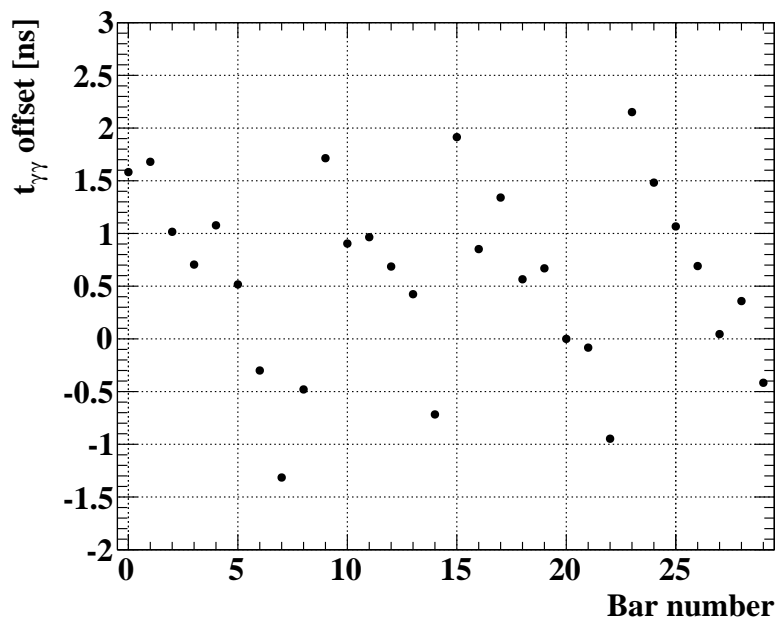


Figure 5.21:  $t_{\gamma\gamma}$  offsets as a function of bar number, referred to the bar number 20.

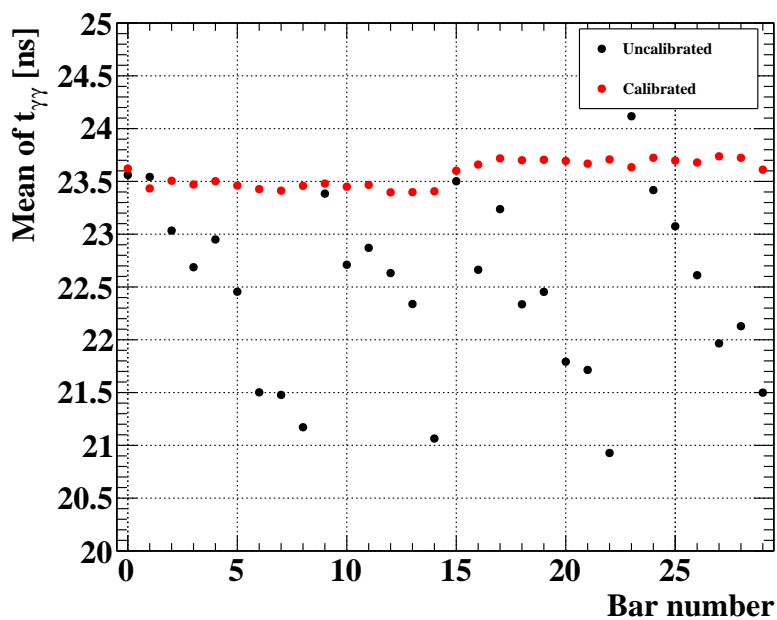
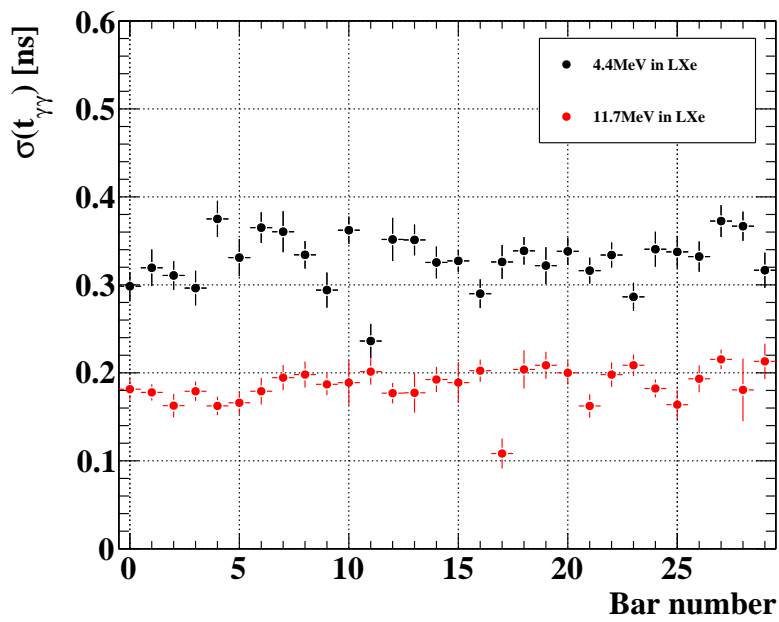


Figure 5.22: Comparison between the mean of  $t_{\gamma\gamma}$  distributions for calibrated (red markers) and uncalibrated (black markers) data samples.

As an exercise, and to evaluate the Timing Counter performances on a data set

different from the standard one (Michel data), one can evaluate the timing resolution on the Boron sample, just taking the width of the time difference distribution as a resolution estimator. The obtained resolutions are shown in fig. 5.23, and were quoted dividing the data in two samples, as a function of the gamma energy reconstructed in the Liquid Xenon calorimeter. As one can expect, the resolution is strongly correlated to the energy of the gamma impinging in the calorimeter, being the time resolution of the latter (roughly) inversely proportional to the squared root of the energy itself. The obtained mean values were  $\sim 180 \div 200$  ps for the higher energy gammas in the Xenon, and  $\sim 300 \div 350$  ps in the opposite case.



**Figure 5.23:** Timing resolution measured on Boron sample. The data were divided in two samples, cutting on the gamma energy reconstructed by the calorimeter. The resolution shows a strong correlation with gamma energy, as one can expect from LXe characteristics.

### 5.5.2 Dalitz sample

The offsets between TC and Xenon can be evaluated also on a different data sample, namely from the Dalitz decay,  $\pi^0 \rightarrow e^+e^-\gamma$  generated during a calibration run: we switch from a muon beam with MEG target to a pion beam with dedicated target. The main purpose of this calibration run is to obtain a reference energy release in Liquid Xenon calorimeter to characterize its energy resolution in the signal region (for an extensive discussion see, for example, [41]).

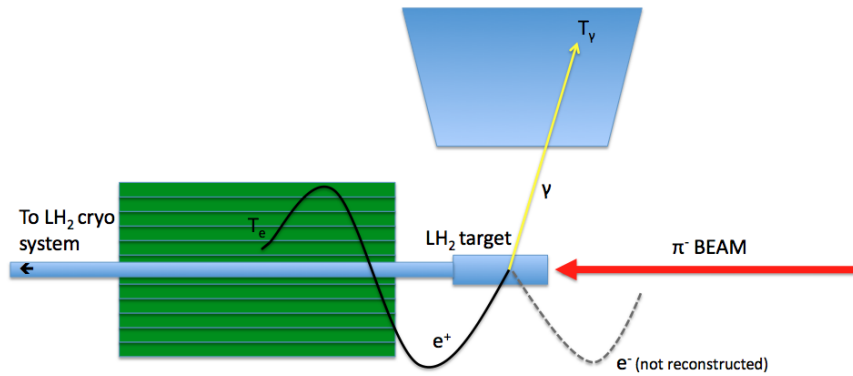


**Figure 5.24:** Sketch of the Dalitz decay sample.

The Dalitz sample is a very useful one, since the Dalitz and the  $\mu \rightarrow e\gamma$  decays have very similar topology. In fact, as shown in fig. 5.24, for electron not reconstructed in the spectrometer, the  $\gamma$  detected in the Xenon and the positron detected in the Timing Counter could mimic a  $\mu \rightarrow e\gamma$  decay. The Dalitz decay hitmap as seen by the timing counter is shown in fig. 5.25.

The Dalitz decay was used as a control sample to determine the absolute offset between Timing Counter and LXe calorimeter. The procedure used is the same as described in sec. 5.5.1: for each bar, the time difference spectrum between the detectors are acquired and fitted by means of a gaussian function. The extrapolated mean of the distribution represents the offset between liquid xenon and the timing counter. Fig. 5.26 shows the results obtained for each bars. They are in good agreement to what already calculated in the Boron sample, confirming the reliability of the used calibration constant.

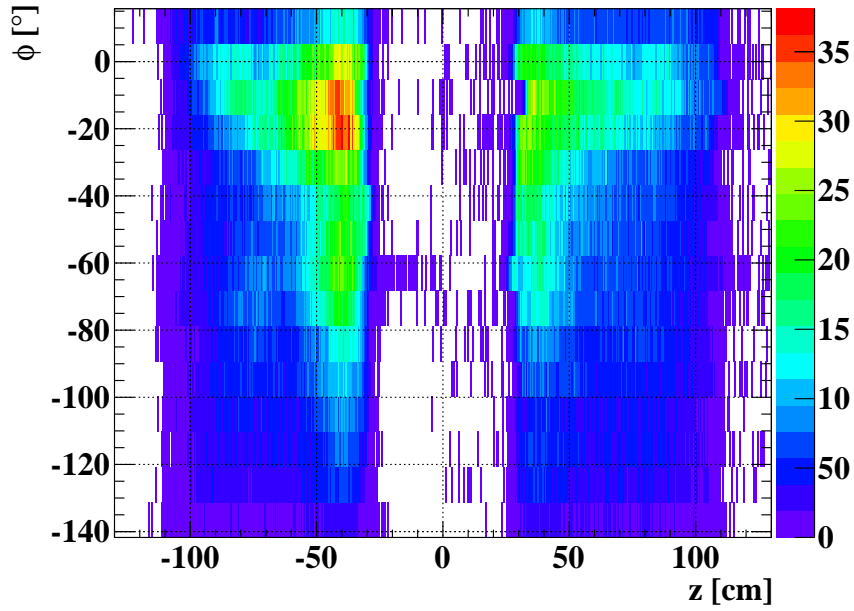


Figure 5.25: Dalitz decay events hitmap.

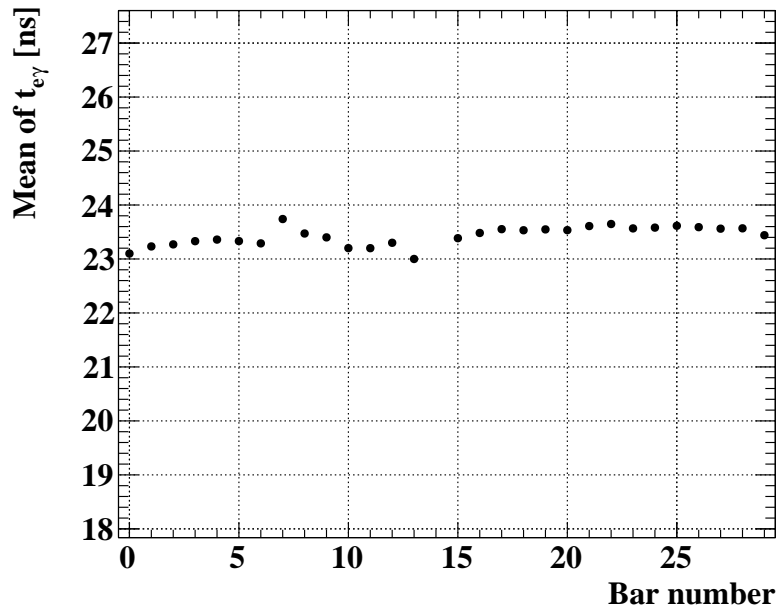


Figure 5.26: Offset calculated on Dalitz sample.

## Chapter 6

# The Timing Counter performances

In this chapter I will review the timing resolution and impact point reconstruction of the Timing Counter in the last two years of data acquisition time (years 2009 ÷ 2010). Then I will report about the TC and LXe combined analysis of the timing of radiative decay events. This is the way for measuring the whole apparatus timing resolution between positron and gamma.

### 6.1 Study of intrinsic Timing Counter resolution

In order to study the Timing Counter timing resolution in the experimental conditions, an analysis tool has been developed, based on the Michel events that involved a set of adjacent bars. In particular, we used the so called “double” and “triple” data sample, meaning a cluster made by 2 or 3 consecutive bars hit in coincidence by the same positron (fig. 6.1).

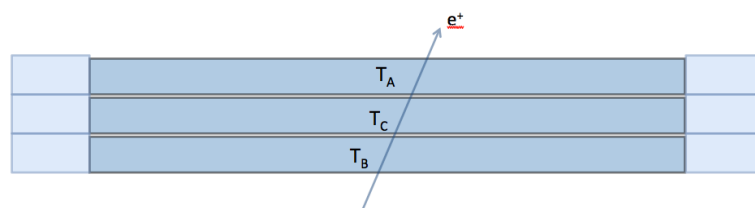


**Figure 6.1:** A triple bars cluster

Clusters with greater multiplicity are not suitable to be used for timing resolution evaluation purposes, both for low statistic and significant multiple scattering effects in the positron propagation between the bars.

Considering a double bar sample, the times measured by each bar are:

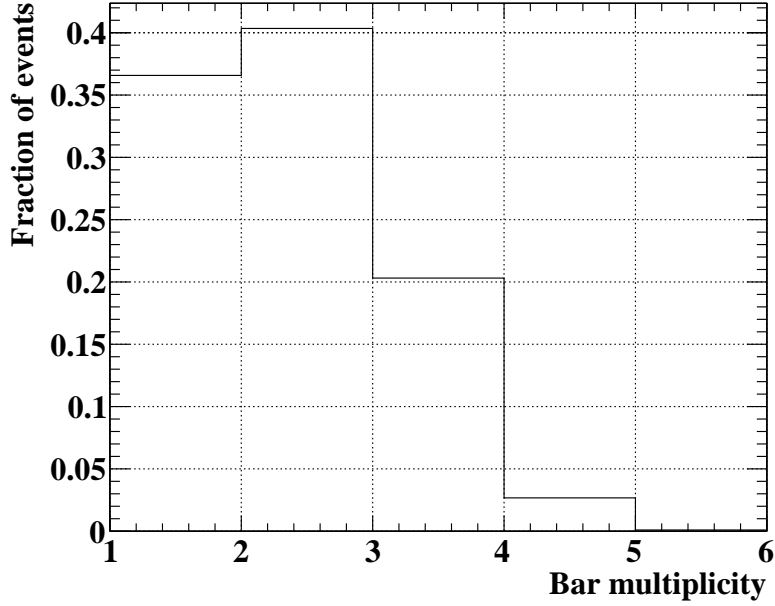


**Figure 6.2:** Distribution of bar multiplicity in Timing Counter clusters.

$$\begin{aligned}
 T_A &= T_{phys} \\
 T_B &= T_{phys} + \frac{l}{c}
 \end{aligned}
 \tag{6.1}$$

where  $T_{phys}$  is the true impact time on Timing Counter and  $l$  is the trajectory length between the two bars. The time difference distribution  $\Delta T = T_B - T_A$  will have a Gaussian shape with mean equal to the mean value of  $l/c$  and width equal to  $\sigma_{\Delta T}$ . We can make the reasonable assumption that the two bars resolutions are equal and that the uncertainty on  $l/c$  is negligible; in this case we can extract the single bar resolution as:

$$\sigma_{\Delta T} = \sqrt{\sigma_{T_A}^2 + \sigma_{T_B}^2} \simeq \sqrt{2}\sigma_T,
 \tag{6.2}$$

that implies:

$$\sigma_T \simeq \frac{\sigma_{\Delta T}}{\sqrt{2}}.
 \tag{6.3}$$

In a similar way, in the case of the triple sample, one can define the difference  $\Delta T$  as:

$$\Delta T = \frac{T_B + T_A}{2} - T_C.
 \tag{6.4}$$

Also in this case the distribution will have Gaussian shape but, differently from the double sample, it will be centered around zero. In fact, the shift related to

the positron propagation is recovered using the triple sample. This technique will be extensively used in the Timing Counter performances evaluation; moreover, substituting the impact time with the impact position measured by each bar, we obtain an useful tool for evaluating also the resolution on the positron impact point.

Making the same assumption made above for the double sample, we can extract the single bar resolution as:

$$\sigma_{\Delta T} = \sqrt{\frac{\sigma_{T_A}^2 + \sigma_{T_B}^2}{4} + \sigma_{T_C}^2} \simeq \sqrt{\frac{3}{2}}\sigma_T$$

$$\sigma_T \simeq \sqrt{\frac{2}{3}}\sigma_{\Delta T}. \quad (6.5)$$

### 6.1.1 Fit of the time difference distributions

As already said in the previous section, the time difference distributions were fitted by using a gaussian function. This method gives quite good results, but does not take into account the tails of distributions, which include uncorrelated events that can generate a worsening of the evaluated resolutions. An example of a time difference distribution fitted by a single Gaussian function is shown in fig. 6.3. In this case, the estimated resolution results to be  $103 \pm 4$  ps.

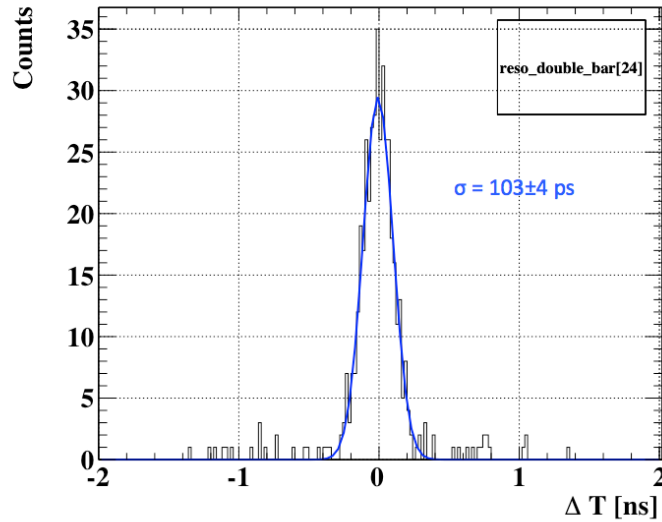


**Figure 6.3:** Plot of the time difference distribution for double events sample, with single gaussian fit superimposed. The estimated resolution results to be  $\sigma = 103$  ps.

In order to have a better estimate, we try to fit the same distribution using a more extended function, namely the sum of a Gaussian function with a second

order polynomial. In this way, also the tails of the distributions should be taken into account; the time resolution can be evaluated as the width of the core gaussian, that results narrower respect to the one obtained by the previous fit, as shown in fig. 6.4, where the same distribution of fig. 6.3 is fitted with the new function, obtaining  $\sigma_T = 85 \pm 3 ps$ .

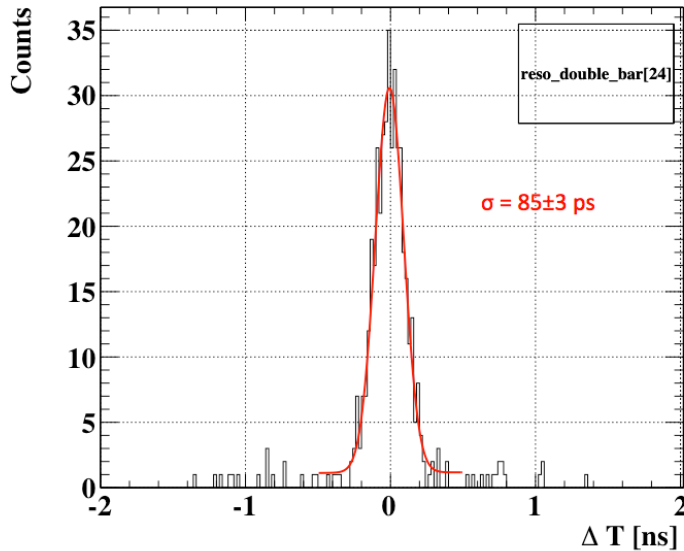


**Figure 6.4:** Plot of the time difference distribution for double events sample, with gaussian + order 2 polynomial fit superimposed. The estimated resolution increases respect to fig.6.3 and results to be  $\sigma = 85 ps$ .

The fraction of events that falls in the tail of the distribution was calculated and resulted to be  $\sim 3\%$  of the total number of events; thus, concerning the statistical effect, this is absolutely negligible. Vice versa, the effect on timing resolution is really appreciable: in fig. 6.5 it is shown the comparison between the resolution evaluated using the two different fit functions. The mean increase in the resolution is  $\sim 10 ps$ , meaning about a 15% improvements in the estimated resolution.

The same test was repeated using a triple bar sample, with the results shown in fig. 6.6, Also in this case, the mean increase in the resolution evaluation is  $\sim 10 ps$ . Therefore we finally decided to use the Gaussian+polynomial function as the default one for the resolution extrapolation from double and triple sample.

### 6.1.2 Run 2010 timing resolutions

In order to estimate the final timing resolution of our detector in the experimental conditions, we analyze a sample of the same data set used for MEG physics analysis, with the technique described in sec. 6.1 and sec. 6.1.1.

The results obtained on the double bar sample are shown in fig. 6.7. All the bar resolutions except one lay in the range  $60 \div 80 ps$ , that is quite close the target

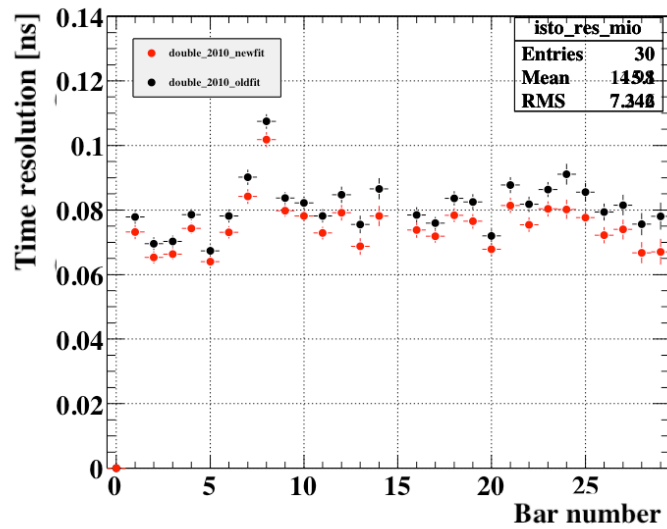


**Figure 6.5:** Summary of the time resolutions obtained on double sample, with two different fit functions: single gaussian (red markers) and gaussian + order 2 polynomial (black markers).

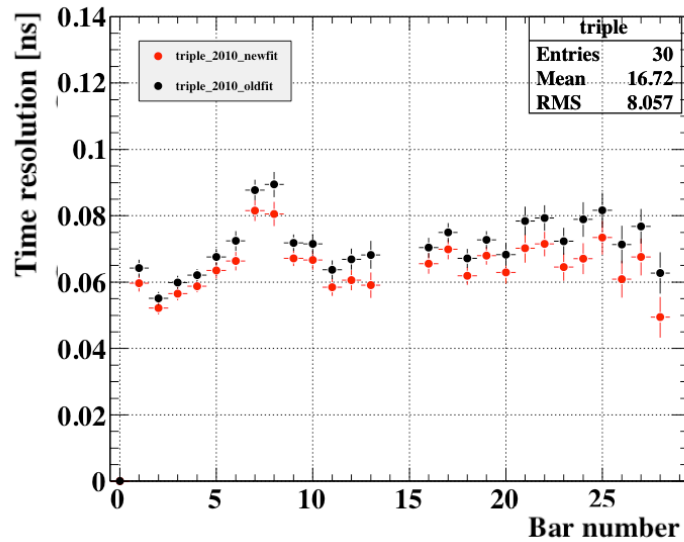


**Figure 6.6:** Summary of the time resolutions obtained on triple sample, with two different fit functions: single gaussian (red markers) and gaussian + order 2 polynomial (black markers).

value (100 ps FWHM, corresponding to  $\sim 45$  ps, see chapter 3), thus showing also a good uniformity detector response.

Fig. 6.8 shows the summary of the results obtained using the triple bar sample: as one can see, the mean improvement of using this sample is  $\sim 10$  ps, laying the

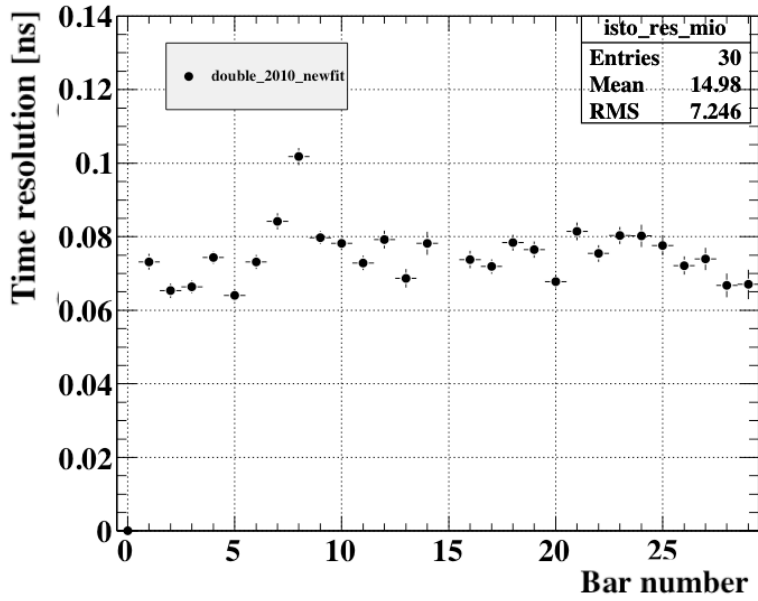


Figure 6.7: Summary of the time resolutions obtained during 2010 run, evaluated on double bars sample.

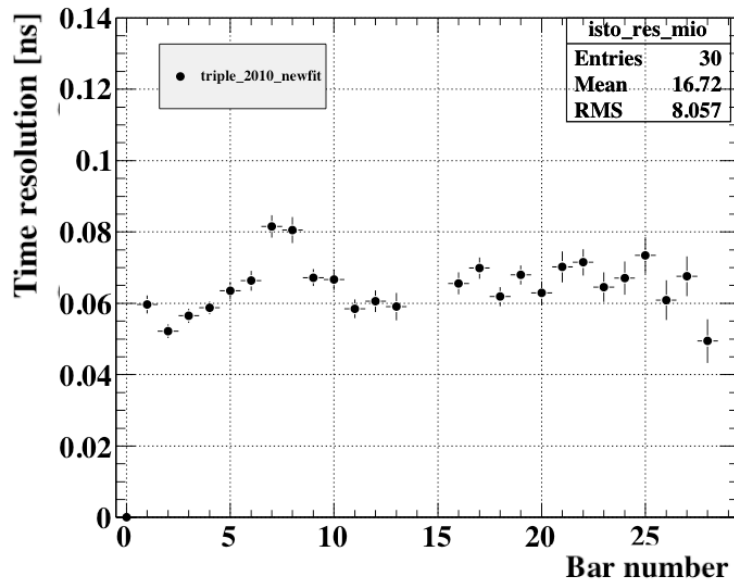


Figure 6.8: Summary of the time resolutions obtained during 2010 run, evaluated on triple bars sample.

resolutions in the range  $50 \div 70$  ps, with exception for two bars<sup>1</sup>.

<sup>1</sup>The anomalous behaviour of bar 8 (7–8 in case of triple sample) has been investigated during the run time; the problem was identified in low gains of the PMTs belonging to bar 7. Due to

Comparing the results obtained during the MEG run time with the ones obtained during the first beam test shown in sec. 3.5, we can notice a mean worsening of  $10 \div 15$  ps. This is not surprising and can be explained considering the different experimental conditions in which the two tests were performed, mainly:

- during the test at the Beam Test Facility (BTF) in National Laboratory of Frascati (LNF), the bar resolution was measured in single bar each time, determining the uncertainty on the  $T_1 - T_2$  quantity using a START-STOP technique [48], [49], thus avoiding effects due to the propagation between 2 bars;
- the energy of the BTF beam can be tuned with high precision (was  $420$  MeV during the test), resulting in a monochromatic beam; moreover, it was possible to have a beam with single-electron multiplicity per bunch, avoiding effects correlated with multiple hits on bar;
- the spot size in the BTF is less than  $5$  mm, resulting in a very good determination of the positron impact point, with respect to the Michel decays in COBRA, that hit almost uniformly the Timing Counter, with consequent effects due to the spread of the trajectories;
- finally, in BTF test there wasn't magnetic field, allowing to operate at higher amplitude pulse.

### 6.1.3 Resolutions stability

The stability of the detector performances was monitored during the whole run time, comparing the Timing Counter timing resolutions evaluated on double and triple data set acquired in different periods.

The results are shown in fig. 6.9 for the double bar sample. The overall stability was found to be quite good, also if some little discrepancy of the order of  $10$  ps appears. Anyway, these effects do not affect the whole detector (Timing Counter and Liquid Xenon)  $t_{e\gamma}$  resolution, that will be described in sec. 6.2.

The triple sample (fig. 6.10) is more stable, with few bars with some differences between different periods, mainly located in the upstream (bar number 15 – 29) sector of the detector.

These results confirmed us the good operations of the Timing Counter during the data acquisition time.

### 6.1.4 Comparison between 2010-2009 results

In order to investigate the detector resolutions during a time interval longer than few months, we enlarged the study of the resolution stability, comparing the results

---

the difficulty in intervene during the run time, and being the involved bars performances not so dramatic, we decided to postpone the maintenance of the PMTs to the 2011 beam shut-down, in order to not waste useful DAQ time.

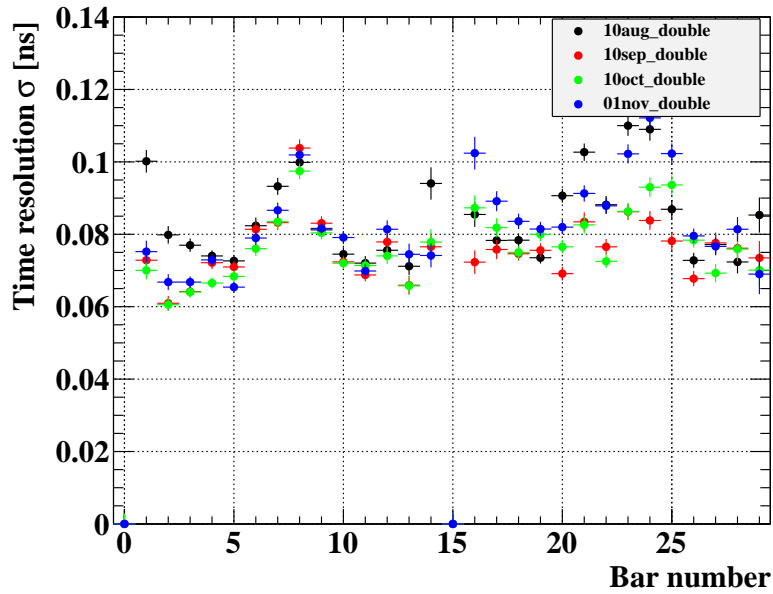


**Figure 6.9:** Resolution stability during run 2010, evaluated on double bar sample. The different markers represent different data acquisition periods.

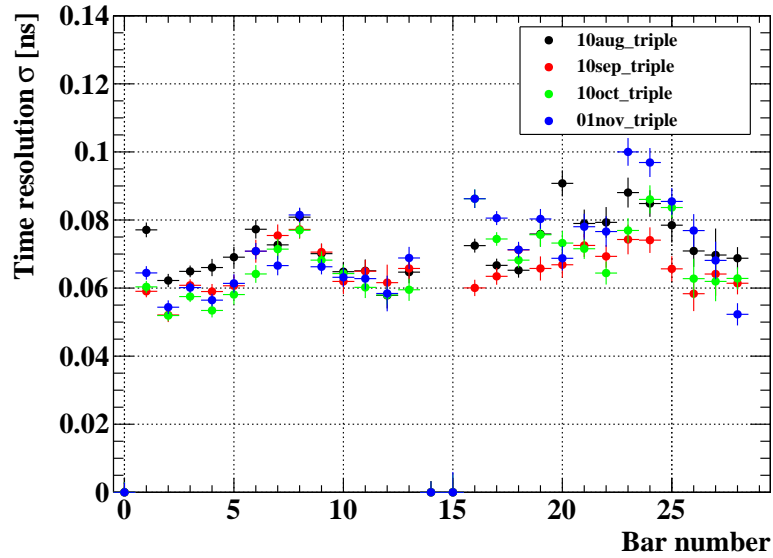


**Figure 6.10:** Resolution stability during run 2010, evaluated on triple bar sample. The different markers represent different data acquisition periods.

obtained during 2010 run with the resolutions measured during the previous data acquisition period (2009).

In this analysis we have to take in mind some crucial differences existing between the two data sets:

- some PMTs that shown a little decreasing of gain response were changed in the detector maintenance performed during the 2010 beam shut down period;
- the full set of calibration described in chapter 5 were repeated at the beginning of each DAQ period; in particular, those concerning the PMTs equalization and consequently the template waveforms for Time Walk corrections (sec. 5.2).

This means that the detector was not exactly in the same experimental conditions between the two data period considered.

The results on the double sample are shown in fig. 6.11. We can notice a little worsening of the resolution between the two data sets. For a couple of bars the worsening is sensible greater, resulting about 20 *ps*. The differences can be better evaluated having a look at fig. 6.12, where the  $\sigma(2010) - \sigma(2009)$  difference as a function of the bar number is plotted. The overall effects, obtained mediating the resolution differences over all the bars is 5 *ps*. The reasons for this effect will be investigated during the 2011 beam shut-down.

In fig. 6.13 the results of the same analysis performed on a triple bar sample are shown. In this case, the worsening is less evident, and mainly concentrate in the upstream sector.

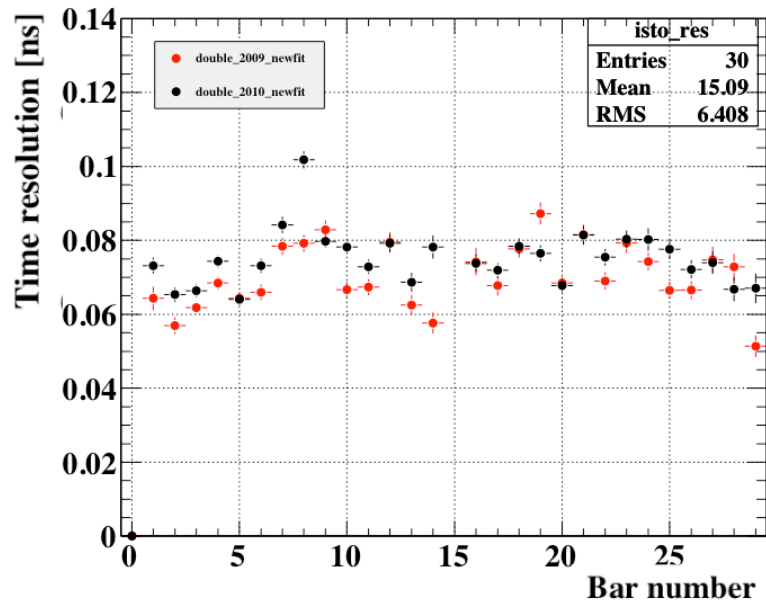


**Figure 6.11:** Comparison between resolution obtained in 2009 and 2010 runs, evaluated on double bars sample.

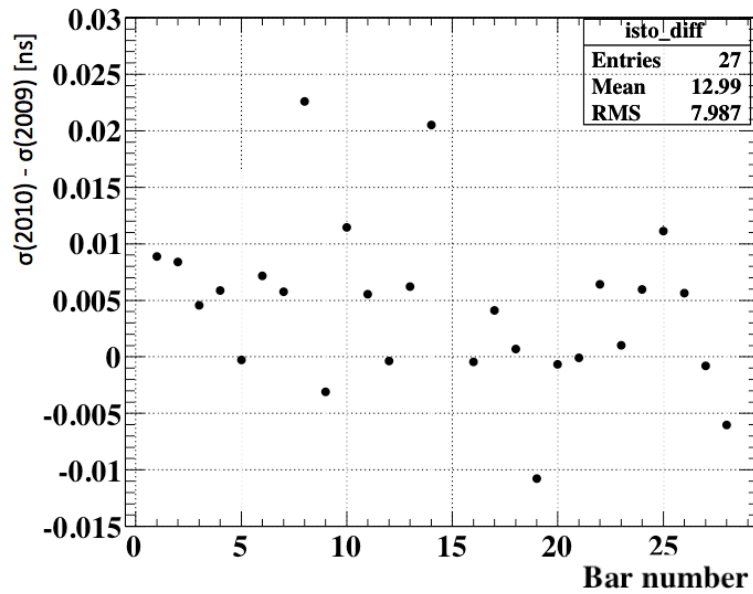


Figure 6.12: Summary of the differences in time resolutions between 2009 and 2010 runs, evaluated on double bar sample.

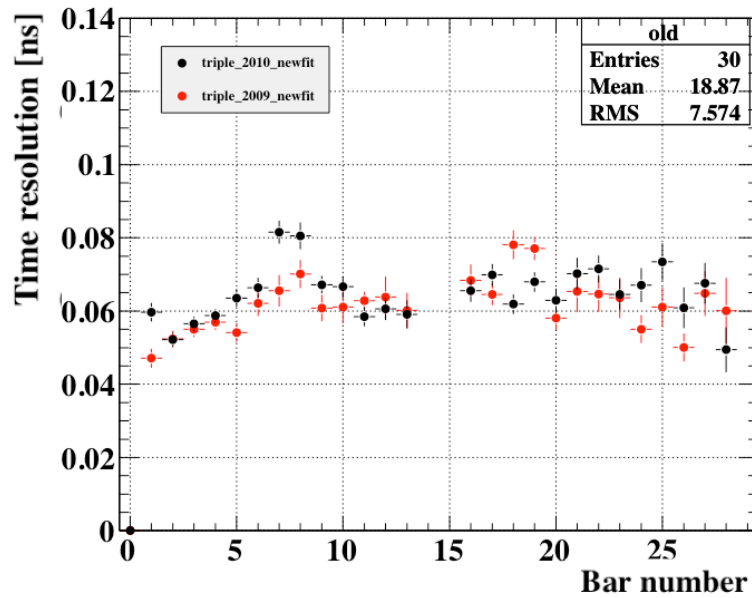
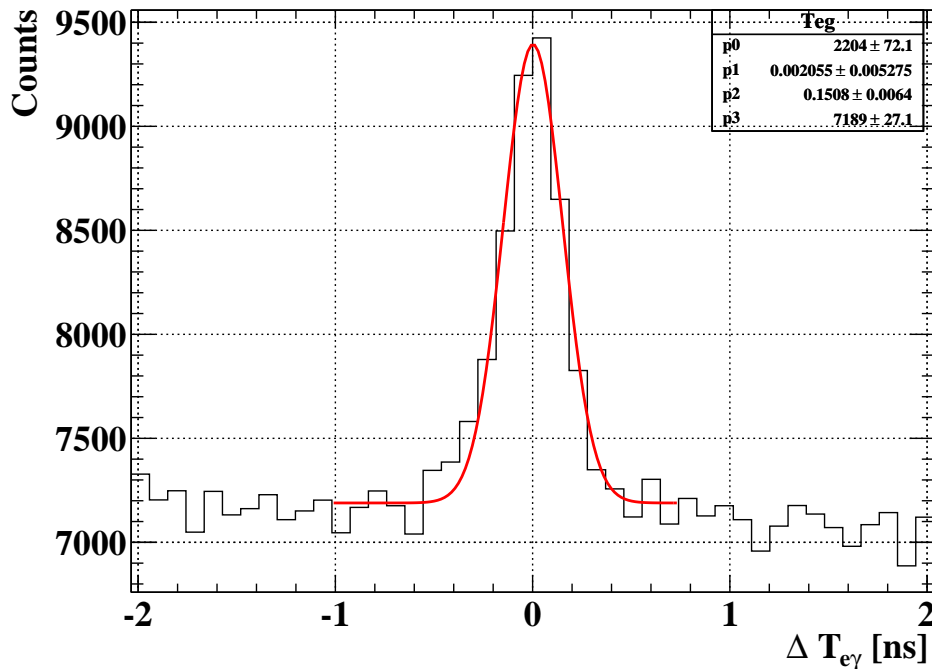


Figure 6.13: Comparison between resolution obtained in 2009 and 2010 runs, evaluated on triple bars sample.

## 6.2 The $t_{e\gamma}$ resolution: the radiative decay sample

The crucial point in the evaluation of the detector performances is the measurement of the  $t_{e\gamma}$  resolution, being this observable directly involved in the background rejection (see sec. 1.4.2 and 1.4.3) and signal selection (see sec. 7.2).

A very useful tool in  $t_{e\gamma}$  resolution is given by the radiative muon decay (RMD)  $\mu^+ \rightarrow e^+ \bar{\nu}_\mu \nu_e$ . This kind of event is characterized by a coincident emission of positron and photon, without any angular coincidence. The RMDs permit to evaluate the overall detector performances, involving both the Timing Counter and Liquid Xenon calorimeter, together with the positron and photons trajectories reconstruction algorithms. The RMD data were taken in dedicated runs during the run time and also during the MEG data acquisition, enabling the relative trigger with an opportune prescale factor.



**Figure 6.14:**  $\Delta T_{e\gamma}$  distributions on radiative decay sample, for run 2010 (Provisional results).

The RMD data sample was selected applying the following cuts on the observables:

- $40 < E_\gamma < 47 \text{ MeV}$ ;
- $45 < E_e < 55 \text{ MeV}$ ;

- $\theta_{e\gamma}, \phi_{e\gamma} < 300$  mrad.

The provisional result for the 2010 run is shown in fig. 6.14. The distribution is fitted with a Gaussian function, that takes into account for the peak of correlated events, plus a constant term, that considers the flat background due to the accidental background events. The  $t_{e\gamma}$  resolution is extrapolated as the width of the Gaussian function, and results to be  $\sigma_{t_{e\gamma}} = 151 \pm 6$  ps.

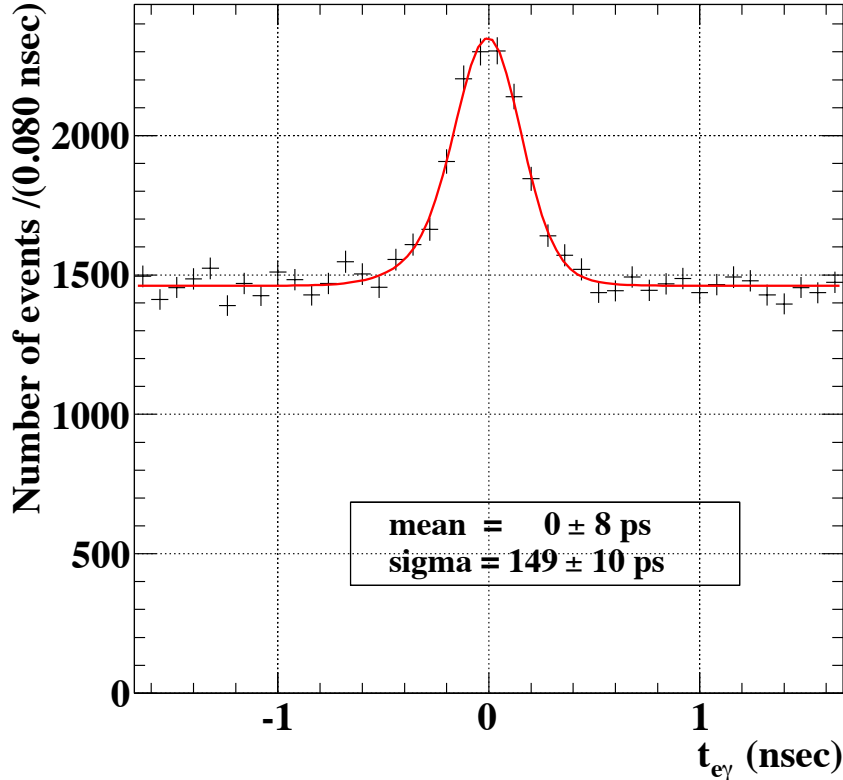


**Figure 6.15:**  $\Delta T_{e\gamma}$  distributions on radiative decay sample, for run 2009.

In fig. 6.15 it is shown the same plot, referred to the 2009 data [74]. The result is almost unchanged with respect to the 2010 performances, being the  $t_{e\gamma}$  resolution in this case  $\sigma_{t_{e\gamma}} = 149 \pm 10$  ps. It is also noteworthy that in both cases the  $t_{e\gamma}$  distribution is absolutely well centered around zero, confirming the good quality of the calibrations applied in order to synchronize the detectors response 5.5.

These results confirmed us the absolutely good stability of the whole detector performances.

### 6.3 Impact point resolution

The evaluation of the positron impact point resolution can be performed with the same technique used for the time resolution estimation (sec. 6.1). Also in this

case, we take advantage of both double and triple bars data samples. We therefore define the “z difference”  $\Delta z$  as follow:

$$\Delta z = z_B - z_A, \quad \text{for double sample,} \quad (6.6)$$

$$\Delta z = \frac{z_B + z_A}{2} - z_C, \quad \text{for triple sample,} \quad (6.7)$$

which permit us to estimate the  $z$  resolution as:

$$\sigma_{\Delta z} = \sqrt{\sigma_{z_A}^2 + \sigma_{z_B}^2} \simeq \sqrt{2}\sigma_z \Rightarrow \sigma_z \simeq \frac{\sigma_{\Delta z}}{\sqrt{2}}. \quad (6.8)$$

$$\sigma_{\Delta z} = \sqrt{\frac{\sigma_{z_A}^2 + \sigma_{z_B}^2}{4} + \sigma_{z_C}^2} \simeq \sqrt{\frac{3}{2}}\sigma_z \Rightarrow \sigma_z \simeq \sqrt{\frac{2}{3}}\sigma_{\Delta z}, \quad (6.9)$$

respectively for the double and triple bar data sample.

An example of a  $\Delta z$  distribution for double bar events is shown in fig. 6.16. Similarly to the time difference distribution, we can fit the distribution by means of a Gaussian function and take the width as an estimate for the impact point resolution. The mean of the distribution is obviously different from zero, because of the inclination of the positron trajectories. So the mean value of the fitted Gaussian function gives the mean distance between the impact positions on two adjacent bars.

The summary of the position resolutions as a function of the bar number is given in fig. 6.17. All resolutions lay in the range  $1.5 \text{ cm} < \sigma_z < 2.5 \text{ cm}$ .

Concerning the triple bar sample, an example of a  $\Delta z$  distribution is shown in fig. 6.18. In this case, the distribution is clearly narrower with respect to the double sample, and also centered around zero.

The summary of the  $z$  resolution evaluated on the triple bar sample as a function of the bar number is shown in fig. 6.18. We can see a clear improvement with respect to the double bar sample: the resolutions lay in the range  $1.0 \text{ cm} < \sigma_z < 1.5 \text{ cm}$ .

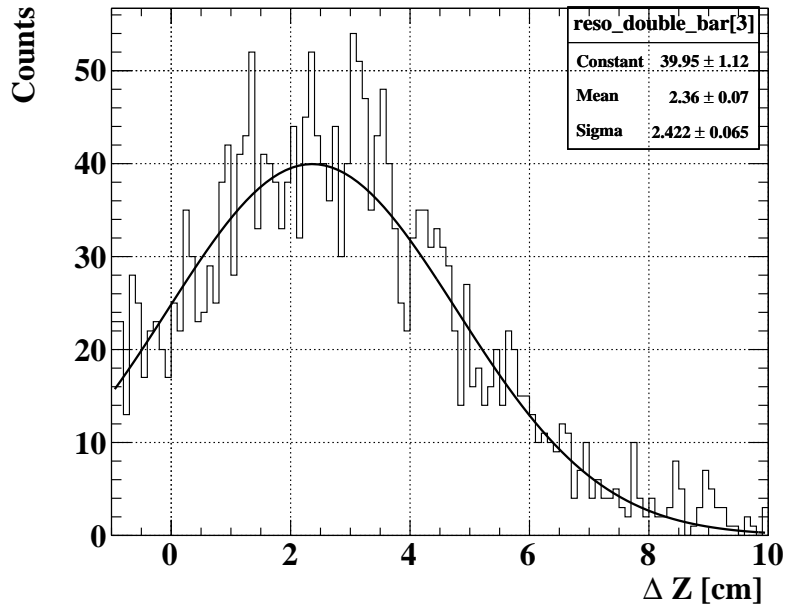


**Figure 6.16:**  $\Delta z$  distributions for double bar sample, with Gaussian fit superimposed. The width and the mean of the Gaussian represent respectively the  $z$  resolution and the mean distance between the impact positions on two adjacent bars.

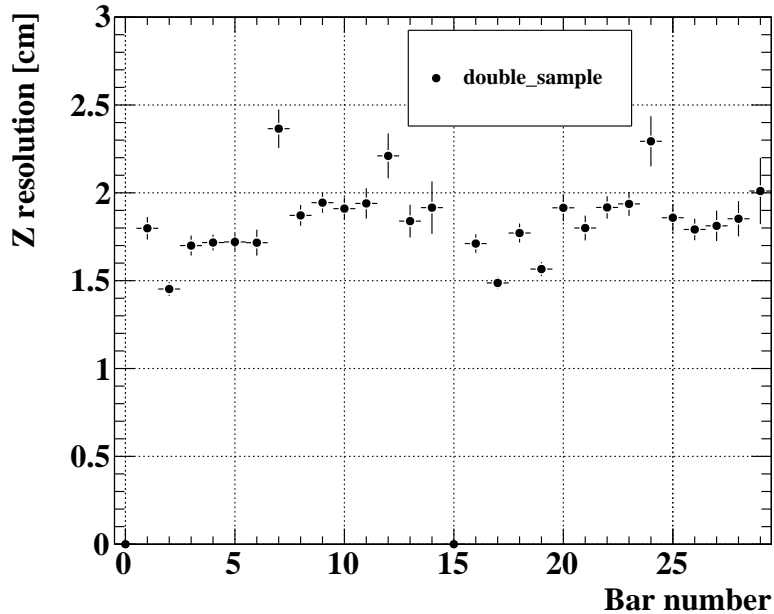


**Figure 6.17:** Summary of the  $z$  resolution as a function of bar number, evaluated on double bar sample.

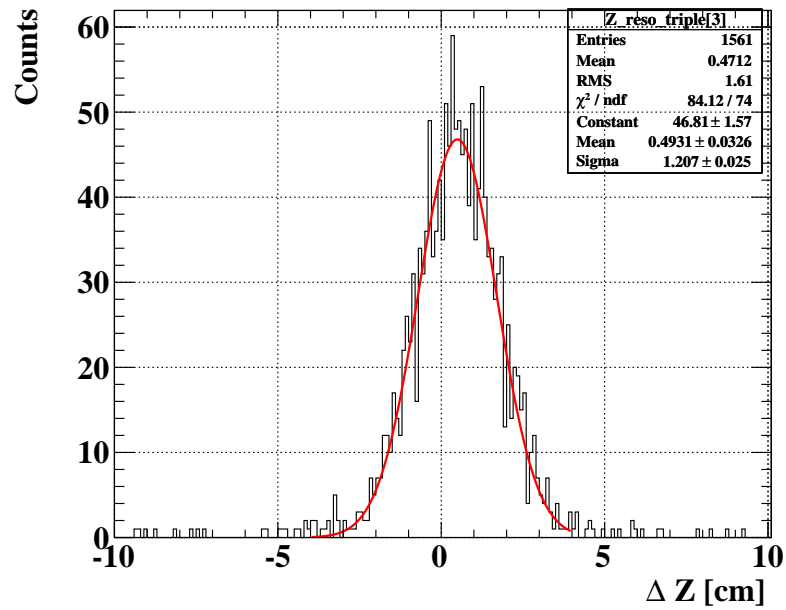


Figure 6.18:  $\Delta z$  distributions for triple bar sample, with Gaussian fit superimposed.

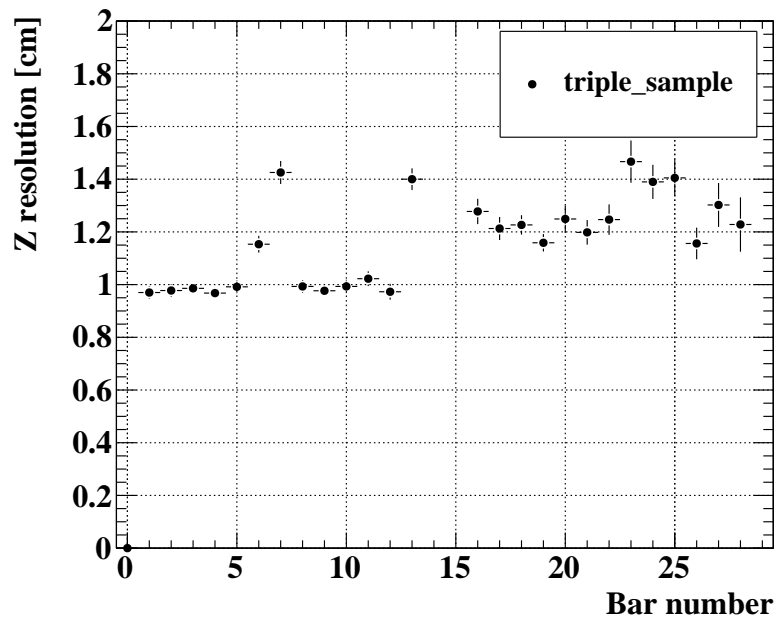


Figure 6.19: Summary of the  $z$  resolution as a function of bar number, evaluated on triple bar sample.



# Chapter 7

## Physics analysis and results

In this chapter the results obtained by the analysis of the 2008 run ( $9.5 \times 10^{13} \mu$  collected in the period September-December) will be presented.

The analysis is based on a “blind analysis” technique in order to avoid any possible bias in results, and it is made by means of a maximum likelihood fit performed on the spectra of the kinematic variables that define the  $\mu \rightarrow e\gamma$  signal. The normalization scheme is constructed in such a way to be independent of the instantaneous beam rate and nearly insensitive to positron acceptance and efficiency factors associated with DC and TC detectors. The confidence level on the resulting branching ratio is evaluated by means of Toy Monte Carlo simulations based on the calculated probability density functions.

### 7.1 Blinding box

At the first stage of the data processing, a data reduction (pre-selection) is performed by selecting events with conservative criteria that require the time of the photon detector signal to be close to that of a timing counter hit, and at least one track to be detected by the drift chamber system. This reduces the data size to 16% of the recorded events. The pre-selected data are again processed and those events falling into a pre-defined window (blinding-box), containing the signal region on the  $\gamma$  energy and the time difference between the  $\gamma$ -ray and the positron, are “hidden”, that means written to a separate data-stream, inaccessible to the experimenter. The use of a blind-box analysis is a consolidate technique in particle physics, especially when one has the need to estimate accurately systematic errors for the measurement, without biases induced by the experimenter himself.

The box is defined in the  $[t_{e\gamma}, E_\gamma]$  plane by the following cuts:

- $48 \text{ MeV} < E_\gamma < 58 \text{ MeV}$ ;
- $|\Delta t_{e\gamma}| \leq 1 \text{ ns}$ .

Event distribution after the pre-selection and blinding processes is shown in fig. 7.1. The data in the region outside the blinding box (namely the side-bands)

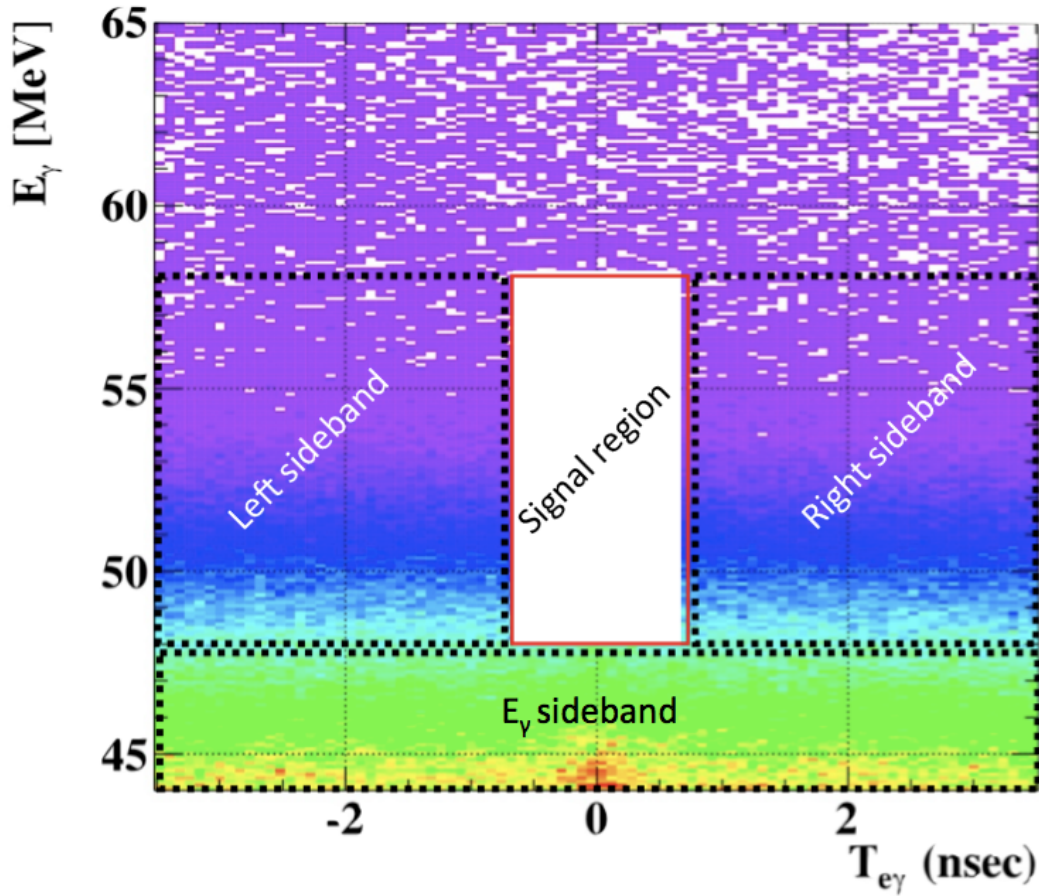


**Figure 7.1:** Plot of the MEG blinding box. Outside the signal box, one can recognize the side-bands used for calibration purposes.

are suitable to be used for calibration and background estimation purposes; in particular, one can identify two kind of side-bands:

- the time side-bands, defined by  $|\Delta t_{e\gamma}| \geq 1 \text{ ns}$ ;
- the energy side bands, defined by  $44 \text{ MeV} \leq E_\gamma \leq 48 \text{ MeV}$ .

Both side-bands are used for background level estimation: the time side-bands are used to study the accidental events spectra, particularly for  $E_\gamma$ , while the energy side-bands, in which the main part of the  $\mu$  radiative decay events accumulates, is used for time resolution and TC-LXe offsets evaluate, and to estimate the number of radiative decay in the analysis region.

## 7.2 Probability density function

In order to extract the number of signal, radiative and accidental background a maximization of a likelihood function is performed. The likelihood function is built

starting from the probability density function (PDF) that describe each kinematic observable. In the following we will describe how each PDF is determined.

### 7.2.1 Signal PDF

The signal PDF  $S$  is defined as the product of the statistical independent PDFs evaluated for each observable:

$$S(E_\gamma, E_e, \theta_{e\gamma}, \phi_{e\gamma}, t_{e\gamma}) = S_1(E_\gamma)S_2(E_e)S_3(\theta_{e\gamma})S_4(\phi_{e\gamma})S_5(t_{e\gamma}). \quad (7.1)$$

The  $\gamma$  energy PDF,  $S_1(E_\gamma)$  (fig. 7.2a), is defined by the calorimeter response function for  $E_\gamma$  measured in dedicated  $\pi^0$  runs. The shape is asymmetric with a low energy tail due to  $\gamma$  rays converting in front of the Liquid Xenon sensitive volume. A tri-dimensional mapping of the parameters is also made, since they depend to some extent on the position of the  $\gamma$ -ray conversion, mainly on the conversion depth inside the detector ( $w$ ). As an example, the average resolution for deep events ( $w > 2 \text{ cm}$ ) is measured to be  $\Delta E/E = (5.8 \pm 0.35)\% \text{ FWHM}$ , with a right tail of  $\sigma_R = (2.0 \pm 0.15 \%)$ .

The positron energy PDF,  $S_2(E_e)$  (fig. 7.2b), is evaluated by fitting the kinematical edge of the measured Michel positron energy spectrum at  $52.8 \text{ MeV}$ . The fit function is formed by folding the theoretical Michel spectrum form with the energy-dependent detector efficiency, and the response function for mono-energetic positrons. The latter is extracted from the Monte Carlo simulation of  $\mu \rightarrow e\gamma$  decays, and is well described by a triple Gaussian function (a sum of a core and two tail components). The resolutions extracted from data are  $374 \text{ KeV}$ ,  $1.06 \text{ MeV}$  and  $2.0 \text{ MeV}$  in sigma for the core component and the two tails, with corresponding fractions of 60%, 33% and 7%, respectively. The uncertainty on these numbers is dominated by systematic effects and was determined by varying both the event selection and fitting criteria.

The angular PDFs  $S_3(\theta_{e\gamma})$  and  $S_4(\phi_{e\gamma})$  (fig. 7.2c,d) are formed combining the contributions of positron emission angles, muon decay vertex reconstruction and photon position resolution in the Liquid Xenon detector.

The positron direction and decay vertex position are determined by projecting the positron back to the target. The  $\gamma$ -ray direction is defined by the line linking its reconstructed conversion point in the LXe detector with the vertex of the candidate companion positron. The resolution of the angles between the two particles is evaluated by combining the angular resolution and the vertex position resolution in the positron detector and the position resolution in the photon detector. The positron angular resolution is evaluated by exploiting tracks that make two turns in the spectrometer, where each turn is treated as an independent track. The  $\theta$  and  $\phi$  resolutions are extracted separately from the difference of the two track segments at the point of closest approach to the beam-axis and result to be  $\sigma_\theta = 18 \text{ mrad}$ ,  $\sigma_\phi = 10 \text{ mrad}$ . Because of this difference in resolution,  $\theta_{e\gamma}$  and  $\phi_{e\gamma}$  are separately treated in the analysis. The vertex position resolutions are measured, using the double turn, technique, to be  $\sim 3.2 \text{ mm}$  and  $\sim 4.5 \text{ mm}$  in the

vertical and horizontal directions on the target plane respectively. These values were confirmed independently by a method which reconstructs the edges of several holes placed in the target.

The position of the photon conversion point is reconstructed by using the distribution of the light seen by the PMTs near the incident position. The performance of the position reconstruction is evaluated by a Monte Carlo simulation and it is validated in a dedicated calibrations runs by placing a lead collimator in front of the photon detector. The average position resolutions along the two orthogonal front-face sides of the LXe detector and the depth direction ( $w$ ) are estimated to be  $\sim 5\text{ mm}$  and  $\sim 6\text{ mm}$  respectively.

On combining the individual resolutions, the averaged opening-angle resolutions of 21 and 14 mrad for  $\theta_{e\gamma}$  and  $\phi_{e\gamma}$  are obtained respectively.

The time  $t_{e\gamma}$  PDF,  $S_5(t_{e\gamma})$  (fig. 7.2e), depends on the positron and gamma timing measured by the detector, corrected for the particles time of flight, and consist in a single Gaussian function with width equal to the  $t_{e\gamma}$  resolution. The resolutions on this observable is quoted on the radiative decay peak that is clearly visible in the  $E_\gamma$  sideband. The  $t_{e\gamma}$  peak is fitted in the region  $40 < E_\gamma < 46\text{ MeV}$ , and, taking into account a small dependence from  $E_\gamma$  observed in  $\pi^0$  runs, the timing resolution is estimated to be  $\sigma_{t_{e\gamma}} = (148 \pm 17)\text{ ps}$ .

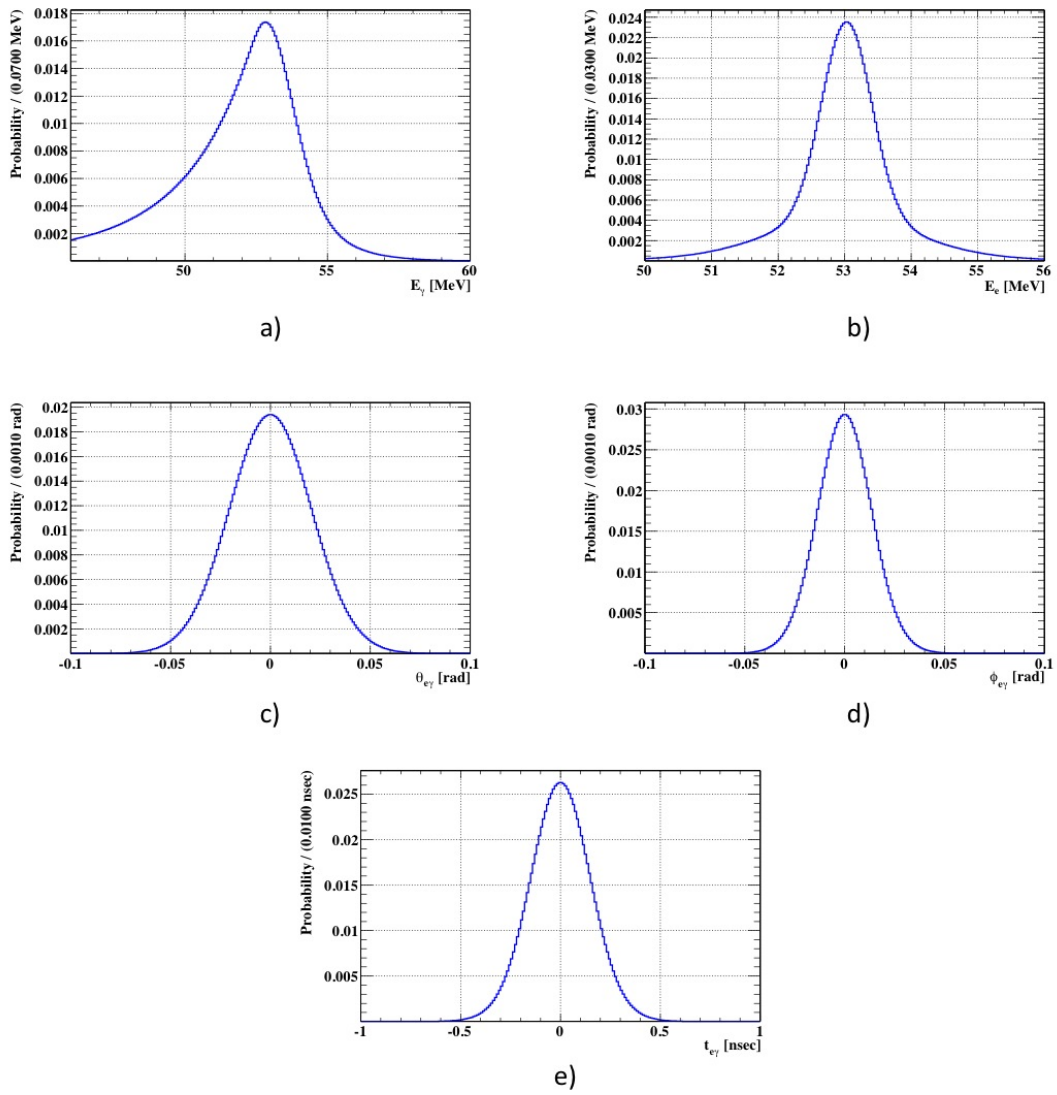


Figure 7.2: PDFs for  $\mu^+ \rightarrow e^+ \gamma$  signal event.

## 7.2.2 Radiative decay PDF

The  $\mu^+ \rightarrow e^+ \nu_e \bar{\nu}_\mu$  kinematical constraints correlate all the observables except of the  $t_{e\gamma}$  one. Thus the RMD PDF can be defined as:

$$R(E_\gamma, E_e, t_{e\gamma}, \theta_{e\gamma}, \phi_{e\gamma}) = R_1(E_\gamma, E_e, \theta_{e\gamma}, \phi_{e\gamma}) R_2(t_{e\gamma}). \quad (7.2)$$

$R_2(t_{e\gamma})$  is defined as the same function as for the  $t_{e\gamma}$  signal PDF, while  $R_1(E_\gamma, E_e, \theta_{e\gamma}, \phi_{e\gamma})$  is obtained by folding the theoretical distribution of the radiative decay with the detector experimental resolutions and acceptance functions.

The projections of the RMD PDF on each variable are shown in fig. 7.3.

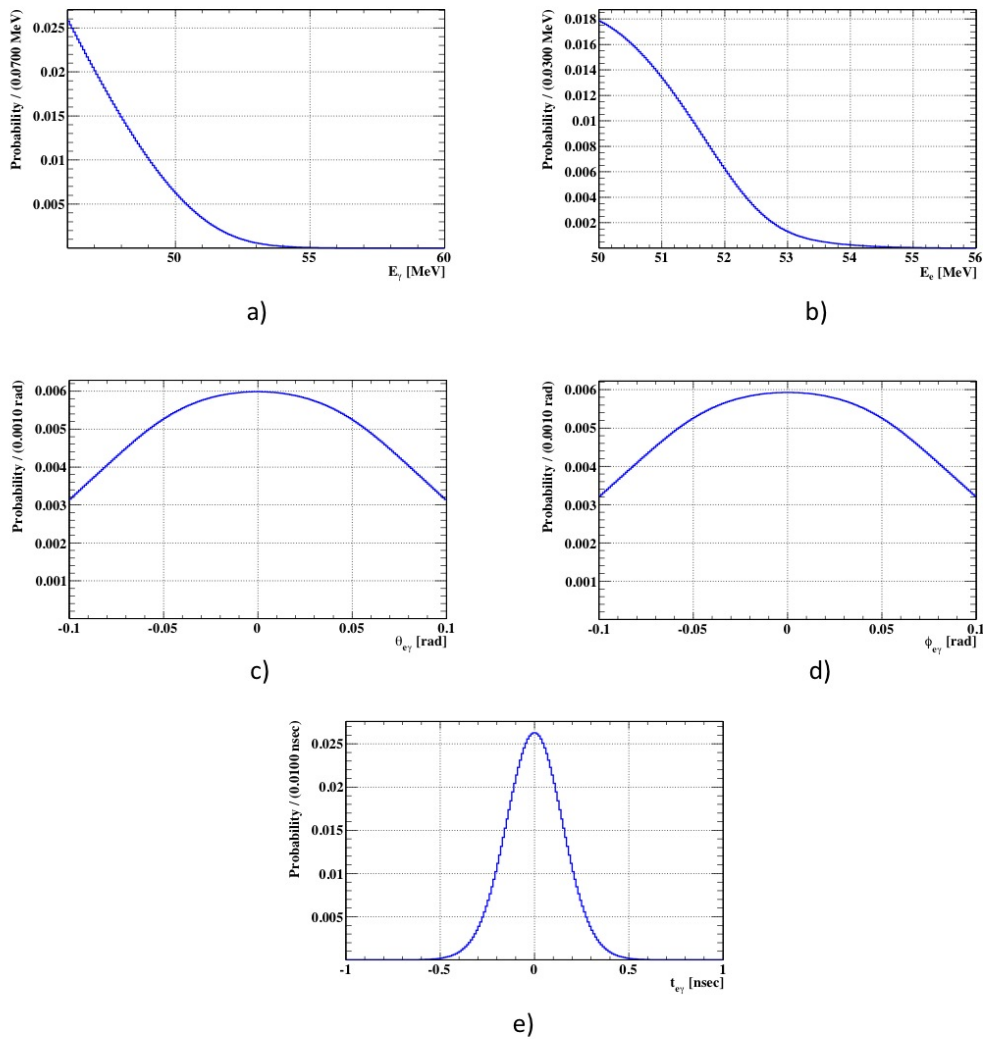


**Figure 7.3:** Radiative PDFs. Panel from a) to d) represent the projection of  $R_1(E_\gamma, E_e, \theta_{e\gamma}, \phi_{e\gamma})$  on each variable, while in e) it is shown  $R_2(t_{e\gamma})$ .

### 7.2.3 Accidental background PDF

As explained in sec. 1.4.3 the accidental background is given by a positron and a  $\gamma$ -ray in time and spatial coincidence, coming from uncorrelated events. Thus there are no correlations between each observables, and the PDF can be defined as the product of statistically independent PDFs for the five observables in a similar way with respect to the signal PDF:

$$B(E_\gamma, E_e, \theta_{e\gamma}, \phi_{e\gamma}, t_{e\gamma}) = B_1(E_\gamma)B_2(E_e)B_3(\theta_{e\gamma})B_4(\phi_{e\gamma})B_5(t_{e\gamma}). \quad (7.3)$$

$B_1(E_\gamma)$  (fig. 7.4a) is obtained by fitting the background spectrum in the  $t_{e\gamma}$  sidebands, measuring separately 38 tridimensional sections of the calorimeter. Each spectrum is fitted by a spectrum evaluated in Monte Carlo simulation smeared by the detector response.

$B_2(E_e)$  (fig. 7.4b) is obtained by fitting the Michel spectrum, and it is common to all the events in the analysis window.

$B_5(t_{e\gamma})$  (fig. 7.4e) is described by a flat distribution, because of the accidental nature of this kind of background.

The angular PDFs,  $B_3(\theta_{e\gamma})$  and  $B_4(\phi_{e\gamma})$  (fig. 7.4c,d), are extracted from all the side-bands data. One would expect to find flat distribution in  $\cos\theta_{e\gamma}$  and  $\phi_{e\gamma}$  but this was not the case. In fact, the experimental data were found to be biased by the online selection algorithm and also by the detector acceptance. Thus the angular PDFs are evaluated along 8 possible directions.

The 5 individual PDFs are shown in fig. 7.4.

## 7.3 Likelihood analysis

The blinding-box is opened after completing the optimization of the analysis algorithms and the background study. The number of  $\mu \rightarrow e\gamma$  events is determined by means of a maximum likelihood fit in the analysis window region defined by the following cuts:

- $46 < E_\gamma < 60 \text{ MeV}$ ,
- $50 < E_e < 56 \text{ MeV}$ ,
- $|t_{e\gamma}| < 1 \text{ ns}$ ,
- $|\theta_{e\gamma}| < 100 \text{ mrad}$ ,
- $|\phi_{e\gamma}| < 100 \text{ mrad}$ .

The analysis window is slightly larger with respect to the signal box: the cuts are approximately ten sigmas wide compared to the measured resolutions, in such a way to fully contain the signal events and to include some background events as well.

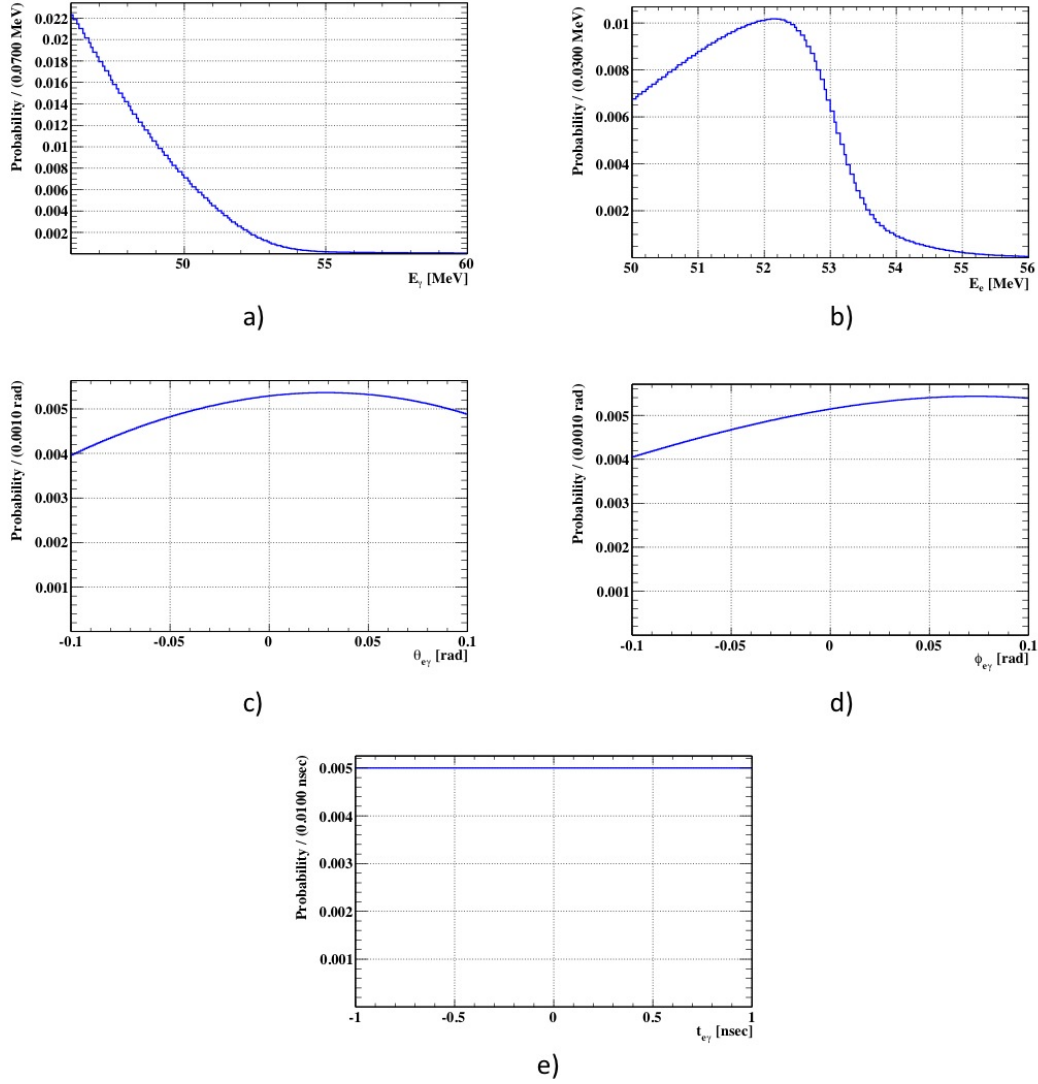


**Figure 7.4:** PDFs for accidental background.

An extended likelihood function  $\mathcal{L}$  is constructed as:

$$\mathcal{L}(N_{SIG}, N_{RMD}, N_{BG}) = \frac{N^{N_{obs}} \exp^{-N}}{N_{obs}!} \prod_{i=1}^{N_{obs}} \left[ \frac{N_{SIG}}{N} S + \frac{N_{RMD}}{N} R + \frac{N_{BG}}{N} B \right], \quad (7.4)$$

where  $N_{SIG}$ ,  $N_{RMD}$ , and  $N_{BG}$  are the number of  $\mu \rightarrow e\gamma$ , RMD and BG events respectively, while  $S$ ,  $R$  and  $B$  are their respective probability density functions (described in sec. 7.2.1, 7.2.2 and 7.2.3).  $N_{obs} = 1189$  is defined as the total number of events observed in the analysis window and  $N = N_{SIG} + N_{RMD} + N_{BG}$ .

The likelihood fit has been initialized with the number of expected RMD in the analysis region. This number is calculated to be  $40 \pm 8$ , evaluated by scaling the

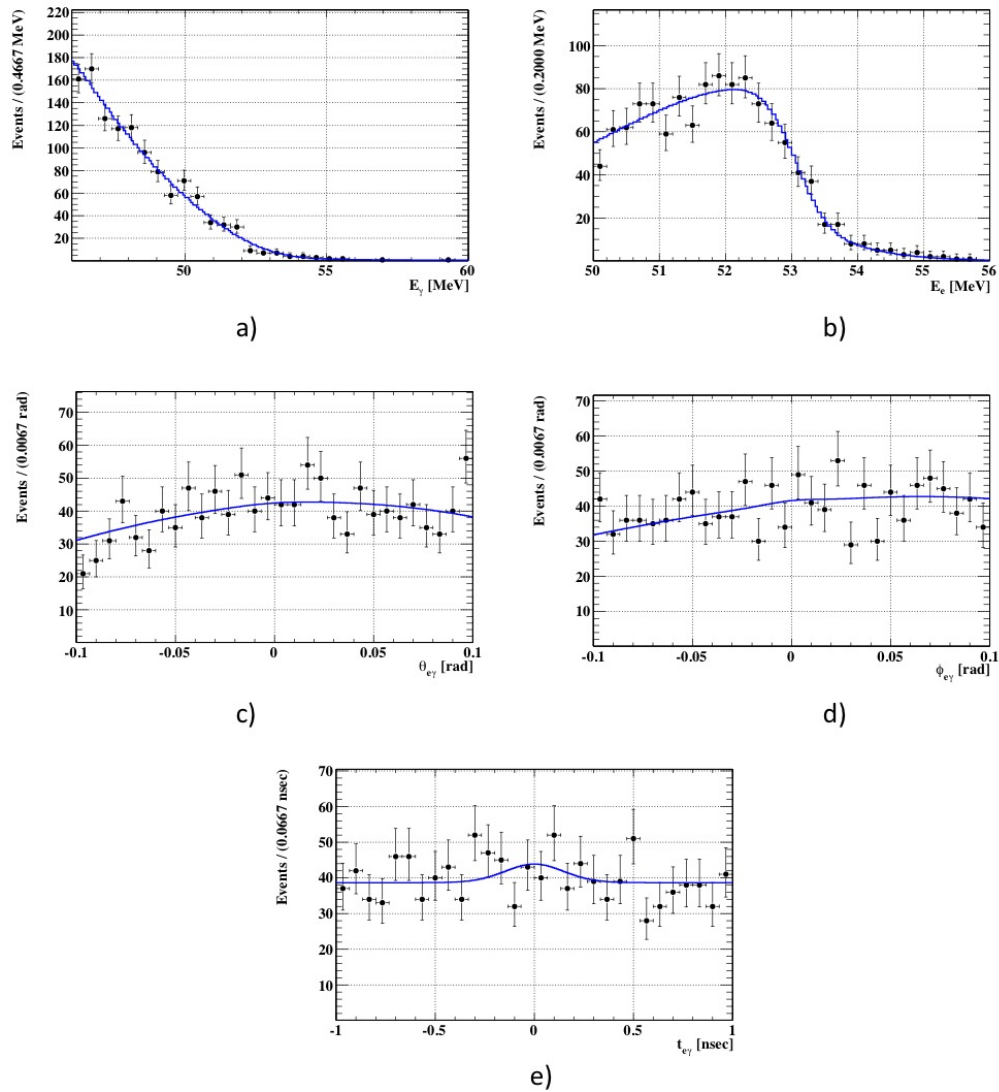


**Figure 7.5:** Projected distributions for each observable, containing all events in the analysis window. A solid line shows the likelihood functions fitted to the data.

number of events in the peak of the  $t_{e\gamma}$  distribution, obtained with lower energy cuts, using the probability ratio in the PDFs.

The maximum likelihood fit results are:

$$\begin{aligned}
 N_{SIG} &= 4.3^{+3.9}_{-2.9} \text{ events} \\
 N_{RMD} &= 25^{+17}_{-16} \text{ events} \\
 N_{BG} &= 1159^{+38}_{-37} \text{ events}
 \end{aligned}$$

The fitted number of radiative decay events agrees with the expected one within the errors.

The event distributions of the five observables for all events in the analysis window are shown in fig. 7.5, together with the projection of the fitted likelihood function.

## 7.4 Normalization scheme

A Branching Ratio is defined as the decay rate for a particular process, normalized to the total one; in MEG, we have:

$$BR(\mu^+ \rightarrow e^+\gamma) \equiv \frac{\Gamma(\mu^+ \rightarrow e^+\gamma)}{\Gamma_{tot}}. \quad (7.5)$$

Because of the total decay rate of  $\mu$  is wholly made up of Michel decay (with a small correction deriving from radiative decays), we can normalized the  $\Gamma(\mu^+ \rightarrow e^+\gamma)$  to the Michel decay rate,  $\Gamma(\mu^+ \rightarrow e^+\nu_e\bar{\nu}_\mu)$ . Therefore we define:

$$BR(\mu^+ \rightarrow e^+\gamma) = \frac{\Gamma(\mu^+ \rightarrow e^+\gamma)}{\Gamma(\mu^+ \rightarrow e^+\nu_e\bar{\nu}_\mu)}. \quad (7.6)$$

Thus, one can calculate the Branching Ratio in such a way to be independent of the instantaneous beam rate and nearly insensitive to positron acceptance and efficiency factors associated with the DCH and TC detectors, as these differ only slightly between the signal and the normalization samples, due to small momentum dependent efficiency [75]. This is a quite useful technique, in particular for 2008 run, because of the DC operations showed some instability during the data acquisition time.

The number of Michel decays  $N_M$  detected can be written as:

$$N_{e\nu\bar{\nu}} = N_\mu \times B_{e\nu\bar{\nu}} \times f_{e\nu\bar{\nu}}^e \times T \times \frac{1}{P_{e\nu\bar{\nu}}} \times \epsilon_{\nu\bar{\nu}}^{trig} \times A_{e\nu\bar{\nu}}^{TC} \times \epsilon_{e\nu\bar{\nu}}^{DC} \quad (7.7)$$

where:

- $N_\mu$  is the number of muon stopped in the target;
- $B_{e\nu\bar{\nu}}$  is the Michel decay branching ratio;
- $f_{e\nu\bar{\nu}}^e$  is the fraction of Michel events with energy greater than 50 MeV (the cut in the analysis window);
- T is the data acquisition livetime;
- $P_{e\nu\bar{\nu}}$  is the trigger prescaling factor (the number of events which have to occur before one of those is recorded by the DAQ);
- $\epsilon_{\nu\bar{\nu}}^{trig}$  is probability to have a trigger fired, if the event satisfy all the selection criteria;

- $A_{e\nu\bar{\nu}}^{TC}$  is the probability to have at least one hit on TC, once a positron is emitted in the acceptance and tracked by the DC;
- $\epsilon_{e\nu\bar{\nu}}^{DC}$  is the tracking efficiency for the positron emitted in the DC geometrical acceptance.

A similar expression can be written for the number of signal events:

$$N_{e\gamma} = N_{\mu} \times B_{e\gamma} \times T \times \epsilon_{e\gamma}^{trig} \times A_{e\gamma}^{TC} \times \epsilon_{e\gamma}^{DC} \times \epsilon_{e\gamma} \times A_{e\gamma}^{GEO} \quad (7.8)$$

with the same meaning of symbols. In eq. 7.8, additional factors are  $\epsilon_{e\gamma}$  and  $A_{e\gamma}^{GEO}$ , defined as  $\gamma$ -ray detection and reconstruction efficiency (including selection criteria) and conditional acceptance of  $\gamma$ -ray detection from  $\mu \rightarrow e\gamma$  events (probability that the  $\gamma$ -ray from  $\mu \rightarrow e\gamma$  decay is detected in the fiducial volume of LXe calorimeter when the corresponding  $e^+$  is detected in the spectrometer). Moreover, in the last equation the prescaling factor is considered to be 1 and thus omitted.

Finally, solving eq. 7.7 and 7.8 for the branching ratios and taking the ratio, one obtain:

$$\frac{B_{e\gamma}}{B_{e\nu\bar{\nu}}} = \frac{N_{SIG}}{N_{e\nu\bar{\nu}}} \times \frac{f_{e\nu\bar{\nu}}^e}{P} \times \frac{\epsilon_{e\nu\bar{\nu}}^{trig}}{\epsilon_{e\gamma}^{trig}} \times \frac{A_{e\nu\bar{\nu}}^{TC}}{A_{e\gamma}^{TC}} \times \frac{\epsilon_{e\nu\bar{\nu}}^{DC}}{\epsilon_{e\gamma}^{DC}} \times \frac{1}{A_{e\gamma}^{geo}} \times \frac{1}{\epsilon_{e\gamma}} = \frac{N_{SIG}}{k}. \quad (7.9)$$

where the normalization factor  $k$  takes into account all the parameters. The definitions and the values of the parameters that appear in eq. 7.9 are summarized in tab. 7.1.

Performing the calculations, the normalizing factor results to be  $k = (5.2 \pm 0.5) \times 10^{11}$ ; this number will be used in sec. 7.6 to obtain the upper limit on  $\mu^+ \rightarrow e^+\gamma$  branching ratio.

$N_{e\nu\bar{\nu}}$	11414
$f_{e\nu\bar{\nu}}^e$	$0.101 \pm 0.006$
$P$	$10^7$
$\epsilon_{e\gamma}^{trig} / \epsilon_{\nu\bar{\nu}}^{trig}$	$0.66 \pm 0.03$
$A_{e\gamma}^{TC} / A_{e\nu\bar{\nu}}^{TC}$	$1.11 \pm 0.02$
$\epsilon_{e\gamma}^{DC} / \epsilon_{e\nu\bar{\nu}}^{DC}$	$1.02 \pm 0.005$
$A_{e\gamma}^{geo}$	$0.98 \pm 0.005$
$\epsilon_{e\gamma}$	$0.63 \pm 0.04$
$k$	$(5.2 \pm 0.5) \times 10^{11}$

**Table 7.1:** Values of the parameters that appear in eq. 7.9 (ratio given as signal to Michel).

## 7.5 Confidence level scan

The 90% confidence level (C.L.) intervals on  $N_{SIG}$  and  $N_{RMD}$  are determined by the Feldman–Cousins approach [76]. A contour of 90% C.L. in the  $[N_{SIG}, N_{RMD}]$  plane is constructed by means of a toy Monte Carlo simulation.

The starting point of this technique is the result obtained by the maximum likelihood fit described in sec. 7.3,  $N_{SIG} = 4.3$  and  $N_{RMD} = 25$ . Then, one pick up a random point  $(N_{SIG}^i, N_{RMD}^i)$  in the  $[N_{SIG}, N_{RMD}]$  plane, and generates a set of pseudo-experiments (1000 for each point) based on the measured PDF distributions, assuming  $N_{SIG}^i$  and  $N_{RMD}^i$  as true expectation value. Moreover, in each simulated experiment the number of signal and radiative decay events can fluctuate accordingly to the Poisson statistic. A maximum likelihood fit is performed to all the simulated experiment, in order to extract  $N_{SIG}^j$  and  $N_{RMD}^j$ , where the upperscript  $j$  denoted the toy experiment number.

Finally, the likelihood ratio for data and toy Monte Carlo are calculated as follow:

$$R_{DATA}^i = \frac{\mathcal{L}(N_{SIG}^i, N_{RMD}^i, N_{BG}^{best_0})}{\mathcal{L}(N_{SIG}^{best_0}, N_{RMD}^{best_0}, N_{BG}^{best_0})} \quad (7.10)$$

$$R_{MC_j}^i = \frac{\mathcal{L}(N_{SIG}^i, N_{RMD}^i, N_{BG}^{best_0})}{\mathcal{L}(N_{SIG}^{best_j}, N_{RMD}^{best_j}, N_{BG}^{best_j})} \quad (7.11)$$

The toy experiment are then classified in a decreasing order, based on the likelihood ratio. After the ordering, the fraction of toy MC which have a likelihood ratio  $R_{MC_j}^i$  greater than the one obtained for the real experiment,  $R_{DATA}^i$  is calculated. If the fraction is  $\leq 0.9$ , then the point  $(N_{SIG}^i, N_{RMD}^i)$  belongs to the 90% C.L. region of the  $[N_{SIG}, N_{RMD}]$  plane.

This procedure is iterated for many choice of the  $(N_{SIG}^i, N_{RMD}^i)$  point, in such a way to scan the contour of the C.L. region. A schematic representation of the C.L. region determination via the Feldman–Cousins approach is shown in fig. 7.6, while the scan of the confidence level versus  $N_{SIG}$  is shown in fig. 7.7.

## 7.6 Upper limit on $\mu^+ \rightarrow e^+ \gamma$ branching ratio

The limit for  $N_{SIG}$  is obtained from the projection of the contour of the 90% confidence level region on the  $N_{SIG}$ -axis. The obtained upper limit is  $N_{SIG} \leq 14.7$ , where the systematic error is included. The largest contribution to the systematic error coming from uncertainties on:

- selection of photon pile-up events ( $\Delta N_{SIG}=1.2$ );
- response function of the positron energy ( $\Delta N_{SIG}=1.1$ );
- photon energy scale ( $\Delta N_{SIG}=0.4$ );

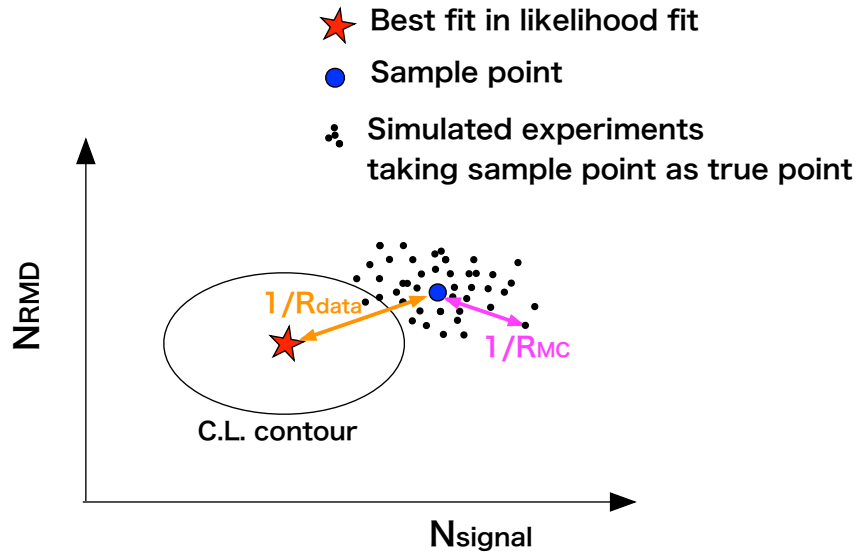


**Figure 7.6:** Schematic representation of the construction of 90% confidence level contour by Feldman-Cousins approach.

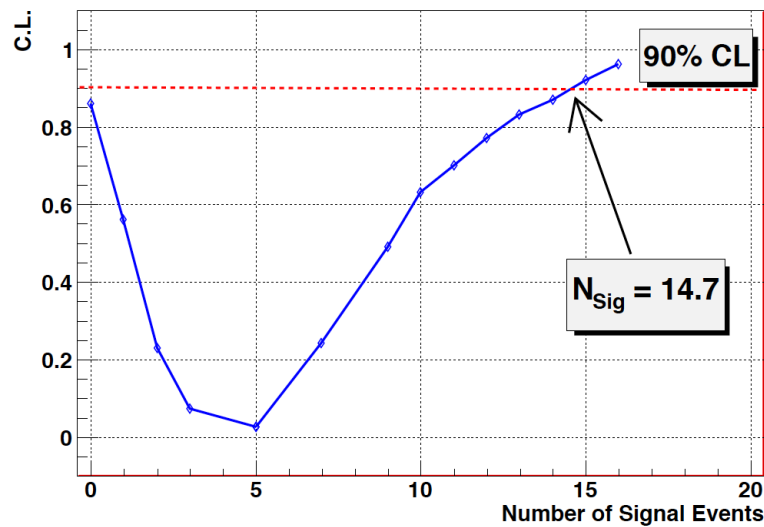


**Figure 7.7:** Confidence level as a function of the expected number of signal events.

- positron angular resolution ( $\Delta N_{SIG}=1.2$ ).

The upper limit on  $\mu^+ \rightarrow e^+\gamma$  branching ratio is then calculated with the technique explained in sec. 7.4. Thus, we finally obtain:

$$BR(\mu^+ \rightarrow e^+\gamma) \leq \frac{N_{SIG}}{k} = \frac{14.7}{5.2 \times 10^{11}} = 2.8 \times 10^{-11} \quad (90\% \text{ C.L.}) \quad (7.12)$$

This result is very close the current best estimation for the upper limit on  $\text{BR}(\mu^+ \rightarrow e^+\gamma)$  set by the MEGA experiment, and show how, starting from the analysis of the 2009 and 2010 data that is currently on going, MEG can really explore new frontiers in the Lepton Flavour Violation physics.

## Conclusions

The MEG experiment has started the physics data acquisition in 2008, looking for the  $\mu \rightarrow e\gamma$  decay. As shown in the final chapter of this thesis, the first published data (related to the 2008 physics run) show the possibility to reach the expected sensitivity on the  $\text{BR}(\mu \rightarrow e\gamma)$ , thus confirming MEG as a cutting edge experiment in the particle physics framework, with remarkable possibility to make a discovery in fundamental physics. The 2009 and 2010 data are currently under analysis, and will give really important indications about the  $\text{BR}(\mu \rightarrow e\gamma)$ .

The good results of MEG follow from the development of a dedicated experimental apparatus, able to measure the kinematic variables that define the  $\mu \rightarrow e\gamma$  with extreme high resolutions, in order to have a reliable background rejection, needed to explore such a little Branching Ratio.

In particular, in this thesis I showed the development, the calibrations and the operations of the Timing Counter detector, which is devoted to the positron timing and impact positron measurement. The detector, split in two sub-detector each realizing different tasks, had long stable operations during the whole data acquisition time, showing performances very close to the expected one.

The achieved time resolution on the positron timing was found to be  $\sigma_t \simeq 60$  ps. This results in an overall  $e^+\text{-}\gamma$  timing resolution  $\sigma(t_{e\gamma}) = 150$  ps, considering the contributions coming from Timing Counter and LXe detector, and particles time-of-flight reconstruction.

The position reconstruction obtained using longitudinal detector shows a resolution  $1.0$  cm  $\leq \sigma_Z \leq 1.5$  cm. The impact point reconstruction with the transverse detector has a slightly worse performances,  $\sigma_Z = 1.6$  cm or  $\sigma_Z = 2.5$  cm, respectively for the down- and up-stream TC module.



# Appendix A

## Background

### A.1 Physics background

The most important physics background to the  $\mu^+ \rightarrow e^+\gamma$  searching is given by the muon radiative decay  $\mu^+ \rightarrow e^+\nu_e\bar{\nu}_\mu$  (BR=1.4% for  $E_\gamma \geq 10 \text{ MeV}$ ), when  $e^+$  and  $\gamma$  are emitted nearly in opposite direction with neutrinos carrying off a negligible amount of energy, thus mimicking a signal event. The differential decay width of this decay has been calculated as a function of the positron and gamma energy,  $E_e$  and  $E_\gamma$  respectively, normalized to the maximum allowed energy, namely  $x = 2E_e/m_\mu$  and  $y = 2E_\gamma/m_\mu$  [77] [78].

The ranges of  $x$  and  $y$  are the following:

$$2\sqrt{r} < x < 1 + r \quad \text{for} \quad 0 < y \leq 1 - \sqrt{r}, \quad (\text{A.1})$$

$$(1 - y) + \frac{r}{(1 - y)} \leq x \leq 1 + r \quad \text{for} \quad 1 - \sqrt{r} < y \leq 1 - r, \quad (\text{A.2})$$

where  $r = (m_e/m_\mu)^2$ .

The kinematic case when  $x \simeq 1$  and  $y \simeq$  is the critical one as background for  $\mu^+ \rightarrow e^+\gamma$  searching. The spectrum of photons from radiative decay was already shown in fig.1.10.

In an approximation of the limit of  $x \simeq 1$  and  $y \simeq$ , with opening angle between  $e^+$  and  $\gamma$  trajectories  $\theta_{e\gamma} \simeq 180^\circ$ , the differential decay width of radiative decay is given by [79]:

$$d\Gamma(\mu^+ \rightarrow e^+\nu\bar{\nu}\gamma) \simeq \frac{G_F^2 m_\mu^5 \alpha}{768\pi^4} \times \left[ (1 - x)^2(1 - P_\mu \cos\theta_e) + \left( 4(1 - x)(1 - y) - \frac{1}{2}z^2 \right) (1 + P_\mu \cos\theta_e) \right] dx dy dz d(\cos\theta_e) \quad (\text{A.3})$$

where  $\theta_e$  is the angle between the muon spin and the  $e^+$  momentum direction,  $G_F$  is the Fermi coupling constant,  $\alpha$  is the fine-structure constant,  $z = \pi - \theta_{e\gamma}$ , and  $\cos z$  is expanded in a polynomial of  $z$ , being  $z$  small; only the terms up to the second order are kept. Moreover, in the case  $x \simeq 1$  and  $y \simeq$ , the effect of the  $e^+$  mass is found to be negligible (order of  $(m_e/m_\mu)^2$ ), and therefore it is omitted. When  $x = 1$  and  $y =$  this differential decay vanishes. However, in a real experiment, the finite detector resolutions introduce background events which would ultimately limit the sensitivity of a search for  $\mu^+ \rightarrow e^+ \gamma$ .

Having defined the detector resolution, the sensitivity limitation from the radiative decay background can be estimated by an integration of the differential decay width over the kinematic signal box, normalized to the total muon decay width:

$$\begin{aligned} dB(\mu^+ \rightarrow e^+ \nu \bar{\nu} \gamma) &= \\ \frac{1}{\Gamma(\mu^+ \rightarrow e^+ \nu \bar{\nu})} &\int_{1-\delta x}^1 dx \int_{1-\delta y}^1 dy \int_0^{\min(\delta z, 2\sqrt{(1-x)(1-y)})} dz \frac{d\Gamma(\mu^+ \rightarrow e^+ \nu \bar{\nu} \gamma)}{dx dy dz} = \\ &= \frac{\alpha}{16\pi} [J_1 + J_2] d(\cos\theta_e) \end{aligned} \quad (\text{A.4})$$

where  $\delta x$ ,  $\delta y$  and  $\delta z$  represent half width of the  $\mu^+ \rightarrow e^+ \gamma$  signal region for  $x$ ,  $y$  and  $z$  respectively;  $\Gamma(\mu^+ \rightarrow e^+ \gamma)$  is the total muon decay width. I have consider here only unpolarized muons, as the MEG case.  $J_1$  and  $J_2$  are given by:

$$J_1 = (\delta x)^4 (\delta x)^2, \quad J_2 = \frac{8}{3} (\delta x)^3 (\delta y)^3, \quad (\text{A.5})$$

in the case  $\delta z > 2\sqrt{\delta x \delta y}$ , or

$$\begin{aligned} J_1 &= \frac{8}{3} (\delta x)^3 (\delta y) \left(\frac{\delta z}{2}\right)^2 - 2(\delta x)^2 \left(\frac{\delta z}{2}\right)^4 + \frac{1}{3} \frac{1}{(\delta y)^2} \left(\frac{\delta z}{2}\right)^8 \\ J_2 &= 8(\delta x)^2 (\delta y)^2 \left(\frac{\delta z}{2}\right)^2 - 8(\delta x) (\delta y) \left(\frac{\delta z}{2}\right)^4 + \frac{8}{3} \left(\frac{\delta z}{2}\right)^6, \end{aligned} \quad (\text{A.6})$$

if  $\delta z < 2\sqrt{\delta x \delta y}$ .

## A.2 Accidental background

Increasing the muon decay rate under observation, the accidental background becomes more important than the physical one. This is the case of the present  $\mu^+ \rightarrow e^+ + \gamma$  search experiment. The accidental event rate normalized to the total decay rate ( $B_{acc}$ ) can be estimated as [24]:

$$B_{acc} = R_\mu \cdot f_e^0 f_\gamma^0 \Delta t_{e\gamma} \left( \frac{\Delta \Omega_{e\gamma}}{4\pi} \right), \quad (\text{A.7})$$

where  $R_\mu$  is the instantaneous muon rate,  $f_e^0$  and  $f_\gamma^0$  are, respectively, the integrated  $e^+$  and  $\gamma$  spectra in the energy signal window. They include their corresponding branching ratios.  $\Delta t_{e\gamma}$  and  $\Delta\Omega_{e\gamma}$  are, respectively, the full widths of relative timing and angles between  $e^+$  and  $\gamma$  close to the expected value dictated by the kinematic constraints.  $\Delta t_{e\gamma}$  and  $\Delta\Omega_{e\gamma}$  are determined by the detector resolution functions.

Given the experimental limits to the size of the signal window,  $B_{acc}$  can be evaluated. Let us take  $\delta x$ ,  $\delta y$ ,  $\delta\theta_{e\gamma}$  and  $\delta t_{e\gamma}$  to be the half width of the signal window for  $e^+$  and  $\gamma$  energy, angle  $\theta_{e\gamma}$ , and relative timing between  $e^+$  and  $\gamma$ , respectively. In this case  $f_e^0$  can be estimated by integrating the Michel spectrum over  $1 - \delta x < x < 1$ , yielding  $f_e^0 \simeq 2(\delta x)$ . Given the angular resolution,  $\delta\theta_{e\gamma}$ , the back-to-back resolution  $\frac{\Delta\Omega_{e\gamma}}{4\pi}$  is represented by  $\frac{\Delta\Omega_{e\gamma}}{4\pi} = \frac{\delta\theta_{e\gamma}^2}{4}$ .

$f_\gamma^0$  is related to the radiative muon decay  $\mu^+ \rightarrow e^+ \nu_e \bar{\nu}_\mu \gamma$  or to  $e^+$  annihilation in flight from the normal muon decay  $\mu^+ \rightarrow e^+ \nu_e \bar{\nu}_\mu$ . As an example, in the first case, the differential branching ratio must be integrated over  $2\pi$  for  $\theta_{e\gamma}$ , and then over the  $\gamma$  energy within the width of the signal region ( $1 - \delta y < y < 1$ ). For unpolarized muons, one obtains:

$$f_\gamma^0 = \int_{1-\delta y}^1 dy \int d(\cos\theta_\gamma) \frac{dB(\mu^+ \rightarrow e^+ \nu \bar{\nu} \gamma)}{dy d(\cos\theta_\gamma)} \simeq \left(\frac{\alpha}{2\pi}\right) (\delta y)^2 [\ln(\delta y) + 7.33]. \quad (\text{A.8})$$

From eq.A.2 one can deduce that  $f_\gamma^0$  for  $\mu^+ \rightarrow e^+ \nu_e \bar{\nu}_\mu \gamma$  is roughly proportional to  $(\delta y)^2$ .

From the above, the effective branching ratio of accidental background is given by:

$$B_{acc} = R_\mu \cdot (2\delta x) \cdot \left[ \frac{\alpha}{2\pi} (\delta y)^2 (\ln(\delta y) + 7.33) \right] \cdot \left( \frac{\delta\theta^2}{4} \right) \cdot (2\delta t) \quad (\text{A.9})$$



# Bibliography

- [1] M. E. Peskin and D. V. Schroeder, *An Introduction to Quantum Field Theory*, Westview Press, 1995.
- [2] C. M. Becchi and G. Ridolfi, *An introduction to relativistic processes and the standard model of electroweak interaction*, Springer, 2006.
- [3] L. B. Okun, *Leptons and Quarks*, North-Holland Company, 1982.
- [4] Y. Nir, Neutrinos in particle physics, Lectures given at ISAPP, 2003.
- [5] R. R. Crittenden *et al.*, *Radiative Decay Modes of the Muon*, Phys. Rev. 121, 1823 (1961).
- [6] W. Bertl *et al.*, [SINDRUM Collaboration], *Search for the decay  $\mu^+ \rightarrow e^+e^+e^-$* , Nucl. Phys. B 260, 1 (1985).
- [7] S. J. Freedman *et al.*, *Limits on neutrino oscillations from  $\bar{\nu}_e$  appearance*, Phys. Rev. D 47, 811 (1993).
- [8] M. L. Brooks *et al.*, [MEGA Collaboration], *New Limit for the Lepton-Family-Number Nonconserving Decay  $\mu^+ \rightarrow e^+\gamma$* , Phys. Rev. Lett. 83, 1521 (1999).
- [9] U. Bellgardt *et al.*, *Search for the decay  $\mu^+ \rightarrow e^+e^+e^-$* , Nucl. Phys. B 299, 1 (1988).
- [10] R. D. Bolton *et al.*, *Search for rare muon decays with the Crystal Box detector*, Phys. Rev. D 38, 2077 (1988).
- [11] Y. Suzuki, [SuperKamiokande Collaboration], *Neutrino oscillations at Super-Kamiokande*, Nucl. Phys. Proc. Suppl. 81, 33 (2000).
- [12] M. Apollonio *et al.*, [CHOOZ Collaboration], *Search for neutrino oscillations on a long base-line at the CHOOZ nuclear power station*, Eur. Phys. J. C27, 331 (2003) [arXiv:hep-ex/0301017].
- [13] E. Kh. Akhmedov, *Neutrino physics*, (2000) [arXiv:hep-ph/0001264v2].
- [14] F. Bohem and P. Vogel, *Physics of massive neutrinos*, Cambridge University Press, (1992).

- [15] A. Masiero *et al.*, *Flavour Physics and Grand Unification*, (2007) [arXiv:0711.2903v1].
- [16] G. Giacomelli *et al.*, [MACRO Collaboration], *MACRO results on atmospheric neutrinos*, Eur. Phys. J. C36, 323 (2004).
- [17] Q. R. Ahmad *et al.*, [SNO Collaboration], *Measurement of the rate of  $\nu_e + d \rightarrow p + p + e^-$  interactions produced by  $^8B$  solar neutrinos at the Sudbury Neutrino Observatory*, Phys. Rev. Lett. 87, 071301 (2001) [arXiv:nucl-ex/0106015v2].
- [18] H. Georgi and S. L. Glashow, *Unity of all elementary-particle forces*, Phys. Rev. Lett. 32, 438 (1974).
- [19] H. Fritzsch and P. Minkowski, *Ordinary predictions from grand principles:  $t$ -quark mass in  $O(10)$* , Ann. Phys 93, 193 (1975).
- [20] H. Georgi and D. V. Nanopoulos, *Unified interaction of leptons and hadrons*, Nucl. Phys. B 155, 52 (1979).
- [21] R. Barbieri and L. J. Hall, *Signals for supersymmetric unification*, Phys. Letter B 338, 212 (1994).
- [22] R. Barbieri, L. J. Hall and A. Strumia, *Violations of lepton flavour and CP in supersymmetric unified theories*, Nucl. Phys. B 445, 219 (1995)
- [23] R. Barbieri, L. J. Hall and A. Strumia, *Hadronic flavor and CP-violating signals of superunification* Nucl. Phys. B 449, 437 (1995).
- [24] Y. Kuno and Y. Okada, *Muon decay and physics beyond the Standard Model*, Rev. Mod. Phys. 73, 151 (2001).
- [25] K. Nakamura *et al.*, [Particle Data Group], *Review of Particle Physics*, J. Phys 37, (2010). <http://pdg.lbl.gov/>
- [26] P. Depommier *et al.*, *New limit in the Decay  $\mu^+ \rightarrow e^+\gamma$* , Phys. Rev. Lett. 39, 1113 (1977).
- [27] A. van der Schaaf *et al.*, *A search for the decay  $\mu^+ \rightarrow e^+\gamma$* , Nucl. Phys. A 340, 1113 (1977).
- [28] W. W. Kinnison *et al.*, *A search for  $\mu^+ \rightarrow e^+\gamma$* , Phys. Rev. Lett. 56, 2461 (1986).
- [29] T. Mori *et al.*, *Search for  $\mu^+ \rightarrow e^+\gamma$  down to  $10^{-14}$  branching ratio* (Research proposal to Paul Scherrer Institute), [http://meg.web.psi.ch/docs/prop\\_psi/proposal.pdf](http://meg.web.psi.ch/docs/prop_psi/proposal.pdf)

- [30] A. Baldini, T. Mori *et al.*, *The MEG experiment: search for the  $\mu^+ \rightarrow e^+\gamma$  decay at PSI* (Research proposal to INFN), [http://meg.web.psi.ch/docs/prop\\_inf/nproposal.pdf](http://meg.web.psi.ch/docs/prop_inf/nproposal.pdf)
- [31] A. E. Pifer *et al.*, *A high stopping density beam*, Nucl. Instrum. and Meth. 135, 39 (1976).
- [32] H-W. Reist *et al.*, *Development of a low momentum surface muon beam for LAMPF*, Nucl. Instrum. and Meth. 153, 61 (1978).
- [33] PSI Graphic Transport Framework by U. Rohrer based on a CERN-SLAC-FERMILAB version by K.L. Brown *et al.*
- [34] PSI Graphic Turtle Framework by U. Rohrer based on a CERN-SLAC-FERMILAB version by K.L. Brown *et al.*
- [35] W. Ootani *et al.*, *Development of a Thin-wall Superconducting Magnet for the Positron Spectrometer in the MEG Experiment*, IEEE Trans. Appl. Superconductivity 14, 568 (2005).
- [36] H. Nishiguchi, *The MEG positron spectrometer*, Nucl. Instrum. and Meth. A 581, 538 (2007).
- [37] H. Nishiguchi, *An Innovative Positron Spectrometer to Search for the Lepton Flavour Violating Muon Decay with a Sensitivity of  $10^{-13}$* , PhD Thesis (2008).
- [38] J. Allison *et al.*, *The diamond shaped cathode pads of the OPAL muon barrel drift chambers*, Nucl. Instrum. and Meth. A 310, 527 (1991).
- [39] A. Baldini *et al.*, *Liquid Xe scintillation calorimetry and Xe optical properties*, IEEE Trans. Dielectr. Electr. Insul. 13, 547 (2006).
- [40] G. Signorelli, *A sensitive search for lepton-flavour violation: the MEG experiment and the new LXe calorimetry*, PhD Thesis, (2002).
- [41] A. Papa, *Search for the Lepton Flavour Violation in  $\mu \rightarrow e\gamma$ . The calibration methods for the MEG experiment*, PhD Thesis, (2009)
- [42] S. Mihara *et al.*, *Development of a method for liquid xenon purification using a cryogenic centrifugal pump*, Cryogenics 46, 688 (2006).
- [43] L. Galli, *An FPGA-based trigger for the search of  $\mu^+ \rightarrow e^+\gamma$  decay in the MEG experiment*, IEEE Nuclear Science Symposium Conference Record (2008).
- [44] L. Galli, *An FPGA-based trigger for the search of  $\mu^+ \rightarrow e^+\gamma$  decay in the MEG experiment*, IEEE Nuclear Science Symposium Conference Record (2008).

- [45] L. Galli, *A real time glance at the Lepton Flavor Violating decay  $\mu \rightarrow e\gamma$  in the MEG experiment*, PhD Thesis (2010).
- [46] S. Ritt, *The DRS chip: cheap waveform digitizing in the GHz range*, *nucl. Instrum. and Meth. A* 518, 470 (2004)
- [47] S. Ritt *et al.*, *Application of the DRS chip for fast waveform digitizing*, *Nucl. Instrum. and Meth. A* 623, 486 (2010).
- [48] S. Dussoni, *Search for Lepton Flavour Violation: the MEG experiment*, PhD Thesis (2006).
- [49] R. Valle, *Development of the Timing Counter of the MEG experiment*, PhD Thesis (2006).
- [50] S. Dussoni *et al.*, *The Timing Counter of the MEG experiment: Design and commissioning*, *Nucl. Instrum. and Meth. A* 617, 387 (2010).
- [51] M. De Gerone, *The Timing Counter of the MEG experiment: Design and commissioning*, *IEEE Nuclear Science Symposium Conference Record* (2010).
- [52] M. De Gerone *et al.*, *The MEG timing counter calibration and performance*, in press on *Nucl. Instrum. and Meth* (doi:10.1016/j.nima.2011.02.044).
- [53] G. F. Knoll, *Radiation detection and measurement*, John Wiley & Sons (2010).
- [54] W. R. Leo, *Techniques for Nuclear and Particle Physics Experiments*, Springer-Verlag (1994).
- [55] [http://sales.hamamatsu.com/assets/pdf/catsandguides/PMT\\_handbook\\_v3aE.pdf](http://sales.hamamatsu.com/assets/pdf/catsandguides/PMT_handbook_v3aE.pdf)
- [56] <http://sales.hamamatsu.com/index.php?id=13189480&language=1&undefined>
- [57] M. Bonesini *et al.*, *A systematic study to characterize fine-mesh PMTs in high magnetic fields* 572, 465 (2007).
- [58] [http://www.detectors.saint-gobain.com/uploadedFiles/SGdetectors/Documents/Product\\_Data\\_Sheet/BC400-404-408-412-416-Data-Sheet.pdf](http://www.detectors.saint-gobain.com/uploadedFiles/SGdetectors/Documents/Product_Data_Sheet/BC400-404-408-412-416-Data-Sheet.pdf)
- [59] Y. Uchiyama, *Analysis of the First MEG Physics Data to Search for the Decay  $\mu^+ \rightarrow e^+\gamma$* , PhD Thesis, (2009).
- [60] M. De Gerone, *Sviluppo del rivelatore a fibre scintillanti per l'esperimento MEG*, Master Thesis (in italian).

- [61] M. De Gerone *et al.*, *Development and characterization of scintillating fiber-APD based detector*, Nucl. Instrum. and Meth. A 610, 218 (2009).
- [62] <http://sales.hamamatsu.com/en/products/solid-state-division/si-photodiode-series/si-apd/part-s8664-55.php>
- [63] J. Marler *et al.*, *Studies of avalanche photodiode performance in high magnetic field*, Nucl. Instrum. and Meth. A 449, 311 (2000).
- [64] K. G. McKay and K. B. McAfee, *Electron multiplication in Silicon and Germanium*, Phys. Rev. 91, 1079 (1953).
- [65] K. Deiters *et al.*, *Properties of most recent avalanche photodiodes for the CMS electromagnetic calorimeter*, Nucl. Instrum. and Meth. A 442, 193 (2000)
- [66] [http://sales.hamamatsu.com/assets/applications/SSD/Characteristics\\_and\\_use\\_of\\_SI\\_APD.pdf](http://sales.hamamatsu.com/assets/applications/SSD/Characteristics_and_use_of_SI_APD.pdf)
- [67] K. G. McKay, *Avalanche breakdown in Silicon*, Phys. Rev. 94, 877 (1954).
- [68] I. Tapan *et al.*, *Avalanche photodiode as proportional particle detectors*, Nucl. Instrum. and Meth. A 388, 79 (1997).
- [69] J. Ch. Vanel *et al.*, *Characterization of avalanche photodiode for calorimetry applications*, Nucl. Instrum. and Meth. A 428, 413 (1999).
- [70] <http://www.detectors.saint-gobain.com/fibers.aspx>
- [71] W. R. Binns *et al.*, *Scintillator-fiber charged-particle track-imaging detector*, Nucl. Instrum. and Meth. A 216, 475 (1983).
- [72] N. A. Amos *et al.*, *Optical attenuation length measurement of scintillating fibers*, Nucl. Instrum. and Meth. A 297, 396 (1990).
- [73] <http://www.tina.com/English/tina/>
- [74] J. Adam *et al.*, [MEG Collaboration], *A limit for the  $\mu \rightarrow e\gamma$  decay from the MEG experiment*, Nucl. Phys. B 834, 1 (2010).
- [75] W. Molzon, *MEG Branching Fraction Measurement Normalization*, MEG Technical Note No.47.
- [76] G. J. Feldman and R. D. Cousins, *Unified approach to the classical statistical analysis of small signals*, Phys. Rev. D 57, 3873 (1998).
- [77] C. Fronsdal and H. Uberall,  *$\mu$ -meson Decay with Inner Bremsstrahlung*, Phys. Rev. 113, 654 (1959).

- [78] S. G. Eckstein and R. H. Pratt, *Radiative muon decay*, Ann. of Phys. 8, 297 (1959).
- [79] Y. Kuno and Y. Okada, *Proposed  $\mu \rightarrow e\gamma$  with polarized muons*, Phys. Rev. Lett. 77, 434 (1996).

# List of Figures

1.1	Feynman diagrams for the $\mu^+ \rightarrow e^+\gamma$ decay in the Standard Model including massive neutrinos. . . . .	11
1.2	Radiative corrections to the Higgs boson mass. . . . .	15
1.3	Cancellation of quadratic terms (divergencies) in Supersymmetric framework. . . . .	16
1.4	Feynman diagrams for the $\mu^+ \rightarrow e^+ + \gamma$ decay in $SU(5)$ SUSY GUT. The closed lines represent the flavor transitions due to the off-diagonal terms of the slepton mass matrices. . . . .	17
1.5	Feynman diagrams in $SO(10)$ SUSY GUT which gave dominant contributions to the $\mu^+ \rightarrow e^+ + \gamma$ process. $(m_{\tilde{\tau}}^2)_{RL}$ and $(m_{\tilde{\tau}}^2)_{LR}$ are proportional to $m_{\tilde{\tau}}$ . . . . .	17
1.6	Predicted branching ratios for the $\mu^+ \rightarrow e^+\gamma$ decay in the $SU(5)$ SUSY GUT based on the minimal supergravity model as a function of the right-handed slepton mass for four different sets of the SUSY input parameters of $M_2$ (the $SU(2)$ gaugino mass) and $\tan\beta$ (the ratio of the two Higgs vacuum expectation values) [24]. . . . .	18
1.7	Predicted branching ratios for $\mu^+ \rightarrow e^+\gamma$ decay in the $SO(10)$ SUSY GUT model [24]. The input parameters are the same as fig. 1.6. . . . .	19
1.8	Scaled $BR(\mu^+ \rightarrow e^+\gamma)$ vs. $M_{1/2}$ . The plots are obtained by scanning the LHC accessible SUSY-GUT parameter space at fixed values of $\tan\beta$ [24]. The horizontal lines are the present (MEGA) and the future (MEG) experimental sensitivities. Note that MEG will test the PMNS case and, for high $\tan\beta$ , constrain the CKM one. . . . .	20
1.9	$\mu^+ \rightarrow e^+\gamma$ event signature. . . . .	21
1.10	Differential branching ratio of the $\mu^+ \rightarrow e^+\nu_e\bar{\nu}_\mu\gamma$ decay as a function of the photon energy ( $y = 2E_\gamma/m_\mu$ ). This branching ratio is obtained by integrating over the $e^+$ energy and the angle between an $e^+$ and a photon. . . . .	22
1.11	Effective branching ratio of the physics background from the $\mu^+ \rightarrow e^+\nu\bar{\nu}\gamma$ decay as a function of the $e^+$ energy resolution ( $\delta x$ ) and photon energy resolution ( $\delta y$ ). . . . .	23
1.12	Integrated rates of backgrounds from annihilation-in-flight (dotted line) and radiative muon decay (dashed line) as a function of the photon energy. The sum of the two is shown by a solid line. . . . .	23

1.13	The improvement of the 90% C.L. upper limit on the $\mu^+ \rightarrow e^+\gamma$ decay branching ratio as a function of the time. . . . .	25
1.14	Layout of the MEGA experiment [8]. . . . .	26
2.1	Side and front view of the MEG experiment detector layout. The coordinates systems used in the experiment are also shown. . . . .	28
2.2	Picture of the Paul Scherrer Institute 590 MeV proton cyclotron. . . . .	29
2.3	Schematic view of the MEG beam line configuration. . . . .	32
2.4	Muon - electron separation in MEG muon beam, after crossing electrostatic separator. . . . .	33
2.5	Picture of the MEG target. The holes on the surface are used for testing the reconstruction algorithm of drift chamber system, and to extract the muon decay vertex resolution. . . . .	33
2.6	The COBRA magnet. . . . .	34
2.7	Schematic draw of the COBRA magnet. . . . .	34
2.8	COBRA magnetic field map. Note how the compensation coils act to reduce field intensity in the calorimeter region. . . . .	35
2.9	Magnetic field intensity as a function of the distance from the COBRA center. . . . .	36
2.10	Rate of Michel positron as a function of the distance from COBRA axis. . . . .	36
2.11	Behavior of particle in an uniform solenoidal magnetic field: (a) trajectory made by a positron emitted at $88^\circ$ respect to the beam axis; (b) trajectories of monochromatic positrons emitted at different angles. . . . .	37
2.12	Advantages for a quasi-solenoidal magnetic field with gradient along beam axis direction: (c) trajectory made by a positron emitted at $88^\circ$ respect to the beam axis; the positron is faster extracted from the DC region; (d) trajectories of monochromatic positrons emitted at different angles. The bending radius results to be independent from emission angle. . . . .	37
2.13	Schematic representation of the drift chambers layout. . . . .	38
2.14	Schematic view of a single drift chamber. . . . .	39
2.15	Picture of a chamber wall. The aluminum deposition is shaped in such way to obtain a particular triangular pattern known as Vernier Pad. . . . .	39
2.16	Drift chamber section and hit reconstruction. . . . .	40
2.17	Picture of the downstream Timing Counter module in front of the COBRA magnet. . . . .	41
2.18	Schematic side view of the Liquid Xenon calorimeter. . . . .	42
2.19	(left) Picture of the cryostat vessel; (right) Picture of the cryostat inside. . . . .	43
2.20	Example of reconstructed event in the Liquid Xenon calorimeter. . . . .	44

2.21	The structure of the trigger system: the two board types are used for the $\gamma$ calorimeter and for the positron tracker. The boards are arranged in a tree-like structure. . . . .	45
2.22	A simplified layout of the Domino Ring Sampler chip. . . . .	47
2.23	Schematic representation of the Data Acquisition System of the MEG experiment. . . . .	47
3.1	Picture of Timing Counter with bar exposed. . . . .	50
3.2	Picture of a Timing Counter bar inside the plastic socket before surface polishing and black painting of the socket. Note the particular shape of the bar section, made in order to optimize the particle trajectories inside the scintillator. . . . .	51
3.3	Definitions of the quantities involved in positron timing. See text for details. . . . .	52
3.4	Sketch of the definitions of the angles $\beta$ ( <i>a</i> ) and $\alpha$ ( <i>b</i> ); $\mathbf{n}$ is the normal to the bar surface. See text for details. . . . .	55
3.5	( <i>up</i> ) Fine mesh dynode layout; ( <i>down</i> ) schematic of HAMAMATSU R5924 PMTs [56]. . . . .	57
3.6	Particular of the PMT displacement with respect to the end of the scintillator bar. The mechanical constraints from COBRA magnet profile and Drift Chamber structure are also shown. . . . .	58
3.7	PMT gain in magnetic field normalized to “null” field gain, as a function of magnetic field intensity measured for different angle between PMT axis and magnetic field lines. . . . .	59
3.8	TTS normalized to “null” field TTS, for a PMT in magnetic field as a function of field intensity, measured for different angle between PMT axis and magnetic field lines. . . . .	59
3.9	Behaviour of the PMT time resolution in magnetic field, as a function of magnetic field intensity for different angles between PMT axis and magnetic field lines. . . . .	60
3.10	Track length distributions inside timing counter bar for michel positron . . . . .	61
3.11	TC bar geometry: ( <i>up</i> ) side view. The cut shape of each end side is optimized to obtain the best tilt angle between PMT axis and magnetic field lines; ( <i>down</i> ) section view. The edges of the bar were shaped in such a way to satisfy the mechanical constraints, together a bar rotation along its major axis. . . . .	62
3.12	Monte Carlo simulation of the impact angle between the projection of the positron track on the $x - y$ plane and the normal to the surface of the bar, $\alpha^*$ . . . . .	63
3.13	Monte Carlo simulation of the impact angle between the projection of the positron track on the $z - y$ plane and the normal to the surface of the bar, $\beta$ . . . . .	63
3.14	Schematic representation of the Timing Counter electronic readout chain. . . . .	64

3.15	Timing counter signals: in red the Double Threshold Discriminator output with the template fit superimposed (black), in blue the analog signal digitized by the DRS. . . . .	65
3.16	Time resolution as a function of impact point position and bar number achieved during the beam test at the Beam Test Facility of Frascati. . . . .	66
4.1	Picture of the Timing Counter with scintillating fiber exposed. . . .	68
4.2	Schematic draw of the multiplication process inside the APD [62]. . .	70
4.3	Schematic draw of HAMAMATSU S8664-55 APD [62]. . . . .	71
4.4	Wiring diagram of the APD breakdown voltage measurement. . . .	72
4.5	Breakdown voltage as a function of temperature, with linear fit superimposed. . . . .	72
4.6	Schematic representation of the two components that characterized the dark current inside an avalanche photodiode (from HAMAMATSU). . . . .	73
4.7	Dark current behaviour as a function of bias voltage, for different working temperatures. . . . .	74
4.8	Sketch of the apparatus used to measure the APD gain. . . . .	75
4.9	APD gain as a function of applied voltage, close to the breakdown point, with exponential fit superimposed. . . . .	77
4.10	Sketch of the experimental setup used in the measurement of the scintillating fibers attenuation length. . . . .	79
4.11	Fiber attenuation length measurement. a) Single exponential fit. b) Double exponential fit. . . . .	80
4.12	Measured fiber emission spectrum. . . . .	81
4.13	Section of transverse detector, highlighting the two different profiles of scintillating fibers end. . . . .	81
4.14	a) Comparison between the performances of the curved fiber with coats under test and the straight fiber. b) Comparison between the coated fiber transport efficiency, normalized to the efficiency of the straight fiber. . . . .	82
4.15	Details of the scintillating fiber with covered surface. . . . .	83
4.16	Comparison between the performances of the covered fibers respect to the naked ones, being the detector bias voltage fixed and varying the distance between source and detector. . . . .	84
4.17	Comparison between the performances of the covered fibers respect to the naked ones, being the detector-source distance fixed and varying the APD bias voltage. . . . .	85
4.18	Wiring diagram of the single channel APD analog signal amplifier. . .	86
4.19	Schematics of a single APD amplifier. . . . .	87
4.20	Bode gain plot of a single channel APD analog signal amplifier. . .	88
4.21	Equivalent circuit for amplifier noise study. . . . .	88
4.22	APD signal as a function of the positron impact point along the fiber. .	90

4.23	Analog signal from 2 FE summed up together (equivalent to 16 APDs), as acquired by the trigger system as a function of the FE applied HV: ( <i>up</i> ) nominal HV value (3 V under BD point); ( <i>centre</i> ) nominal HV value increased by 1 V; ( <i>down</i> ) nominal HV value increased by 2 V. . . . .	91
4.24	Plot of the $\Delta Z = Z_{fiber} - Z_{bar}$ distributions for upstream (green) and downstream (red) Timing Counter sectors. . . . .	92
4.25	Sketch of the TRG type used for determination of APD system efficiency (TRG24, see text for details). . . . .	93
5.1	Pulse spectra for different PMTs with Landau fit superimposed. The amplitude equalization is achieved within 10%. . . . .	96
5.2	Example of charge Landau distribution with fit superimposed. . . . .	97
5.3	Summary of the fitted Landau peak. . . . .	98
5.4	Time walk effect . . . . .	99
5.5	Time vs amplitude with time walk correction with fit superimposed. . . . .	99
5.6	Comparison between the time difference distributions for two adjacent bars; the red line represents uncalibrated data, the black line represents the calibrated ones. . . . .	100
5.7	Comparison between the resolution obtained on double sample using calibrated (black markers) and uncalibrated (red markers) . . . . .	101
5.8	Comparison between the resolutions obtained on double sample using TW calibrated data, with two different values of the low level threshold: 10 mV (red markers) and 25 mV (black markers). The best results were achieved using 25 mV as LLT. . . . .	102
5.9	Plot of the difference between the inverted template waveform and the time calculated by means of eq. 5.2. . . . .	103
5.10	$\Delta t$ distribution for cosmic rays events with fit superimposed. . . . .	104
5.11	Comparison between uncalibrated (upper panel) and calibrated (lower panel) cosmic rays hitmaps. . . . .	105
5.12	Comparison between uncalibrated (upper panel) and calibrated (lower panel) Michel events hitmaps. The offsets used here are the same calculated for fig. 5.11 . . . . .	106
5.13	Comparison between calibrated (red markers) and uncalibrated (black markers) bar offsets, calculated on cosmic rays sample. . . . .	107
5.14	Example of $z_{dc} - z_{tc}$ distribution evaluated on Michel data, with gaussian fit superimposed. The mean of the distribution correspond to the offset of the bar. . . . .	108
5.15	Comparison between offset calculated using cosmic rays data (black markers) and Michel data (red markers). . . . .	109
5.16	High level threshold efficiency. . . . .	110
5.17	Sketch of the experimental layout in the Boron events. . . . .	111
5.18	$\gamma$ energy spectrum for Boron events. The peaks at 4.4 MeV and 11.7 MeV are clearly recognizable. . . . .	111
5.19	Example of $t_{\gamma\gamma}$ distribution. . . . .	112

5.20	Mean of $t_{\gamma\gamma}$ distributions as a function of bar number. . . . .	112
5.21	$t_{\gamma\gamma}$ offsets as a function of bar number, referred to the bar number 20. . . . .	113
5.22	Comparison between the mean of $t_{\gamma\gamma}$ distributions for calibrated (red markers) and uncalibrated (black markers) data samples. . . . .	113
5.23	Timing resolution measured on Boron sample. The data were divided in two samples, cutting on the gamma energy reconstructed by the calorimeter. The resolution shows a strong correlation with gamma energy, as one can expect from LXe characteristics. . . . .	114
5.24	Sketch of the Dalitz decay sample. . . . .	115
5.25	Dalitz decay events hitmap. . . . .	116
5.26	Offset calculated on Dalitz sample. . . . .	116
6.1	A triple bars cluster . . . . .	117
6.2	Distribution of bar multiplicity in Timing Counter clusters. . . . .	118
6.3	Plot of the time difference distribution for double events sample, with single gaussian fit superimposed. The estimated resolution results to be $\sigma = 103$ ps. . . . .	119
6.4	Plot of the time difference distribution for double events sample, with gaussian + order 2 polynomial fit superimposed. The estimated resolution increases respect to fig.6.3 and results to be $\sigma = 85$ ps. . . . .	120
6.5	Summary of the time resolutions obtained on double sample, with two different fit functions: single gaussian (red markers) and gaussian + order 2 polynomial (black markers). . . . .	121
6.6	Summary of the time resolutions obtained on triple sample, with two different fit functions: single gaussian (red markers) and gaussian + order 2 polynomial (black markers). . . . .	121
6.7	Summary of the time resolutions obtained during 2010 run, evaluated on double bars sample. . . . .	122
6.8	Summary of the time resolutions obtained during 2010 run, evaluated on triple bars sample. . . . .	122
6.9	Resolution stability during run 2010, evaluated on double bar sample. The different markers represent different data acquisition periods. . . . .	124
6.10	Resolution stability during run 2010, evaluated on triple bar sample. The different markers represent different data acquisition periods. . . . .	124
6.11	Comparison between resolution obtained in 2009 and 2010 runs, evaluated on double bars sample. . . . .	125
6.12	Summary of the differences in time resolutions between 2009 and 2010 runs, evaluated on double bar sample. . . . .	126
6.13	Comparison between resolution obtained in 2009 and 2010 runs, evaluated on triple bars sample. . . . .	126
6.14	$\Delta T_{e\gamma}$ distributions on radiative decay sample, for run 2010 (Provisional results). . . . .	127
6.15	$\Delta T_{e\gamma}$ distributions on radiative decay sample, for run 2009. . . . .	128

---

6.16	$\Delta z$ distributions for double bar sample, with Gaussian fit superimposed. The width and the mean of the Gaussian represent respectively the $z$ resolution and the mean distance between the impact positions on two adjacent bars. . . . .	130
6.17	Summary of the $z$ resolution as a function of bar number, evaluated on double bar sample. . . . .	130
6.18	$\Delta z$ distributions for triple bar sample, with Gaussian fit superimposed.	131
6.19	Summary of the $z$ resolution as a function of bar number, evaluated on triple bar sample. . . . .	131
7.1	Plot of the MEG blinding box. Outside the signal box, one can recognize the side-bands used for calibration purposes. . . . .	134
7.2	PDFs for $\mu^+ \rightarrow e^+ \gamma$ signal event. . . . .	137
7.3	Radiative PDFs. Panel from a) to d) represent the projection of $R_1(E_\gamma, E_e, \theta_{e\gamma}, \phi_{e\gamma})$ on each variable, while in e) it is shown $R_2(t_{e\gamma})$ .	138
7.4	PDFs for accidental background. . . . .	140
7.5	Projected distributions for each observable, containing all events in the analysis window. A solid line shows the likelihood functions fitted to the data. . . . .	141
7.6	Schematic representation of the construction of 90% confidence level contour by Feldman-Cousins approach. . . . .	145
7.7	Confidence level as a function of the expected number of signal events.	145



# List of Tables

1.1	Quantum numbers of elementary fields in the minimal Standard Model, also including right handed neutrino and Higgs boson. The $SU(3)_C$ , $SU(2)_L$ and $U(1)_Y$ representations are given. . . . .	4
1.2	Electroweak bosons masses, Higgs boson masses and electric charge expressed as a function of the SM parameters. . . . .	5
1.3	Non-LFV and LFV muon decay modes. . . . .	8
1.4	Particle content of Minimal Supersymmetric Standard Model. . . . .	15
1.5	Historical progress of search for $\mu^+ \rightarrow e^+\gamma$ since the era of meson factories with 90% C.L. upper limits. The resolutions quoted are given as a full width at half maximum (FWHM). . . . .	25
2.1	Main characteristics of PSI cyclotron proton beam. . . . .	30
2.2	Main characteristics of $\pi E5$ beam line. . . . .	31
2.3	Main characteristic of COBRA magnet. . . . .	35
2.4	Main characteristics of Xenon as scintillating medium. . . . .	43
2.5	Summary of the experimental apparatus performances during the run 2008-2009. The resolution values are given in $\sigma$ . The achieved sensitivity and the final results are also listed. . . . .	48
3.1	Main characteristic of HAMAMATSU R5924 photomultiplier tubes. . . . .	57
3.2	Main characteristic of BC404 plastic scintillator. . . . .	61
4.1	Main characteristics of HAMAMATSU S8664-55 APD. . . . .	70
4.2	Summary of the values the parameters of eq. 4.6 and 4.8 . . . . .	76
4.3	Main characteristics of multicladding BCF20 scintillating fibers, compared with single cladding scintillating fibers (data from Saint-Gobain). . . . .	78
4.4	Transverse detector efficiency. . . . .	93
7.1	Values of the parameters that appear in eq. 7.9 (ratio given as signal to Michel). . . . .	143